ULTRATHIN FILMS AND INTERFACIAL PHENOMENA - A Comparison of Different Molecular Organization Processes

A Thesis Submitted to the College of
Graduate Studies and Research
In Partial Fulfillment of the Requirements for the
Degree of Doctor of Philosophy
In the Department of Chemistry
University of Saskatchewan
Saskatoon

By
Samuel Hilton Gyepi-Garbrah

Permission to Use

In presenting this thesis in partial fulfillment for the requirements for a Postgraduate degree from the University of Saskatchewan, I agree that the Libraries of this University may make it freely available for inspection. I further agree that permission for copying this thesis in any manner, in whole or in part, for scholarly purposes may be granted by the professor or professors who supervised my thesis work or, in their absence, by the Head of the Department or the Dean of the College in which my thesis work was done. It is understood that any copying or publication or use of this thesis or parts thereof for financial gain shall not be allowed without my written permission. It is also understood that due recognition shall be given to me and to the University of Saskatchewan in any scholarly use which may be made of any material in my thesis.

Requests for permission to copy or make any other use of material in this thesis in whole or in part should be addressed to:

Head of the Department of Chemistry
University of Saskatchewan
110 Science Place
Saskatoon, Saskatchewan
Canada, S7N 5C9

Abstract

The objective of this thesis was to investigate what effect the method of preparing a monolayer had on its organization and electrical properties. Gold electrodes were modified with alkanethiols, *n* – hexadecanethiol (HDM) and n-octadecanethiol (ODM), by (i) self-assembly (SA) from a dilute solution of the alkanethiols, and (ii) Langmuir-Blodgett (LB) deposition techniques from Langmuir films at the air-water interface, in order to compare the effects of each film-forming strategy on the resulting Self-Assembled Monolayers (SAMs) and LB films. In addition to the alkanethiol SAMs, self-assembled 11-mercaptoundecanoic acid (MUA) was also studied so as to observe the effect of the terminal group. Prior to LB deposition, Langmuir films of HDM and ODM were studied at the air-water interface on a 0.01M ammonium chloride subphase between 8 and 20°C. The films were found to be more stable at lower temperatures.

The modified electrodes were studied by Alternating Current - Electrochemical Impedance Spectroscopy (AC-EIS) and Cyclic Voltammetry (CV) in 3mM $[Fe(CN)_6]^{4-/3-}$ / 0.1M KCl over a temperature range from 15°C to 65°C. A strong temperature dependence of the films' electrical features was observed for each film. Upon heating, all films show markedly different behaviour below and above a transition temperature (T_{tr}) that is characteristic for each film. From the impedance data, it was possible to model bare gold and the alkanethiol-modified electrodes with the Randles circuit over the whole temperature range examined, but a different equivalent circuit was required to

describe the SAM of MUA-modified electrodes before heating above the T_{tr}. The results are interpreted in terms of a phase transition in these monolayers, and the possible nature of this two-dimensional (2D) phase transition is discussed.

CV measurements exhibited the same transition temperatures for a given compound in each type of film (SAM and LB film). However, a comparison of the absolute electrical properties of the LB films and the SAMs suggests that the LB deposition process, in which molecular organization precedes chemisorption, produces films that are less permeable, and therefore more highly organized than those produced by the SA process, in which chemisorption precedes molecular organization. Surprisingly, in the SAMs of HDM, and ODM, there was a second inflexion (transition) at higher temperatures that was not observed in the LB films.

In order to explain this temperature dependant phase transition, gold colloids capped with HDM and ODM, three-dimensional (3D) analogues of SAMs, were synthesized and studied by Differential Scanning Calorimetry (DSC) and Nuclear Magnetic Resonance (NMR). In general, DSC revealed the same temperature dependant phase behaviour that was observed in the 2D analogues by CV. However, in the 3D systems, the low temperature transition was observed only in the HDM system and not in the ODM system. It was thus concluded that this transition was less pronounced in the longer chain ODM system due to the curvature in the 3D system, which causes the end groups of ODM to be further apart than those of HDM in the colloid configuration. Thus

the first or (lower temperature) transition was attributed to the disordering of the alkyl chains starting from the end closest to the terminal groups.

Acknowledgments

I would like to thank my supervisor, Dr. Roberta Silerova, for all of her encouragement, help, and support during this work. Roberta, I enjoyed the learning process and a worthwhile graduate research studies under you.

I am grateful to our collaborator, Prof. P. Simon (Slovak University, Bratislava) for all his help and advice for the DSC work and also Dr. M. Landl, a former post-doc of our lab, also from the Slovak Republic.

My sincere gratitude to members of my graduate committee: Profs. R.E. Verrall, A.S. Baranski, S.G. Urquhart and C.E.J. Mitchell for their help and support throughout this work, especially Dr. Baranski with his rich knowledge of interfacial electrochemistry including ac-impedance spectroscopy.

I thank the Chemistry Department for financial assistance as a TA, and the College of Graduate Studies and Research for the award of a Graduate Teaching Fellowship. Thanks are also due to the support staff, including past and present secretaries, Pat Curie (Lab Co-ord.), Garth Parry and Devin Beaudoin (Electronic shop), Dr. Keith Brown (NMR), Ken Thoms (FT-IR), Dwight Reynaud (Stores) and his crew, Perry and Blair (Physics Machine Shop), Dr. T. Sutherland and the Kraatz Group for their help, creativity and suggestions. To Kurt Tischler, Jacquie and Germaine of the ISO, thank you also for your support.

Thanks to my lab mates especially, Jason Maley (Best Lab mate) for all his help and suggestions that I cannot quantify, and Edwige Otero.

To the Pastor, Bro. Menno Friesen and beloved congregation of Saskatoon Tabernacle I owe you a great deal of appreciation and thanks for your spiritual and physical devotion in the past six years.

To my mum and dad, brothers and sisters, as well as my in-laws, I owe you much gratitude for your help since I left for further studies in Saskatoon.

I would like to thank my wife Martha and daughters: Marrion and Meda for their loving support, patience and understanding throughout the course of my studies. You sacrificed so I could pursue this endeavour. And it is with a gladdened heart, I say, "All the regular shifts you endured has been rewarding".

Dedication

This thesis is dedicated to

The work of the Ministry of all in the service of the

Lord Jesus Christ

...In whom are hidden all the treasures of wisdom and Knowledge...

Colossians 2: 3

And

To my wife

Martha Gyepi-Garbrah

And my daughters,

Meda Nana Esi Nyamekye Gyepi-Garbrah and

Marrion Nana Araba Nyamekye Gyepi-Garbrah

Table of Contents

List of Tables

List of Figures

List of Abbreviations

3D	Three-dimensional
A	Area
A	Electrode surface area
α	Electron transfer coefficient
A_c	Critical area
AC-EIS	Alternating current-Electrochemical Impedance Spectroscopy
A_d	Decrease in the area occupied by the monolayer on the water surface during transfer
AFM	Atomic force microscopy
A_o	Limiting molecular area per molecule
A_s	Area of a substrate
B	Strength of the magnetic field at the nucleus
BAM	Brewster angle microscopy
BAS	Bioanalytical systems
C	Capacitor/capacitance
CE	Counter electrode
CA	Chronoamperometry
C_{dl}	Double layer capacitance
C_{ox}	Bulk concentration of oxidized species in solution
C_p	Heat capacity at constant pressure
CPE	Constant phase element
C_{red}	Concentration of reduced species in the bulk solution
CV	Cyclic voltammetry or Cyclic voltammogram
CVA	Chemical vapour deposition
δ	Bending vibration
ΔE	Potential difference
ΔH	Total heat or enthalpy change
D_{ox}	Diffusion coefficient of the oxidant
ΔQ	Difference between Q_s and Q_R

DSC	Differential Scanning Calorimetry
ΔT	Difference in temperature
E	Cell potential,
e	Pure sinusoidal voltage
E	Amplitude
e^-	Electron charge
$E_{1/2}$	Half-wave potential
E_f	Final Potential
E_i	Initial Potential
EIS	Electrochemical Impedance Spectroscopy
E^o	Standard electrode potential
E_{pa}	Anodic peak potential
E_{pc}	Cathodic peak potential
E_s	Switching Potential
ET	Electron transfer
E_{upd}	The potential for deposition of copper atoms on gold
F	Faraday constant
ϕ	Phase angle
FID	Free induction decay
ϕ_m	Absolute electrostatic potentials for the metal electrode
FMa	Ferrocene monocarboxylic acid
FRA	Frequency response analyzer
FRD	Frequency response detector
ϕ_s	Absolute electrostatic potentials for the bulk solution
FTIR	Fourier-transform Infrared
γ	Surface tension of film-covered surface
GIA	Grazing Incidence Angle
GIXRD	Grazing Incidence Synchrotron X-ray Diffraction
γ_m	Magnetogyric ratio
γ_o	Surface tension of clean subphase
Γ_{ox}	Surface concentration of Ox adsorbed on the electrode of area **A**
HDM	n-hexadecanethiol

I	Current
i_c	Total charging current
IHP	Inner Helmholtz plane
i_l	Limiting current
i_p	Peak current
I_p	In-plane vibrations
I_{pa}	Anodic peak current
I_{pc}	Cathodic peak current
J	Complex number
L	Inductance
LB	Langmuir-Blodgett
LSV	Linear Sweep Voltammetry
MUA	11-Mercaptoundecanoic Acid
N	Number of moles of converted species
$\boldsymbol{N}$	Mean aggregation number
N	Number of electrons exchanged between one molecule of reactant species and the electrode
ν	Scan/sweep rate
ν_{as}	Antisymmetric stretching vibration
NEXAFS	Near edge x-ray absorption spectroscopy
NLLSF	Non-linear least square fit
NMR	Nuclear magnetic resonance
ν_s	Symmetric stretching vibrations
ν_{sv}	Stretching vibration
OD	Octanethiol
ODL	Octadecanol
ODM	n-Octadecanethiol
OHP	Outer Helmholtz plane
Ox	Oxidizing species
π	Surface pressure
Q	Electrical charge
θ	Angle between the direction of the applied field and the axis of nuclear rotation I

Q'	CPE related to the double layer capacitance
Q''	CPE also called Warburg impedance, related to diffusion and associated with the mass transport
Q_{ad}	Charge associated with the reduction of the adsorbed species
Q_M	Charge on the electrode surface
Q_r	Power to the reference in a DSC experiment
Q_s	Power to the sample in a DSC experiment
R	Gas constant
$\mathbf{R_1}$	Solution resistance
R	Pure resistor/resistance
$\mathbf{R_2}$	Activation resistance
$\mathbf{R_3}$	Extra resistance associated with the modified electrode of MUA
Red	Reducing species
RE	Reference electrode
RF	Radio-frequency
SA	Self-assembly
SAMs	Self –assembled monolayers
SHE/NHE	Standard/normal hydrogen electrode SHE/NHE
STM	Scanning tunnelling microscopy
T	Time
T	Temperature
T_m	The characteristic peak of such a plot provides the temperature (T_m) at which the reaction is half-complete
TR	Transfer ratio
$\mathbf{T_{tr}}$	Phase transition temperature
UPD	Underpotential deposition
UV	Ultraviolet
VDW	van der Waals
ω	Angular frequency
WE	Working Electrode
X_1	Distance
X_c	Capacitive reactance
X-PEEM	X-ray Photoelectron Emission Microscopy

$\mathbf{Z}(\omega)$	Impedance of a circuit
Z_{Im}	Imaginary parts of the impedance
Z_{Re}	Real parts of the impedance

Chapter One – Introduction and Review

1.1. Introduction to Interfacial Phenomena and Ultrathin Films

In the study of high performance and speciality organic molecules, there is great interest in both surface and bulk properties of the materials.[1] In many applications, the performance of an organic material is determined by its surface structure and interfacial interactions. However, organic materials are difficult to characterize and their interfacial interactions are complex.[2] Ultrathin organic films formed on metal surfaces and at the air-water interface are promising models for fundamental studies aimed at understanding the influence of surface chemical structure on interfacial interactions. When the molecules in ultrathin films are highly oriented, their macroscopic properties can be quite different from those of randomly oriented bulk materials. To explore the effect of molecular orientation, one has to identify the processes leading to the orientation. These processes are collectively referred to as molecular organization.

Molecular organization is a process whereby an ensemble of uncorrelated molecules, such as is found in liquid or gas phase, forms an organized superstructure.[3] Everyday examples of this range from the formation

of crystals in supersaturated solutions to the spontaneous formation of complex biological structures in living systems.[4] The essence of these processes is that no external intervention is necessary to guide them once they are started, that is the necessary rules for organization are coded into the molecular structure and conditions themselves. Furthermore, since the process is thermodynamically favourable, the resultant structures are quite stable within environments similar to the original one of formation.[3] In molecular organization, the molecules involved are often surfactants. Surfactants are amphiphilic molecules having distinct hydrophobic and hydrophilic regions. These regions are: a long hydrophobic tail that has a high affinity for oil or any non-polar medium, and a hydrophilic headgroup, which has a high affinity for polar media. The hydrophilic headgroup may be non-ionic, cationic, anionic, or zwitterionic. The hydrophobic moiety can be of different lengths, may contain unsaturated bond(s)), and/or may consist of two or more chains. Such molecules can organize in two-dimensional (2D) and/or three-dimensional (3D) systems.

1.1.1 Two- and Three-Dimensional Organized Systems

Organized 2D assemblies are systems that organize at a fixed plane or interface. Some important 2D systems include micelles(depending on shape and size of molecules)[5,6] or hemimicelles, self-assembled monolayers (SAMs) and Langmuir-Blodgett (LB) films on solid planar surfaces, Langmuir films at the

air-water interface and lipid membranes.[7] Organized 3D assemblies on the other hand are systems that organize such that they are spatially oriented and can be described in 3 dimensions in an x-y-z plane depending upon the relative values of the x,y or z scales. Figure 1.1 illustrates some 2D and 3D systems.

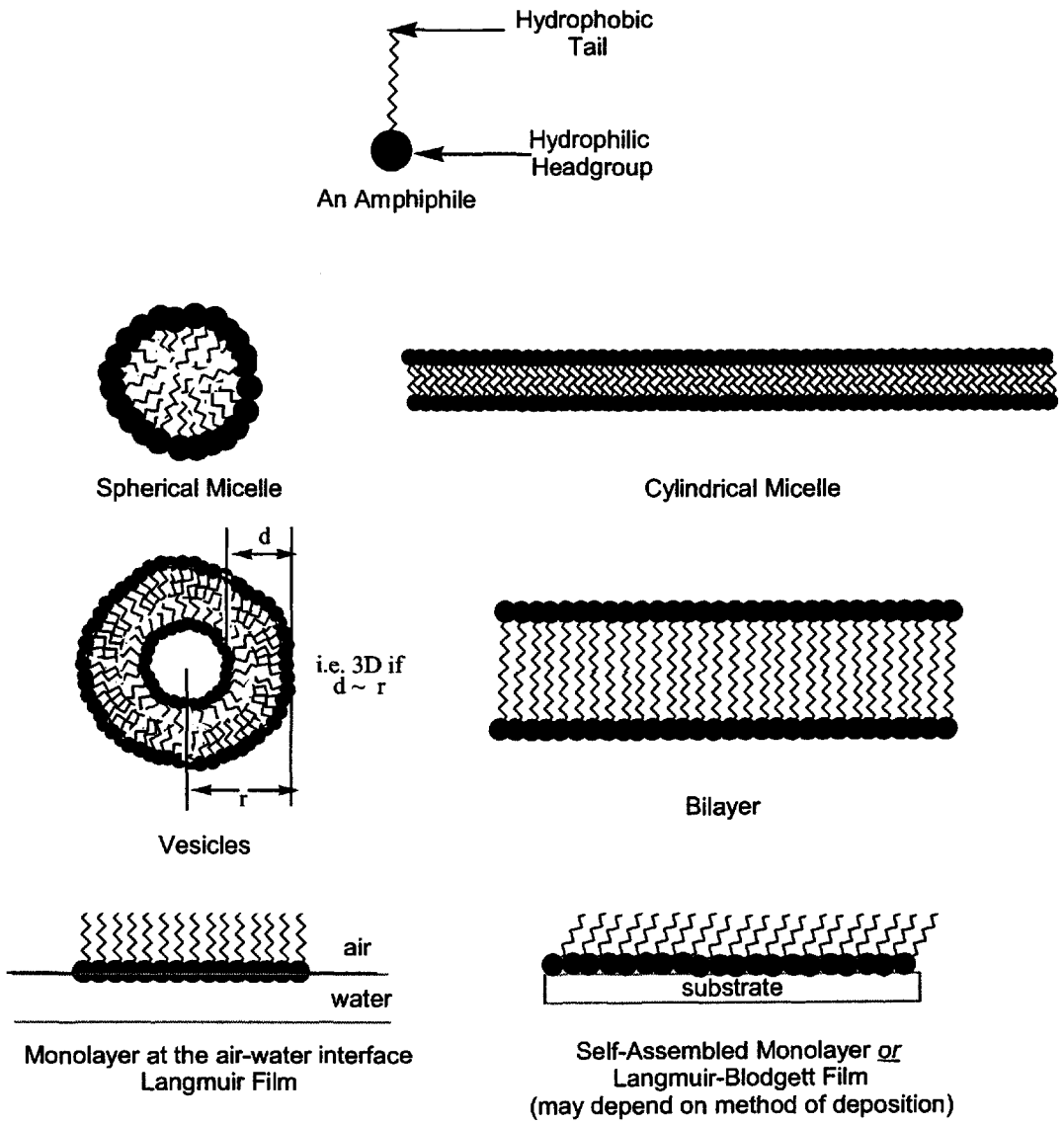

Figure 1.1. Illustration of some 2D and 3D systems.

These 3D organized systems include molecular systems such as micelles,[4,8-10] microemulsions,[4,9] mono- and bilayer vesicles,[4,11] nanopores,[12-19] and metal-stabilized colloids (3D SAMs).[20-24] It is worthy of note that 3D systems of metal-stabilized colloids are defined as molecules that assemble on gold, silver, or silica colloidal particle surfaces where the surface of the particles is curved on a nanoscale. These are called 3D SAMs to distinguish them from SAMs on planar surfaces.

Although the physicochemical characteristics of 2D and 3D systems vary widely, they share certain features such as molecular level organization and well-ordered architecture.[25,26] Indeed, some systems will form both 2D and 3D systems depending on various experimental conditions.[27] For example, micelles can form either 2D or 3D system, depending on conditions such as the concentration of the surfactant in solution. SAMs can do the same depending on the geometry of the underlying substrate.

Self-assembly (SA) of objects at the nanometer length scale is a topic that is currently attracting a great deal of attention.[28,29] Surfactant molecules that self-assemble on metal surfaces have proved to be an excellent method for obtaining ordered arrays of nanocrystals. Examination of 2D and 3D assemblies will be made in the next two sections.

1.1.1.1 Two-Dimensional Systems

Organized 2D systems are generally defined as monolayers of molecules fixed at an interface. This interface can be a liquid-vapour interface, a liquid-liquid interface, a solid-liquid interface or a solid-vapour interface.

One such system is formed when Langmuir films assemble, usually at the air-water interface. The formation of Langmuir films is often characterized by an isotherm, a plot showing dependence of surface pressure (π) on the mean molecular area (MMA). Ideally it can be divided into three main parts: a gaseous, a liquid (condensed expanded) and solid region. In the gaseous region, Langmuir films are often thought of as being similar to a 2D gas in which molecules are relatively separated from one another. In the solid region, the film can be considered, as a 2D solid. While these simple models are useful aids in understanding 2D systems, the actual behaviour is often more complex. A detailed study of monolayer formation and film structure at the air-water interface can provide insight into how molecules organize in two dimensions. Analyzing the structures of different phases and structural changes during phase transitions can reveal a great deal about the dynamics of molecular organization. It is this understanding of molecular organization dynamics that directs the design of amphiphiles and allows construction of thin films with useful properties.

SAMs are ordered molecular assemblies formed by the adsorption of an active surfactant on a solid surface.[1,30] The simplicity of this process makes SAMs inherently manufacturable and thus technologically attractive for building superlattices and for surface engineering. A spontaneous chemical assembly process at the interface indicated by the change in Gibbs energy drives order in 2D-SAM systems, as the system approaches equilibrium. Although SAMs can be formed from many different types of surfactant molecules, the most frequently used and well-studied molecules in SAM investigations are functionalized long-chain hydrocarbons.

1.1.1.2 Three-Dimensional Systems

One system that can switch from 2D to 3D assemblies is a micelle system. In aqueous solution, surfactant molecules can reversibly assemble into a variety of spatially organized structures. A common feature in these systems is the tendency for the hydrophobic tails of the surfactant to organize them so as to minimize contact with water. The surfactant association is driven by the balance between weak hydrophobic interactions between tail groups and electrostatic forces, repulsive or attractive, depending upon whether the head groups are charged or uncharged. As well, the degree of counter ion association of micelles plays an important role in determining the optimum energy conditions for self-organization of charged amphiphiles. Depending on

the surfactant concentrations, a variety of highly-ordered structures can form (i.e., cubic, hexagonal or lamellar phases), as well as some disordered phases at lower concentrations. When the concentration of surfactant exceeds a critical concentration (the so-called critical micelle concentration (cmc)), structures such as a spherical micelle often form (Figure 1.1).

Micelles are loose aggregates of amphiphile molecules in water or organic solvents. In the field of micelle research, reference is often made to a critical temperature (the Krafft point). Below the Krafft temperature, clear micellar solutions become turbid and the amphiphile molecules form 3D hydrated liquid crystalline phases. Below the cmc, the surfactant exists in monomeric or small aggregates. Above the cmc, the micelles of mean aggregation number ***n*** are formed; ***n*** essentially remains stable over a wide range of concentration for spherical micelles only. When ellipse or rod-like micelles are formed, ***n*** can increase. Micellar solutions are stable and remain clear over long periods of time although the individual micelle usually falls apart within a few milliseconds.[31] The reason for this is the fact that the interaction between solvent molecules is stronger than the interaction between the solvent and the solute.[32] This effect alone would lead to a precipitation of the solute, but the head groups are strongly hydrated and repulse each other. The hydration and sterric forces[32] which are made responsible for this repulsion effect, prevent cyrstallization above the Krafft point and also above cmc. Where the formation of 3D crystals is impeded, the smallest possible droplet is formed, removing the

alkyl chains from the solvent. The interactions between solvent molecules are therefore disturbed to a minimal extent, allowing the head groups to be solvated with a minmal entropy loss. Micelles formation therefore only occurs as a result of a solvation of head groups and non-solvation of a solvophobic core.[33] Note, the reverse effect can also happen when the terminal end is solvated producing reverse micelles.[34]

Vesicles (Figure 1.1), another important 3D system, are sealed, extremely thin (< 10nm), and often spherical bilayers.[32] The same solvophobic effect, that cause micelles to form are responsible for holding the molecules together, and solvation forces together with surface undulations prevent crystallization. The vesicle membrane is essentially fluid in character. A commonly used and stable vesicle system is obtained from oleate or forms a 1:1 fatty acid-fatty alcohol mixture. Supramolecular ordering within vesicle bilayers is negligible, but synthetic vesicles can be organized because they are long-lived and have very low critical concentrations (< 10^{-5} M).

Another form of 3D organized system is the alkanethiol-stabilized metal colloid system. (Figure 1.2) The way in which these systems organize themselves depends on the type of metal (substrate) and its metal core diameter, and the nature of the surfactant. Thiolized nanocrystals readily arrange into 3D arrays on removal of solvent.[35]

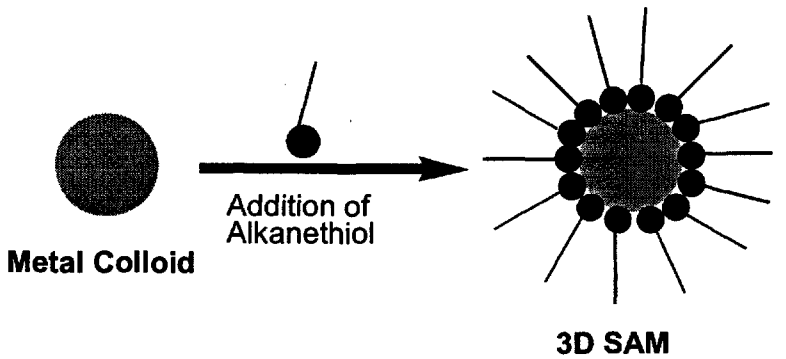

Figure 1.2. Surface modification of colloidal nanoparticles to form 3D SAMs.

In the original report of these systems, Brust and co-workers demonstrated that alkanethiol molecules spontaneously self-assemble on the surface of colloidal gold particles.[23] It was demonstrated that aqueous chloroaurate ions transferred to an organic phase using phase-transfer molecules could be reduced in the presence of the alkanethiol molecules in the organic phase, leading to extremely stable thiolized colloidal gold particles.[23] Figure 1.2 illustrates a simple diagram of this 3D SAM. Such surfactant-stabilized metal colloids can be easily precipitated out of solution and redissolved in organic solvents without any significant variation in the particle size distribution.

Several similar systems have since been reported, including gold and silver particles coated with alkanethiol,[36-41,41,42] aromatic thiol,[24,43-46] alkylamine,[47] dialkylsulfide[48] and cyclodextrin molecules.[49,50] Terminally functionalized molecules may also be self-assembled on colloidal particle surfaces and, as in the case of terminally functionalized 2D SAMs, such surface-

derivatized colloidal particles have a number of exciting applications.[20,21,42,44,45,51,52]

As illustrated in Figure 1.2, the further the hydrocarbon chains extend away from the colloidal particle surface, the packing of the hydrocarbon chains in the 3D SAMs on the colloidal particle surface decreases. It is therefore clear that there would be considerable disorder in the terminal methyl groups of 3D SAMs, for longer chains.

A number of interactions that operate in 2D SA of molecules on planar surfaces may also be present in the 3D SAMs. Electrostatic interactions, hydrogen bonding, covalent bonds with surfaces, are some of the forces that drive the organization of 3D SAMs. [53] One of the simplest ways to produce monolayers of 3D SAMs is by the solvent-evaporation technique. The synthesis and stabilization of the colloidal particles in an organic medium enables facile formation of hexagonally close-packed nanoparticle arrays on a range of surfaces by simply dropping the colloidal solution on the desired surface and evaporating the solvent.[41,54,55] It has been observed that the nanoparticles organize into close-packed structures within annular rings.[56] This ring formation has been explained in terms of a thermodynamic model. [57,58]

1.1.2 Objective, Strategy and Reason for this Work

1.1.2.1 Objective

The main objective of this thesis work is to compare and contrast different molecular organization processes for some alkanethiol modified electrodes formed by the SA and LB deposition methods. The primary alkanethiols used to modify the electrodes are n-hexadecanethiol (HDM) and octadecanethiol (ODM). (Figure 1.3). This objective was approached in several different ways. Taken together, these constitute the strategy, and are listed below.

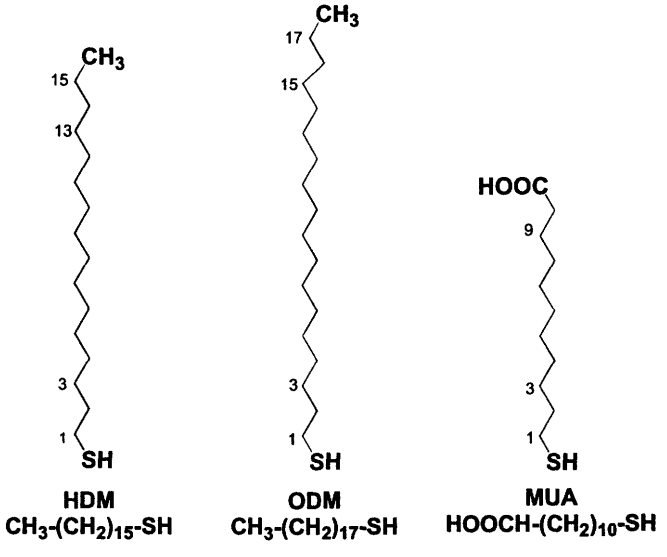

Figure 1.3. Alkanethiols used for this study.

1.1.2.2. Strategy

1. Two methods - SA and LB deposition - were used to prepare densely packed monolayers of the same molecules on the same substrates.
2. All films were investigated by observing the effect of each monolayer on the redox activity of a probe molecule in solution as a function of temperature. Cyclic Voltammetry (CV) and Alternating Current - Electrochemical Impedance Spectroscopy (AC-EIS) were used for these investigations.
3. A thiol with a polar group (-COOH) at the end of the hydrophobic tail (11-Mercaptoundecanoic Acid) (MUA) (see Figure 1.1) was also studied to determine the importance of the end group in defining the properties of the monolayers.
4. Alkanethiol-capped gold colloids (3D SAMs) were synthesized as 3D analogues of the monolayers, in order to use techniques not normally applicable to 2D systems - Differential Scanning Calorimetry (DSC) and Nuclear Magnetic Resonance (NMR).
5. LB films of alkanethiols on glassy carbon electrodes were studied using CV and AC-EIS to determine the role of chemisorption in defining the properties of the monolayers.

1.1.2.3. Reason for this Work

Alkanethiol compounds and their derivatives are revealing themselves to be an exceedingly important and widely explored class of compounds for different applications, particularly in electrooptical- biomedical-, and sensor-related areas.[59,60] Their attraction lies in their ability to form chemisorbed monolayers on gold surfaces with strong lateral intermolecular forces, known as SAMs when they are formed through a process of SA.[61-65] In addition, they can be derivatized in order to attach a wide range of chemical functional groups to the surface below, a template to surface modification.[66,67]

Chemisorption of alkanethiols (RSH) on clean gold (Au) is thought to proceed through formation of a Au(I)-thiolate (RS^-) species. The reaction may be considered as an oxidative addition of the S-H bond to the gold surface, followed by a reductive elimination of hydrogen. When a clean surface is used, the hydrogen atoms probably form a hydrogen molecule. This can be deduced from the fact that monolayers can be formed from gas phase,[23,68,69] in the absence of oxygen. Reaction is given from Scheme 1.

$$R - S - H + Au^{o}_{n} \longrightarrow R - S^{-} Au^{+} + \tfrac{1}{2}H_2 \quad \text{(Scheme 1)}$$

The combination of hydrogen atoms at the metal surface to yield H_2 molecules may be an important step in the energetics of the overall

chemisorption.[30] That the adsorbing species is the thiolate (RS^-) has been shown by X-ray photoelectron spectroscopy,[61,70-72] Fourier transform-infrared (FT-IR) spectroscopy,[73] electrochemistry[72] and Raman spectroscopy.[74-76]

The basic "technology" of self-assembly of thiol derivatives onto gold is now well known, and a successful protocol for film formation well established.[77-81] However, it can be argued that certain critical experimental parameters have been overlooked in the development of this protocol. In particular, the temperatures at which alkanethiol monolayers on gold are prepared and investigated are, with a few exceptions,[82,83] very loosely reported. The results presented here show clearly that this is unwise, as temperature can have a drastic and irreversible effect on several key features of these monolayers. The effect of potential is also known to effect features of these monolayers.[84-86]

As mentioned above, SA is a convenient route to densely packed well-ordered organic monolayers. SA involves two consecutive processes, chemisorption and subsequent lateral organization. For long chain n-alkanethiols adsorbed onto gold, the chemisorption occurs when the gold surface reacts with the thiol moiety, displacing hydrogen and forming a gold-thiolate bond.[70,87-91] The subsequent molecular organization is driven by lipophilic interactions between neighbouring alkyl chains, and occurs more slowly than the chemisorption, often taking up to days.[1]

Another route to the formation of organized monolayers is LB transfer, which consists of molecular organization at the air-water interface into Langmuir

films, followed by transfer onto the desired substrate by the LB deposition technique.[1,92-94] Some long chain surfactants such as octadecanol can be compressed at the air-water interface to form well-ordered Langmuir monolayers, but attempts to transfer these films onto hydrophilic solid supports such as gold surfaces to produce good passivating films (in the presence of redox probes to block electron transfer) have been largely unsuccessful.[95,96]

Presumably if the additional stability offered by chemisorption could be incorporated into the LB deposition process, the resulting LB films would have greater integrity. The reaction of thiols with gold offers one possibility in this regard, but this would involve forming Langmuir films of alkanethiol derivatives, and depositing these onto gold surfaces. Alkanethiols are notoriously unstable at the air-water interface.[97-99] LB transfer of ODM at the air-water interface produced LB films that were insufficiently compact to form passivating films on gold surfaces,[95,99] raising doubts about the true nature of the transferred film. No Langmuir or LB monolayers of any other alkanethiols have been reported. Thus, to date, LB techniques have not produced good, passivating monomolecular films of alkanethiols on gold electrode surfaces.

CV has previously been used to study phase transitions in two SAMs of alkanethiols [HS - C_nH_{2n+1} n = 16, 18] on gold electrodes.[82] The effect of the monolayers on the redox activity of a probe molecule in solution was studied as a function of temperature. Any inhibition of the probe molecule's redox activity was attributed to an impermeability of the monolayer to charge transfer

processes. An increase in observable redox activity was attributed to an increase in the permeability of the monolayer, which itself was attributed to a 2D phase transition.

However, in CV the effect of certain interfacial parameters such as the solution resistance, double layer charging, and currents due to diffusion and other surface processes occurring in the SAM are difficult to evaluate quantitatively from CV data because they are not directly observed.[100] Furthermore, the irreversible nature of the increase in permeability does not support the idea of a phase transition, and raises the possibility of thiol desorption.

AC-EIS is an important and powerful method for studying surface processes. As such, it targets the surface of the SAM, and also the SAM-solution interface, exclusively and the interfacial parameters outlined above are observed more explicitly. Therefore, it produces results faster than CV, giving direct electrical readout of activity at the surface of modified electrodes. It involves the measurement of the frequency dispersion of the impedance or admittance of a system.[101-103] One advantage is that AC-EIS measurements are performed in the frequency domain, while CV measurements are taken in the time domain. In AC-EIS, the frequency dispersion of the complex impedance may be analysed by modelling the interface as a collection of ideal circuit elements with the physical model being a simple equivalent circuit.[104] The various circuit elements can then be related to features of the system under

study such as ionic conductivity, solution resistance, double layer capacitance, and Warburg diffusion. The final equivalent circuit parameters provide a complete description of the electrical properties of the interface. The specific advantages of AC-EIS over CV as a tool for the investigation of SAMs have been outlined in more detail elsewhere.[84,105]

Alkanethiol-capped gold colloids are 3D analogues of the SAMs on planar surfaces. (2D SAM)[85] In order to overcome the limitations to the structural and dynamic studies that can be performed on the 2D SAMs, 3D SAMs were synthesized, which could be characterized by FT-IR,[86,106-112] NMR[36,86,111,113-117] and DSC[36,86,110,111,118119] techniques. In particular, the irreversible nature of the temperature phase behaviour is investigated in the 3D SAMs using DSC and NMR.

1.2 Methods of Monolayer Formation

The modification of surfaces involves the process of attaching molecules to a substrate surface by physisorption or chemisorption.[120] Monolayers on solid substrates can be prepared by many different methods including SA,[1,30,62,63,85,88,121-125] the LB deposition,[1,95,126-134] Langmuir electrodeposition,[135] and Chemical Vapour Deposition.[136] Monolayers can also be prepared by Langmuir films of various molecular systems at the air-water interface.[1,95,107,130,137-146] However in this work, only SA and LB deposition are

employed. LB layers and SAMs have been studied extensively over the past decade.[1] Interestingly, they have seldom been compared directly, partly because systems amenable to one technique are often not conducive to the other, as will be discussed.

1.2.1 Self-Assembly

The formation of monolayers by SA of surfactant molecules is one example of the general phenomena of SA. In nature SA results in supermolecular hierarchical organization of components to produce very complex systems.[147] In the perspective of this study, SA is the process by which molecular assemblies are formed spontaneously by the immersion of an appropriate substrate into a solution of an active surfactant in an organic solvent. SA can also occur in solution between molecules without the presence of a solid substrate. The resulting assemblies are called SAMs. SAM formation involves a two-step process - the first is an exothermic process, namely chemisorption of the headgroup moiety on the substrate surface. In the exothermic head group-substrate interactions, molecules try to occupy every available binding site on the surface. This interaction has energies of 167-190 $kJmol^{-1}$.[148] It is this spontaneous molecular adsorption that bring molecules close enough together to allow for subsequent short-range, dispersive, London-type, van der Waals (VDW) forces that constitutes the second step. Typically,

the second step involves lateral organization of alkyl chains and the head groups through weak VDW forces and other molecular interactions, and has energies about less than 10 $kJmol^{-1}$.[1] Even though VDW forces are the dominant forces for simple alkyl chains (C_nH_{2n+1}), when a polar bulky group is substituted into the alkyl chain there can be long-range electrostatic interactions that, in some cases are energetically more important than the VDW attractions.

SAMs have been formed on every common electrode material. The common electrode metals- gold, silver, platinum and mercury- have all been coated with SAMs containing sulphur compounds, especially thiols, disulphides, and sulphides. Sulphur's affinity for these metal surfaces explains why they are so popular for the formation of SAMs. These sulphur compounds most commonly contain alkyl chains of varying lengths. Less common are SAMs based on adsorption of isonitriles onto gold and copper surfaces.[149,150] Chlorosilanes with long alkyl chains self-assemble on doped metal oxides such as SnO_2,[151] silicon with a thin oxide coating[152] and gold without any oxide after proper prehydration.[153,154] Generation of alkane radicals near an oxide-free silicon surface results in the formation of a densely packed SAM in which the methylene carbon is directly bonded to a silicon surface atom.[155,156] Though these and many other SA systems have since been investigated, monolayers of alkanethiolates on gold are probably the most studied SAMs to date.[1,30] There are many advantages of thiol-based SAMS over other systems.

The first advantage of the alkanethiol system is the ease with which SAMs are formed. A monolayer is deposited on the order of seconds to minutes. The SA does not require anaerobic or anhydrous conditions, nor does it require a vacuum and is relatively insensitive to the choice of solvent. While organic-free metal surfaces are desirable, the high affinity of the sulphur for the metal enables the assembling layer to displace more weakly adsorbed impurities. Curvature or accessibility of the metal surface is not a factor; substrates can range from macroscopic to submicroscopic, and from smooth to highly porous.

A second advantage arises from the reaction of sulphur with the metal and the strength of the bond formed, which is about 167.5 $kJmol^{-1}$.[148] In addition there is the need for extra energy to penetrate into monolayer to break the bond. Because of this, SAMs are exceedingly robust. For example, they can survive prolonged exposure to vacuum. It is also possible to have a wide range of functional groups in the adsorbing molecule without disrupting the SA process or destabilizing the SAM. For ω-substituted alkanethiols alone, a great range of terminal substituents have been investigated including alkanes (linear, branched, perfluorinated, perdeuterated), alkene, alkyne, aromatic, halide, ether, alcohol, aldehyde, carboxylic acid, amide, ester, amine and nitrile.[157-159] The "body" of the molecule may contain, for example, heteroatoms,[160-163] aromatic groups,[164-166] conjugated unsaturated links,[167-169] and other rigid rod structures,[170-172] sulfones,[163,173] or amides.[174,175] If the SAM is uniform in

composition and densely packed, then a single functional group is exposed on the external surface.[176]

1.2.1.1 The Molecular Interactions that Lead to Self-Assembly

For a stable monolayer to be formed, three main interactions must be considered. These interactions determine the monolayer structure. They are

(1) adsorption of the surface-active groups onto the substrate by chemisorption

(2) the interactions between the alkyl chains, mainly by hydrophobic interactions

(3) the interaction between the terminal functional groups themselves.

1.2.1.1.1 Chemisorption

The adsorption of the surface-active sulphur group onto the substrate is by chemisorption. Chemisorption (or chemical adsorption) is adsorption in which the surface and adsorbate form a covalent bond. The problem of distinguishing between chemisorption and physisorption is basically the same as that of distinguishing between chemical and physical interactions in general. The following are some features useful in recognizing chemisorption:

(a) the phenomenon is characterized by chemical specificity;

(b) changes in the electronic state may be detectable by suitable physical means (e.g. ultra-violet., infrared or microwave spectroscopy, electrical conductivity, magnetic susceptibility);

(c) the chemical nature of the adsorptive(s) may be altered by surface dissociation or reaction in such a way that on desorption the original species may not be recovered; in this sense chemisorption may not be reversible;

(d) the energy of chemisorption is of the same order of magnitude as the energy change in a chemical reaction between a solid and a fluid: thus chemisorption, like chemical reactions in general, may be exothermic or endothermic and the magnitudes of the energy changes may range from very small to very large;

(e) the elementary step in chemisorption sometimes involves an activation energy;

(f) when the activation energy for adsorption is large (activated adsorption), true equilibrium may be achieved slowly or in practice not at all. For example, in the adsorption of gases by solids, the observed extent of adsorption, at a constant gas pressure after a fixed time, may in certain ranges of temperature increase with rise in temperature. In addition, where the activation energy for desorption is large, removal of the chemisorbed species from the surface may be possible only under

extreme conditions of temperature or high vacuum, or by some suitable chemical treatment of the surface;

(g) since the adsorbed molecules are linked to the surface by valence bonds, they will usually occupy certain adsorption sites on the surface and only one layer of chemisorbed molecules is formed, known as the monolayer.

1.2.1.1.2 Intermolecular Interactions

Intermolecular forces are the forces between molecules or ions and molecules. Those not involving ions are collectively known as VDW forces. In SAMs, these interactions can exist between the terminal functional groups and the outer medium, between adjacent terminal groups, between adjacent chains, and also between chains. Chain-chain interactions, including hydrogen bonding and dipole-dipole interactions can cause chains to be very tightly packed.

The various types of intermolecular forces that have been observed in SAMs, the principal factors responsible for interaction, and the energies involved are summarised in Table 1.1.

One of the most important interactions that can occur in SAMs is hydrogen bonding, which is a form of dipole-dipole interaction. This interaction occurs primarily between terminal groups as illustrated in Figure 1.4.

Table 1.1. Summary of intermolecular forces

Type of Interaction	Principal Factors Responsible for Interaction	Approximate Magnitude of Energy (kJ/mol)
Ion-Dipole	Ionic charge; dipole moment	400 – 600
Dipole-Dipole	Dipole moment	5 -25
Dipole - Induced Dipole	Dipole moment; polarizability	2 - 10
Induced Dipole-Induced Dipole	Polarizability	.05 - 40

Hydrogen bonding is an intermolecular dipole-dipole interaction between alkanethiols with terminal head groups containing a hydrogen atom covalently bonded to a very electronegative atom in one molecule. This hydrogen atom is attracted to the non-bonding electrons of an electronegative atom (generally F,O,N) of a neighbouring molecule.[177]

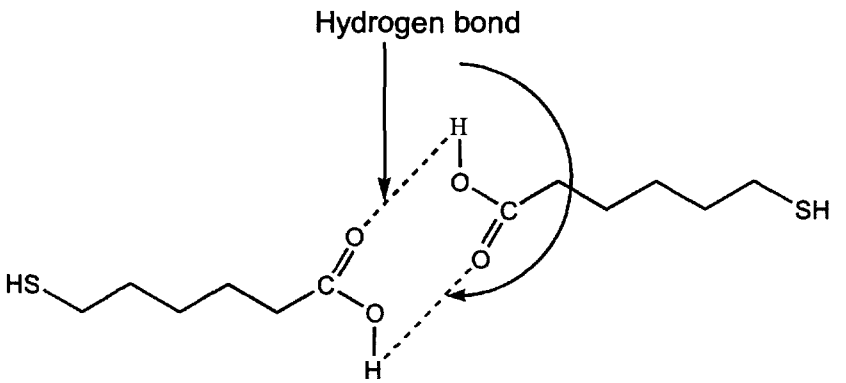

Figure 1.4. Intermolecular H-bonding between the terminal carboxylic acid groups in an ω-mercaptocarboxylic acid.

Another VDW force, which plays a central role in molecular SA, is the hydrophobic interaction. This interaction describes the strong attraction between hydrophobic portions of a molecule in the presence of polar solvents like water. For example, the VDW interaction energy between two methyl groups in free space is 2.5 x 10^{-21}J, while in water it is –14 x 10^{-21}J.[32] The change in sign is due to the hydrophilicity of water. Hydrophobic alkyl chains may interact by this phenomenon, which can act as a driving force after chemisorption, helping the molecules to organize into a well-ordered compact SAM.

1.2.1.2 Substrate and its Preparation

Gold is the most popular substrate for thiol SAMs. Owing to its noble character, and can survive harsh chemical treatments, which remove organic contaminants. Gold substrates may be composed of bulk gold, either polycrystalline or single crystal, or thin films deposited on various secondary substrates. The choice of secondary substrate is often dictated by the application of the SAM. For a highly-oriented crystalline SAM, a single crystal and atomically flat substrate is required. When the SAMs function is to block access of molecules to the gold, a minimum density of pinholes is sought. While the origin of pinholes in SAMs is still unclear, impurities such as inorganic oxides and holes situated in defects sites on substrates are likely sources. Hence, the

purity of the gold surface appears to be more important than its smoothness.[178] Both requirements are met by evaporated or sputtered gold films (typically 50-200 nm thick) on glass, silicon or cleaved mica substrates. To improve the adhesion of the gold film to the oxide surface, a thin (1-5 nm) layer of chromium or titanium is often deposited first. There is evidence that defects in the underlayer of Cr or Ti can be a source of pinholes in the final SAM.[179] If the gold film is annealed at high temperatures, then the gold surface is largely composed of Au(111) domains. Golan et. al have reported a comparison of grain size and crystalllinity of thermally evaporated and sputtered gold on glass, silicon and cleaved mica substrates.[180] Some subtle effects of the substrate identity and gold deposition protocol on the resulting SAMs have been noted.[180-182] Procedures are available for the preparation of ultraflat[183,184] or optically transparent gold substrates.[185,186] Cleaning and etching steps are often part of the deposition protocol. For bulk gold heating, the gold in a gas or air flame results in a hydrophilic surface indicating that all organics have been removed. Electrochemical cycling into the oxide formation region in dilute acid functions as both a cleaning and an annealing process; the resulting voltammogram provides an assay of the cleanliness and crystalllinity of the gold and its true surface area.[187] Etching the bulk gold in dilute aqua regia removes polishing damage and improves the blocking properties of the SAM.[188] Evaporated or sputtered gold films are frequently immersed into the thiol deposition solution as soon as they are removed from the gold deposition unit. Despite the fact that the gold

surfaces are hydrophobic and therefore contaminated, SAM deposition proceeds unimpeded. Alternatively, organic contaminants can be removed via exposure of the gold to a powerful oxidant. Popular oxidants include "piranha" solution (a 1:3 mixture of 30% hydrogen peroxide and concentrated sulfuric acid at ca. 100°C), oxygen plasma, and ozone generated by UV (ultraviolet) light. These treatments leave a surface oxide which can become trapped under a self-assembling thiol monolayer, and which can affect the properties of the SAM deleteriously.[189,190] An ethanol rinse rapidly removes the gold oxide. The other coinage metals (silver, copper, and platinum) have been used as substrates for thiol SAMs. For freshly evaporated silver or copper thin films, surface oxides exist prior to SAM deposition. The SA process appears to remove the oxide layer from silver but not from copper, yielding lower quality SAMs on the latter substrate.[191-194] The oxide layer can be removed by an acid soak[195] or electrochemical reduction.[196,197] A recent innovation has been to form a single atomic layer of copper or silver on a gold surface by underpotential deposition (UPD) and to assemble the monolayer on the UPD layer.[198-201] There is growing evidence that the bond between the sulfur and the UPD atom is stronger than the bond between the sulfur and gold atoms, resulting in a more stable SAM. Liquid mercury avoids the issues of surface crystalllinity, roughness and morphology, but is easily oxidized in the presence of thiols. It is possible to prepare homogenous and densely packed SAMs of alkanethiols on mercury via solution deposition.[202-205] Other substrates for thiol SAMs include nickel,[206,207]

indium tin-oxide,[208] indium phosphide,[209] and a Tl-Ba-Cu-O high-temperature superconductor.[210]

1.2.1.3. Preparation of Self-Assembled Monolayers

The most common approach for depositing a SAM is immersion of the substrate into a homogenous solution of the self-assembling molecule at room temperature, followed by rinsing. The monolayer spontaneously forms upon exposure of the substrate to the solution. Successful SA requires a chemical bond between the substrate and an atom in the molecule.[211] Ideally, the strength of the head group-substrate bonds, lateral interactions and the density of packing result in sufficient stability of the monolayer that, it resists removal by a solvent rinse.[70,87]

Studies into the formation of highly oriented monolayers of thiols on gold substrates have led to some important empirical observation regarding several experimental parameters in the SA process, including substrate morphology, electrode cleaning, potential, solution concentration and deposition time.[84-86,212] The concentration of adsorbent and time of immersion of the substrate in the deposition solution are considered in combination since these two parameters are fundamentally linked.

The thiol concentration can be varied from micromolar levels to pure thiol liquid. Very low concentrations of thiols are favored by those seeking

large crystalline domains of alkanethiols via slow SA,[213] but are not a guarantee of SAM quality.[214] Lower concentrations of the thiol (micromolar) require longer deposition times because of mass transport limitations of the thiol to the surface of the electrode.[215] The deposition time seems to be strongly dependent on the type of thiol and the length of the alkyl chain. It has been reported that at millimolar concentrations, monolayers of the thiol assembles on the gold in seconds.[158] After deposition, there is a slower transformation over a period of hours to days into a highly ordered monolayer, driven by a combination of lateral interactions including hydrophobic,[158] dipole-dipole interactions, H-bonding or VDW interactions.[216]

Usually any solvent capable of dissolving the adsorbent is suitable for SA. Ethanol is the most popular solvent for thiols.[158] Figure 1.5 illustrates the formation of SAMs.

Considerable effort has been made to study the kinetic processes involved in forming a well-organized layer. To remove kinetically trapped disordered states, the SAM is sometimes annealed by soaking it in hot deposition solution,[217] exposing it to warm temperatures in a gaseous environment,[218] or subjecting the electrode to CV and repeated immersions in the deposition solution.[80] When two thiols are being co-deposited, the solvent, time and temperature all affect the mole fraction of each component in the SAM.[63,64,191,194] The less soluble thiol is deposited first and thereafter the more soiluble SAM displaces some of the less soluble ones. High concentrations of

thiols, long adsorption times and high temperatures encourage the SAM composition to approach equilibrium with the solution. The result is an abrupt transition of the SAM composition from one component to a mixed SAM as a function of the mole ratio of the two components in solution at equilibrium.[191]

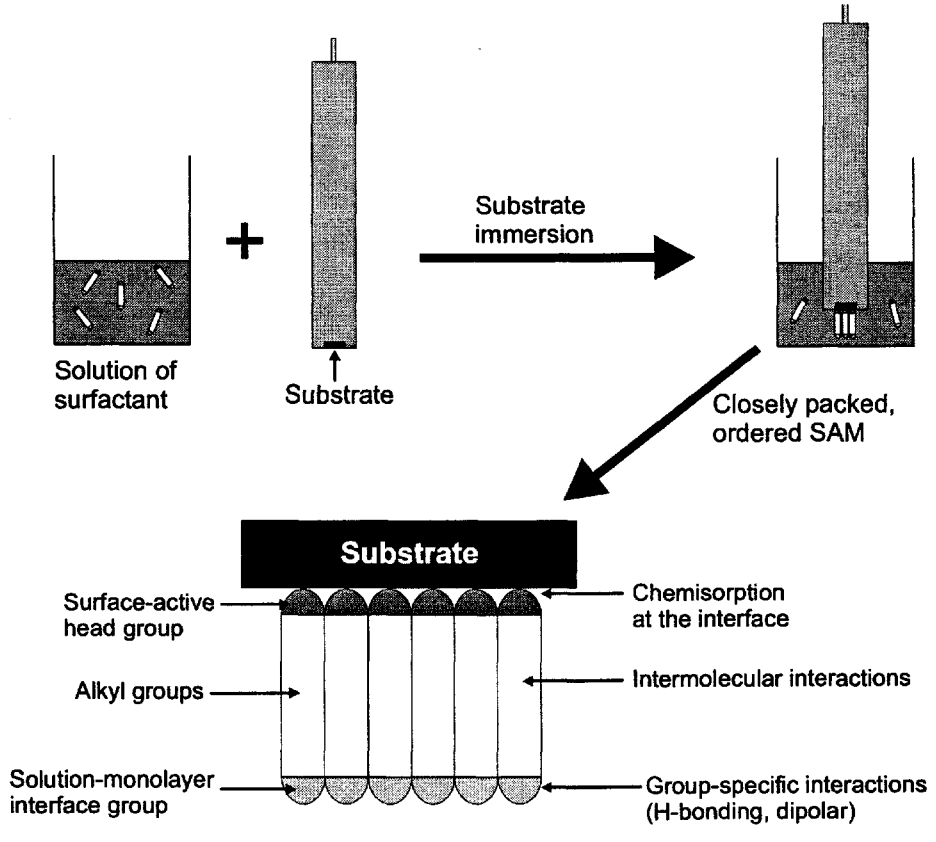

Figure 1.5. A schematic representation for the preparation of an ordered alkanethiol monolayer – a SAM.

1.2.2 Langmuir-Blodgett Deposition

Over the last two decades, the precision and sensitivity of a number of surface analysis techniques have been improved to such an extent that they can now be used to probe the structure and arrangement of surface active molecules in extremely thin films such as floating monolayers on an aqueous subphase (Langmuir films), and LB films on solid substrates. The early literature on Langmuir and LB films has been comprehensively reviewed by Gaines[127] and later by Ulman.[1] The LB films are simply Langmuir films transferred in one or more layers to a solid substrate, and therefore the two are often examined and discussed together in any experimental investigation.[219] Carboxylic acids and their salts are the traditional Langmuir film forming molecules. These molecules have a hydrophobic hydrocarbon chain, and a hydrophilic terminal acid headgroup. The hydrophilic headgroup is attracted to water while the hydrophobic chains organize themselves through intermolecular and hydrophobic interactions to form a 2D monolayer at the air-water interface.

1.2.2.1 The Surface Film Balance and Trough

The surface film balance has been the principal instrument for manipulating and examining floating monolayers since its invention by Agnes Pockels in the 19th century. Over that time there have been improvements in

precision and convenience, culminating with the introduction of computer control and data collection. One of the significant improvements was the introduction of the Wilhelmy plate for measuring surface pressure,[134] another the Teflon-coated trough. Presently, platinum Wilhelmy plates are commonly used.[1,132,133,220-225] Langmuir monolayers are produced and characterized in an apparatus that has been traditionally referred to as a Langmuir trough, which consists of a trough usually made up of hydrophobic materials like Teflon to contain the subphase water and movable barrier(s) that span the water surface. The trough also has a dipper used for upward and downward movements to enable Langmuir films to be deposited as LB films on a substrate. A typical Langmuir trough is shown in Figure 1.6.

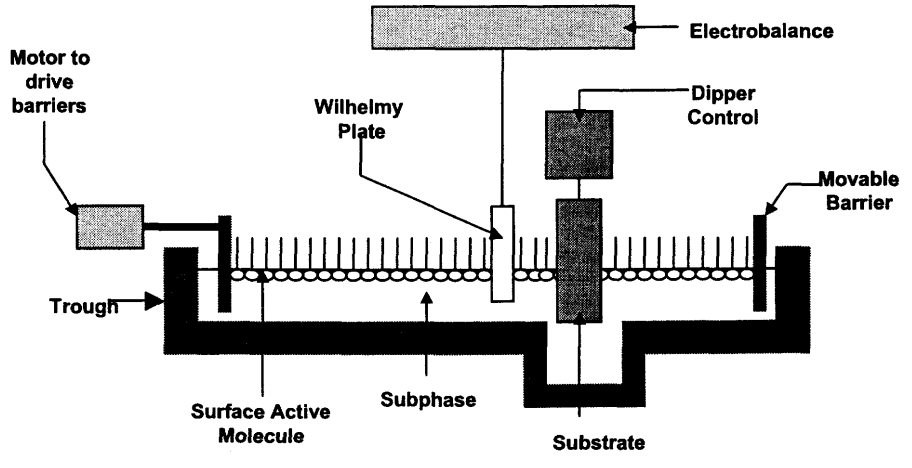

Figure 1.6. Schematic representation of a Langmuir trough that contains the Wilhelmy plate for measuring surface pressure using an electrobalance and the dipper employed for transferring LB films onto a solid substrate.

Stringent conditions must be adopted in order to obtain reproducible results with a Langmuir Film. These include:

(a) use of pure materials and spreading solvents (HPLC grade solvents and AR grade salts are normally recommended)

(b) accurate weighing of monolayer material

(c) use of optimal spreading solvent

(d) regular and thorough cleaning of trough and barriers

(e) use of ultrapure water for subphase and

(f) maintenance of a clean and vibration-free environment for carrying out experiments with controllable subphase temperature, which may be achieved by water circulation underneath the trough.

The main purpose of the rigid conditions described above is to eliminate any possibility of impurities concentrating at the air-water interface. Polar liquids, such as water, which are often used as the subphase, have strong intermolecular interactions and thus high surface tensions. Any factor, which decreases the strength of this interaction, will lower surface tension. Thus, any contamination will lower surface tension and compromise the integrity of the film and its π –**A** isotherm at the air-water interface. Furthermore, any contaminants that are surface active will be concentrated at the air-water interface in such a way that, even in very small bulk concentrations, they will be prominent in a Langmuir film and significantly change the properties of the film.

1.2.2.2 Monolayer Experiments and Surface Pressure Isotherms

In a common procedure for Langmuir film formation, a known amount of amphiphilic material is dissolved in a water-immiscible, volatile organic solvent such as chloroform, and spread on the water surface. After evaporation of the solvent, the monolayer material is compressed with the movable barriers as shown in Figure 1.6.

The most common approach to characterize a Langmuir monolayer is to record surface pressure (π) as a function of the area (**A**) available per molecule on the aqueous subphase surface at constant temperature (π –**A** isotherm). The measurement is usually carried out by continuously compressing the monolayer while monitoring the surface pressure. Surface pressure (π) is defined as the difference in surface tension between the clean surface of the subphase (γ_0) and the film-covered surface (γ), and is given by $\pi = \gamma_0 - \gamma$. Thus it is in fact, a measure of the decrease in surface tension, or a 2D analogue of pressure.

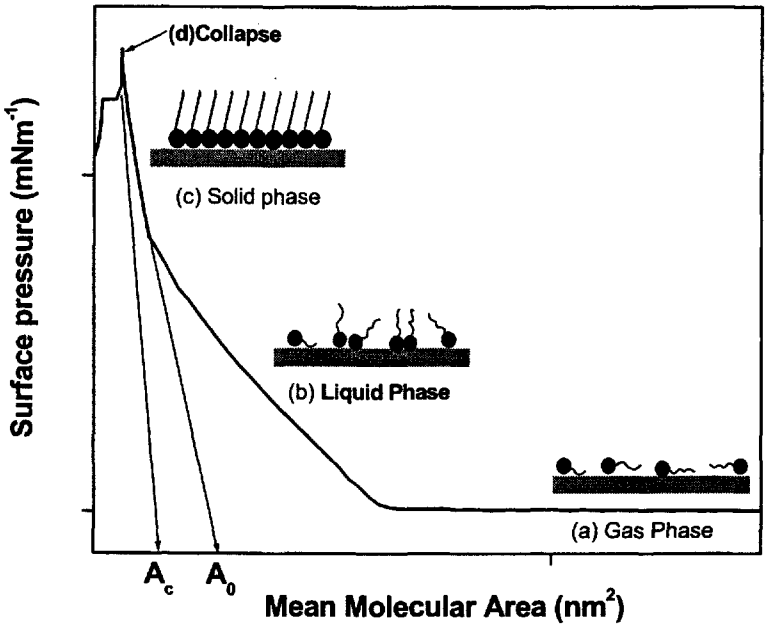

Figure 1.7. Illustration of **π–A** isotherm of a Langmuir film at the air-water interface. The various phases are marked in the isotherm namely (a) gaseous phase, (b) liquid phase, (c) solid phase and (d) collapse.

Figure 1.7 shows a typical **π –A** isotherm of a Langmuir Film. When the surface active molecules are spread on the aqueous subphase surface, they are well separated and form a pseudo gas phase as shown in Figure 1.7 with large molecular areas and very low **π** (a). As the barriers are brought together, there is a transition at which the pressure suddenly starts to increase more rapidly. This change in compressibility signifies the onset of the pseudo liquid phase in which there is no long range order but the molecules are not as free to move about as in the gas phase indicated by the gradual increase in π (b). This is unlike a 3D liquid phase, which is much less compressible. As the barriers are

closed even further, the transition to a nearly incompressible solid phase (c) is indicated by an onset of yet another change in slope. At low molecular areas and high pressures, this solid phase typically has a 2D lattice and an extrapolated molecular area of A_0 known as the limiting molecular area per molecule. A_0 is obtained by extrapolating the solid phase (c) to zero on the mean molecular area axis as shown in Figure. 1.7. Compressing the layer further beyond (d) would "collapse" the monolayer at an extrapolated critical mean molecular area A_c. The collapse pressure depends on the equilibrium spreading pressure (ESP) which is the greatest surface concentration hat can be achieved by a monolayer while remaining in a thermodynamically stable phase.[127] After collapse, π decreases abruptly and bilayers and/or multilayers may form. The collapse pressure may sometimes depend on the compression rate of the barriers.

1.2.2.3. Langmuir-Blodgett Deposition

After formation of a Langmuir monolayer, the next step is the deposition of the LB film onto a solid support. The transfer of a floating monolayer onto a solid substrate is called LB deposition or transfer and the resulting film is a LB Film. Figure 1.8 illustrates the spreading, compression and formation of a Langmuir film as well as deposition of an LB film.

This can be achieved by slowly lowering a hydrophilic solid positioned perpendicular to the Langmuir film through the liquid surface covered with the

monolayer. By repeating this vertical dipping of the substrate in and out of monolayer-covered liquid surface a multilayer LB film is produced. This is known as the vertical deposition mode.[1,127,127,226]

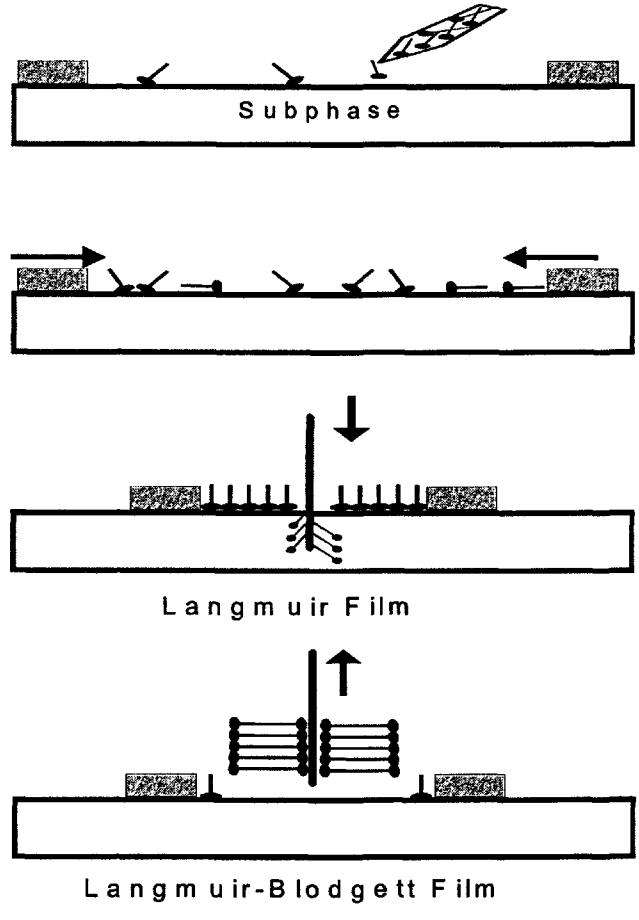

Figure 1.8. Illustration of spreading, compression and formation of a Langmuir film as well as deposition of an LB film.

Langmuir and Schaefer[134] suggested a horizontal deposition mode by which the floating monolayer can be transferred to a hydrophobic solid surface

by lowering a solid surface held parallel to the Langmuir film until it touches the monolayer at the air-water interface.

LB deposition is usually effected at surface pressures near the collapse point, in the solid phase. For example, deposition of fatty acids and their salts (collapse pressures 20 to 40 mNm^{-1} at room temperature) are normally performed at 30-35 mNm^{-1} at room temperature[227]. While the monolayer is transferred onto the substrate during LB deposition, the area of the floating monolayer is normally reduced continuously in order to keep surface pressure constant. A simple parameter to characterize the quality of the deposition is the transfer ratio (TR) and is defined in equation 1.1. For satisfactory deposition TR~ 1 is desired.

$$TR = \frac{\text{decrease in area of Langmuir Monolayer}}{\text{area of the solid substrate}} \qquad (1.1)$$

There are three types of LB deposition: X, Y and Z types.[1] These lead to the formation of multilayers and are not relevant in monolayer studies.

When only a single LB film is required, the deposition usually involves raising the substrate upward through the monolayer-covered surface. For this, the substrate must be immersed prior to spreading of the Langmuir film. Alternatively, one could dip down and then clear the surface of the Langmuir film, even though this may not be convenient.

1.2.2.4. Molecular Interactions

In the LB deposition process, molecular organization at the air-water interface is brought about by an increase in surface concentration. By the time LB deposition is effected, the molecular organization is already in place. In a typical deposition, the monolayer is mostly physisorbed on the substrate. However in a few cases, chemisorption may occur depending on the substrate.[133] It should be noted that chemisorption is not a necessary component of the LB deposition process. Physisorbed LB films are in fact more common than chemisorbed ones, owing to the greater flexibility in substrate material. The integrity of the physisorbed film is largely due to strong lateral intermolecular interactions.

1.2.2.5. Langmuir Films Versus Langmuir-Blodgett Films

The structure of LB films may differ from those of Langmuir films, even for simple, model amphiphilic molecules. This is not unexpected, since the factors governing the equilibrium packing arrangement of the molecules in Langmuir and LB films are different. Indeed, the transfer of a monolayer from a liquid surface to a solid surface significantly changes the interaction between the head groups of the monolayer molecules and the substrate. Various research groups have made efforts to investigate Langmuir films directly at the air-water

interface, employing "in situ" measurements rather than simply analysing the transferred LB films and making a correlation to the Langmuir monolayer. Some of the measurements made on Langmuir films are fluorescence microscopy,[228,229] X-ray and neutron reflectivity,[230] ultra-violet visible spectroscopy,[231] FT-IR,[232] Brewster angle microscopy (BAM),[233-238] Raman spectroscopy,[239] fluorescence spectroscopy[240] and grazing incidence synchrotron X-ray diffraction (GIXRD)[241] among others.[1,127,226]

For instance, while comparing surface potential values of Langmuir films and corresponding LB films, one needs to consider the possibility of charge injection from the metal electrode in the latter films. There are some parameters such as degree of mixing between components in a mixed monolayer and composition (provided there is no specific interaction between the monolayer material and the substrate) of the monolayer, and the degree of ionisation of headgroups, which can conveniently be assumed as unchanged during the transfer process.

1.3. Methods of Monolayer Characterization

The development of analytical tools for the study of thin organic films has been dramatic in the last decade. Some of the properties measured include the thickness and uniformity of freshly prepared films, the wetting properties, surface free energies, and surface order. Other techniques are used to

investigate the direction of transition dipoles, and to evaluate dichroic ratios, molecular orientation, packing and coverage, the coherence of a film at the air-water interface and on metal surfaces. In addition, surface composition and monolayer structure as well as surface topography can all be studied.[1,127,226]

1.3.1. Electrochemistry

Electrochemistry has developed into an established branch of physical chemistry since its remarkable beginnings starting with the contributions of notable chemists such as Galvani, Volta and Faraday. Electrochemical methods can be divided into two general classes: interfacial and bulk methods. Interfacial methods are those based on phenomena taking place at the electrode solution interface; voltammetric techniques are a perfect example of interfacial methods. In contrast, bulk methods are those concerned with phenomena occurring in the core of the sample, such as conductometric techniques.

Interfacial electrochemical methods can be further classified as equilibrium and dynamic methods. The first class is characterized by measurements performed under equilibrium conditions, with no current flowing through the electrochemical cell (i=0). The prototype example is found in potentiometric techniques. In dynamic methods, the electrochemical cell is purposely taken far from equilibrium, while measurements are made under

conditions of controlled current or controlled potential. Typically, nonzero currents flow through the cell under these experimental conditions. In controlled potential methods, a potential (or potential function) different from the equilibrium value is applied to the cell, while current is measured as a function of time or potential. Examples include coulometry, voltammetry, and amperometric titrations. In the less popular controlled current methods, the potential of the cell is monitored as a fixed current is forced across the cell. Among all the dynamic electrochemical techniques, the group of methods collectively referred to as voltammetry is by far the most common.

1.3.1.1. Potential, Current and Charge

The magnitudes of electrical potential and current are the core of any discussion of electrochemistry. Electrode potentials are defined using a relative scale because the accurate experimental measurement of absolute electrode potential values is not accessible. This relative scale is established by assigning the potential 0.00V to the following half-cell: Pt/H^+ (a=1.0), H_2 (1.0 atm). This half-cell or electrode is called the standard or normal hydrogen electrode (SHE or NHE) and constitutes the primary reference electrode.

The potential of any electrode or half-cell of interest is determined by setting up a cell in which the electrode of interest would be the cathode and the NHE the anode. The potential of a cell would be equal to the potential of the

electrode of interest in the NHE scale or the difference in potential between the electrode of interest and the NHE. A certain half-cell's standard electrode potential (E^0) is the potential of the half-cell in which all the species participating in the half reaction are present in their standard states. The E^0 value for a particular reaction as shown in Scheme 2, provides a relative indication of the oxidizing power of the species Ox as well as the reducing ability of the species Red.

$$Ox + ne^- \rightleftharpoons Red \quad \text{(Scheme 2)}$$

Current is the second significant quantity in dynamic electrochemical methods - by contrast in equilibrium methods the current is zero. Current provides a measurement of the instantaneous rate of the electrochemical reaction (r) according to Equation 1.2.

$$i = nFA \qquad (1.2)$$

where i is the current, n is the number of electrons involved in the transfer, and F is the Faraday constant, and $\boldsymbol{A}$ represents the electrode area.

The facile measurement of instantaneous reaction rates is a unique feature of electrochemical techniques. A third quantity of interest, the electrical charge Q, can be obtained by integration of the current over time as shown in Equation 1.3.

$$Q = \int i\,dt \qquad (1.3)$$

The charge passed through a cell in a given period of time can be directly correlated to the amount of material that has undergone electrochemical conversion using Faraday's Law (Equation 1.4)

$$Q = nFNA \qquad (1.4)$$

where N is the number of moles of converted species.

Faradaic currents dominate the current-potential response for systems of interest in which redox activity occurs. However, current that is nonfaradaic in origin may also have to be considered in certain cases.

1.3.1.2. Three Electrode System

Controlled potential techniques represent the largest class of electrochemical techniques, and are used to study the redox reactions of a species at an electrode by measuring current as a function of potential or time. The basic experimental set-up, shown in Figure 1.9, is similar for all controlled potential methods.

The electrochemical cell consists of three electrodes (working, reference, and counter) immersed in a solution containing the electroactive species and a supporting electrolyte. Reactions are studied at the working electrode (WE).

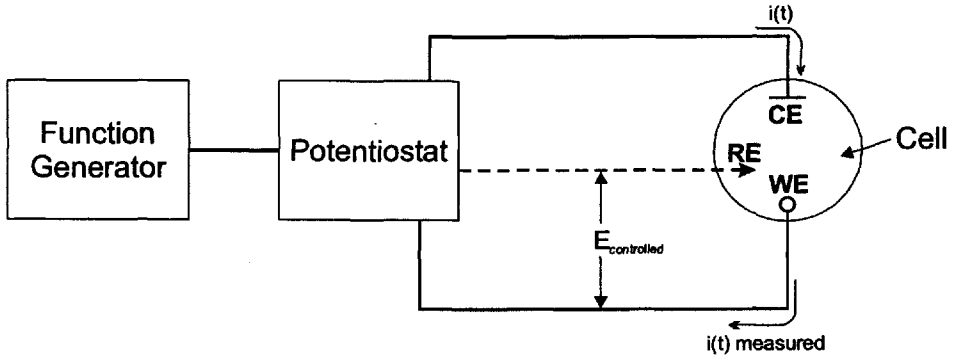

Figure 1.9. Schematic experimental arrangement for controlled potential experiments. WE – Working Electrode; RE – Reference Electrode; CE – Counter Electrode.

The reference electrode (RE) provides a fixed potential that does not vary during the experiment. The counter electrode (CE) supplies the current required by the WE without limiting the measured response of the cell. Thus, current flow is between the WE and the CE, enabling the potential of the RE to remain constant.

A typical experiment begins with the function generator supplying the appropriate waveform signal to the potentiostat. Each controlled potential method has a characteristic waveform that varies with time. The potentiostat adjusts the potential (E) across the WE–CE pair by sending a current (i) through the WE to maintain the potential difference between the WE–RE pair. Because i and E are related functionally (E = iR), i is the experimental observable.

1.3.1.3. The Electrode-Solution Interface

When a given potential is applied to an electrode in solution, charged species and solvent molecules will form layers in response to the charge accumulated at the electrode surface. These layers are collectively called the electrical double layer.

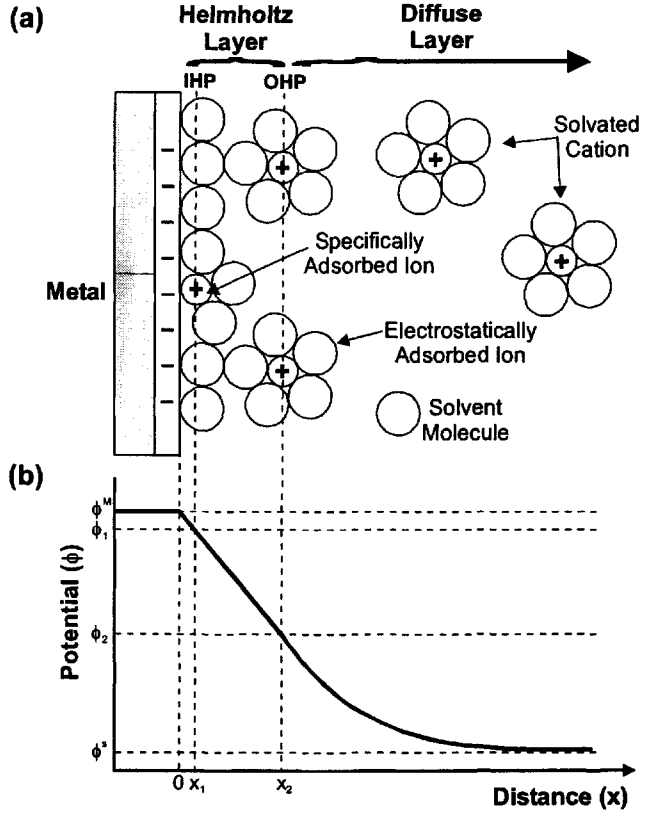

Figure 1.10. (a) Diagram illustrating the electrical double layer in solution when a negative potential is applied to the electrode. IHP – Inner Helmholtz Plane; OHP – Outer Helmholtz Plane (b) Distribution of the electric potential near the electrode surface. ϕ^M, and ϕ^s are the absolute electrostatic potentials for the metal electrode, and bulk solution, respectively.

Figure 1.10(a) illustrates the electrical double layer at the electrode–solution interface when a negative potential is applied to the electrode. The potential profile across the electrical double layer is shown in Figure 1.10(b). The inner or Helmholtz layer is only one or two molecular diameters in thickness and a linear decay in the potential profile is observed. Within the Helmholtz layer, a monolayer containing both dipole-oriented solvent molecules and specifically adsorbed species (ions or molecules) is present at the surface of the electrode. The imaginary plane that passes through the centres of the specifically adsorbed ions at a distance x_1 is called the Inner Helmholtz plane (IHP). A second layer of fully solvated ions is separated from the electrode's surface by the monolayer, and interaction between the solvated ions and the charged electrode surface involves only long-range electrostatic forces. These solvated ions are referred to as non-specifically adsorbed ions, and the plane that passes through the centres of these solvated ions is called the Outer Helmholtz plane (OHP). Beyond the Helmholtz layer defined by the OHP, the ions in solution are influenced by the electrical field, which increases the order of the molecules, and thermal forces, which increase the disorder of the system, resulting in the diffuse layer. The diffuse layer contains an excess of solvated ions near the electrode, which are needed to balance the electrode charge. Its thickness increases with a decrease in electrolyte concentration. A logarithmic decay towards the potential of the bulk solution is observed in the diffuse layer because the concentration of electrolyte is greatest next to the electrode

surface, and decreases progressively until a homogeneous distribution of ions persists in the bulk electrolyte.

It should however be noted that there is a change in this potential profile described above when a surfactant as a monolayer is present on the electrode surface.

1.3.1.4. Nonfaradiac Processes

Nonfaradaic processes, which are always present during an electrochemical experiment, involve no redox processes, but arise from changes in the electrode area, potential, and solution composition. Nonfaradaic current is commonly called the capacitance current. The evolution of nonfaradaic current is shown in Figure 1.11(a) on a current-time scale. Figure 1.11(b) shows the same evolution for faradaic current, for comparison. Each process can be described by a corresponding electrical circuit as shown in Figure 1.11.

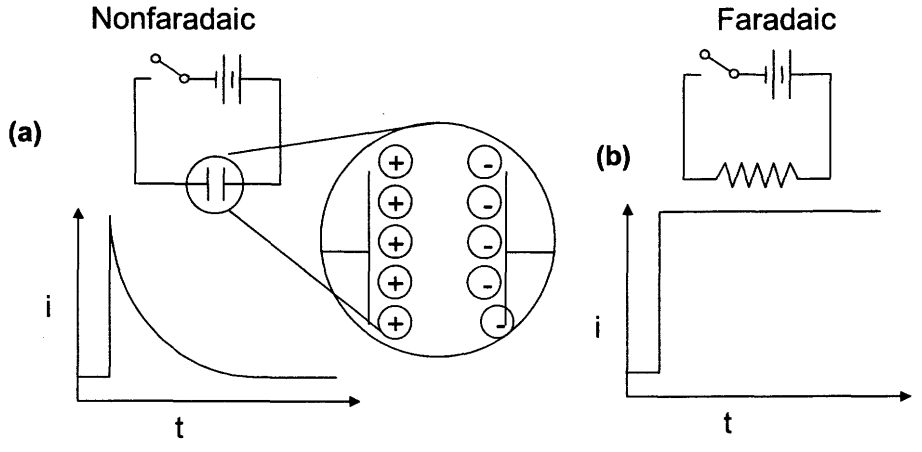

Figure 1.11. (a) Nonfaradaic process and (b) Faradaic process.

The origin of nonfaradiac current is the following. The electrode-solution interface resembles a capacitor; the total charging current is generated whenever there is a change in potential. However, the relationship between charge and potential is not linear for this capacitor, so the total charging current (i_c) consists of two parts, and is given by the equation:

$$i_c = C_{dl}\frac{dE}{dt} + E\frac{dC_{dl}}{dt} \qquad (1.5)$$

where C_{dl} is the double layer capacitance given by the equation:

$$C_{dl} = \frac{dq^M}{dE} \qquad (1.6)$$

and q^M is the charge on the electrode surface. Any change in the structure of the double layer will be reflected in a change in the capacitance and consequently in the magnitude of the charging current. Experimental

parameters that influence i_c include the electrolyte concentration, the electrode area, and the adsorption or blocking of molecules or ions from the electrode surface. Most electrochemical methods correct for i_c through background subtraction of the current obtained from an experiment collected in the absence of electroactive species under the assumption that only non-faradiac current is present.

For electrodes modified with a non-electroactive species, the Helmholtz layer changes from a mixture of ions and solvent with a high dielectric constant to an ion-free layer with a low dielectric constant. In this study, the nonfaradiac currents are considerably diminished by the non-electroactive species, specifically the long chain alkanethiol SAM. This blocking property is attributed to the densely packed structure of the hydrocarbon chains in the SAM, which impedes the approach of solution ions to the Helmholtz layer. Nonfaradiac current measured by CV can therefore be used to check the integrity of a densely packed SAM.

1.3.1.5. Faradaic Processes

Faradaic processes involve the transfer of electrons across the electrode–solution interface through a redox reaction, and occur when sufficient potential is applied to oxidize or reduce the electroactive species. These

processes occur in the region between the OHP and bulk solution known as the Nernst diffusion layer.

Consider the electrode reaction in Scheme 2, at negative E; electrons will accumulate at the surface of the electrode. As E becomes more negative, the energy of the electrons is raised to a high enough level to move into vacant states of Ox located at electrode surface, and Ox is reduced to Red by the flow of electrons from the electrode to the solution (reduction current). Similarly, applying more positive potentials lowers the energy of electrons to an eventual state in which electrons from Red move into the vacant states on the electrode surface, creating a flow of electrons from solution to the electrode (oxidation current).

If it is assumed that the potential of an electrode is sufficiently negative (or positive) so that all reactant species arriving at the electrode by linear diffusion are immediately reduced (or oxidized), then the resulting faradaic "limiting current" (i_l) can be described by Cottrell's equation:

$$i_l(t) = \frac{nFD_{Ox}^{1/2}\mathbf{A}c_{Ox}^{\infty}}{\pi^{1/2}\tau^{1/2}} \qquad (1.7)$$

where n is the number of electrons exchanged between one molecule of reactant species and the electrode, F is the Faraday constant, D_{ox} is the diffusion coefficient of the reactant, **A** is the electrode surface area, C_{Ox}^{∞} is the concentration of reactant in the bulk solution, and τ is the electrolysis time.

Cottrell's equation shows that current will vary with the bulk concentration of reactant, and that current will decrease over time.

An electrochemical cell is considered to be at equilibrium when the net current is zero. However, when no net current is flowing, a dynamic equilibrium exists at the surface of the WE, where reduction and oxidation processes are occurring at the same rate. At equilibrium, the potential of the WE is given by the Nernst equation:

$$E = E^{\circ} + \frac{RT}{nF} \ln \frac{c^{\infty}_{Ox}}{c^{\infty}_{Red}} \qquad (1.8)$$

where E is the cell potential, E° is the standard electrode potential for the Ox/Red couple, R is the gas constant, T is the temperature, and C^{∞}_{Ox}, C^{∞}_{Red} are the bulk concentrations of Ox and Red, respectively. Equation 1.8 indicates that when an electrode reaction is reversible, (E- E°) = 59 mV/n at a temperature of 25°C. This relation also allows the evaluation of n.

In this study, alkanethiol SAMs suppress faradaic processes such as electrode oxidation and reduction, and the exchange of electrons between the electrode and solution redox couples. This blocking property is attributed to the densely packed structure of the hydrocarbon chains, which impede the approach of ions and molecules to the electrode surface. Charged endgroups can also prevent electron transfer through electrostatics by the Frumkin effect.

1.3.1.6. Factors Affecting Electrode Reaction Rate

An electrode reaction in an electrolytic solution involving a redox species and an electrode can be written as in Scheme 2 in which Ox is reduced to Red. Figure 1.12 illustrates the various possible processes accompanying an electrochemical reaction.

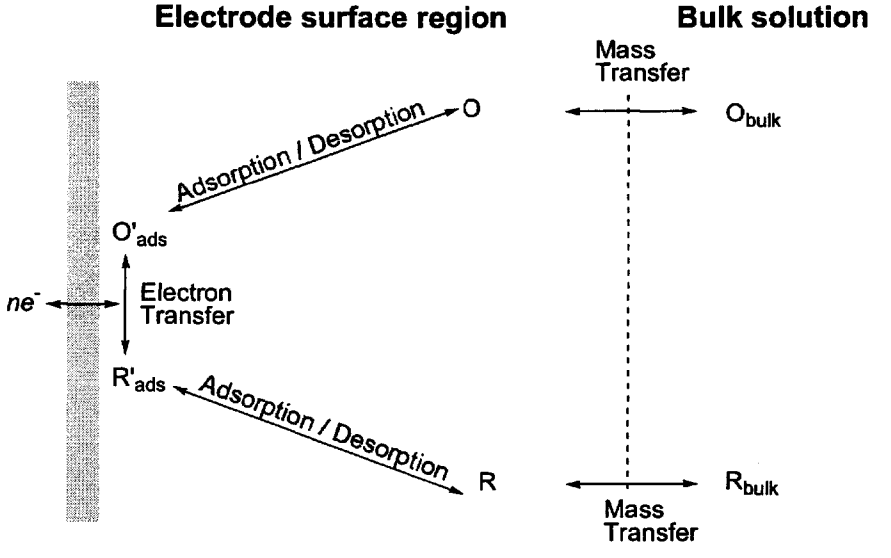

Figure 1.12. Pathway of a general electrode reaction involving a redox species. O and R are oxidised and reduced species,respectively. O_{bulk} and R_{bulk} are the oxidised and reduced species in the bulk solution, respectively. O_{ads} and R_{ads} are the adsorbed oxidised and reduced species, respectively at the electrode solution interface.

In general, two processes determine the magnitude of the current of a redox process: mass transfer and electron transfer (ET) at the electrode surface. For a redox process in solution, the oxidized species must first move

from the bulk solution through the diffuse layer and the OHP, and then onto the electrode surface as shown in the top half of Figure 1.12.

This is the mass transfer step that occurs before the ET at the electrode surface. Upon reduction of O_{ads} to R_{ads}, the reduced species leaves the electrode surface by desorption followed by a similar mass transfer process.[34,36]

These processes that occur at the electrode-solution interface can be studied by a number of techniques. Here, CV and AC-IS will be discussed.

1.3.1.7. Cyclic Voltammetry

1.3.1.7.1. General Cyclic Voltammetry

A voltammetric experiment consists of measuring the current response of an electrode as a function of the varying potential difference imposed between the electrode and a reference electrode. In the last two decades, CV has become very popular and perhaps, the most common electrochemical technique for acquiring qualitative information about electrochemical reactions. For instance, CV of a new electroactive species may afford data about all its accessible oxidation states, the formal potentials of the corresponding redox couples, and the relative stability of the electrogenerated species. In addition, it can provide information on the thermodynamics and kinetics of any electron

transfer reactions, involving both species in solution and species adsorbed at an electrode surface.

CV consists of cycling the potential of a WE using the waveform shown in Figure 1.13(a). The potential sweep, is characterized by its initial potential (E_i), a switching potential (E_s) and a final potential (E_f).

The excitation function is characterized by the rate of potential variation, called the scan rate (ν),. usually expressed as mVs^{-1}. During the potential sweep, the potentiostat measures the current resulting from the applied potential, and the resulting current-potential plot is termed a cyclic voltammogram [Figure 1.13(b)].

Consider the cyclic voltammogram shown in Figure 1.13(b) for the electrode reaction Red $\rightleftharpoons$ Ox + ne^- where $E_i < E_s$ and only Red is initially present in solution. Initially, the applied potentials are more negative compared to the standard potential for the reaction and no faradaic current flows at the WE. Eventually, at Point A, anodic current begins to flow as an applied potential is reached where Red is oxidized to Ox. A rapid increase in current occurs in the region of A to B as the surface concentration of Red is replenished continuously from Red located in the diffusion layer.

(a)

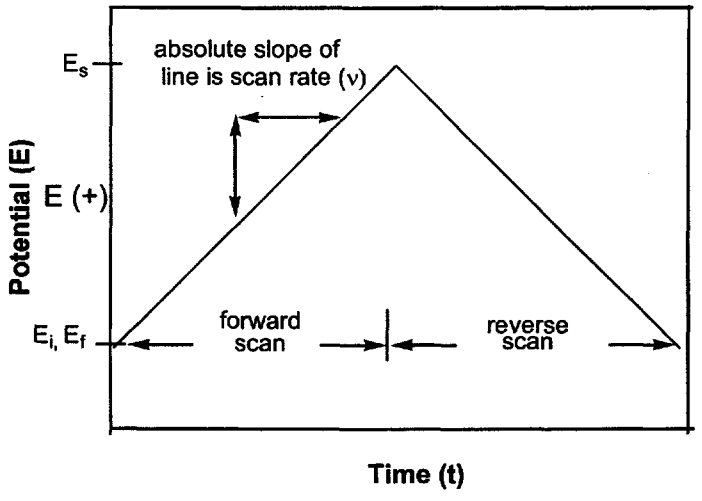

(b)

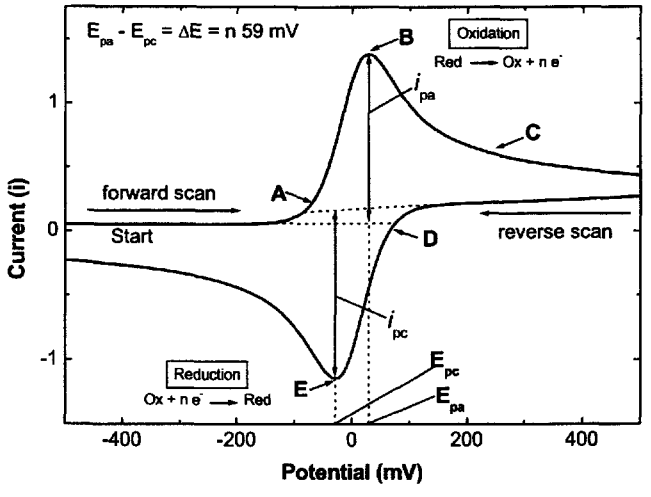

Figure 1.13. (a) CV involves a triangular waveform. The forward scan consists of a potential sweep from the initial potential (E_i) to a switching potential (E_s) and the reverse scan consists of a potential sweep from E_s to the final potential (E_f). The sweep rate (ν) is given by the slope of the line. (b) Cyclic voltammogram for the reaction Red $\rightleftharpoons$ Ox + n e^- where $E_i < E_s$ and only Red is initially present. (See text for details of labels).

At Point B, the anodic current reaches a maximum at the anodic peak potential (E_{pa}). Beyond E_{pa}, the surface concentration of Red cannot be replenished to its equilibrium value because additional Red is located further

away from the electrode surface, which results in a decrease in anodic current (Point C). At E_s, the scan direction is reversed to E_f. However, the current continues to be anodic, because the potentials are still positive enough to cause oxidation of Red until Point D, where the potential is enough to reduce the Ox back to Red. In the region of D to E, cathodic current flows as Ox that is near the electrode surface is reduced to Red. At point E, the cathodic current reaches a maximum at the cathodic peak potential (E_{pc}). Beyond E_{pc}, the cathodic current decreases as the Ox that was generated in the anodic sweep is used up by the cathodic reaction. At E_f, the current has not reached its initial value because some Ox diffuses into the bulk solution and cannot be reduced on the timescale of the CV experiment.

The important parameters in a CV are the cathodic peak current (i_{pc}), anodic peak current (i_{pa}), the cathodic peak potential (E_{pc}), the anodic peak potential (E_{pa}), and the potential difference (ΔE) between E_{pa} and E_{pc}. The half-wave potential ($E_{1/2}$) for the electrode reaction is given by the equation:

$$E_{1/2} = \frac{E_{pc} + E_{pa}}{2} \qquad (1.9)$$

At this potential, the concentrations of Ox and Red at the surface are equal. Therefore, from equation 1.8, $E_{1/2}$ is approximately equal to E^o for the O/R couple.

The reversibility of an electrochemical reaction will depend on the rate of electron transfer at the electrode. If the rate of electron transfer is fast with

respect to the timescale of the CV experiment, then the reaction is reversible, and the peak current (i_p) at 25 °C can be expressed by the Randles-Sevčik equation: Where D_{ox} is the diffusion coefficient of the oxidized species.

$$i_p = 2.69x10^5 n^{3/2} c_{Ox}^{\infty} D_{Ox}^{1/2} \nu^{1/2} \mathbf{A} \qquad (1.10)$$

For an irreversible electrochemical reaction, the rate of electron transfer is slow with respect to the timescale of the experiment, such that the rate of diffusion is greater than the rate of electron transfer. This causes ΔE to be greater than the equilibrium value of 59mV/n. A totally irreversible system will have no reverse peak. An electrochemical reaction whose properties lie between reversible and irreversible is known as quasi-reversible. The diagnostic tests for evaluating the reversibility of an electron transfer reaction are summarized in Table 1.2.[242]

Table 1.2. Diagnostic tests for evaluating the reversibility of a diffusion-controlled electron transfer reaction.[242]

	Reversible	**Quasi-Reversible**	**Irreversible**
1.	$\Delta E = 59/n$ mV	$\Delta E > 59/n$ mV and ↑ with ↑ν	No reverse peak
2.	E_p independent of ν	E_{pc} shifts negatively with ↑ν	E_{pc} shifts $RT/2F\alpha_c n_c$ mV for each decade ↑ν
3.	$i_p \propto \nu^{1/2}$	i_p ↑ with $\nu^{1/2}$, but not $\propto$ to it	$i_{pc} \propto \nu^{1/2}$
4.	$\left\|\frac{i_{pa}}{i_{pc}}\right\| = 1$	$\left\|\frac{i_{pa}}{i_{pc}}\right\| = 1$ if α=0.5	No reverse peak

α = electron transfer coefficient (measure of symmetry for the activation energy barrier; typically found in electron transfer kinetic equations where $\alpha_a + \alpha_c = 1$).

1.3.1.7.2. Cyclic Voltammetry of Electrodes Modified with Electroactive Species

Modified electrode surfaces have found widespread use as versatile models for studying interfacial electron transfer, biological interactions, molecular recognition, double layer structure, adhesion and other interfacial phenomena.[243] The CV of an electron transfer reaction in which Ox is adsorbed onto the surface of the electrode is considerably different than a CV of a solution-based reaction. The main differences are that current is not controlled by mass transport because Ox is adsorbed at the surface, and only a fixed amount of Ox is available for reduction. Thus if the electron transfer is reversible, then the reduction and oxidation peaks will be symmetrical, and there will be no peak separation ($\Delta E = 0$)

The peak current for an adsorbed species at 25 °C can be expressed by the modified Randles-Sevčik equation:

$$i_p = 9.39x10^5 n^2 \mathbf{A} \Gamma_{Ox} \nu \qquad (1.11)$$

where Γ_{ox} is the surface concentration of Ox adsorbed on the electrode of surface area **A**. Equation 1.11 shows that i_p is proportional to ν, rather than $\nu^{1/2}$ as for diffusion controlled processes (Equation 1.10). Therefore, a quick test to determine if a reaction is diffusion controlled is a plot of log i_p versus log ν where a slope of ½ corresponds to a diffusion controlled process and a slope of 1 indicates an adsorbed species.

For an adsorbed redox species, the surface concentration of Ox can be determined by the equation:

$$\Gamma_{Ox} = \left| \frac{Q}{nF\mathbf{A}} \right| \qquad (1.12)$$

where Q is the charge associated with the reduction of the adsorbed layer and determined by the area under the cathodic peak.

1.3.1.7.3. Cyclic Voltammetry of Electrodes Modified with Non-Electroactive Species

CV may also be used to investigate electrodes modified with non-electroactive species. For example, the electrochemical behaviour of a redox probe such as $Fe(CN)_6^{4-/3-}$ in solution, has been studied at SAM-coated electrodes by CV to characterize the blocking behaviour or passivating character of these SAM-modified electrodes.[30,62-65,82,100,244-247] The formation of a blocking film on an electrode will decrease the capacitance and hence decrease the capacitance current (nonfaradaic current) compared to that of a bare electrode, since the distance of closest approach of counter ions, *d*, will be increased by the thickness of the modifying layer.[248] The extent of blocking by the monolayer can be assessed in a number of ways including CV.[187,245]

Incomplete coverage of the electrode surface by adsorbed substances may be attributed to surface roughness of the electrodes or pinholes, which are the holes in the film, located at defect sites. This partial blocking of an electrode

surface toward electron transfer, which in this case may be a blocking film sprinkled with a large number of microscopic active sites behaving as pinholes.[249] Under such conditions, the average size of the active sites and the average distance between them are small compared to total diffusion layer. With respect to electron transfer, these exposed active sites may act as an individual ultramicroelectrodes.[248] This induces non-linear diffusion effects that interfere in the competition between the rate of diffusion and the rates of the various steps taking part in the electrochemical reaction.[249] In this case, each of the ultramicroelectrodes contribute its current from the electron transfer process, giving a non-linear diffusion pattern. As these pinholes get larger they may resemble linear diffusion in a bare electrode from a CV. For example in the case of SAMs with electroinactive compounds non-linear effects may result from incomplete blocking of the electrode and depending on how poorly blocked the electrode may be, its CV wave may be like that of an array of ultramicroelectrodes and very similar to that of the bare electrode to the extent that one may be inclined to accept that there was no proper monolayer formed or desorption has taken place in the case of variable temperature study.

1.3.1.8. Alternating Current-Electrochemical Impedance Spectroscopy

The dynamics of charge transfer at the electrochemical interface are strongly influenced by the nature of the electrode surface and the structure of

the electrical double layer.[250] In CV, effects of certain interfacial parameters such as the solution resistance, double layer charging and currents due to diffusion or other processes occurring in the modified electrodes, cannot be easily and accurately monitored.[101,251] However, another electrochemical method known as Electrochemical Impedance Spectroscopy (EIS), is well suited to probing the electrode-solution interface, and so can provide complementary information to CV data for many systems.

The use of a phase-sensitive voltmeter for the study of the electrical response of the interphase is an accurate method for the measurement of the double layer capacitance. By combining a phase-sensitive voltmeter, also called a lock-in-amplifier, with a variable frequency sine-wave generator one obtains an electrochemical impedance spectrum. In this technique, modern instrumentation, which is commercially available, covers a frequency range of about 12 orders of magnitude, from 10^{-5} Hz to 10^{7} Hz. This is a very wide range of frequencies when compared to other fields: visible light extends over twofold range of frequencies, and from vacuum ultra violet to the far infrared covers no more than three orders of magnitude. The range of frequencies that can be used in EIS measurements is limited more by the electrochemical aspects of the system than by instrumentation. Such instruments are commonly combined with a microcomputer, which makes it easy to probe the interphase over a wide range of frequencies, and to record and analyze the data.

Since frequency and time are inversely related, the lowest frequency component provides the highest temporal resolution of the impedance data. While it is technically possible to make measurements at 10^{-5} Hz, this would take longer than a day and the changes in the interphase during the measurement of a single frequency could make the result meaningless. At the high frequency end, stray capacitances and inductances combine with possible non-uniformity of current distribution at the electrode surface to make the results unreliable. For these reasons, EIS experiments are usually conducted in the range of 10^{-3} to 10^{6} Hz.[252]

EIS involves the measurement of the frequency dispersion of the impedance or admittance of a system.[102,103] The advantage of measurements in the frequency domain over those in time domain is that the analysis of the frequency dispersion of the (complex) impedance can be carried out by modeling the interface as a collection of ideal circuit elements with the physical model being a simple equivalent circuit.[253] The various circuit elements are related to the respective electrical features of the system under study, such as ionic conductivity, solution resistance, double layer capacitance and Warburg impedance. In the end, a complete electrochemical description of the interface is achieved by measuring the impedance as a function of frequency, redox species concentration and electrode potential.

The advantages of AC-EIS can be summarised as follows:

1. Analysis of impedance data over a wide frequency range provides a complete picture of the electrical properties of the system including capacitances and resistances in the presence or absence of electron transfer processes.
2. AC-impedance measurements involve the application of a minute voltage perturbation (typically a few mV), thus inducing minimal disturbance to the monolayer, unlike voltammetry, which requires voltage variations of hundreds of millivolts.[105]

1.3.1.8.1 Theory

A pure sinusoidal voltage can be expressed as

$$e = E \sin \omega t \qquad (1.13)$$

where ω is the angular frequency, which is 2π times the conventional frequency in Hz. The voltage can be considered as a rotating vector (or phasor), with a length equal to the amplitude E, and a frequency of rotation equal to ω as shown in Figure 1.14.

For two related sinusoidal signals, such as current, *i*, and the voltage, e, each can be represented as a separate phasor $\dot{E}$ or $\dot{I}$ rotating at the same frequency. As shown in Figure 1.15 they generally will not be in phase, thus their phasors will be separated by a *phase angle* ϕ. One of the phasors (usually $\dot{E}$) is taken as a reference signal, and ϕ is measured with respect to it.

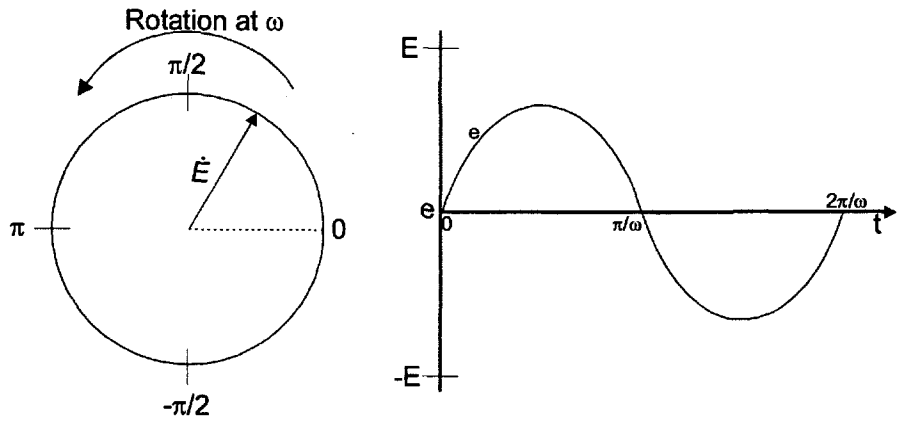

Figure 1.14. Phasor diagram for an alternating voltage, e = E sin ω t.

In Figure 1.15, the current lags the voltage and this can be expressed generally as

$$i = I \sin(\omega t + \phi) \qquad (1.14)$$

where ϕ is a signed quantity.

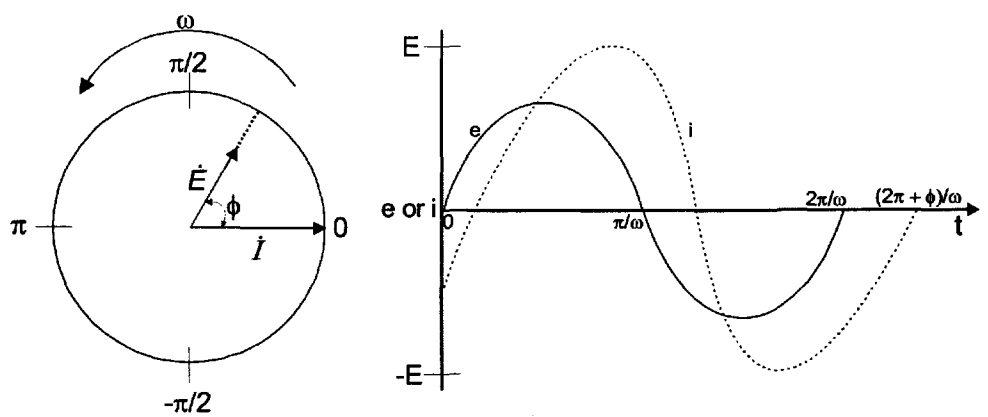

Figure 1.15. Phasor diagram showing relationship between alternating current and voltage signal at frequency ω.

The relationship between two phasors at the same frequency remains constant as they rotate; hence the phase angle is constant. In a simple circuit, in which a sinusoidal voltage, e = E sin ωt, is applied across a pure resistor R, Ohm's law always holds, and the current is (E/R) sin ωt, in phasor notation,

$$I = \frac{E}{R} \tag{1.15}$$

$$E = IR \tag{1.16}$$

The phase angle is zero, and the vector diagram is shown in Figure 1.16.

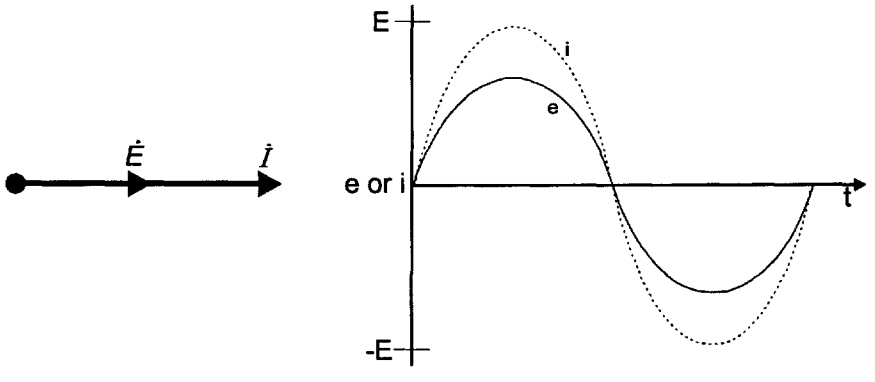

Figure 1.16. Relationship between the voltage across a resistor and current through the resistor.

If a pure capacitance, C, is substituted for the resistor, the fundamental relation of interest is then q = Ce, or *I* = C (*de/dt*), so that

$$i = \omega CE\cos\omega t \tag{1.17}$$

$$I = \frac{E}{X_c}\sin\left(\omega t + \frac{\pi}{2}\right) \tag{1.18}$$

where X_c is the capacitive reactance, $1/\omega C$.

The phase angle is $\pi/2$, and the current leads the voltage as shown in Figure 1.17. Since the vector diagram has now expanded to a plane, it is convenient to represent phasors in terms of complex notation. Components along the ordinate are assigned as imaginary and multiplied by $j = \sqrt{(-1)}$. Components along the abscissa are real. In circuit analysis, it is advantageous to plot the current phasor along the abscissa as shown in Figure 1.17.

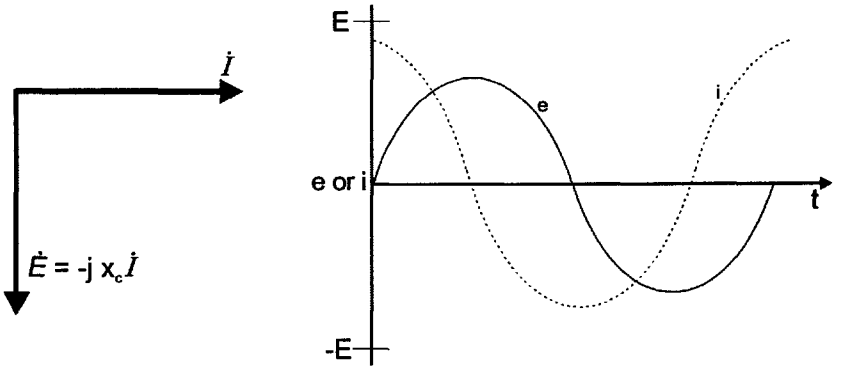

Figure 1.17. Relationship between an alternating voltage across a capacitor and the alternating current through the capacitor.

It implies that

$$E = -j\, X_c\, I \qquad (1.19)$$

Equation 1.19 must hold regardless of how I is plotted with respect to the abscissa, since only the relationship between E and I is significant. A

comparison of equations 1.18 and 1.19 shows that although X_c carries dimensions of resistance, unlike R, its magnitude falls with increasing frequency.

Now consider a resistance R, and a capacitance, C, in series. A voltage E, is applied across them, and at all times it must be equal to the sum of the individual voltage drops across the resistor and the capacitor, thus in this way,

$$E = E_R + E_C$$

$$E = I(R - jX_C) \qquad (1.20)$$

$$E = IZ,$$

so that the voltage is linked to the current through a vector

$$\mathbf{Z} = R - jX_c \qquad (1.21)$$

This is called impedance. In general impedance can be represented as

$$Z(\omega) = Z_{\mathrm{Re}} - jZ_{\mathrm{Im}} \qquad (1.22)$$

where Z_{Re} and Z_{Im} are the real and imaginary parts of the impedance. The impedance of a circuit ($\mathbf{Z}(\omega)$) at any frequency ω, can be represented in both polar and cartesian form with magnitude Z and phase angle ϕ.

$$Z(\omega) = E(t)/I(t) = Z\exp(-j\phi)$$

$$Z = Z\cos\phi - jZ\sin\phi = Z \qquad (1.23)$$

The magnitude of **Z**, written as $\mathbf{Z}$, is given by

$$Z^2 = R^2 + X_c^2 = Z_{\mathrm{Re}}^2 + Z_{Iim}^2 \qquad (1.24)$$

and the phase angle ϕ is given by

$$\tan\phi = Z_{\mathrm{Im}} / Z_{\mathrm{Re}} = X_c / R = 1/\omega RC \qquad (1.25)$$

The variation of impedance with frequency is often of interest and can be displayed in different ways. In the Bode plot, log **Z** and ϕ are both plotted against log ω. An alternate representation is the Nyquist plot, which displays Z_{Im} vs. Z_{Re} for different values of ω.

1.3.1.8.2. Electrical Equivalent Circuit

The fundamental laws governing the relationship between the charge and the potential and the properties of linear systems, are similar for electronic and ionic materials. Therefore as a first approximation, it is reasonable to assume that a direct connection exists between the behaviour of a real electrochemical system and that of an electrical circuit consisting of discrete components such as resistors, capacitors and inductors. [254] Randles[103,254] suggested that an electrical equivalent circuit can be used to represent various features in an electrochemical system, in order to describe the way various conducting elements in the electrochemical cell are connected and behave. The equivalent circuit approach in data analysis is even more popular in the study of solid ionic materials, as detailed microscopic models of all possible electrode and electrode

processes for such systems are generally not available or are extremely complex.[254]

A frequently used circuit, the Randles equivalent circuit, is shown in Figure 1.18.

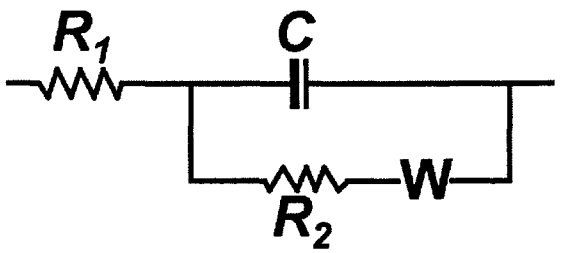

Figure 1.18. Randles equivalent circuit of an electrochemical cell

This circuit assumes a simple electrode process. In this process, the total cell or electrode impedance as a function of the frequency is measured from which the faradaic impedance (consisting of the low frequency limit known as the mass transfer represented by **W** and the high frequency kinetic control region known as the activation resistance R_2), the solution resistance R_1 and the double layer capacitance **C** are extracted from the results. Many other circuits have been devised in order to account for more complex systems, such as adsorption of electroreactants, multistep charge transfer, or homogeneous chemistry.

The circuit elements that make up equivalent circuits represent various macroscopic features involved in the transport of charge and mass. The dispersion relations for most equivalent circuit elements are very simple. If the

complex impedance diagrams show distinct features that can easily be related to specific subcircuits of the equivalent circuit model, analysis is simple, and can often be accomplished by graphical means using extrapolation of parameters. However, if the time constants of the respective subcircuits are close together, or if elements like Warburg impedance or a constant phase element (CPE) are involved, a more sophisticated analysis procedure is needed.

1.3.1.8.3. Data Analyses and Circuit Elements

The results of impedance experiments can be presented as complex impedance plots of the Nyquist type, namely the imaginary (out of phase) plotted versus the real (in phase) components of the impedance at various frequencies.[253] The data is analysed using a Non-Linear Least Square Fit (NLLSF) program with which frequency dispersion data of electrochemical systems can be analysed in terms of an equivalent circuit.[253,255,256] With the aid of a unique Circuit Description Code (CDC), different equivalent circuits may be used, depending on the data being analysed. This CDC is a string of symbols, each representing a specific type of element (for example, R for resistance).

In addition to the ideal circuit elements such as resistors, capacitors and inductors, there are other elements, which do not have simple physical equivalents. Some of these are Warburg impedance (W), which accounts for mass transport and diffusion, and a constant phase element (CPE),[257] which is

used to account for the frequency dispersion of the double layer capacitance as well as mass transport and diffusion.

The CPE is found in various electrochemical systems.[258,259] Physically the CPE represents a non normalizable distribution of relaxation times. It is the distribution of this that is often observed in impedance studies of solid electrodes. For example, for a thick polycrystalline bulk or rough electrode surface, a fractal behavior on its surface can be ascribed as cause for the occurrence of a CPE element. CPE has a non-integer power dependence on the frequency and can be expressed by

$$Q(\omega) = Q_0(j\omega)^n \qquad -1 < n < 1. \tag{1.26}$$

or separated into a real and an imaginary part:

$$\begin{aligned} Q &= Q_0\omega^n \cos\frac{1}{2}n\pi, \\ Q &= Q_0\omega^n \sin\frac{1}{2}n\pi, \end{aligned} \tag{1.27}$$

In fact, Q represents a very general dispersion relation. For n = 1, it models a capacitance with $C = Q_0$; for n= 0, a resistance with $R = Q_0^{-1}$; and for n = -1, an inductance with $L = Q_0^{-1}$. A special case is obtained for n = ½, that is, the so-called Warburg element W), which models semi-infinite diffusion or mass transport.[103]

The CPE dispersion is a common phenomenon, which can be attributed to a number of causes: ion relaxation processes,[260] roughness of the electrode

surface,[261] kinetic effects,[262] and the dielectric relaxation of molecules adsorbed on the electrode surface.[263,264]

A summary of the dispersion equations and CDC symbols is given in Table 1.3.

Table 1.3. Dispersion equations and CDC – symbols for simple elements.

Element	Symbol	Dispersion Relation in Impedance
Resistance	R	R
Capacitance	C	$-j / \omega C$
Inductance	L	$j \omega L$
Warburg	W	$(1-j) / Q_0 / \sqrt{2\omega}$
CPE	Q	$\omega^n[\cos½n\pi \pm j\sin½n\pi]Q_0$

1.3.1.8.4. Instrumentation and Experiment

Impedance measurements can be made in either the frequency domain, with a frequency response analyzer (FRA), or in the time domain using Fourier transformation with a spectrum analyzer. The advantage of measurements taken in the frequency domain over time domain is that the frequency response gives direct impedance which can be described directly and analytically using the equivalent circuit whilst fourier transformation is needed in time domain to yield frequency-dependent impedance. Such transformed frequency spectrum is not directly controlled,and so the impedance may not be well determined over all desired frequencies.

The basic principles of the FRA in measuring the impedance of an electrochemical cell are shown in the block diagram in Figure 1.19.

The FRA generates a signal e(t) = $\Delta E \sin(\omega t)$ that is fed to the potentiostat. This is added to E_{dc} and fed to the cell. In practice, care must be taken to avoid phase and amplitude errors that can be introduced by the potentiostat, particularly at high frequencies.

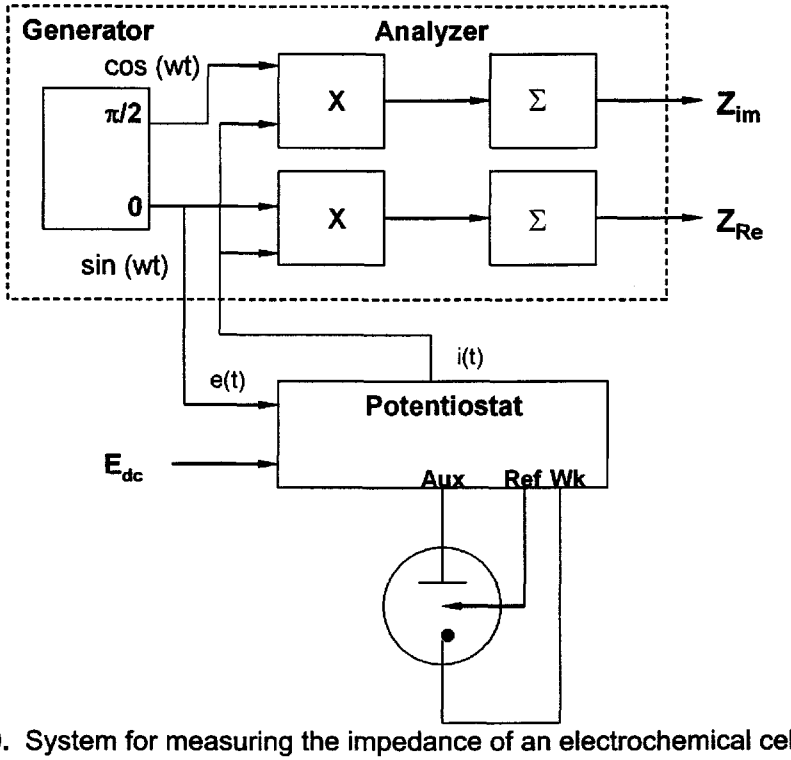

Figure 1.19. System for measuring the impedance of an electrochemical cell based on a frequency response analyzer (FRA).

The resulting current, i(t), or more precisely the voltage signal proportional to the current, is fed to the analyzer, mixed with the input signal, and integrated over several signal periods to yield signals that are proportional

to the real and imaginary parts of the impedance (or the magnitude and phase angle of impedance). Most commercial FRAs cover the frequency range of 10μHz to 20MHz. However, the typical potentiostat may limit the frequency range in an experiment. Usually the instrument is interfaced to a computer for data acquisition, and for sweeping the frequency over a given range and storing the resulting impedance data for further analysis.

1.3.1.8.5. Studies of Modified Electrodes

AC-EIS has been used to study the ionic insulating properties of alkanethiol SAMs. It was revealed that the phase angle at an ion-diffusion-related frequency (1 Hz) is independent of the electrolyte concentration, indicating that the thiol chains act as a dielectric material. Both the phase angle and the complex dielectric constant in the low-frequency region show the film's ability to act as an ionic insulator.[84]

SAMs have been investigated by AC-EIS in the absence of a redox probe. SAM permeability can be elucidated by studying the behaviour of the phase angle at frequencies less than ~50 Hz, the frequency domain characteristic of diffusion processes. The permeability of these non-functionalized SAMs as a function of an applied potential falls into two regimes. One regime corresponds to a state where the SAM is an ionic insulator and is well described by the Helmholtz capacitor model.[84,265-267] The other regime is described by the Randles circuit (Figure 1.18).

In the present study, AC-EIS is used to investigate the blocking behaviour of SAMs. The electrode is biased at the Nernst potential (close to E^0) of an electrolyte containing both the oxidized and the reduced forms of a probe redox couple. A complete electrochemical description of the electrode-solution interface is achieved by measuring the impedance as a function of frequency, redox species concentration, and electrode potential. The impedance results of an electrode undergoing heterogenous electron transfer can be described by the Randles circuit (Figure 1.18) and presented as complex impedance plots of the Nyquist type as shown in Figure 1.20.

In the Randles circuit, it is assumed that the resistance to charge transfer and the diffusion impedance are both in parallel with the interfacial capacitance. This parallel combination of R_2 and C gives rise to a semicircle in the complex plane plot, indicated on Figure 1.20 as section A. The mass transport term, which cannot be presented by classical circuit elements, but as W, is observed as a low frequency spur with a slope of unity (section B in Figure 1.20

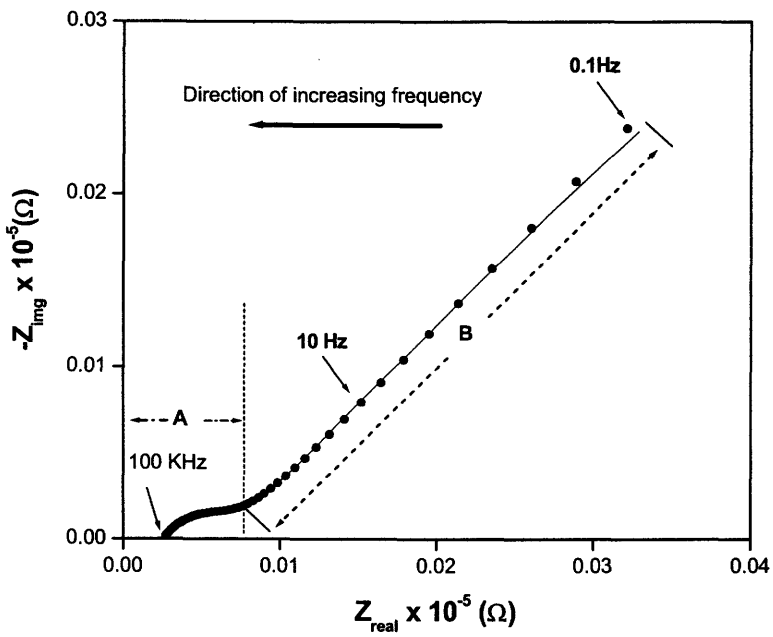

Figure 1.20. Simulation of the Nyquist plot of an EIS experiment involving a bare gold electrode in $Fe(CN)_6^{4-/3-}$ redox probe.

In the SAM-modified electrodes in the present study, the more dominant section of the Nyquist plot is expected to be section A, as the blocking behaviour of the SAM increases the capacitance and hence the resistance, R. Furthermore, mass transport is drastically reduced and is virtually almost absent or very insignificant in a SAM-modified electrode. The solution resistance is obtained by measuring the impedance of the system at a very high frequency (> 10kHz), as indicated on Figure 1.20. Thus, AC-EIS allows one to observe the magnitude of the interfacial electrical circuit elements better than that for measurements based on CV.

AC-EIS data sometimes agree qualitatively with the observed CV. It is tempting to relate the peak current in the CV and the magnitude of the charge transfer resistance to the coverage of the electrode by assuming that electron transfer reactions occur at only bare spots on the electrode surface and that diffusion to these defect sites is planar and that linear diffusion predominates. This assumption is not correct, as the magnitude of the CV fractional coverage is always less than the fractional coverages obtained from AC-EIS data.[100] This method for describbing fractional coverage has been proved to be inappropriate[249,268] because of the dominance of radial diffusion (non-linear diffusion) near each defect site. One may therefore have to consider another technique based on an analysis of the pore size distribution in the SAM. The discrepancy therefore in the fractional coverage estimates is explained better if radial diffusion to the micropores dominates. Finklea et al. [245,269]have established that, if radial diffusion to the micropores is occurring, then the peak current observed is not a simple function of the exposed area of the SAM coated electrode.

1.3.2. Calorimetry

Thermal techniques are among the most fundamental means of studying phases of matter. They give information on properties ranging from bulk material thermal stability to intermolecular interactions. A wide variety of

processes can give rise to thermal effects that can be detected with thermal analysis. These can range from mass loss on heating to endotherms or exotherms due to phase transitions (solid-solid, rigid glass-supercooled liquid, solid-liquid, liquid-vapour, miscible-immiscible, etc.) and/or reactions.[270] Differential Scanning Calorimetry (DSC) is one of the most common and often the most useful thermoanalytical technique.

1.3.2.1. Differential Scanning Calorimetry

DSC is based on the measurement of the difference between power requirements for heating a sample, and those for heating a reference, both at the same constant rate. As the name implies, the measurement is differential (between the sample and reference), scanning over temperature so that equilibrium is not established. DSC applies heat energy over a wide range of temperatures to measure the progress of a chemical or physical process.

A schematic diagram of a typical DSC is shown in Figure 1.21. A small sample (typically 10-30mg) encased in a metal pan is heated (or cooled) such that the temperature is a linear function of time. The reference chamber is heated (or cooled) at the same rate, so that there is no temperature difference between the thermometer in contact with the sample and the thermometer in contact with the reference, that is $\Delta T = 0$.

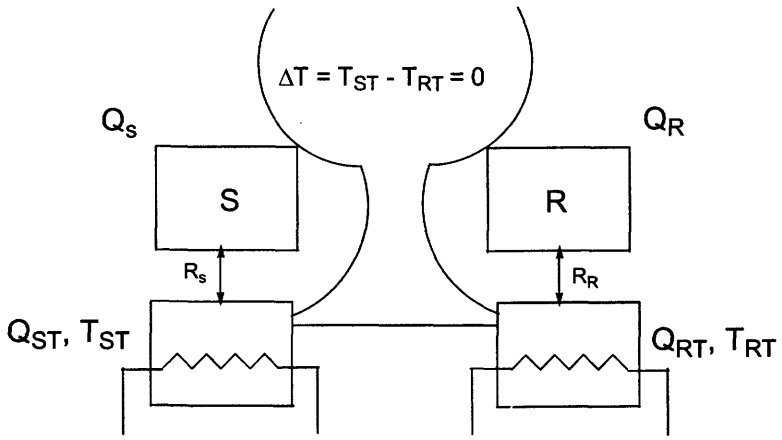

Figure 1.21. Schematic diagram of a typical calorimeter for DSC. The sample (S) and the reference (R) are heated (or cooled) at a constant rate such that their temperatures are kept equal ($\Delta T = 0$).[270]

The DSC equipment is designed to measure ΔQ, the difference between Q_s, the power to the sample, and Q_R, the power to the reference ($\Delta Q = Q_S - Q_R$ here, although it could also be defined with the opposite sign). In the DSC experiment ΔQ is plotted as a function of temperature, which is proportional to time, as shown in Figure 1.22.

The resulting plot would be flat ($\Delta Q = 0$) if the sample and reference were perfectly matched thermally throughout the temperature range of the experiment. An endothermic process in the sample will give rise to a peak in one direction ($Q_s > Q_R$) and an exothermic process in the sample will exhibit a peak in the opposite direction ($Q_s < Q_R$), as shown in Figure 1.22.

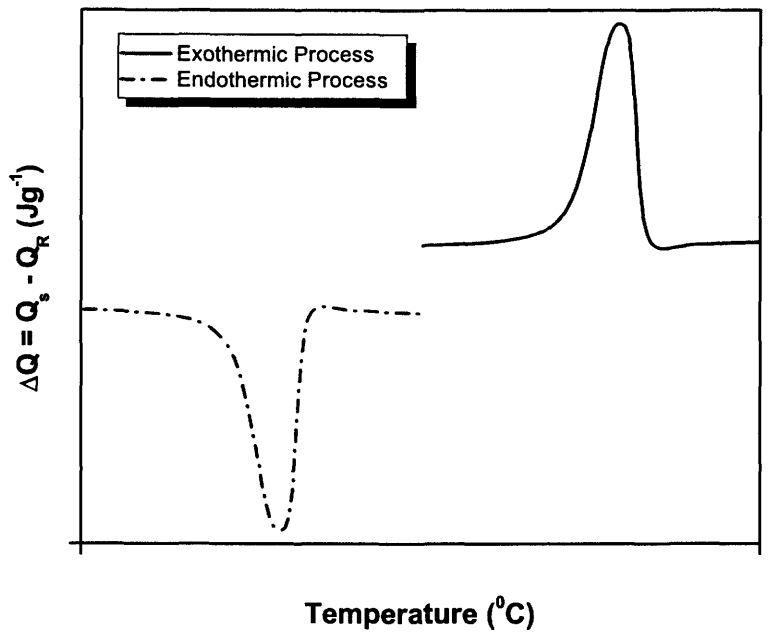

Figure 1.22. A simulated DSC thermogram showing an endothermic process followed by an exothermic process. As shown, the baseline is usually flat.

1.3.2.1.1. Typical Differential Scanning Calorimetry Experiment

During a DSC experiment, a sample is heated over a temperature range. At some temperature, the material starts to undergo a chemical or physical change that releases or absorbs heat. As the temperature increases, the process continues to completion. If one plots heat released as a function of temperature, then the area under the curve represents the total heat or enthalpy change (ΔH) for the entire process. The peak of such a plot indicates the

temperature (T_m) at which the reaction is half-complete. From the shape and midpoint of the curve, one can obtain the heat capacity (C_p) of the material.

1.3.2.1.2. Determination of Phase Transitions in Alkanethiol-Capped Gold Colloids

The energetics of the self-organization and the phase behaviour of alkanethiols chemisorbed on planar gold surfaces are difficult to investigate by traditional calorimetry. The 2D character of SAMs when they are chemisorbed on planar gold surfaces limits the experiments by which they can be probed. Gold colloids stabilized with chemisorbed alkanethiols provide a 3D analogue of 2D monolayers that can be investigated by additional conventional (i.e., 3D) methodologies, including thermal methods.[36,119]

The transformation at equilibrium from one condensed matter phase to another always has an associated entropy change and hence an associated enthalpy change. Thus DSC can be very useful in the characterization of phase transitions.[271] In this context, the 3D alkanethiol-stabilized colloids offer a relatively quick method to investigate enthalpies associated with phase transitions by DSC.

Organized systems that have been characterized by DSC include alkanethiols,[36,86,111,272,273] proteins and nucleic acids,[118,274] lipids and membrane components,[275,276] among others[1]. Relatively little sample material is required

and the sample can be studied repeatedly on heating and cooling cycles, giving information on reversibility and thermal history effects of phase transformations.[86,272]

Of particular interest to this work are studies of alkanethiol-capped gold colloids (3D SAMs). The temperature and the enthalpy of the phase transition have previously been investigated in an attempt to characterize the phase behaviour of these colloids.[36,272] The DSC thermograms clearly showed that the RS/Au colloids in the solid state undergo distinct phase transitions associated with reversible order/disordering of the alkyl chains. Both the peak maximum temperature and the enthalpy associated with the DSC transition were found to increase with increasing chain length. This trend strongly parallels that seen in analogous lipid bilayers,[272] as well as other materials undergoing gel-liquid crystalline transitions, such as diacylphospholipid vesicles. The DSC peak maximum temperature and enthalpy measured for RS/Au colloids (R= C_{12} - C_{20}) are very close to that of n-diacylphosphatidycholines of equivalent chain length.[36,272] It has been demonstrated that this transition originates in the chain terminus region and propagates toward the middle of the chain as the temperature increases. However, it has been shown that this disordering does not extend to the tethered sulphur head group.[86]

Similar temperature dependant behaviour has been observed for alkanethiol SAMs on planar gold by variable temperature electrochemistry.[82] In this work, DSC is used to investigate alkanethiol-capped gold colloids (3D

SAMs) and to correlate the results with parallel variable temperature studies on 2D SAMs using CV and AC-EIS.

1.3.3. Nuclear Magnetic Resonance Spectroscopy

NMR spectroscopy is one of the most powerful tools available to the chemist for elucidating the structure and orientation of chemical species. It is based on the measurement of absorption of electromagnetic radiation in the radio-frequency (RF) region of roughly 4 to 900 MHz. The theoretical basis for NMR spectroscopy is that certain atomic nuclei have a spin and a magnetic moment, such that exposure to an external magnetic field leads to splitting of their energy levels.

1.3.3.1. Nuclear Spin and Energy Levels in a Magnetic Field

Subatomic particles (electrons, protons and neutrons) can be imagined as spinning on their axes. In many atoms such as ^{12}C, these spins are paired against each other, such that the nucleus of the atom has no overall spin. However, in some atoms such as ^{1}H and ^{13}C the nucleus does possess a net spin.

Quantum mechanics suggests that a nucleus of an overall spin I will have $2I + 1$ possible orientations. A nucleus with a spin of ½ will have 2 possible

orientations. In the absence of an external magnetic field, these orientations are degenerate. If a magnetic field is applied, then the energy levels split, as shown in Figure 1.23.

Each level has a magnetic quantum number, m. When the nucleus is in a magnetic field, the initial populations of the energy levels are determined by thermodynamics, as described by the Boltzmann distribution. This means that the lower energy level will contain slightly more nuclei than the higher level. It is possible to excite these nuclei into the higher level with electromagnetic radiation of a frequency determined by the difference in energy between the energy levels.

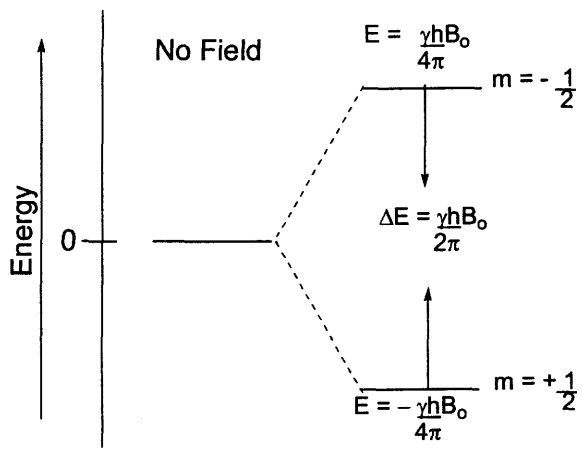

Figure 1.23. Energy Levels for a nucleus with spin quantum number ½.

The nucleus has a positive charge and a spin, I, generating a small magnetic field. The nucleus therefore possesses a magnetic moment, μ, which is proportional to its spin, I.

$$\mu = \frac{\gamma I h}{2\pi} \qquad (1.28)$$

The constant, γ, magnetogyric ratio, is a fundamental nuclear constant, that has a different value for every nucleus and h is the Planck constant. The energy of a particular energy level is then given by

$$E = -\frac{\gamma h}{2\pi} mB \qquad (1.29)$$

where B is the strength of the magnetic field at the nucleus. The energy difference between levels (the transition energy) can be found from

$$\Delta E = \frac{\gamma h B}{2\pi} \qquad (1.30)$$

This means that if the magnetic field, B, is increased, so is ΔE. It also means that if a nucleus has a relatively large magnetogyric ratio, then ΔE is correspondingly large.

Imagine a nucleus (of spin ½) in a magnetic field. This nucleus is in the lower energy level (i.e., its magnetic moment does not oppose the applied field). The nucleus is spinning on its axis. In the presence of a magnetic field, this axis of rotation will precess around the magnetic field B_0 (Figure 1.24).

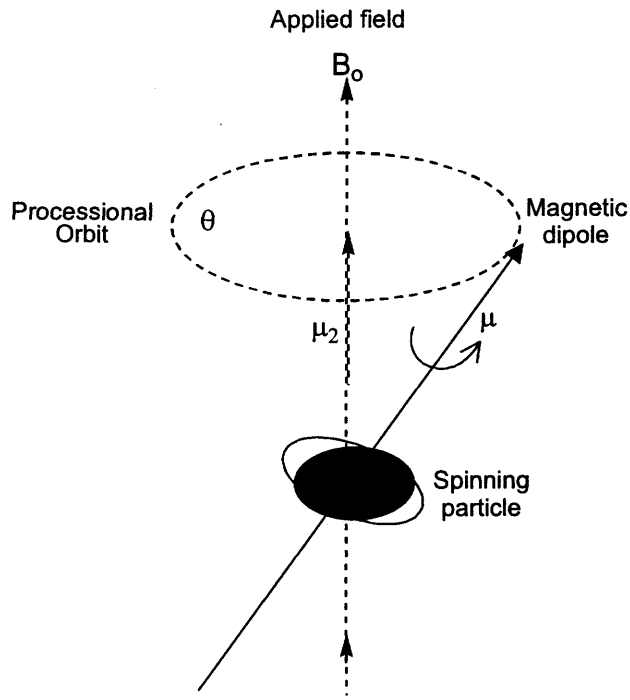

Figure 1.24. Precession of a rotating particle in a magnetic field

The frequency of precession is termed the Larmor frequency, which is identical to the transition frequency. The potential energy of the precessing nucleus is given by;

$$E = - \mu B_0 \cos \theta \qquad (1.31)$$

where θ is the angle between the direction of the applied field and the axis of nuclear rotation, and μ is the magnetic moment. If energy is absorbed by the nucleus, then the angle of precession, θ, will change. For a nucleus of spin ½ , absorption of radiation "flips" the magnetic moment so that it opposes the applied field (the higher energy state). Only a small proportion of "target" nuclei

are in the lower energy state (and can absorb radiation). There is the possibility that by exciting these nuclei, the populations of the higher and lower energy levels will become equal. If this occurs, then there will be no further absorption of radiation. The spin system is saturated. Relaxation processes such as spin-lattice (longitudinal) relaxation and spin-spin (transverse) relaxation will return nuclei to the lower energy state.

1.3.3.2. Chemical shift

When a molecule containing the nuclei under observation is placed in the magnetic field, the electrons within the molecule shield the nuclei from the external applied field. That is the magnetic field at the nucleus (equation 1.29) is not equal to the applied magnetic field. The difference between the applied magnetic field and the magnetic field at the nucleus is termed the nuclear shielding and this is proportional to the applied field.

The chemical shift is defined as the nuclear shielding divided by the applied field. It is only a function of the nucleus and its environment. That is it is a molecular quantity. It is normally measured relative to a reference compound. For ^{1}H NMR, the reference is usually tetramethylsilane ($Si(CH_3)_4$).

1.3.3.3. Instrumentation

Figure 1.25 is a simplified block diagram showing the instrumental components of a typical Fourier Transform NMR spectrometer. The central component of the instrument is a highly stable magnet in which the sample is placed. A transmitter/receiver coil surrounds the sample.

A crystal controlled frequency synthesizer having an output frequency of νc produces RF radiation. This signal passes into a pulser switch and power amplifier, which creates an intense and reproducible pulse of RF current in the transmitter coil. The resulting RF radiation impinges on the sample contained inside the coil. The length, amplitude, shape, and phase of the pulse are selected by the operator, entered into the console, and controlled by the computer.

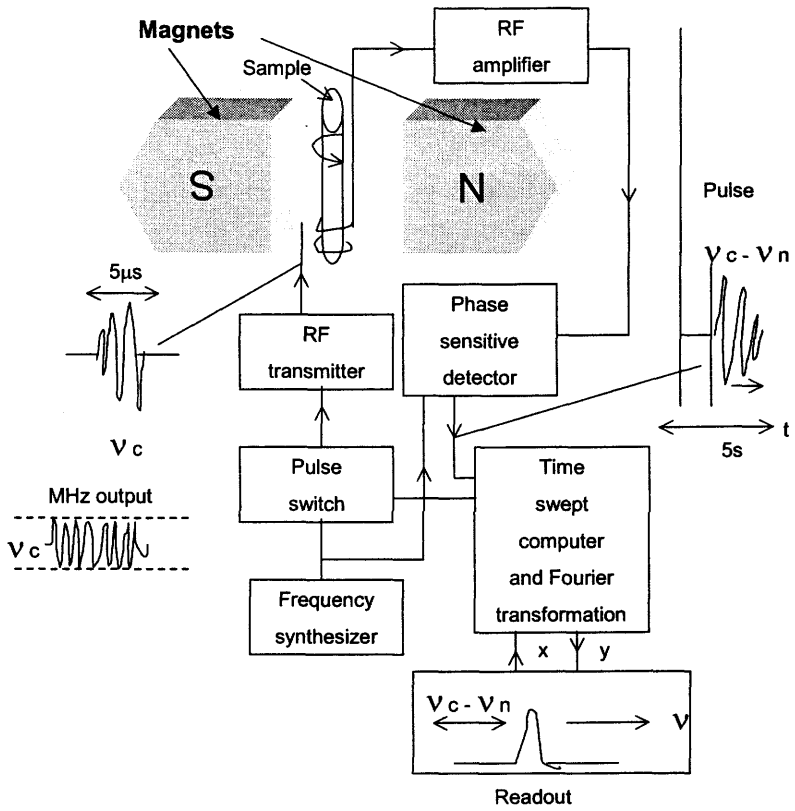

Figure 1.25. Block diagram of a fourier transform NMR Spectrometer.[277]

In Figure 1.25, a 5-μs pulse is shown. The resulting FID signal is picked up by the same coil, which now serves as a receiver. The signal is then amplified and transmitted to the phase-sensitive detector. The detector circuitry produces the difference between the nuclear signals ν_n and the crystal output ν_c, which leads to the low-frequency time domain signal shown on the right of Figure 1.25. This signal is digitized and collected in the memory of the computer for analysis by a Fourier transform program and other data analysis

software. The output from this program is plotted, giving a frequency-domain spectrum. [278]

1.3.3.4. Nuclear Magnetic Resonance Studies of Alkanethiol-Capped Gold Colloids

As stated in section 1.3.2.1.2, stabilization of gold colloids with chemisorbed alkanethiol provided a 3D system analogous to 2D SAMs with which to exploit some conventional analysis techniques, including thermal methods, IR and NMR,[36,112,119] that couldn't be employed with 2D SAMs on planar metal surfaces.

In ^{13}C NMR, frequencies depend on the carbon position relative to the gold-hydrocarbon interface. In view of this, solution[119] and solid state[36,272,279] NMR spectroscopy have been used to investigate the chain melting behaviour in alkanethiol-capped gold colloids by observing chemical shift differences as a function of temperature.

Variable temperature solid state ^{13}C NMR of the colloids reveals that they undergo disordering transitions, which span broad range of temperatures,[113-115,117,119,280] similar to a gradual growth of the population of disordered chains observed by DSC.[119] Well-resolved peaks are observed, as the ^{13}C chemical shifts for all-trans extended chains are shifted downfield from chains containing gauche defects. In the hydrocarbon moiety of the colloids, thermal chain

disordering manifests itself as the gradual increase in the gauche conformers and a decrease in the all-trans peak. This was confirmed by deuterium NMR spectroscopy. The chain disordering process is reversible, as the ^{13}C NMR spectrum returns to its original, trans-dominated state upon cooling to room temperature. For a given chain length, the chain ordering process occurs over the same temperature range in the alkanethiols, phosphonates, and carboxylate 3D SAMs. Solid-state ^{1}H NMR reveals results similar to those of ^{13}C.

Solution NMR on the other hand, does not reveal any disordering transition, presumably because in solution, the chains are already in a liquid-like state. Differences in chemical shifts as a function of temperature are negligible for each particular alkanethiol-capped gold colloid.

In this work, both solution ^{1}H and ^{13}C NMR is used to perform temperature studies on alkanethiol-capped gold colloids, to help explain parallel studies on 2D SAMs using CV and AC-EIS.

Chapter Two – Experimental

2.1. Chemicals

Hexadecanethiol (HDM) [Aldrich 92%] was redistilled and octadecanethiol (ODM) [Aldrich 98%] was recrystallized from hexane [BDH]. Aqueous solutions were prepared with deionized Millipore water [18.2 $M\Omega cm^{-1}$] obtained from a Milli-Q water system. Bulk polycrystalline gold electrodes (0.0227 cm^2) and glassy carbon electrodes (0.0710 cm^2) were obtained from Bioanalytical Systems (BAS). All other chemicals were used as received.

2.2. Electrochemistry

2.2.1. Electrochemical Cell and Instrumentation

The electrochemical cell used a conventional three-electrode configuration, with a counter electrode of Pt wire and a Ag/AgCl reference electrode (3M NaCl, BAS). A regular cell was employed for room temperature

experiments and a water-jacketed cell connected to a thermostated water bath (Neslab) was used in the variable temperature measurements. The temperature was monitored directly in the cell by a DP460 Omega thermocouple to ±0.1°C. The whole set-up was enclosed in a grounded Faraday cage. The working electrodes were bulk polycrystalline gold electrodes (Figure 2.1) or glassy carbon electrodes. CVs were recorded using an EG&G M2783 potentiostat and AC-EIS was measured using an EG&G M1025 FRD interfaced to the potentiostat. The data acquisition and control was handled by a computer interfaced to the FRD and potentiostat via an IEEE – 488 General Purpose Interface Bus (GPIB) and run with software for CV (M270) and AC-EIS (M398). The instruments were calibrated using dummy cells, and a collection of high quality resistors and capacitors were used to calibrate the impedance data.

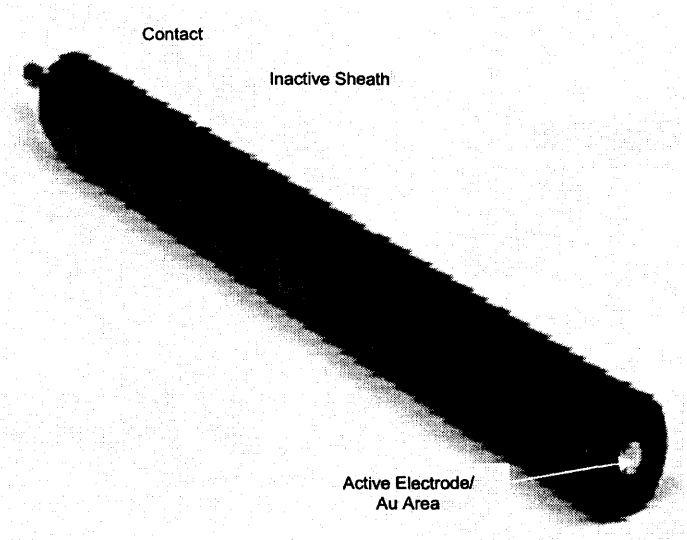

Figure 2.1. Button-type polycrystalline gold electrode (BAS) comprised of an active electrode area confined by an inactive sheath, and connected to an electrical contact.

2.2.2. Procedure

2.2.2.1. Cleaning of Gold Electrodes

Bulk polycrystalline gold electrodes were polished on microcloths pads with alumina slurries, and rinsed in absolute ethanol and/or water. Removing the thiols from the gold electrodes after each experiment was important in this work. To clean the electrodes, a simple protocol was developed and is described below.

All gold electrodes previously modified with thiol compounds were polished with alumina slurry. Linear sweep voltammetry (LSV) of the polished electrode was then carried out in 0.5 M KOH solution from 0.0 to –1.2 V to remove any remaining traces of thiol by reductive desorption. These steps were repeated until the reductive desorption step produced no characteristic thiolate reduction peak between –0.8 and –1.2 V. LSV on the gold electrode in 0.1 M H_2SO_4 from 0.0 to 1.4 V was used to oxidize the clean gold surface. The gold electrode was then incubated in absolute ethanol for about 10 minutes to reduce the gold oxide surface to pure gold. The electrode was then rinsed in water prior to incubation in thiol solution, or to electrochemical characterization. The procedure described above, provided a reproducible bare gold surface as determined by CV. The surface roughness of the gold electrodes was determined by under potential deposition (UPD) of copper[281] and is described in 2.2.2.4.

2.2.2.2. *Cleaning and Polishing of Glassy Carbon Electrodes*

A cleaning procedure for the glassy carbon electrode was adopted from the literature.[103,111,282,283] The electrode was successively polished with three grades of alumina slurry (particle sizes 1 μm, 0.3 μm, 0.05 μm). Between polishing steps, the electrode was sonicated in water for approximately 5 minutes to remove any adsorbed alumina.

2.2.2.3. *Self-Assembled Monolayer Preparation of Alkanethiols*

After the gold electrodes were cleaned, they were ready for either LB deposition (see 2.3.3.) or SAM formation. Electrodes designated for SAM formation were immersed in 1-5 mM ethanolic solutions of the thiol compounds and incubated at 23 ± 2 °C for times ranging from 24 hours to 1 week. Reproducibility of the resulting films was greatly enhanced when the modified electrodes were subsequently incubated for 24 hours in Millipore water prior to characterization. It is believed that with the favourable association of like molecules, this procedure enhanced hydrophobic ineraction between the alkyl chains as it was in a hydrophilic environment of the water. The modified electrodes were rinsed with absolute ethanol followed by water prior to CV and AC-EIS measurements.

2.2.2.4. *Determination of Surface Roughness*

The surface area of clean gold electrodes was determined by the copper coverage on an Au(III) surface.[281] A potential step method using chronoamperometry (CA) was performed in 1.0 mM $Cu(ClO_4)_2.6H_2O$ /0.1 M $HClO_4$ from a potential range of 500 – 0 mV with a scan rate of 50 mVs^{-1}. This resulted in the deposition of copper atoms. Because the E^o of Cu^{2+}/Cu^0 is less than that of E_{upd} (the potential for deposition of copper atoms on gold), which is an underpotentail with respect to the E^o for Cu^{2+}/Cu^0, this makes it electrochemically feasible to deposit monolayer of copper atoms on the surface of the gold working electrode. LSV was then used to strip off the copper from the surface of the gold electrode by oxidizing it from a potential of 150- 500mV. The amount of charge required to strip the monolayer gave the number of copper atoms deposited, which in turn gave the active surface area of the bare gold electrode.

2.2.2.5. *Cyclic Voltammetry*

After incubation or deposition of a film, CV experiments were run in solutions of 3 mM $K_3Fe(CN)_6$ and 3 mM $K_4Fe(CN)_6$ in 0.1 M KCl. Potentials were changed between 0 – 500 mV at 50 mV s^{-1}.

2.2.2.6. *Alternating Current-Electrochemical Impedance Spectroscopy*

AC-EIS measurements were done on films in solutions of 3 mM $K_3Fe(CN)_6$ and 3 mM $K_4Fe(CN)_6$ in 0.1 M KCl, with an applied bias voltage of 250 mV versus Ag/AgCl, and with a 5 mV (rms) sinusoidal excitation amplitude. A small amplitude of 5 mV was used because at a bias voltage of 250 mV where there is no net redox reaction occurring, the only external driving force for the reaction would have a minimal effect on the monolayer.[284] The data was measured and collected for 48 harmonic frequencies from 0.1 Hz to 100 kHz at 8 steps per decade.

2.2.2.7. *Temperature Studies*

Temperature studies were performed over the range of 10 to 65°C. The temperature was increased with heating rates of 0.5° C min^{-1}. All variations in temperature were initially performed from low to high temperatures (heating), and then from high to low (cooling).

2.3. Langmuir and Langmuir-Blodgett Films

2.3.1. Instrumentation

The Langmuir Film balance and trough - a KSV 3000 model (Netherlands) is a computer controlled and user programmable LB instrument

for automated Langmuir Film experiments and for unsupervised deposition of LB films onto solid substrates. The trough was equipped with a platinum Wilhelmy plate, and a dipping well (115 mm x 25 mm x 100 mm) with a dipping arm for LB deposition

2.3.2. Langmuir Films

Spreading solutions of MUA, HDM and ODM (7.4-8.3 $mgmL^{-1}$) were prepared freshly by dissolving appropriate amounts of the alkanethiol in chloroform. Aliquots of these solutions (50μL) were delivered to the surface of the subphase at several locations, and were allowed to evaporate for ~ 5 minutes. The concentrations and salts used for the subphases were ammonium chloride (0.001, 0.01 and 0.1 M), barium chloride (0.001, 0.01 and 0.10 M), gadolinium chloride (0.01, 0.1 and 1.0 M), hydrochloric acid (0.1 M), potassium chloride (0.01 and 0.1 M) and sodium chloride (0.01 and 0.1 M). The purity of the subphase and the chloroform were verified by running the appropriate blank isotherms prior to the spreading of each solution.

Langmuir films were compressed at a maximum speed of 5mm min^{-1} with a limiting rate of increase in surface pressure of $1mNm^{-1}min^{-1}$. The resulting surface pressure-area (**π-A**) isotherms were recorded. The effect of temperature was investigated by running isotherms at subphase temperatures ranging from 8 to 20°C. During these experiments, the subphase temperature

was kept constant to within ±0.1°C by circulating water-ethylene glycol mixtures (50 : 50 v/v) from a Neslab water bath. The temperature of the subphase was monitored using a thermistor.

2.3.3. Deposition of Langmuir-Blodgett Films

In order to provide a valid comparison between previously reported SAMs and the present LB films, the same electrode was used – a button-type polycrystalline Au electrode from Bioanalytical Systems (BAS) (Figure 2.1).

A holder that attaches to the LB trough dipping arm was designed (Figure 2.2) such that the Au electrode surface is held perpendicular to the air-water interface, and hence the Langmuir monolayer.

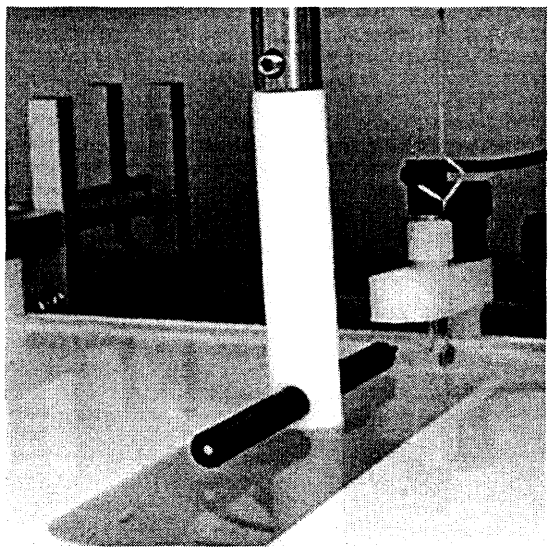

Figure 2.2. Holder for polycrystalline gold electrode (BAS) used for LB deposition.

LB monolayers of compressed films were transferred under Argon onto the gold electrodes, at subphase temperatures ranging from 8 to 20°C, in the following sequence: First, the electrode (after thorough cleaning with successive rinsing with water and ethanol and sonicating in water) was immersed in the clean subphase between fully expanded barriers, and then the spreading solution was deposited onto the subphase surface and compressed as described in Section 2.3.2 (Figure 2.3). When the desired deposition surface pressure was reached, the gold electrode was lifted through the Langmuir film at a rate of 1mm min^{-1} using the automation control.

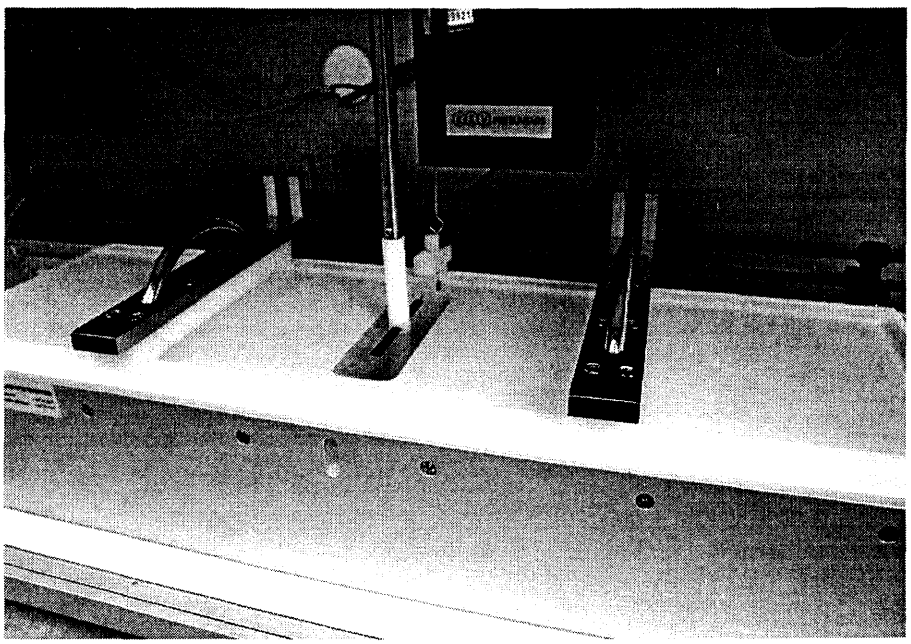

Figure 2.3. Extended barriers of LB film balance with the dipping arm and electrode below the surface of the water during compression of Langmuir film at the air-water interface.

After LB transfer, the modified electrodes were rinsed with absolute ethanol and Millipore water, then stored in water overnight prior to CV and AC-EIS measurements.

To avoid impurities and contamination, disposable gloves were worn when delaing with the LB trough and film balance. The whole setup was protected with a custom-made transparent plexiglass cover.

2.4. Alkanethiol-Capped Gold Colloids

Gold colloids were derivatized with HDM and ODM to produce alkanethiol-capped gold colloids. They were prepared following the procedure of Brust and co-workers.[23]

2.4.1. Synthesis and Characterization

The synthesis involved a two-phase (water-toluene) synthesis illustrated in Figure 2.4. The gold salt, $HAu(III)Cl_4.3H_2O$, was dissolved in water and transferred to the alkanethiol/toluene solution via a phase transfer agent tetraoctylammonium bromide $[(C_8H_{17})_4NBr]$ ($AuCl^-_4$ is the species transferred to the toluene layer from the water layer). Upon addition of the reducing agent, $NaBH_4$, it reduced the gold in the presence of ODM or HDM at the toluene/water interface and the organic phase changed from orange to deep brown within a few seconds – an evidence of derivatization of the alkanethiol. Flocculation

occurred slowly for 24 hours at –20°C using a dry ice-acetone bath. The reactions were carried out using the ratios of 1.1 : 1 $HAuCl_4$/RSH, 4.4 : 1 $(C_8H_{17})_4NBr$: $HAuCl_4$ and 11 : 1 $NaBH_4$/ $HAuCl_4$ under ambient conditions for 3 hours with constant stirring . The resulting black sample was filtered by suction filtration (0.2μm pore, Schleicher and Schuell, Keene, NH).

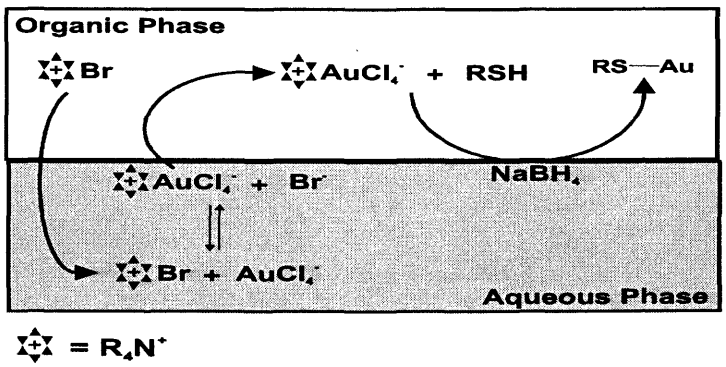

Figure 2.4. Two phase water-toluene synthesis illustrated.

Elemental analysis, FT-IR and ^1H and ^{13}C NMR, were used to characterize the colloids . Details of the procedure and measurements are given below.

2.4.1.1. Elemental Analysis

A Perkin Elmer 2400 CHN Elemental analyser was used to analyse for the percentages of the colloids of HDM and ODM. Details for C, H, S and Au are presented in Table 2.1 below. Au was found by difference.

Table 2.1. Percentages of elements from elemental analysis of colloids

Elements	HDM (%)		ODM (%)	
	Found	Calculated	Found	Calculated
C	22.65	22.8	24.65	24.55
H	3.92	4.03	4.25	4.25
S	3.78	3.88	3.64	3.64
Au	69.65	69.29	67.56	67.56

2.4.1.2. Fourier Transform - Infrared

Approximately 3mg of the gold colloid was mixed with 5mg of KBr and made into a pellet. The FT-IR spectra were acquired at ambient temperature using a Bio-Rad FTS 40 mid-IR spectrometer. The spectrum was collected in the transmission mode at a resolution of $2cm^{-1}$ with 128 scans between 4000 and $600cm^{-1}$. The FT-IR sample was purged with nitrogen. Background spectra of the clean KBR pellet was collected and subtracted from the sample spectra.

The FT-IR spectra of the colloids were taken and compared to the spectra of the molecular alkanethiols of HDM and ODM (Figures 2.5 and 2.6, respectively). An extensive FT-IR investigation of the alkanethiol-capped gold colloids (solids, KBr pellets)[279] has shown that their alkyl chain

microenvironment mimics crystalline bulk hydrocarbons[116] and alkanethiol monolayers on flat gold surfaces.[106]

For example, in Figures 2.5 and 2.6, the methylene chains in both the HDM and ODM colloids are predominantly trans based, sharp wagging and rocking progression bands (as shown in Table 2.2).

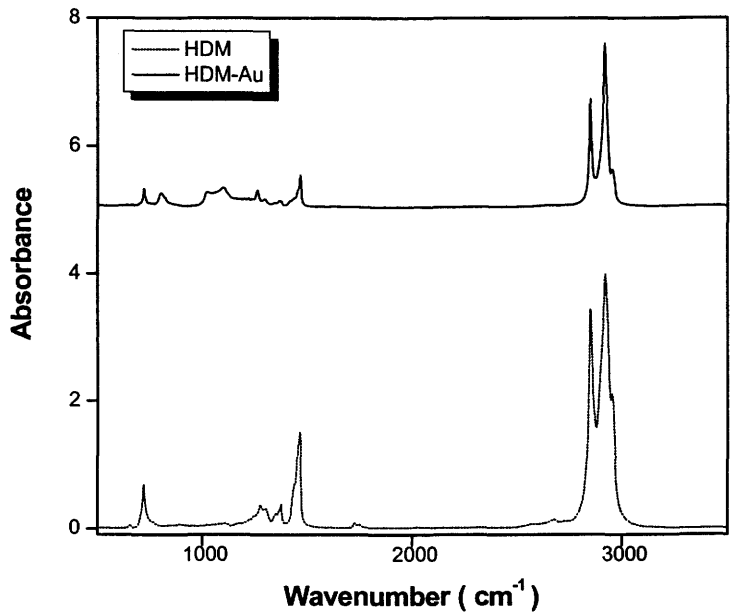

Figure 2.5. FT-IR spectrum of HDM and HDM on colloidal gold (KBR pellet).

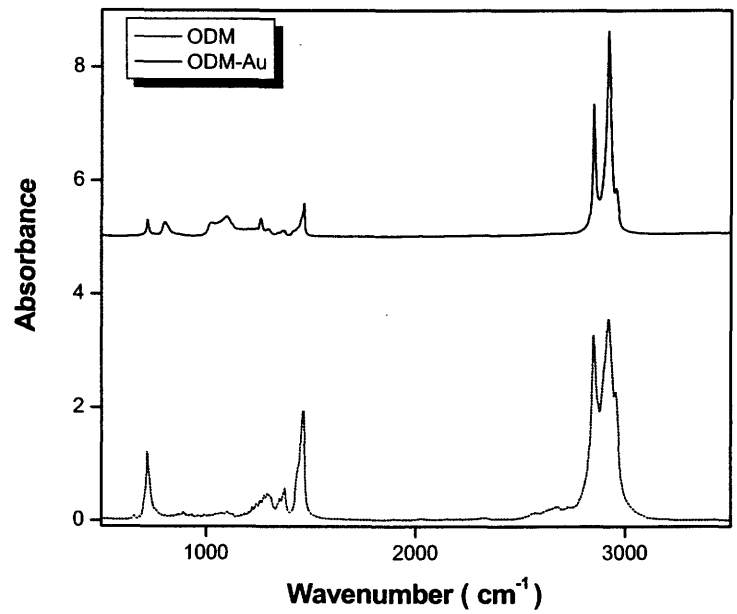

Figure 2.6. FTIR spectrum of ODM and ODM on colloidal gold (KBR pellet).

Table 2.2. Assignments of FT-IR absorption bands.

Assignment[a]	HDM	HDM on Au	ODM	ODM on Au
	Absorption bands (cm^{-1})			
νC-H-	2922	2919	2922	2920
νC-H	2852	2849	2851	2850
$\nu C\text{-}C_{ip}$	1465	1467	1463	1467
νC-C	1377		1373	
νC-C	1277	1248	1283	1261
$\delta C\text{-}H_{ip}$		1098		1098
$\delta C\text{-}H_{op}$		805.0		803.1
νC-S	720.9	720.7	720.8	720.5

[a] $_{ip}$ refers to the in-plane and $_{op}$ refers to the out of plane vibrations respectively, δ-bending, and ν-stretching vibrations.

2.4.1.3. Nuclear Magnetic Resonance

Solution state ^{1}H NMR spectra were recorded on a Bruker Advance 500 NMR spectrometer with a broadband tuneable dual 5mm probe operating at 500 MHz at ambient temperature (25°C). The ^{13}C NMR spectra were also recorded using the same NMR spectrometer at a frequency of 125 MHz.

In Figures 2.7 to 2.10, the solution state ^{1}H and ^{13}C NMR spectra of HDM and ODM alone and bound to gold nanoparticles are displayed along with some carbon site assignments. Upon bonding to the gold, the resonances of ^{13}C NMR spectra of the thiols broaden and the carbon sites closest to the sulphur headgroup, C1 and C2 at 24.8 and 32.6 ppm, appear to vanish completely. This is probably due to the strong interaction of the gold with the sulphur. The C3 peak which is at 28.9 ppm for pure HDM and ODM may have shifted underneath the broad resonance of the interior methylenes in the colloids. The same changes are observed in the ^{1}H NMR solution spectra. That is the resonances of the protons attached to the first two carbons closest to the sulphur headgroup are not visible in the alkanethiol-capped gold colloids of HDM and ODM. Other workers reported this observation.[36,86,119]

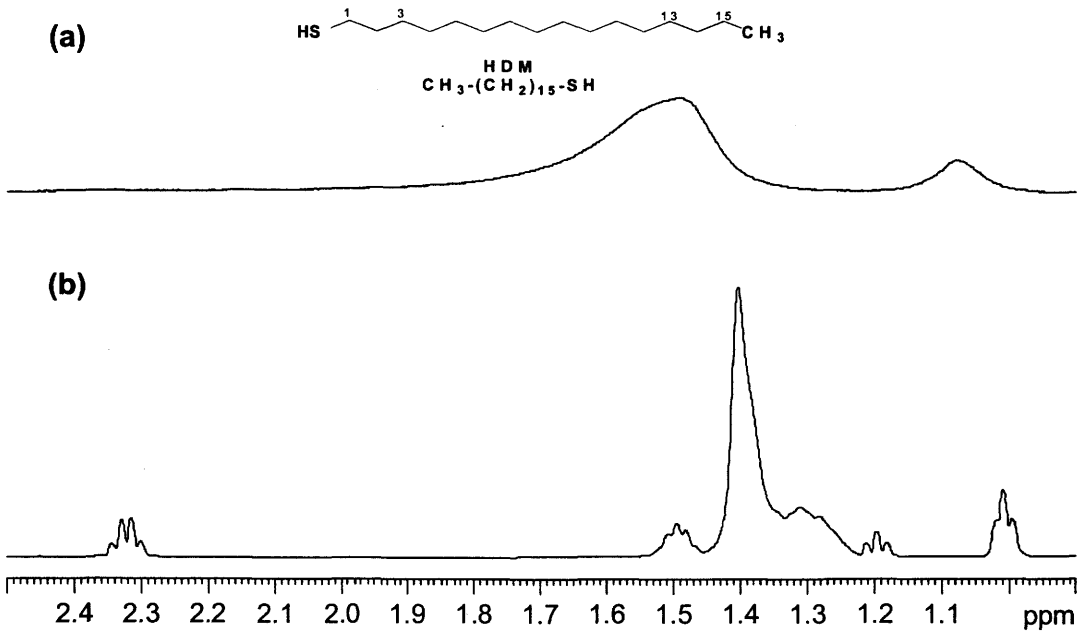

Figure 2.7. ^{1}H-NMR spectra in benzene-d_6 of (a) HDM on colloidal gold (b) Pure HDM (inset is the chemical structure of HDM).

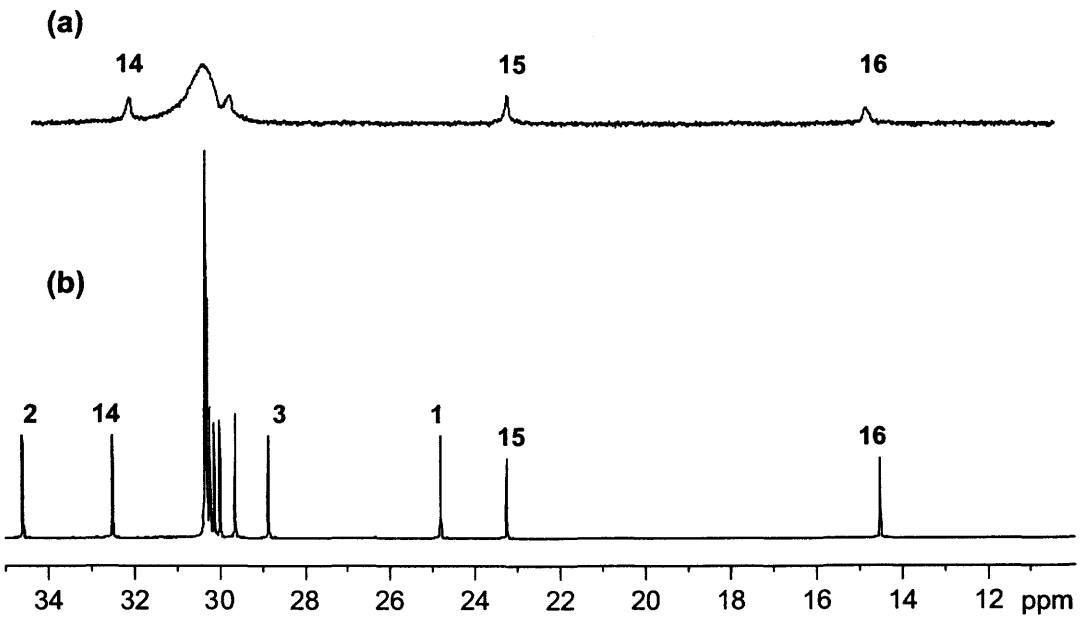

Figure 2.8. ^{13}C-NMR spectra in benzene-d_6 showing some carbon site assignments of (a) HDM on colloidal gold (b) Pure HDM.

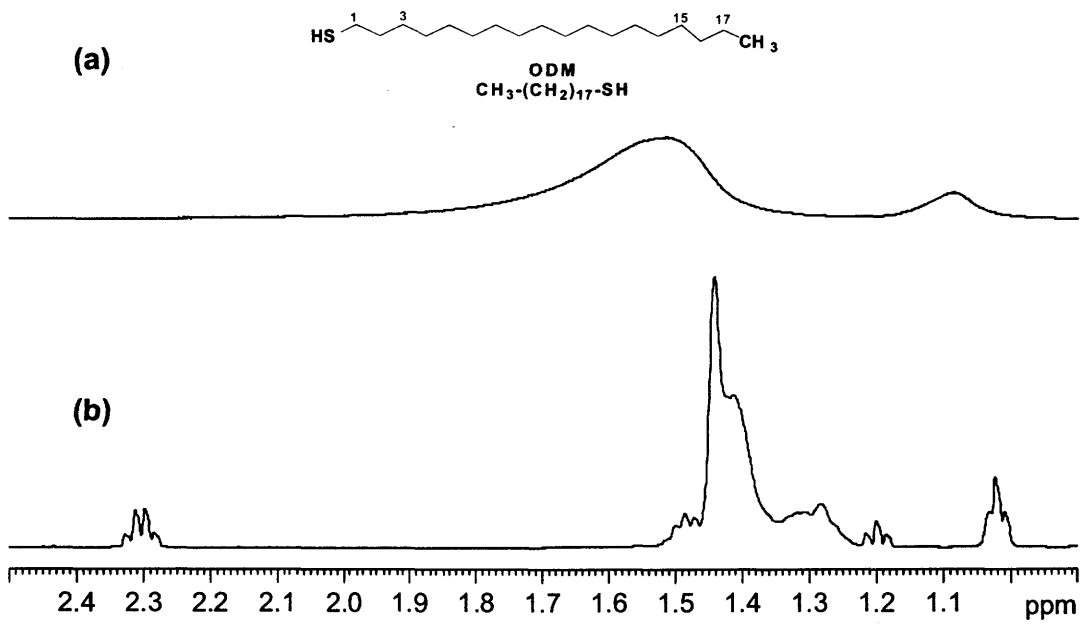

Figure 2.9. ^{1}H-NMR spectra in benzene-d_6 of (a) ODM on colloidal gold (b) Pure ODM (inset is the chemical structure of ODM).

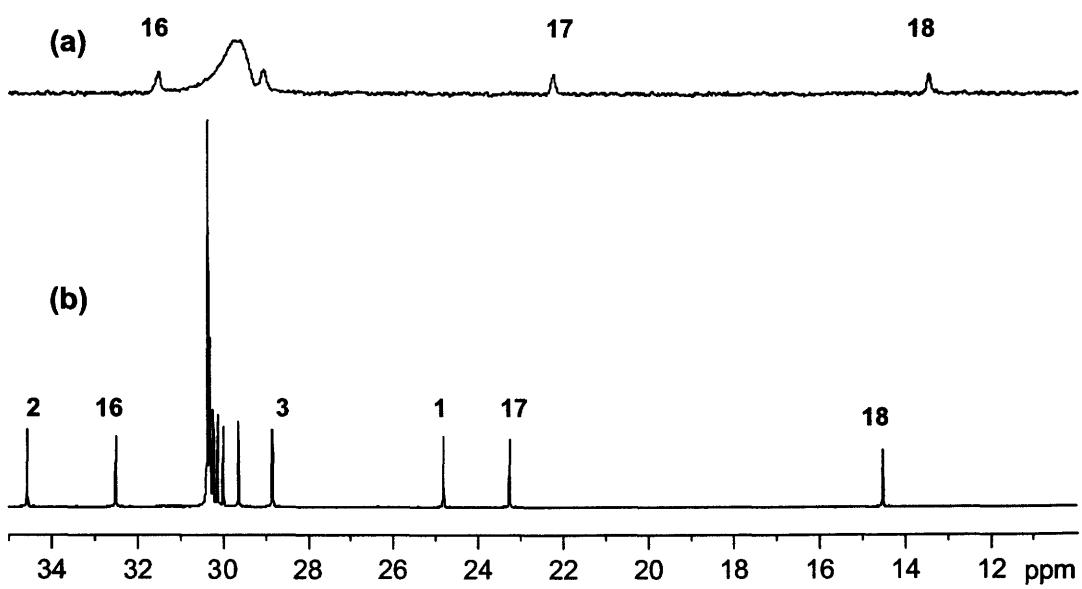

Figure 2.10. ^{13}C-NMR spectra in benzene-d_6 showing some carbon site assignments of (a) ODM on colloidal gold (b) Pure ODM.

2.4.2. Variable Temperature Studies

The purpose of the variable temperature studies was to investigate and confirm the presence of the characteristic phase transitions observed in SAMs and LB films.[133,244]

2.4.2.1. Differential Scanning Calorimetry

The synthesized alkanethiol-capped gold colloids were stored in tightly sealed brown sample bottles, and sent to the Slovakia Technical University in Bratislava, Slovak Republic where they were subjected to DSC studies.

The DSC experiments were run using a Perkin-Elmer DSC-7. The temperature scale was calibrated using the standards cyclopentane and water and observing their phase transitions, (cyclopentane solid/solid, -93.43°C and melting temperature of ice 0°C) whilst the enthalpy scale was calibrated to the heat of fusion of ice. (333.5 Jg^{-1}). The weight of samples used was between 3 and 4 mg. The samples were crimped in standard aluminium pans with an empty pan used as reference. Helium was used as the purging gas.

The following temperature program was used and is outlined below

Step 1: cooling from ambient temperature to –100 °C

Step 2: 1st heating from -100 °C to 100 °C

Step 3: cooling from 100 °C to –100 °C

Step 4: 2nd heating from -100 °C to 100 °C

Step 5: cooling from 100 °C to –100 °C

Step 6: 3rd heating from -100 °C to 100 °C.

The sample was also examined for any changes in mass after step 6 in the temperature program. There were no differences found in any of the samples studied.

2.4.2.2. Nuclear Magnetic Resonance

Variable temperature studies were performed on the colloids and pure HDM and ODM. The pure compound served as controls to observe any changes due to temperature.

Heating and cooling of the NMR samples was accomplished by using air, and a calibrated variable temperature control unit 3000 (Bruker) that was controlled manually at a rate of $0.5°Cmin^{-1}$. For each colloid sample, an initial spectrum was acquired at 25°C and then spectra were collected at progressively higher temperatures. The temperatures were 35, 40, 45, 55, 60, 65 and 70°C. A sample equilibration time of 30 minutes was allowed at each temperature before the start of spectral acquisition. The samples were then cooled while spectral acquisition was repeated at progressively lower temperatures until 25°C was reached.

Chapter Three – Results

3.1. Bare Gold

3.1.1. Cleaning of Bare Gold Electrodes

3.1.1.1. Cleaning Protocol

Cleaning of electrodes is very essential in electrochemistry. In the case of gold-thiol systems, cleaning of the thiol after usage to get a reproducible geometric and clean surface area of bare gold is critical because of the strong gold-thiolate bonds formed in the chemisorption process.[23] Some workers use severe and harsh methods for gold surface cleaning[265] that raise questions about the integrity of the surface of the electrodes thereafter. A simple, but reproducible and reliable procedure has been developed to address this situation using electrochemical methods of CA and LSV.[285] These methods allow the reductive desorption of thiols at the surface of the gold electrodes, subsequent oxidation of the gold electrode, and the reduction of the gold oxide to a clean gold surface.

A CV run in 3 mM $[Fe(CN)_6]^{3-/4-}$ with a typical bare gold electrode after the above cleaning procedure is illustrated in Figure 3.1.

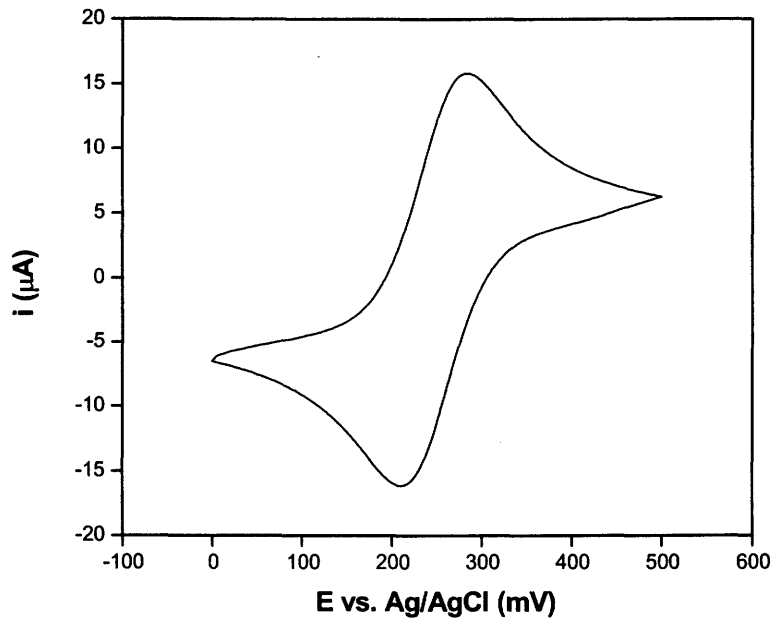

Figure 3.1. CV at 50 mVs^{-1} for bare gold in 3 mM $K_3Fe(CN)_6$ and 3 mM $K_4Fe(CN)_6$ / 0.1 M KCl at room temperature.

CA was used in order to monitor the oxidation of the gold electrode over time. A potential step from 0 mV to 500 mV was performed. Times of 1 to 10 minutes were used and it was observed that 5 minutes was adequate to oxidize the gold surface into its oxide. LSV of the oxidation of gold electrode at room temperature before incubation in absolute ethanol is shown in Figure 3.2. Several oxidation/reduction cycles of bare gold in 0.1 M H_2SO_4 are often recorded but always end with an oxidation LSV.

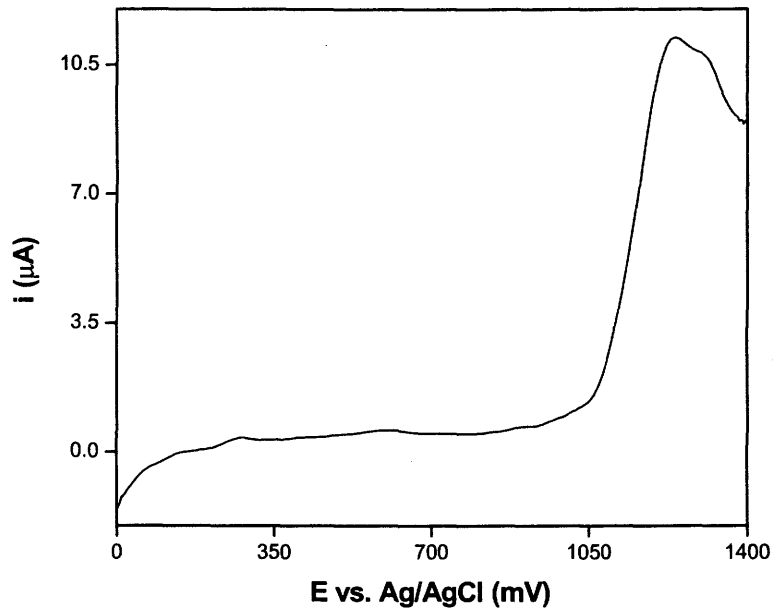

Figure 3.2. LSV at 50 mVs^{-1} for bare gold in 0.1 M H_2SO_4 at room temperature.

Figure 3.3 show the results for varying oxidation times from 1 to 5 minutes. After the adequate oxidation time (5 min) was determined as indicated ealier, the next stage was to incubate the electrode in ethanol to reduce the gold oxide to a clean gold surface.[111] The electrodes after oxidation were incubated at times ranging from 1 minute to 10 minutes and a LSV was then run from 1400 to 0 mV in 0.1 M H_2SO_4 to verify that no gold oxide remained.

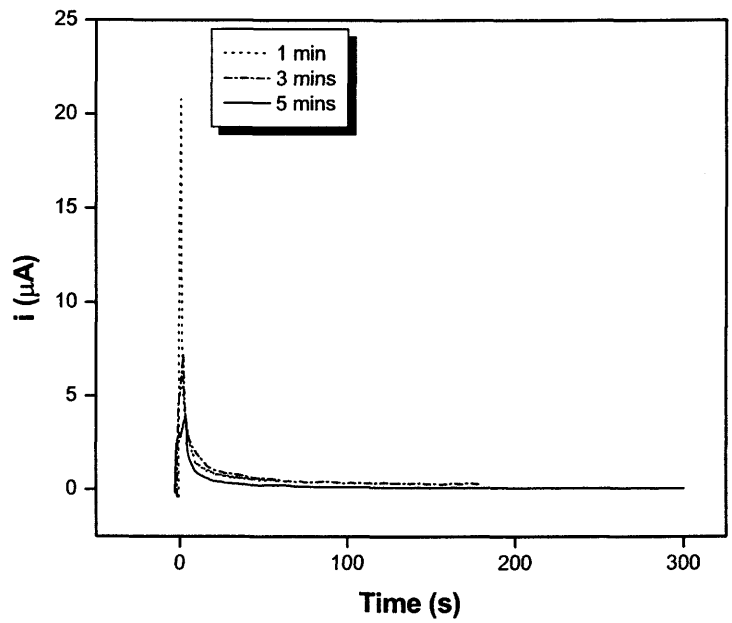

Figure 3.3. CA using a potential step from 500 mV to 0 mV in 0.1 M H_2SO_4 at room temperature and various times to determine the maximum time for oxidation of bare gold electrode surface.

LSV revealed that after 5 minutes, there was virtually no reductive current, indicating that the oxidized surface of the gold electrode had been completely chemically reduced. LSV after 1 minute of incubation time for the electrode in ethanol still had a reductive peak, but the LSV after 10 minutes of chemical reduction was similar within the limits of experimental errors to the one run after 5 minutes of chemical reduction.

3.1.1.2. *Underpotential Deposition of Copper for Surface Roughness Evaluation*

UPD of Cu[281] was used to determine the surface roughness of bare gold, after cleaning the electrode. The UPD involved a CA experiment with a potential step from 500 mV to 0 mV in 1.0mM of $Cu(ClO_4)_2.6H_2O$ / 0.1 M $HClO_4$. This caused the reduction of Cu^{2+} to Cu^0, which was deposited as a monolayer of copper atoms on the surface of the gold electrode in a time window of 20 seconds. It is known that it is within this potential window that reduction of Cu^{2+} to Cu^0 is observed as illustrated by Figure 3.4.

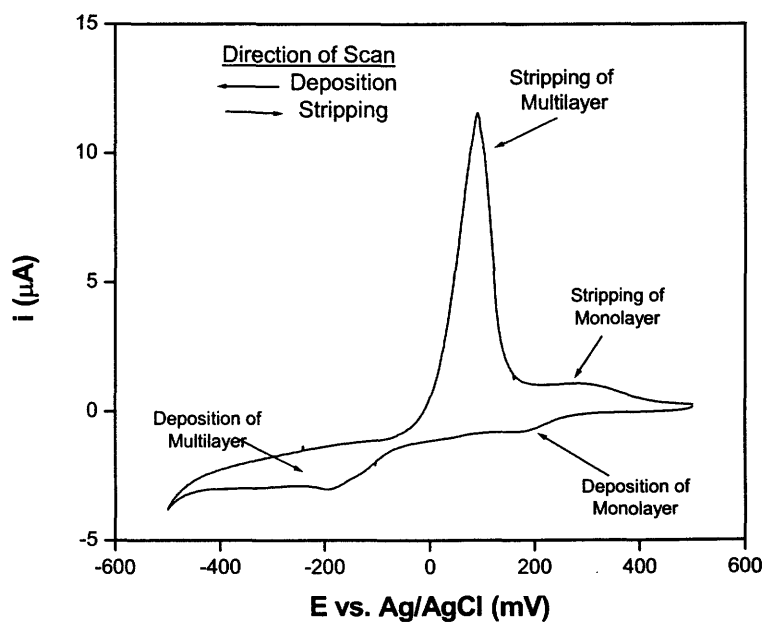

Figure 3.4. CV at 50 mVs^{-1} for bare gold electrode in 1.0 mM of $Cu(ClO_4)_2.6H_2O$ / 0.1 M $HClO_4$ at room temperature showing potential windows for both the deposition and stripping of monolayers and multilayers.

Then using LSV, an oxidizing sweep was applied at a scan rate of 50 mVs^{-1} from 150mV to 500 mV to strip off the freshly formed copper monolayer from the surface of the bare gold electrode by converting Cu^0 to Cu^{2+} as shown in Figure 3.5. The copper oxidation at 0.3V corresponds to the stripping of the UPD layer.

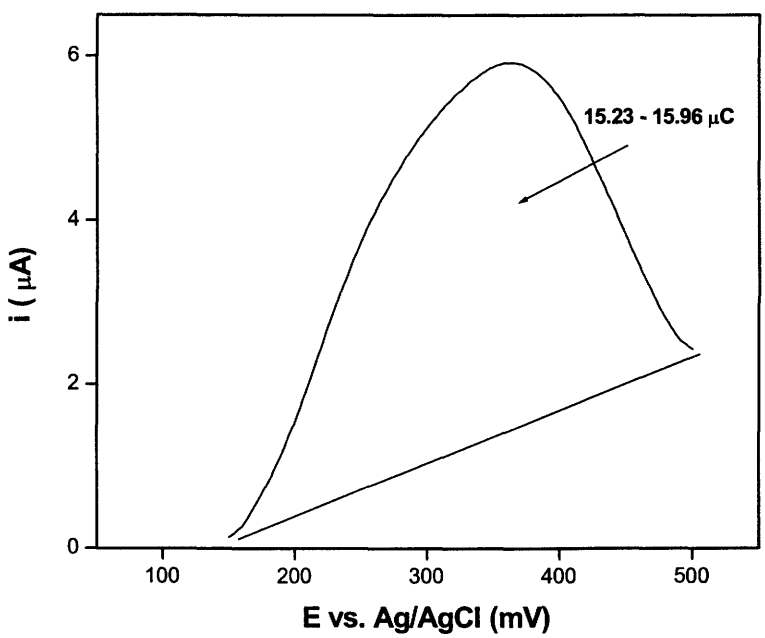

Figure 3.5. CV at 50 mVs^{-1} for stripping of copper atoms from bare gold electrode in 1.0 mM of $Cu(ClO_4)_2.6H_2O$ / 0.1 M $HClO_4$ at room temperature.

The total oxidizing charge was obtained by integrating the area under the curve in the LSV for the stripping of copper (Figure 3.5). The number of copper atoms being released from the surface of the electrode is converted into

electrode area, assuming monolayer coverage. Calculations as shown below in Scheme 3 were done based on a theoretical expected surface coverage of copper atoms on Au(111) of 2.3×10^{-9} molcm^{-2}.

Scheme 3 - Sample Calculation for Surface Roughness

1 mole of Copper atoms = 2 Faraday = 193000 C

Theoretical Surface Coverage Area of Au(111) by copper atoms

$= 2.3 \times 10^{-9}$ molcm^{-2}

Experimental charge required to strip copper atoms = 15.96×10^{-6} C

# of moles of Copper deposited = 15.96×10^{-6} / 193000 Cmole^{-1}

$= 8.26 \times 10^{-11}$ moles

$$\text{Area of Au surface covered by Copper atoms} = \frac{\text{\# of moles of copper}}{\text{Surface coverage area}}$$

$$= \frac{8.26 \times 10^{-11} \text{ moles}}{2.3 \times 10^{-9} \text{ mole cm}^{-2}}$$

$$= 3.59 \times 10^{-2} \text{ cm}^2$$

Geometric Surface Area of Au (111) electrode = 2.27×10^{-2} cm^2

$$\text{Surface Roughness} = \frac{\text{Experimental Area}}{\text{Geometric Surface Area}}$$

$$\text{Surface Roughness} = \frac{3.59 \times 10^{-2} \text{ cm}^2}{2.27 \times 10^{-2} \text{ cm}^2} = 1.58$$

The total oxidizing charge was found to be as 15.23 – 15.96 μC, corresponding to an electrode of 0.0343 - 0.0359 cm^2.

The ratio between experimental area and the actual geometrical area of the Au(111) electrode is what is known as the surface roughness of the bare gold electrode. This was calculated as shown above to be between 1.58 - 1.62. One reason for the high experimental surface area may be step edges and defect sites from the gold, surface. Thus the expected coverage by copper atoms on a Au(111) surface, which from the literature[281] is given as 2.3 X 10^{-9} mol cm^{-2}, may be different from that on the surface of the polycrystalline gold that was used in this study. Since other surfaces of gold will have different packing densities.

3.1.2. Room Temperature Studies of Bare Gold in Redox Probe

$[Fe(CN)_6]^{3-/4-}$ redox probe was first characterized with bare gold electrode at room temperature. $[Fe(CN)_6]^{3-/4-}$ and electrolyte concentrations were optimized at this time. They were characterized mostly by CV and AC-EIS.

3.1.2.1. Cyclic Voltammetry at Room Temperature of Bare Gold

An equimolar solution of $[Fe(CN)_6]^{3-/4-}$ in background electrolyte (KCl), was required for studies of the blocking by alkanethiols of bare gold from the $[Fe(CN)_6]^{3-/4-}$ couple. The background electrolyte had to produce sufficiently low capacitive currents so that small Faradaic currents could still be detected

against the background. A 3 mM equimolar solution of $[Fe(CN)_6]^{3-/4-}$ with 0.1 M KCl as background electrolyte was chosen.

3.1.2.2. Alternating Current-Electrochemical Impedance Spectroscopy at Room Temperature of Bare Gold

AC-EIS of bare gold electrode in $[Fe(CN)_6]^{3-/4-}$ redox probe solution was used to choose the optimal applied bias voltage. It would be a potential range over which virtually no net redox activity occurs, i.e., the reversible potential range of the redox couple (3 mM $[Fe(CN)_6]^{3-/4-}$) in solution, so 250mV was chosen. The open circuit potential was found to range between 245 mV to 254 mV. Over this potential range, the bare gold electrode gave identical impedance plots dominated by a perfect linear Warburg line over almost the entire frequency range, with a small kinetic semicircle at high frequencies (Figure 3.6).

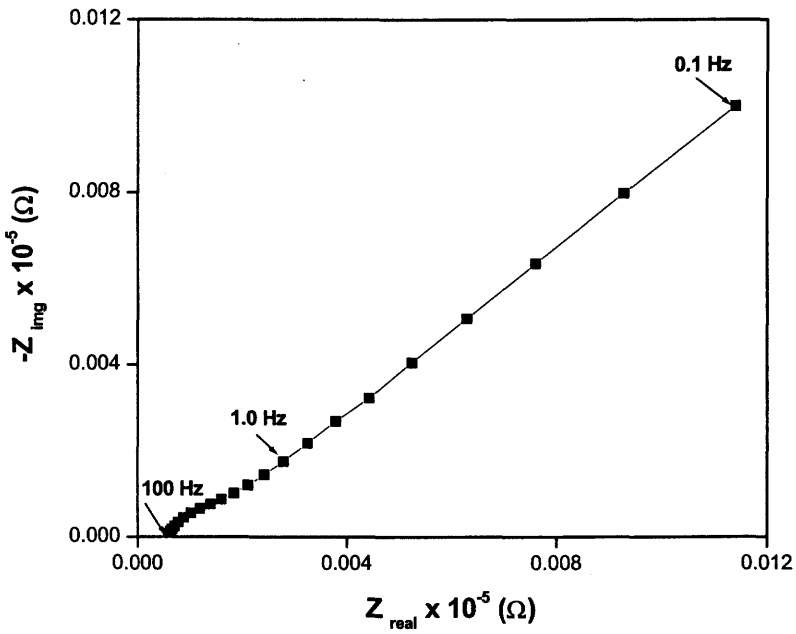

Figure 3.6. Nyquist plots showing AC-EIS behaviour at an applied bias voltage of 250 mV with respect to Ag/AgCl and ac amplitude of 5 mV rms for bare gold in 3 mM $K_3Fe(CN)_6$ and 3 mM $K_4Fe(CN)_6$ / 0.1 M KCl at room temperature (From 100 kHz to 0.1 Hz).

3.1.3. Variable Temperature Studies of Bare Gold in Redox Probe

In temperature dependent studies of the modified electrodes, bare gold was used as a reference. CV and AC-EIS were both used to study the effect of temperature on the redox process of $[Fe(CN)_6]^{3-/4-}$ at bare gold. This was done to provide a reference for the investigation of temperature effects in SAMs and LB films.

3.1.3.1. Variable Temperature Cyclic Voltammetry of Bare Gold

Figure 3.7 shows the effect of temperature on the redox process of $[Fe(CN)_6]^{3-/4-}$ at a bare gold electrode at 25.5°C and 53.7°C. The E^o value shifted by 60 mV to lower potentials as temperature was increased but the ΔE value remained fairly constant at 74 mV. Even though ΔE is larger than 59mV, this is expected as the $[Fe(CN)_6]^{3-/4-}$ redox couple is known to be only quasi-reversible. There was also a gradual increase in Faradaic current with increase in temperature, because increase in temperature leads to increase in diffusion and thermal motion.

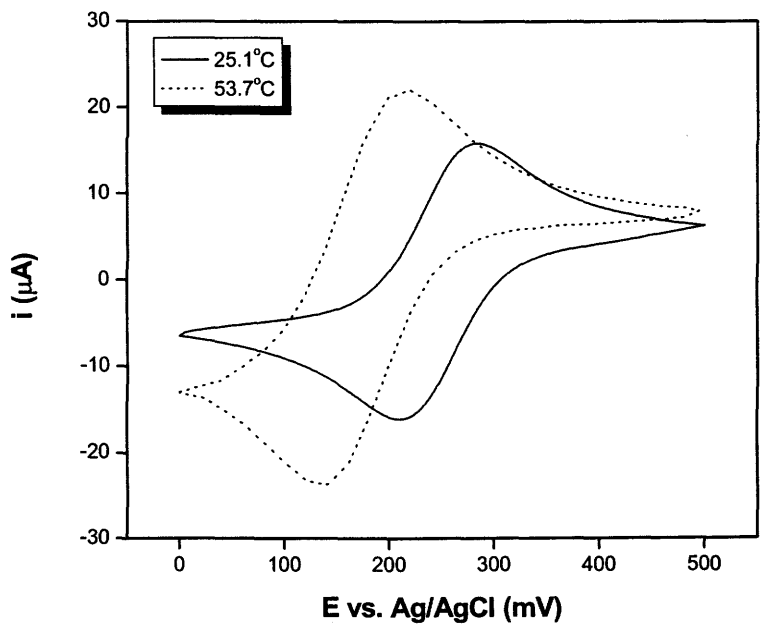

Figure 3.7. CV at 50 mVs^{-1} of bare gold in 3 mM $K_3Fe(CN)_6$ and 3 mM $K_4Fe(CN)_6$ / 0.1 M KCl at different temperatures.

3.1.3.2. *Variable Temperature Alternating Current-Electrochemical Impedance Spectroscopy of Bare Gold*

The results of the AC-EIS experiments are presented as Nyquist plots.[253] In variable temperature AC-EIS data for $[Fe(CN)_6]^{3-/4-}$ at bare gold, there was not a significant temperature effect except for the decrease in size of the small kinetic semicircle at high frequencies. This is shown in Figure 3.8 at 25.5°C and 55.0°C.

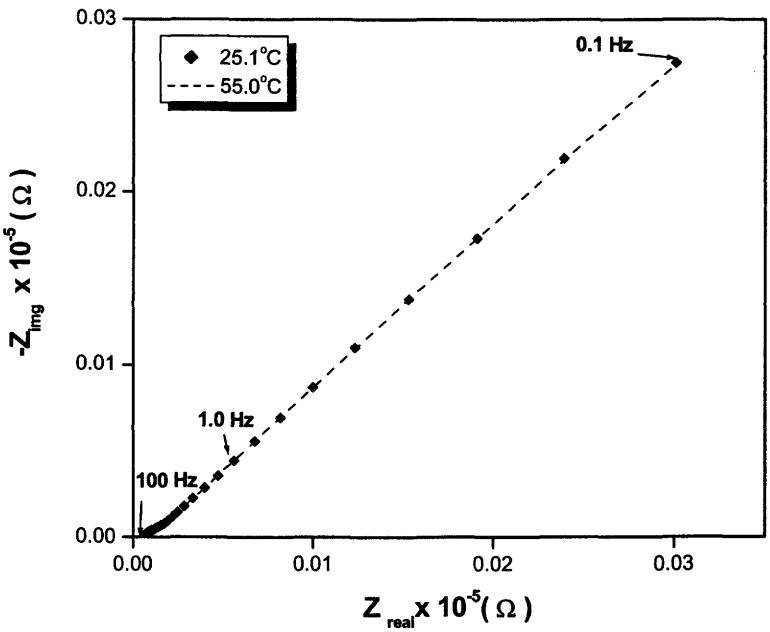

Figure 3.8. Nyquist plots showing AC-EIS behaviour at an applied bias voltage of 250 mV with respect to Ag/AgCl and ac amplitude of 5 mV rms for bare gold in 3 mM $K_3Fe(CN)_6$ and 3 mM $K_4Fe(CN)_6$ / 0.1 M KCl at two different temperatures (From 100 kHz to 0.1 Hz).

3.2. Self-Assembled Monolayers of Alkanethiols on Gold

The permeability of the modified electrodes was studied by observing the blocking of the $[Fe(CN)_6]^{3-/4-}$ couple from the gold electrode surface.[82] Films of HDM, ODM and MUA on gold were examined using CV and AC-EIS.

3.2.1. Cyclic Voltammetry of Modified Gold Electrodes

Room temperature studies of $[Fe(CN)_6]^{3-/4-}$ were done with octanethiol (OD) - , HDM – and ODM - modified electrodes using CV for preliminary studies. The degree of blocking of the redox couple from the electrode was taken as a measure of the quality of the resulting SAM. Once a film forming protocol was established at room temperature, the degree of blocking of several optimized films was investigated as a function of temperature.

3.2.1.1. Film Forming Protocol for Modified Gold Electrodes

Initially the films were studied at room temperature to find out whether there is effective blocking of the electrode to the redox process below.

$$[Fe(CN)_6]^{3-} + e^- \rightleftharpoons [Fe(CN)_6]^{4-} \qquad \text{Scheme 4}$$

In this way, parameters in the film forming protocol such as concentration of the thiol and incubation times were investigated. It was observed that even though a degree of blocking was achieved after very short incubation times, a good and reliable close packed film is only formed after about 5 days in ethanolic solutions of 2-5 mM alkanethiol.[244] It was found that incubation of the modified electrodes in Millipore water overnight prior to electrochemical studies improved the formation of reproducible and closely packed films. Likely the presence of water which is hydrophilic provided an association between the hydrophobic chains and the methyl headgroups of the alkanethiols.

Typical results for blocking behaviour of the $[Fe(CN)_6]^{3-/4-}$ redox reaction by electrodes modified for different incubation times are shown in Figures 3.9 and 3.10.

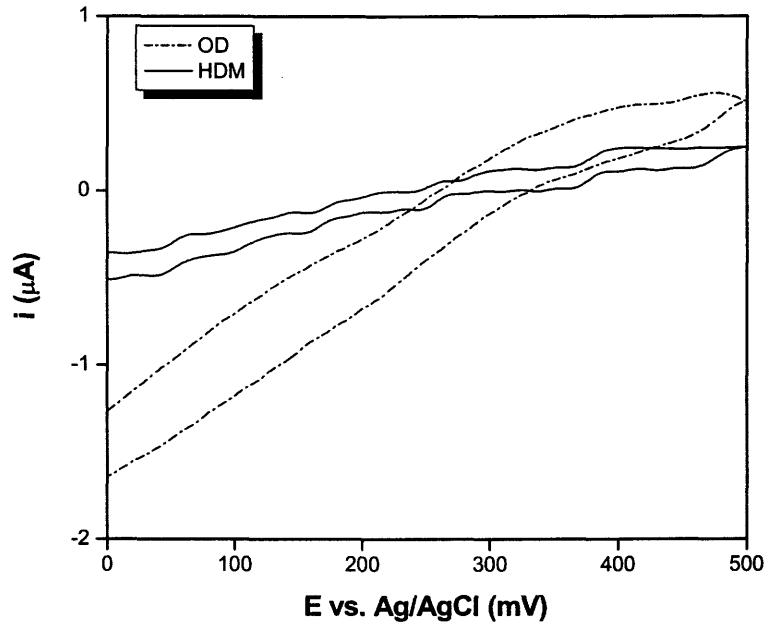

Figure 3.9. CV at 50 mVs^{-1} of HDM and OD-modified gold electrodes in 3 mM $K_3Fe(CN)_6$ and 3 mM $K_4Fe(CN)_6$ / 0.1 M KCl at room temperature after 30 minutes of incubation time.

In Figure 3.9, it can be seen that after 30 minutes of incubation, there is blocking of the redox reaction of $[Fe(CN)_6]^{3-/4-}$ by both HDM - and OD - modified electrodes. However, from the magnitude of the currents, the film of HDM is more closely packed than that of OD, leading to better blocking behaviour. Increasing incubation time to 48 hours as shown in Figure 3.10 improved the blocking by both modified electrodes but that of HDM was still superior to OD in blocking the redox reaction of $[Fe(CN)_6]^{3-/4-}$ since the longer HDM may have less defects and pinholes as opposed to OD.

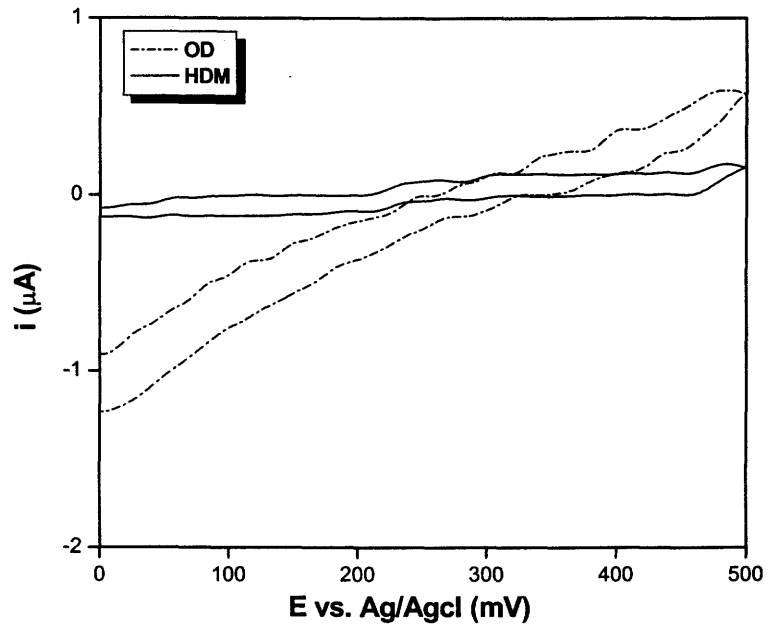

Figure 3.10. CV at 50 mVs^{-1} of HDM and OD-modified gold electrodes in 3 mM $K_3Fe(CN)_6$ and 3 mM $K_4Fe(CN)_6$ / 0.1 M KCl at room temperature after 48 hours of incubation time.

3.2.1.2. Variable Temperature Cyclic Voltammetry of Modified Gold Electrodes

The effect of several SAMs on the redox activity of a $[Fe(CN)_6]^{3-/4-}$ probe in solution was studied as a function of temperature. For these studies, two long chain species - ODM and MUA - were used in addition to HDM. OD was no longer investigated, as its unusual temperature behaviour occurred below room temperature.

The low temperature inhibition of the probe by each film decreased drastically above a certain characteristic temperature, T_{tr}. This temperature was different for each film. Figures 3.11 and 3.12 show the behaviour of each film at two different temperatures, one below and one above T_{tr}.

From the CVs in Figures 3.11 and 3.12, it can be observed that the order of blocking of the redox process $[Fe(CN)_6]^{3-/4-}$ by the modified electrodes is in the order ODM > HDM > MUA. However, the CV of ODM and HDM modified electrodes appear to be superimposed in Figure 3.12 due to the slight difference.

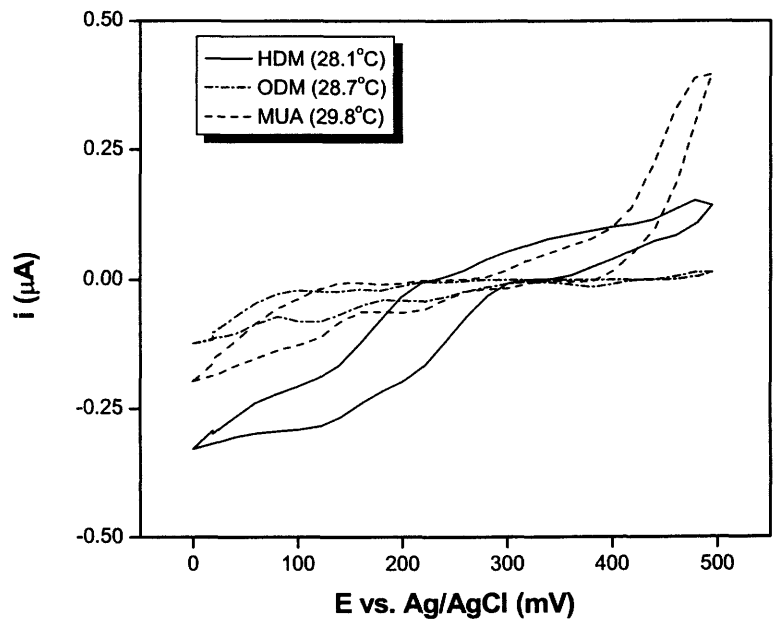

Figure 3.11. CV at 50 mVs^{-1} of HDM, ODM and MUA-modified gold electrodes at temperatures below T_{tr} in 3 mM $K_3Fe(CN)_6$ and 3 mM $K_4Fe(CN)_6$ / 0.1 M KCl.

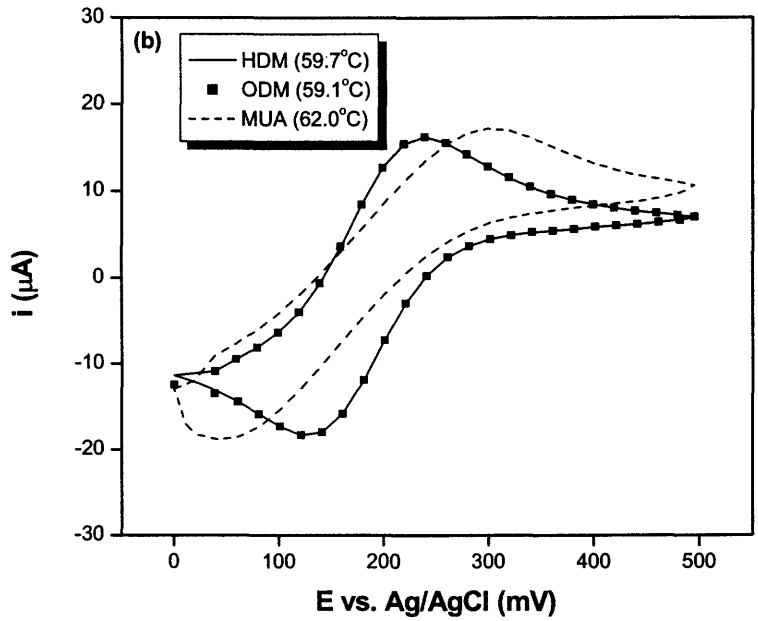

Figure 3.12. CV at 50 mVs^{-1} of HDM and ODM and MUA-modified gold electrodes at temperatures above T_{tr} in 3 mM $K_3Fe(CN)_6$ and 3 mM $K_4Fe(CN)_6$ / 0.1 M KCl.

The drastic change in current can best be observed if a monolayer above T_{tr} is superimposed over a monolayer below T_{tr} as shown in Figure 3.13 for HDM. A CV of bare gold electrode in the same solution is included as reference. The currents from CVs above T_{tr} for the modified electrodes are close in magnitude to the bare gold electrode and deceptively portrays that coverage is almost zero above T_{tr} . This can be due to non-linear diffusion effects arising from defects and pinholes that exposes active sites above T_{tr} and makes them appear like arrays of ulramicroelectrodes.[249]

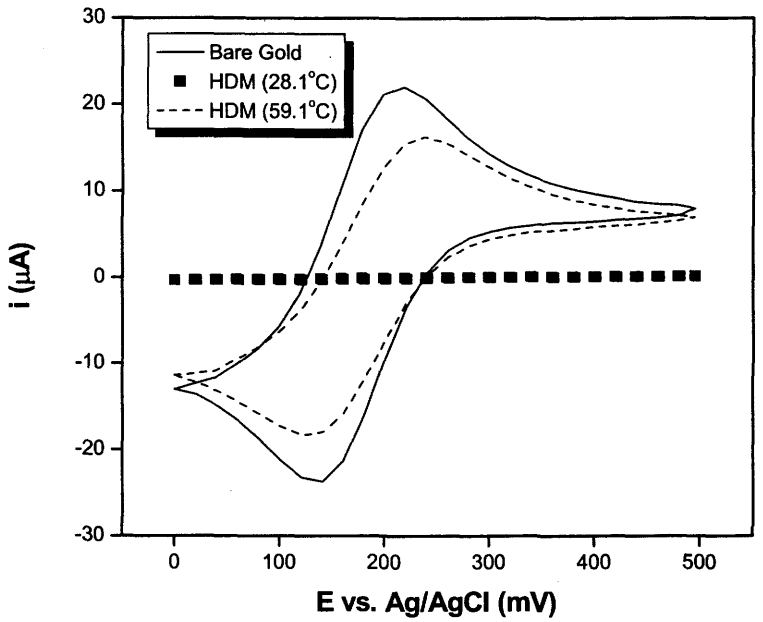

Figure 3.13. CV at 50 mVs^{-1} of HDM modified electrodes below and after T_{tr} compared to bare gold in 3 mM $K_3Fe(CN)_6$ and 3 mM $K_4Fe(CN)_6$ / 0.1 M KCl.

It can be seen from Figure 3.13 that the CV of the HDM - modified electrodes in $[Fe(CN)_6]^{3-/4-}$ below T_{tr} show very low currents when compared to a CV of HDM – modified electrode above T_{tr}. This behaviour is also observed for the other modified electrodes. Similarly, the magnitude of currents in the HDM modified electrodes after Ttr compared with that of bare gold can also be attributed to the effect of non-linear diffusion.[249]

3.2.1.3. Reversibility of Temperature-Dependent Behaviour of Monolayers

It should be noted that the drastic changes observed by CV of the monolayers after they have been heated above T_{tr} in solution are not reversible on the time scale of this experiment, generally speaking. Previously heated films were re-measured up to two weeks after cooling with no reversibility observed.

Oven studies were also done to find out if the monolayer could be returned to its original state if the resulting process was carried out in air, rather than in solution. A freshly prepared SAM of HDM was heated in an oven from room temperature to approximately 60°C and immediately transferred into a redox probe solution held at 60°C, and a CV taken. The modified electrode was then cooled in the electrochemical cell to 22.0°C. Figure 3.14 illustrates the results. As can be seen, the film of HDM on gold did not recover its original blocking abilities around room temperature (see for example Figure 3.13). However, the comparison with bare gold also shows that the HDM - modified electrode heated to 60°C did not reach the response of bare gold around the same temperature.

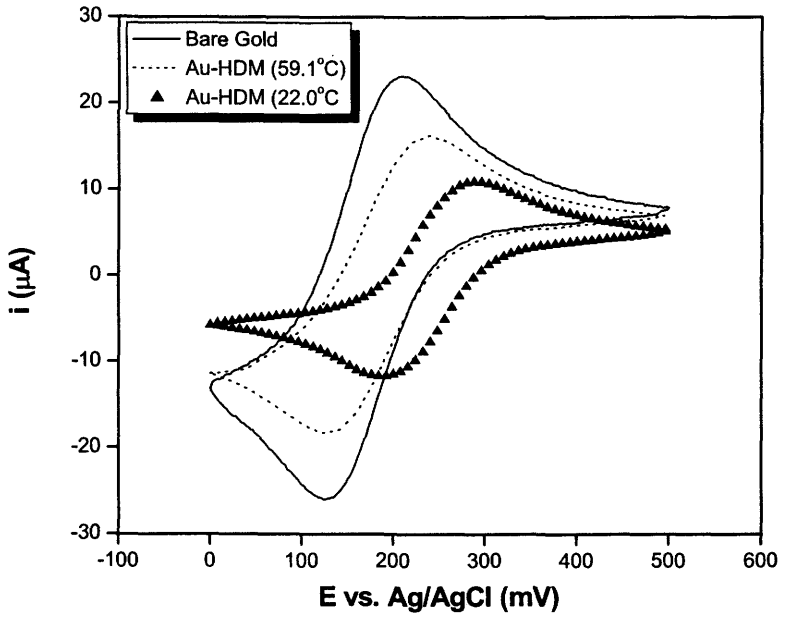

Figure 3.14. CV at 50 mVs^{-1} of HDM-modified electrodes heated in an oven and cooled in an electrochemical cell to test for reversibility of monolayer in 3 mM $K_3Fe(CN)_6$ and 3 mM $K_4Fe(CN)_6$ / 0.1 M KCl.

When the HDM-modified SAM was left in the oven to cool, after heating to 60.5°C, Figure 3.15 was obtained. It is worthy of note that this experiment was done in the oven and air, without contact with a condensed fluid phase. However, this type of experiment was not very reproducible. This experimental result most closely follows the solid-state NMR or DSC measurements in which reversibility of temperature-dependant behaviour was observed.[36,86]

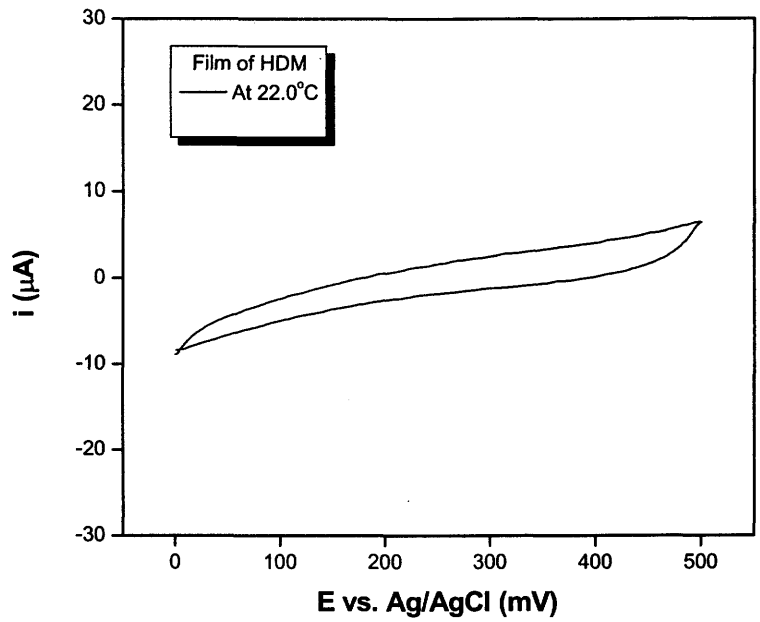

Figure 3.15. CV at 50 mVs^{-1} of HDM-modified electrode heated and cooled in air in an oven to test for reversibility of monolayer in 3 mM $K_3Fe(CN)_6$ and 3 mM $K_4Fe(CN)_6$ / 0.1 M KCl.

3.2.2. Study of Monolayer in Organic Solvent

The purpose of this experiment was to investigate further the increase in solution redox activity observed at higher temperatures to ascertain whether this increase in solution redox activity is indeed due to an increase in permeability of the films modifying the electrode.

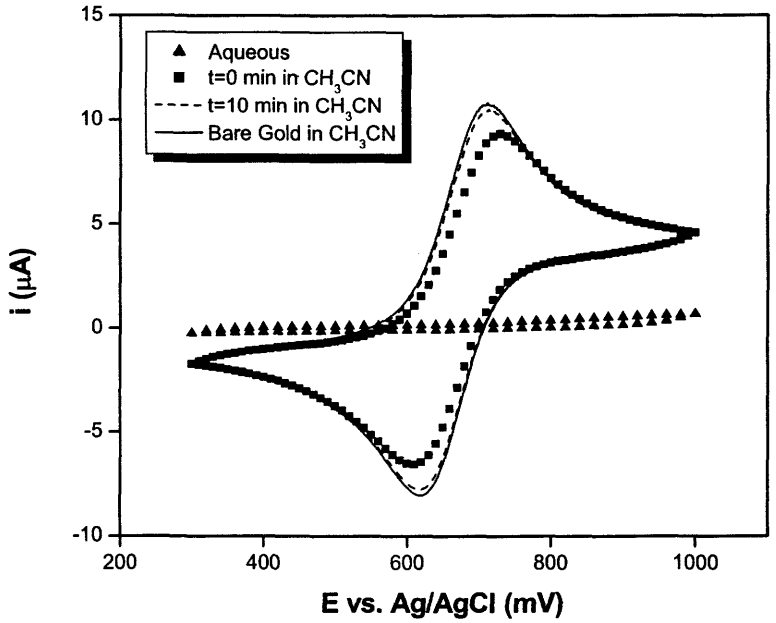

Figure 3.16. CV at 50 mVs^{-1} of HDM-modified electrodes in aqueous and organic solvent media at room temperature. (Aqueous: 3 mM $K_3Fe(CN)_6$ and 3 mM $K_4Fe(CN)_6$ / 0.1 M KCl; Organic: 1 mM FMa / 0.1 M $(Bu)_4NBF_4$ in CH_3CN). Bare gold included as reference.

Figure 3.16 shows studies of the monolayer films in acetonitrile and aqueous medium at room temperature. The response of the HDM - modified gold electrode in an aqueous medium of $[Fe(CN)_6]^{3-/4-}$ revealed blocked redox activity of $[Fe(CN)_6]^{3-/4-}$. However when the same modified electrode was run in an organic medium (acetonitrile) containing ferrocene monocarboxylic acid (FMa), the modified electrode is permeable to the FMa redox probe at time t = 0. After 10 minutes in the organic medium of acetonitrile, the response of the modified electrode to the FMa redox probe is similar to that of bare gold. It is

very likely that the long-alkyl-chain thiols, which block the modified electrode from redox activity of $[Fe(CN)_6]^{3-/4-}$ in aqueous solution are solvated in the organic medium of acetonitrile[89], disordered and permeable to the FMa redox probe.

3.2.3. Specific Surface Coverage of Self-Assembled Monolayers

UPD[281] was used to obtain available gold accessible surface sites with the SAMs of HDM, ODM and MUA. The experiments were similar to those described in section 3.1.1.2. The aim of this experiment was to deposit copper on any exposed portion of the modified gold electrode. The calculations are similar to those shown in Scheme 3. The results obtained are shown in Table 3.1 below.

Table 3.1. Experiment to determine available gold accessible surface* of alkanethiol modified electrodes using the UPD method.

Electrodes	Experimental Surface Coverage x 10^{-5} (cm^2)	
	Before T_{tr} (± 0.001)	**After T_{tr} (± 0.05)**
HDM-modified	8.111	20.27
ODM- modified	5.047	19.37
MUA-modified	16.67	27.04

* Bare gold electrode has available gold accessible surface of (2400 – 2540) x 10^{-5} cm^2.

From the values indicated in the Table 3.1, there is copper deposition both below and above T_{tr}. MUA is the modified electrode with much more sites exposed to copper atoms both below and above T_{tr}. From Table 3.1, there is copper deposition when the film is not permeable to the ferricyanide redox probe. (specifically below T_{tr}). Though this is surprising, it could be presumed that permeability to the ferricyanide redox reaction and the deposition of copper are two different things, and thus even when ferricyanide is blocked from reduction, copper atoms are still able to be deposited on gold. It is also likely that the mechanism of electron transfer for copper and ferricyanide are quite different. It would have been interesting to pinpoint the T_{tr} by a different "marker" than the ferricyanide, but this was not achieveable.

3.2.4 Alternating Current-Electrochemical Impedance Spectroscopy of Modified Gold Electrodes

AC-EIS was used to investigate the SAM - modified electrodes in the presence of the redox probe $[Fe(CN)_6]^{3-/4-}$. The Nyquist plots are used to represent the raw data.[253]

3.2.4.1 *Room Temperature Alternating Current-Electrochemical Impedance Spectroscopy of Modified Gold Electrodes*

Room temperature AC-EIS measurements allowed the reproducibility of the films to be investigated. Different gold electrodes were incubated under the same conditions with the same alkanethiol and their Nyquist plots compared as shown in Figure 3.17. The figure revealed that small variations can exist between two electrodes, and are attributed simply to film reproducibility.

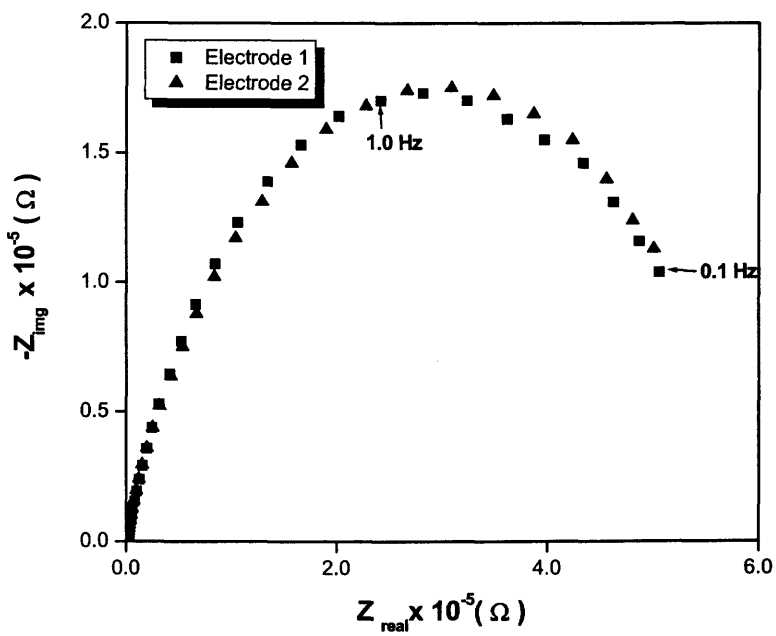

Figure 3.17. Nyquist plots showing AC-EIS behaviour at an applied bias voltage of 250 mV with respect to Ag/AgCl and ac amplitude of 5 mV rms for two different HDM-modified gold electrodes incubated and run under the same experimental conditions in 3 mM $K_3Fe(CN)_6$ and 3 mM $K_4Fe(CN)_6$ / 0.1 M KCl at room temperature (From 100 kHz to 0.1 Hz).

3.2.4.2 *Variable Temperature Alternating Current-Electrochemical Impedance Spectroscopy of Modified Gold Electrodes*

The same abrupt change observed for CV data below and above a certain characteristic temperature T_{tr} was observed in Nyquist plots. Figure 3.18 shows a typical response for each film below their respective T_{tr} temperatures. Each measurement was made on a film that had not yet been heated above T_{tr}.

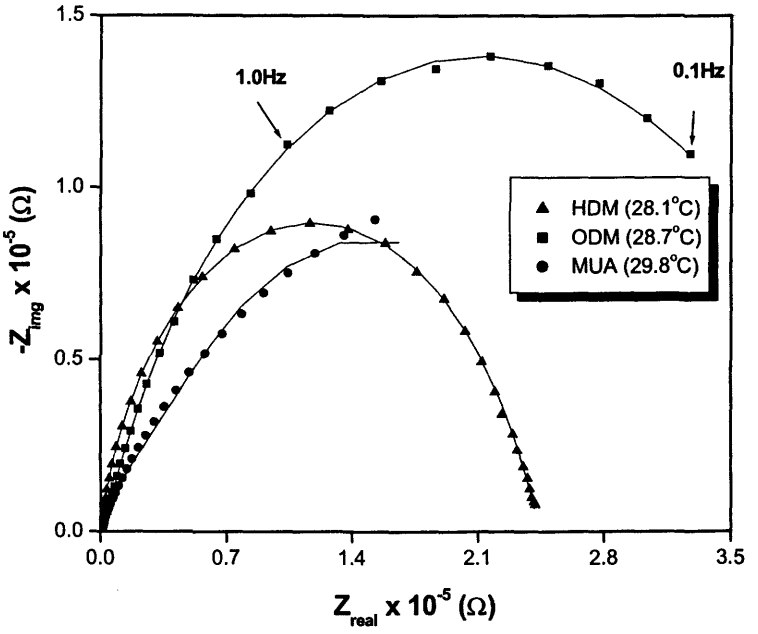

Figure 3.18. Nyquist plots showing AC-EIS behaviour at an applied bias voltage of 250 mV with respect to Ag/AgCl and ac amplitude of 5 mV rms for behaviour of modified electrodes below T_{tr} in 3 mM $K_3Fe(CN)_6$ and 3 mM $K_4Fe(CN)_6$ / 0.1 M KCl (Lines show the theoretical fits for each monolayer) (From 100 kHz to 0.1 Hz).

Figure 3.19 shows a typical response for each film above their respective T_{tr} temperatures. In both Figures, the data points are superimposed by theoretical fits to the data. This will be discussed later. Fundamentally, the shapes of the Nyquist plots are different for each of the three films, including that the three films behave different with respect to the blocking of $[Fe(CN)_6]^{3-/4-}$ redox probe. However, in Figure 3.18 (below T_{tr}) all of them show high impedances indicating that the modified electrodes are significantly blocked towards $[Fe(CN)_6]^{3-/4-}$. The higher the impedance, the better the blocking, that is the order of blocking is ODM > HDM > MUA.

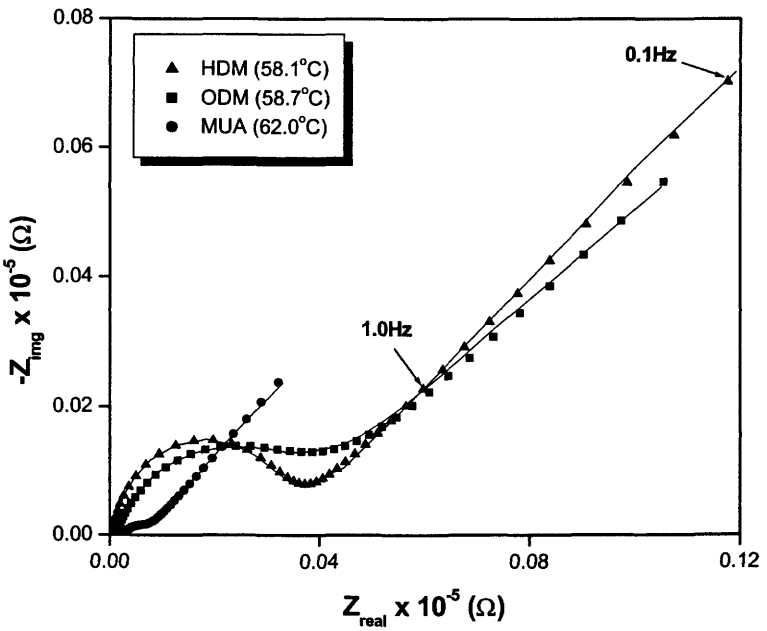

Figure 3.19. Nyquist plots showing AC-EIS behaviour at an applied bias voltage of 250 mV with respect to Ag/AgCl and ac amplitude of 5 mV rms for behaviour of modified electrodes above T_{tr} in 3 mM $K_3Fe(CN)_6$ and 3 mM $K_4Fe(CN)_6$ / 0.1 M KCl. (Lines show the theoretical fits for each monolayer) (From 100 kHz to 0.1 Hz).

Above T_{tr}, as indicated in Figure 3.19, there is a drastic decrease in impedance compared to Figure 3.18. It is worthy of note that even though the Nyquist plots of modified electrodes above T_{tr} have a shape similar to that of bare gold (Figure 3.6), they still have higher impedances than that of bare gold. In fact, it is very difficult to superimpose the bare gold impedance response on Figure 3.19 due to the differences in scales. The shapes of HDM and ODM - modified electrode plots are similar in magnitude both below and above T_{tr}, while those of MUA have lower impedance compared to HDM and ODM - modified electrodes.

3.2.4.3 Reversibility of Temperature – Dependent Behaviour of Monolayers

As observed in CV data, the AC-EIS results did not show any reversibility in the transition of the monolayers at high temperature in solutions of the redox probe. However, at no temperature did the response of any of the films resemble that of a bare gold electrode either in magnitude or in shape.

The purpose of these experiments was to verify how reversible the films' transition was when it is heated in an oven and cooled in an electrolyte solution as opposed to heating in an oven and cooling in air without any electrolyte solution since it is probable that the electrolyte plays a role in the lack of reversibility.

When heating in an oven at 62.0°C followed by cooling to 20.5°C was performed in an electrochemical cell, the shapes of the resulting Nyquist plots at 62.0°C and at 20.5°C (Figure 3.20) do not look the same but the response did not indicate complete blocking of the $[Fe(CN)_6]^{3-/4-}$ redox process.

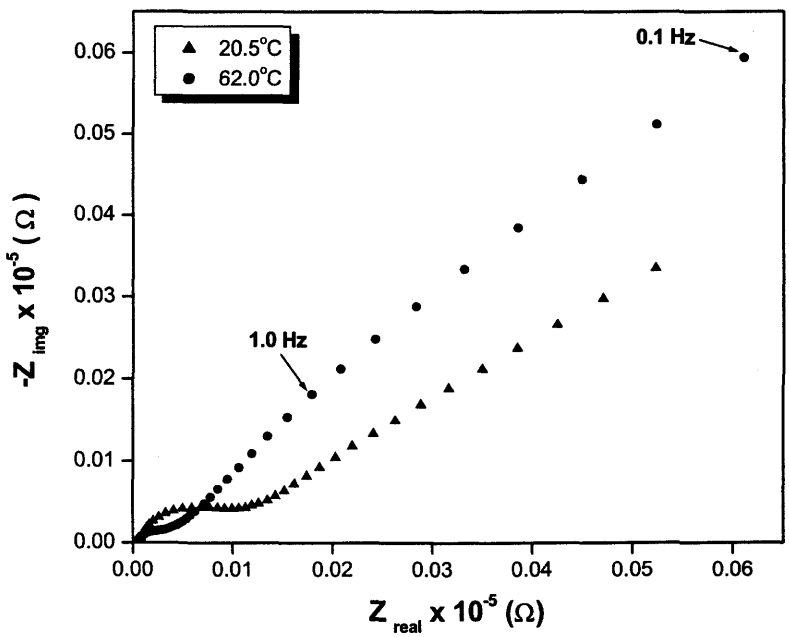

Figure 3.20. Nyquist plots showing AC-EIS behaviour at an applied bias voltage of 250 mV with respect to Ag/AgCl and ac amplitude of 5 mV rms for HDM-modified electrodes heated in an oven and cooled in an electrochemical cell; to test for reversibility of monolayer in 3 mM $K_3Fe(CN)_6$ and 3 mM $K_4Fe(CN)_6$ / 0.1 M KCl (From 100 kHz to 0.1 Hz).

In Figure 3.21, both the heating and cooling were done in the oven and air respectively without any electrolyte solution, before the impedance data was collected at 20.5°C. There is better blocking of the $[Fe(CN)_6]^{3-/4-}$ redox process

and this is indicated by the higher impedance observed in Figure 3.21 compared to that of Figure 3.20.

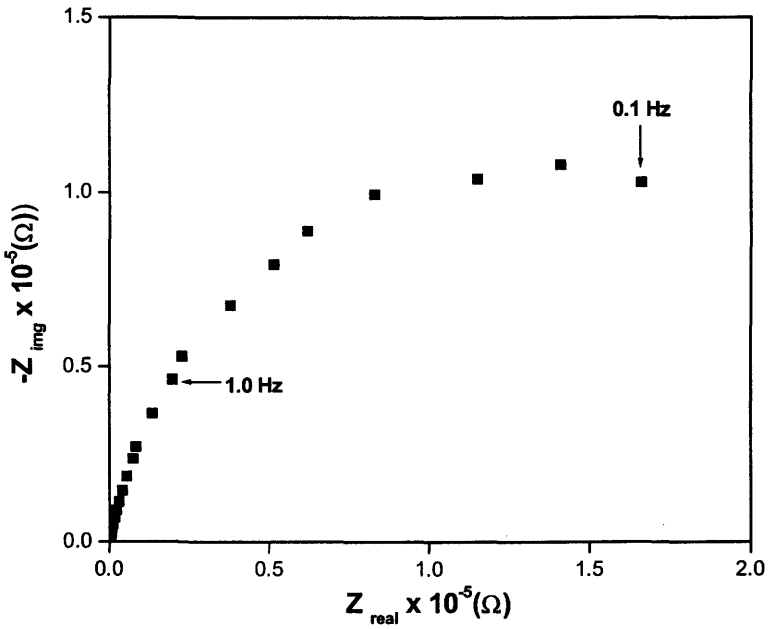

Figure 3.21. Nyquist plots showing AC-EIS behaviour at an applied bias voltage of 250 mV with respect to Ag/AgCl and ac amplitude of 5 mV rms for behaviour of HDM-modified electrodes heated and cooled in air in an oven to test for reversibility of monolayer electrodes below T_{tr} in 3 mM $K_3Fe(CN)_6$ and 3 mM $K_4Fe(CN)_6$ / 0.1 M KCl at 20.5°C (From 100 kHz to 0.1 Hz).

3.3 Langmuir-Blodgett Films of Alkanethiols on Gold

The aim of this work was to produce stable LB monolayers of alkanethiols on gold electrodes, and to compare these monolayers with analogous films produced by SA reported previously.[244] Their blocking behaviour was characterized by CV and AC-EIS using $[Fe(CN)_6]_3^{-/4-}$ as a redox probe. The LB

films were also studied as a function of temperature in an analogous manner to studies of the self-assembled monolayers. It is expected that any difference in the two types of films can be attributed to the fundamentally different processes of film formation.

LB transfer of a monolayer from the air-water interface to a solid substrate[23] requires stability of the monolayer on the water surface[110] (floating or Langmuir film). In order to achieve the required stability of the alkanethiol Langmuir films, various aqueous subphases were investigated to stabilize the Langmuir film at the air-water interface.

3.3.1. Langmuir Films

Initially pure water was used as the subphase. It produced Langmuir films of the alkanethiols with inconsistent mean molecular areas due to solubility of the alkanethiols in the subphase. Although it was observed that by decreasing the temperature of the subphase, the solubility of the alkanethiols was reduced, it was still difficult to overcome the variation in the mean molecular areas.

Table 3.2 gives a summary of the compounds investigated for use in the subphase.

Of all the salts used, ammonium chloride, barium chloride and gadolinium chloride gave reliable Langmuir films but the films formed on gadolinium chloride and barium chloride subphases were not stable enough to effect any LB

deposition. From Table 3.2, the ammonium chloride subphase offered the best results and it was therefore chosen and used for the rest of the study on LB films.

Table 3.2. Various subphase compositions used and their response.

Compounds Used	Composition (mM)	Collapse Pressure of Monolayer (mNm^{-1})	Response
Ammonium Chloride (99.5 %)	100	5-15	Film is stable, Slightly soluble Solubility decreases considerably with decrease in temperature
	10.0		
	1.00		
Barium Chloride (99.5 %)	100	5-10	Film is stable, Slightly soluble
	10.0		
	1.00		
Gadolinium Chloride (99.9%)	10.0	10-12	Film is stable, Slightly soluble
	1.00		
	0.100		
Hydrochloric Acid (36.5 - 38.0 %)	100	N/A	Dissolution of film with time
Potassium Chloride (99.5%)	100	5-10	Dissolution of film with time
	10.0		
Sodium Chloride (99.0%)	100	5-10	Dissolution of film with time
	10.0		

100 mM (0.1 M) gave inconsistent surface pressures and 1 mM ($1x\ 10^{-3}$ M) gave problems with alkanethiol solubility. An aqueous subphase with a composition of 10.0 mM ($1x\ 10^{-2}$M) ammonium chloride was chosen for LB deposition experiments.

3.3.1.1. Surface Pressure – Area Isotherms

The **π-A** isotherms[110,286] for HDM and ODM at various subphase temperatures (8-20°C) are shown in Figures 3.22 - 3.25. Isotherms were independent of the amount of thiols spread on the subphase provided the trough was not "overloaded". The shape of the isotherms resembles that of octadecanol (ODL).[96]

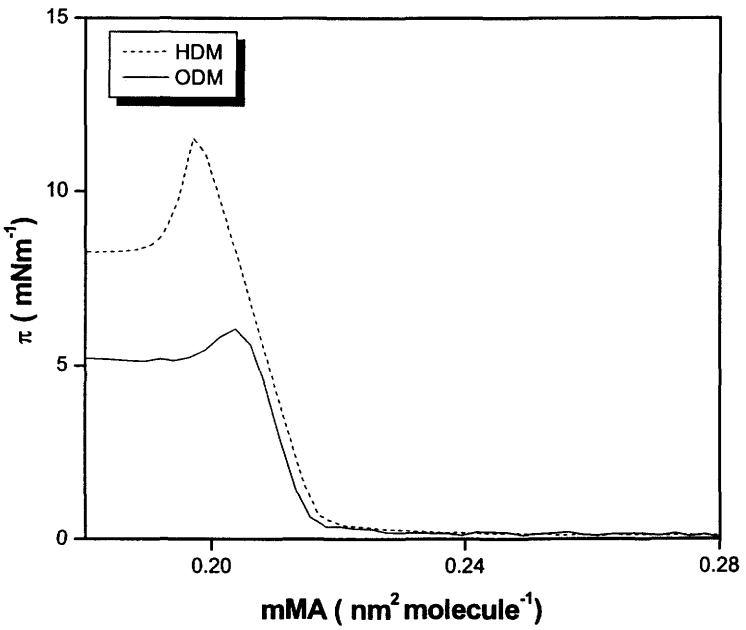

Figure 3.22. **π –A** isotherms of HDM and ODM on a 0.01 M NH_4Cl subphase at a subphase temperature of 8°C.

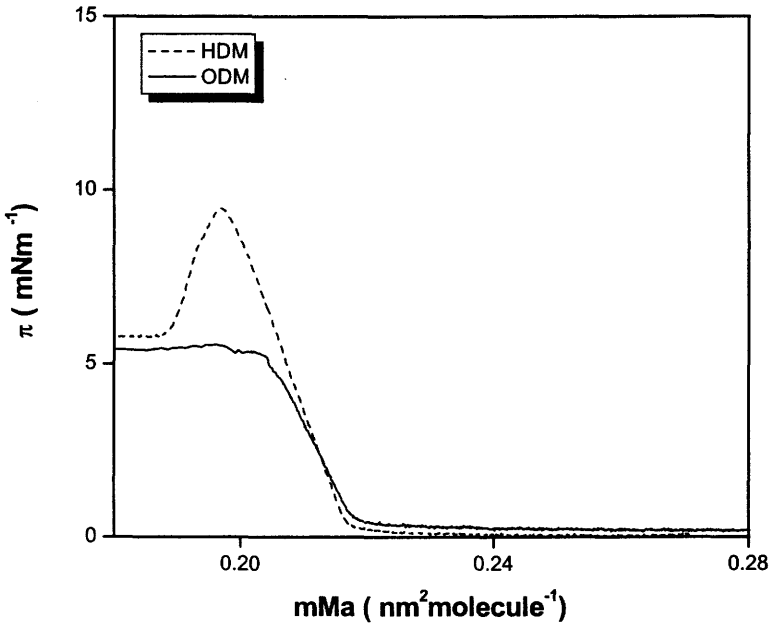

Figure 3.23. π–**A** isotherms of HDM and ODM on a 0.01 M NH_4Cl subphase at a subphase temperature of 12°C.

The limiting areas were evaluated by extrapolation from the first increase in surface pressure observed in the compression isotherm, and are listed in Table 3.3. They show little variation with subphase temperature or chain length. The collapse pressures of HDM decreases with increasing temperature and that of ODM remain constant. Since the films were compressed at a maximum speed of 5mm min^{-1} with a limiting rate of increase in surface pressure of 1$mNm^{-1}min^{-1}$, this trend was not due to any kinetic effects of collapse and compression as the limiting rate eliminated the effect of compression speed. The same information for ODL at room temperature is shown in Table 3.4.

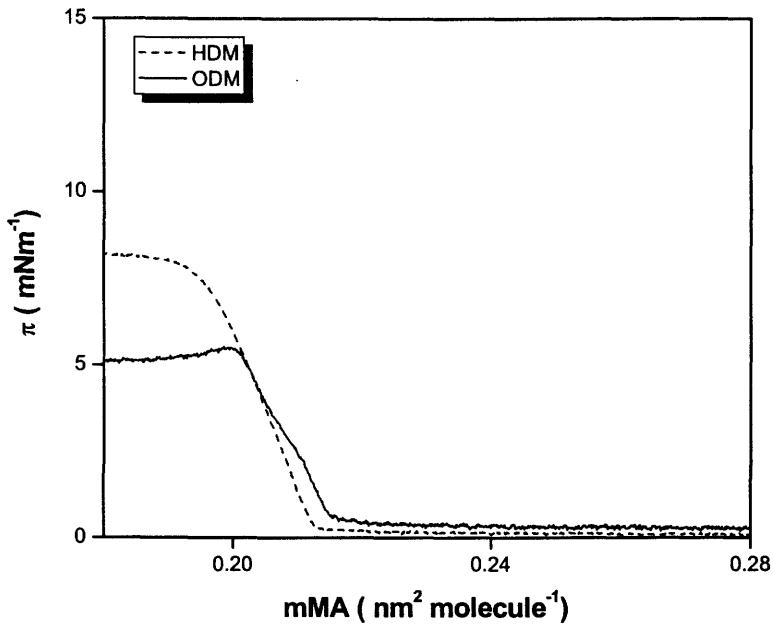

Figure 3.24. π –**A** isotherms of HDM and ODM on a 0.01 M NH_4Cl subphase at a subphase temperature of 16°C.

Films left compressed on the surface of the subphase for more than 12 hours exhibited no significant decrease in pressure or shift in the isotherm. This is in contrast to what was reported for ODM on 0.005 - 0.1 M NaOH subphases.[95] This is important because it indicated that the films produced at the air-water interface were very stable over a long period of time. And therefore the time it took for deposition of the films on gold substrates were performed with film of the same properties and morphology.

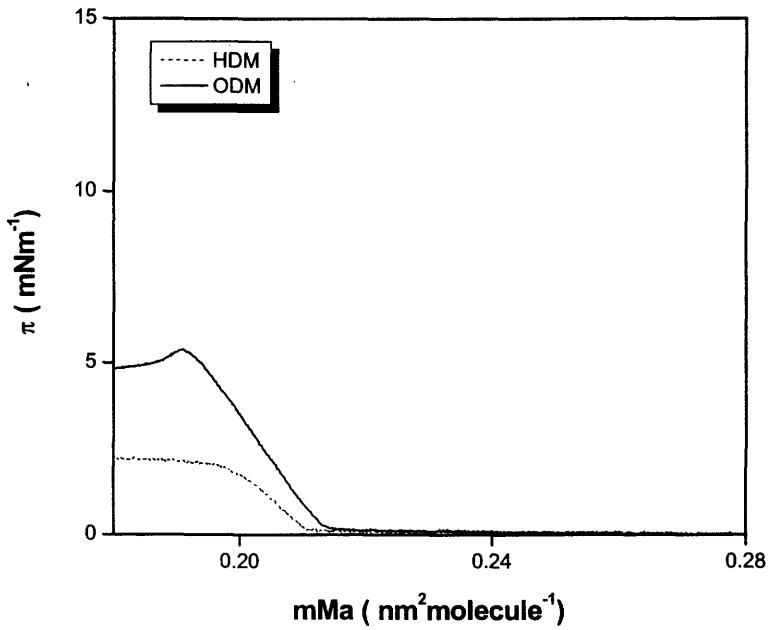

Figure 3.25. π–**A** isotherms of HDM and ODM on a 0.01 M NH_4Cl subphase at a subphase temperature of 20°C.

Table 3.3. Properties of HDM and ODM Langmuir films on a 0.01 M NH_4Cl subphase at different temperatures.

Temperature (°C)	Mean Molecular Area (nm ^{2}molecule^{-1}) ± 0.005		Collapse Pressure (mNm^{-1})	
	HDM	ODM	HDM	ODM
8	0.218	0.216	11.0-12.0	5.5-6.0
12	0.217	0.219	9.0-9.5	5.5-6.0
16	0.213	0.216	8.0-8.5	5.5-6.0
20	0.223	0.214	3.0-4.0	5.5-6.0

Table 3.4. Comparison of mMa and Collapse Pressure after Calibration of Langmuir film balance.

Compound	Mean Molecular Areas (nm^2)		Collapse Pressures (mNm^{-1})	
	Experimental	**Literature**	**Experimental**	**Literature**
Octadecanol	0.230 ± 0.010	0.210 ± 0.005	35-40	~ 40

It is worthy to note that MUA was very difficult to study on the trough because of its high solubility. Surface pressures were always less than 5mNm^{-1} and inconsistent. Due to this reason no further studies were performed on MUA with the Langmuir film balance.

3.3.1.2. Deposition of Langmuir-Blodgett Film

LB deposition of monolayers of HDM and ODM were attempted at subphase temperatures of 8, 12 and 16°C. Monolayers were transferred onto gold and glassy carbon electrodes. An attempt to transfer ODM onto gold at a subphase temperature of 20°C resulted in a poorly blocked electrode with a transfer ratio of 0.05. No attempt was made to transfer HDM at this temperature because of the inconsistent surface pressures and resulting unstable films.

Transfer from the air-water interface to the electrode was at 1 mNm^{-1} lower than the collapse pressure for HDM and ODM, respectively. The LB-transfer ratio is defined as A_d/A_c where A_d is the decrease in the area occupied

by the monolayer on the water surface during transfer, and A_c is the substrate area. This ratio varied from 0.40-0.70 for gold electrodes in all subphase temperatures except 20°C. The transfer ratios for glassy carbon electrodes were generally lower. Before deposition, Langmuir films were compressed at a maximum speed of 5 mmmin^{-1} with a limiting rate of increase in surface pressure of 1mNm^{-1}min^{-1} until the deposition surface pressure was reached (7.0-9.0 mNm^{-1} for HDM, and 5.0 mNm^{-1} for ODM, the former depending on the subphase temperature, with lower surface pressures being used for the higher temperatures). The electrode was then lifted through the Langmuir film at the air-subphase interface at a rate of 1 mmmin^{-1}. The same deposition parameters were used for both the gold and glassy carbon substrates.

3.3.2. Cyclic Voltammetry of Modified Electrodes

The passivating nature of LB films deposited from the air-water interface was studied by CV of the redox couple $[Fe(CN)_6]^{3-/4-}$.

3.3.2.1. Choosing Deposition Temperature for Langmuir-Blodgett Films

Figures 3.26 - 3.29 show CVs of $[Fe(CN)_6]^{3-/4-}$ with gold electrodes modified at different deposition temperatures. They reveal that films deposited

at lower temperatures are more passivating. Unless otherwise stated, all subsequent films were deposited at 8°C.

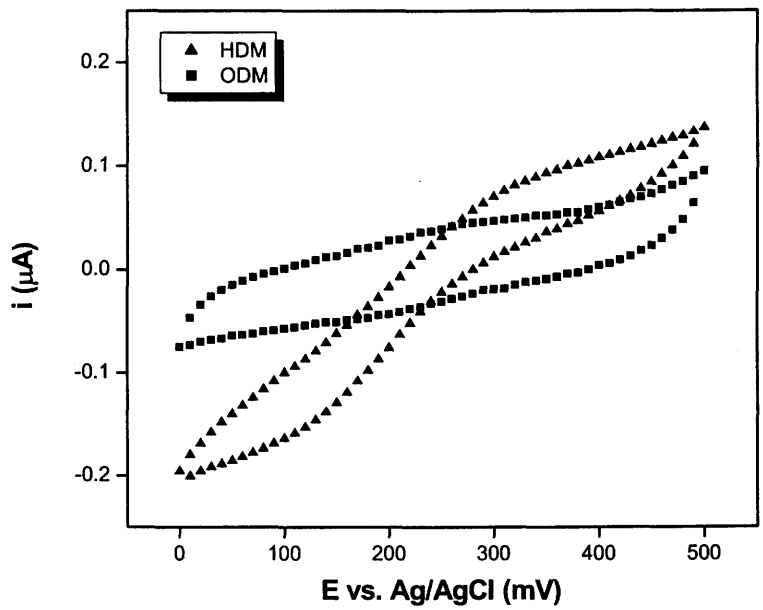

Figure 3.26. CV at 50mV s^{-1} of HDM and ODM LB modified electrodes deposited at 8.0°C and run in 3 mM $K_3Fe(CN)_6$ and 3 mM $K_4Fe(CN)_6$ / 0.1 M KCl at room temperature.

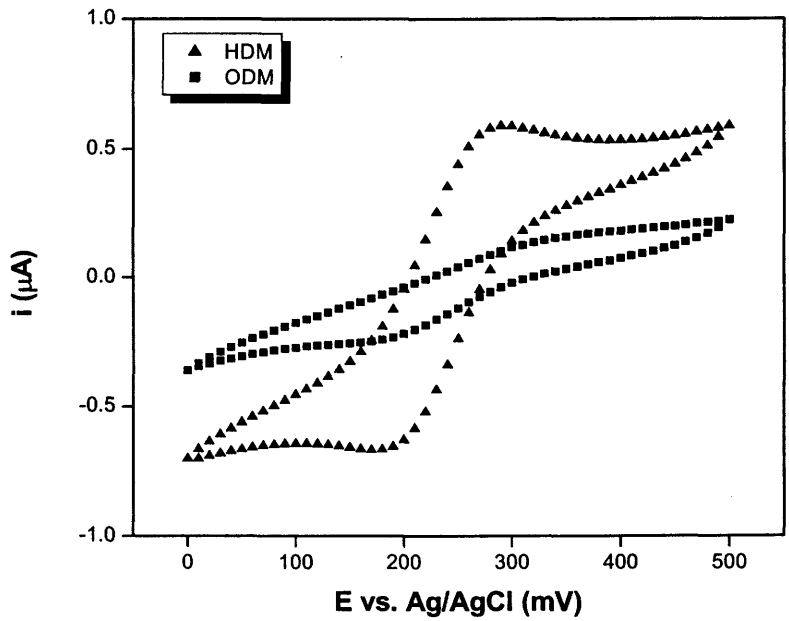

Figure 3.27. CV at 50 mVs^{-1} of HDM and ODM LB modified electrodes deposited at 12.0°C and run in 3 mM $K_3Fe(CN)_6$ and 3 mM $K_4Fe(CN)_6$ / 0.1 M KCl at room temperature.

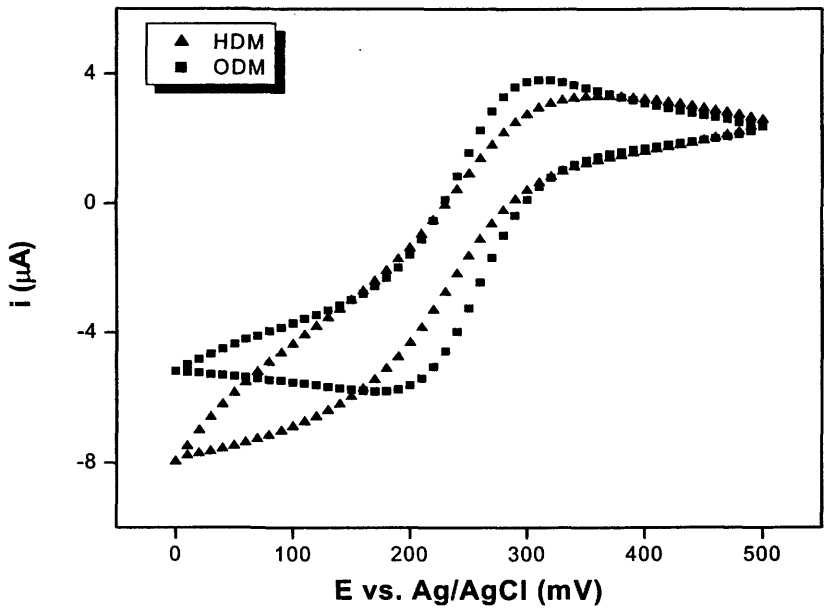

Figure 3.28. CV at 50 mVs^{-1} of HDM and ODM LB modified electrodes deposited 16.0°C and run in 3 mM $K_3Fe(CN)_6$ and 3 mM $K_4Fe(CN)_6$ / 0.1 M KCl at room temperature.

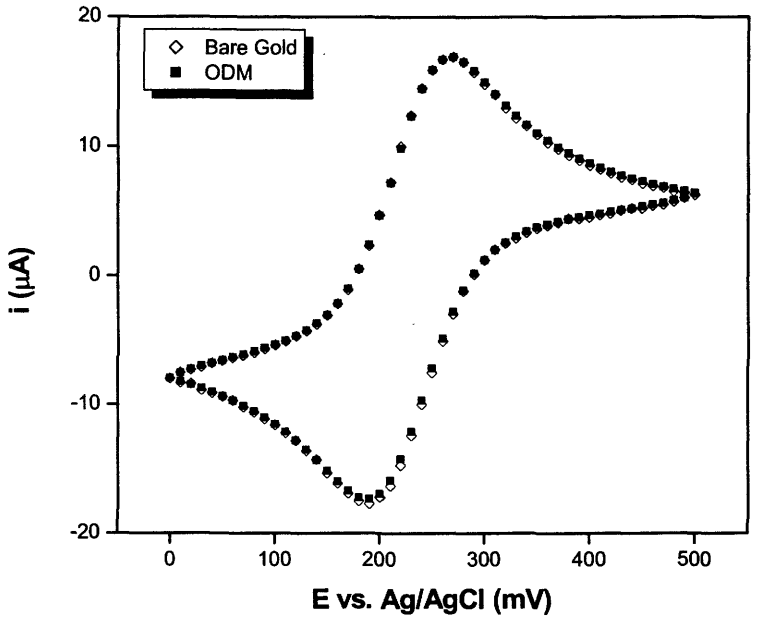

Figure 3.29. CV at 50 mVs^{-1} of bare gold and ODM LB modified electrodes deposited at 20.0°C and run in 3 mM $K_3Fe(CN)_6$ and 3 mM $K_4Fe(CN)_6$ / 0.1 M KCl at room temperature.

Figure 3.30 shows the CV of $[Fe(CN)_6]^{3-/4-}$ with two ODM LB-modified electrodes, both deposited at 8.0°C, one on gold and the other on glassy carbon. (These CVs have been presented as current density rather than current, because of the difference in effective geometrical areas of the two electrodes). There is a significant difference in the blocking abilities of the two modified electrodes. The ODM LB modified gold electrode blocks the redox reaction far better than the ODM LB-modified glassy carbon electrode.

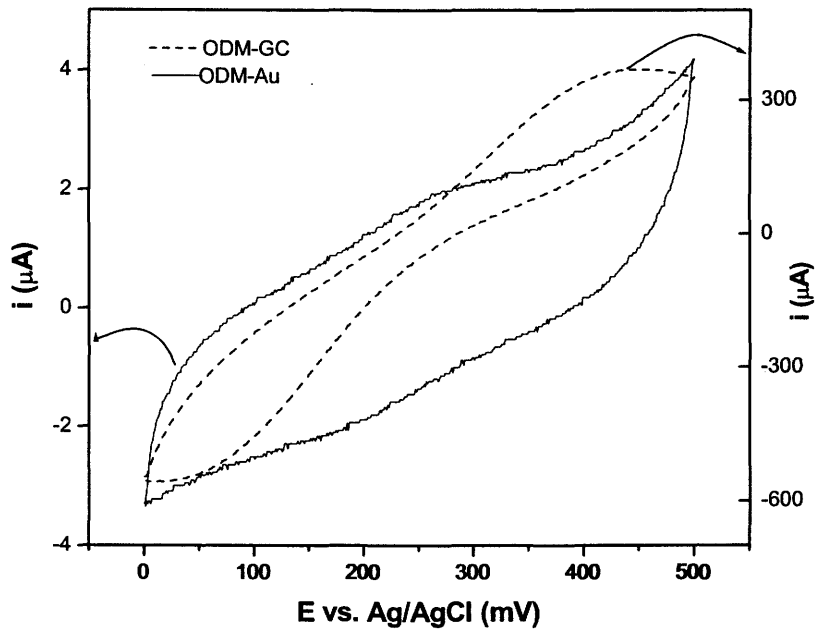

Figure 3.30. CV at 50 mVs^{-1} of gold and glassy carbon - ODM LB modified electrodes deposited at 8.0°C and run in 3 mM $K_3Fe(CN)_6$ and 3 mM $K_4Fe(CN)_6$ / 0.1 M KCl at room temperature.

3.3.2.2. Variable Temperature Behaviour of Langmuir-Blodgett Films

The effect of the LB films, produced on gold and glassy carbon electrodes on the redox activity of $[Fe(CN)_6]^{3-/4-}$ in solution was studied as a function of temperature.

3.3.2.2.1. Modified Gold Electrodes

CV was used in variable temperature studies, to study the LB films on gold, as it was used in similar studies of SAMs. Again, good blocking of the redox probe $[Fe(CN)_6]^{3-/4-}$ for the electrode was observed at low temperatures,

and a drastic increase in the redox activity of the probe was observed at temperatures above T_{tr} where T_{tr} is characteristic for each film. Figure 3.31 shows the behaviour of the alkanethiol LB films below T_{tr}. LB films of ODM blocked better than LB films of HDM, in a trend similar to that observed in SAMs.

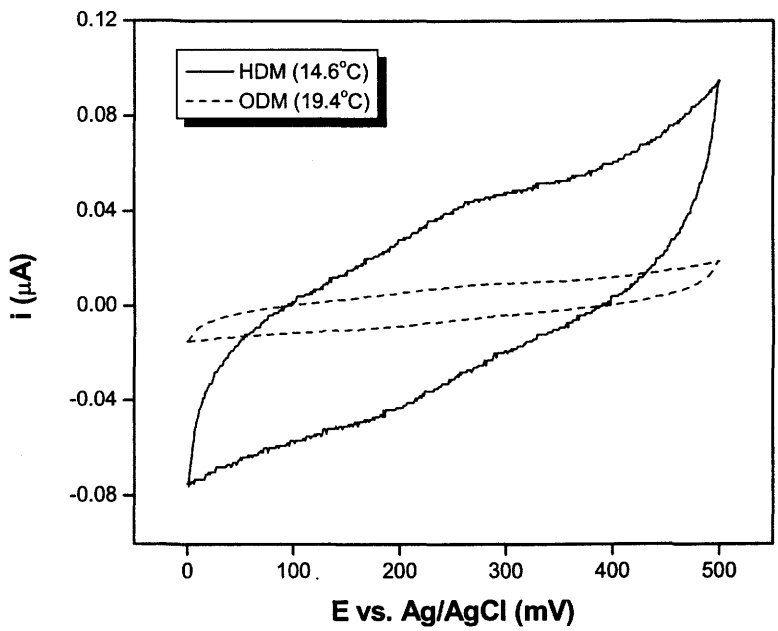

Figure 3.31. CV at 50 mVs^{-1} of HDM and ODM LB-modified electrodes below T_{tr} in 3mM $K_3Fe(CN)_6$ and 3 mM $K_4Fe(CN)_6$ / 0.1 M KCl.

The CV results of the LB films of HDM, ODM, together with that of bare gold electrode above T_{tr} are shown in Figure 3.32. This trend is similar to that in the SAMs shown earlier in Figure 3.13.

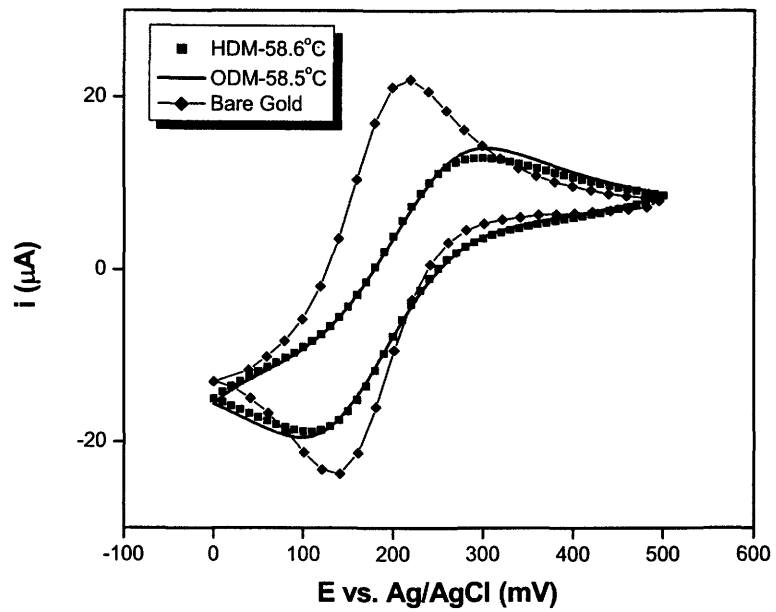

Figure 3.32. CV at 50 mVs^{-1} of bare gold, HDM and ODM LB modified electrodes above T_{tr} in 3 mM $K_3Fe(CN)_6$ and 3 mM $K_4Fe(CN)_6$ / 0.1 M KCl.

3.3.2.2.2. Bare and Modified Glassy Carbon Electrodes

The CV of the redox couple $Fe(CN)_6^{3-/4-}$ measured with bare glassy carbon at room temperature is shown in Figure 3.33. A glassy carbon electrode modified by an LB film of ODM is shown in Figure 3.34. It is seen that the current of the modified electrode increases steadily with increasing temperature, and there is no drastic or abrupt change in behaviour and no transition temperature exhibited by the films. LB films of HDM on glassy carbon electrode exhibit the same behaviour as the ODM modified films

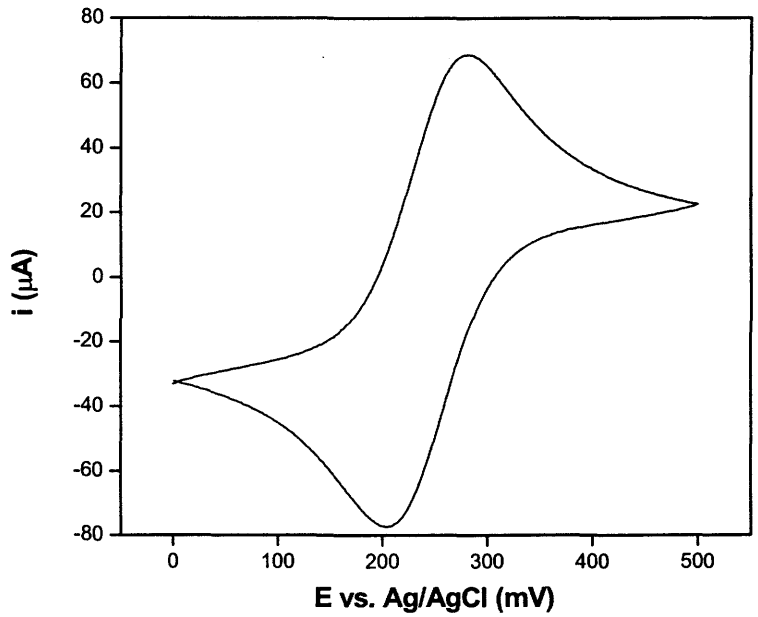

Figure 3.33. CV at 50 mVs^{-1} for bare glassy carbon in 3 mM $K_3Fe(CN)_6$ and 3 mM $K_4Fe(CN)_6$ / 0.1 M KCl at room temperature.

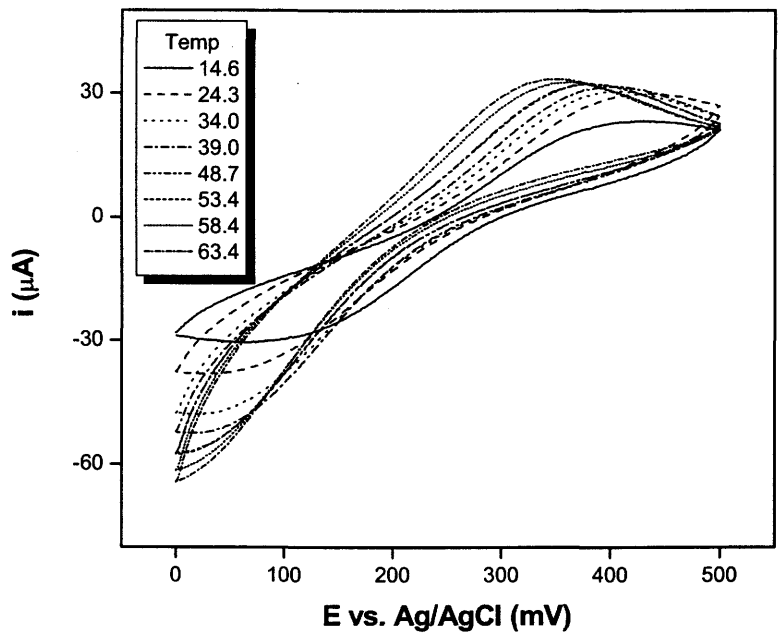

Figure 3.34. CV at 50 mVs^{-1} of glassy carbon electrode modified with ODM in 3 mM $K_3Fe(CN)_6$ and 3 mM $K_4Fe(CN)_6$ / 0.1 M KCl at different temperatures.

3.3.3. Alternating Current-Electrochemical Impedance Spectroscopy of Modified Electrodes

AC-EIS was used to study the same LB film over a wide temperature range (~15 - 65°C) to compare with parallel studies done on SAMs.[244] The results were collected in Nyquist plots at various frequencies.

3.3.3.1. Variable Temperature Behaviour of Langmuir-Blodgett Films

3.3.3.1.1. Modified Gold Electrodes

The results for the LB –films of HDM and ODM on gold were not very different from the AC-EIS results of SAMs.[244] Typical Nyquist plots for an ODM LB film below and above T_{tr} are shown in Figures 3.35 and 3.36.

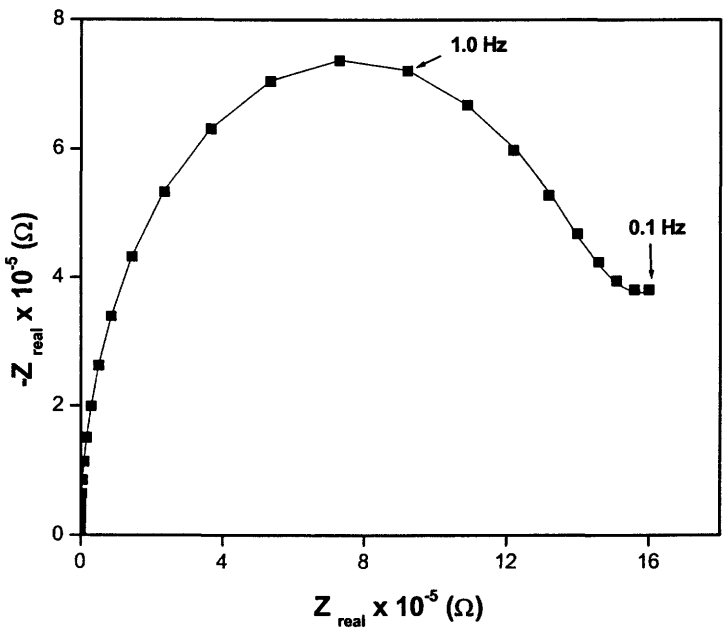

Figure 3.35. Nyquist plots showing AC-EIS response at an applied bias voltage of 250 mV and ac amplitude of 5 mV rms for LB films of ODM on gold below T_{tr} in 3 mM $K_3Fe(CN)_6$ and 3 mM $K_4Fe(CN)_6$ / 0.1 M KCl. (Lines show theoretical fit) (From 100 kHz to 0.1 Hz).

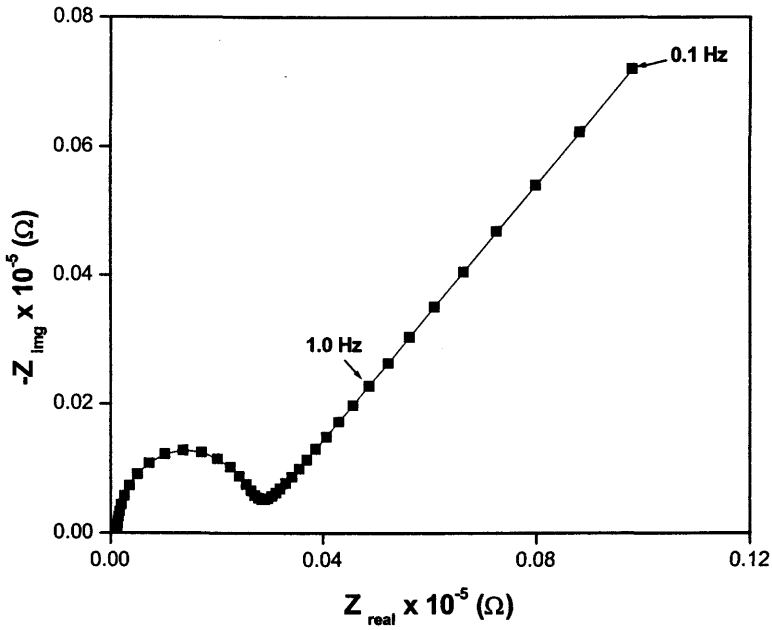

Figure 3.36. Nyquist plots showing AC-EIS response at an applied bias voltage of 250 mV and ac amplitude of 5 mV rms for LB films of ODM on gold above T_{tr} in 3 mM $K_3Fe(CN)_6$ and 3 mM $K_4Fe(CN)_6$ / 0.1 M KCl. (Lines show theoretical fit) (From 100 kHz to 0.1 Hz).

3.3.3.1.2. Bare and Modified Glassy Carbon Electrodes

Figure 3.37 is the Nyquist plot of bare glassy carbon electrode in $[Fe(CN)_6]^{3-/4-}$. Figure 3.38 shows the Nyquist plots of ODM-LB films on glassy carbon in redox couple $[Fe(CN)_6]^{3-/4-}$. This is similar to the behaviour observed by CV. The LB films of HDM on glassy carbon exhibit the same behaviour as the LB films of ODM in Figure 3.38.

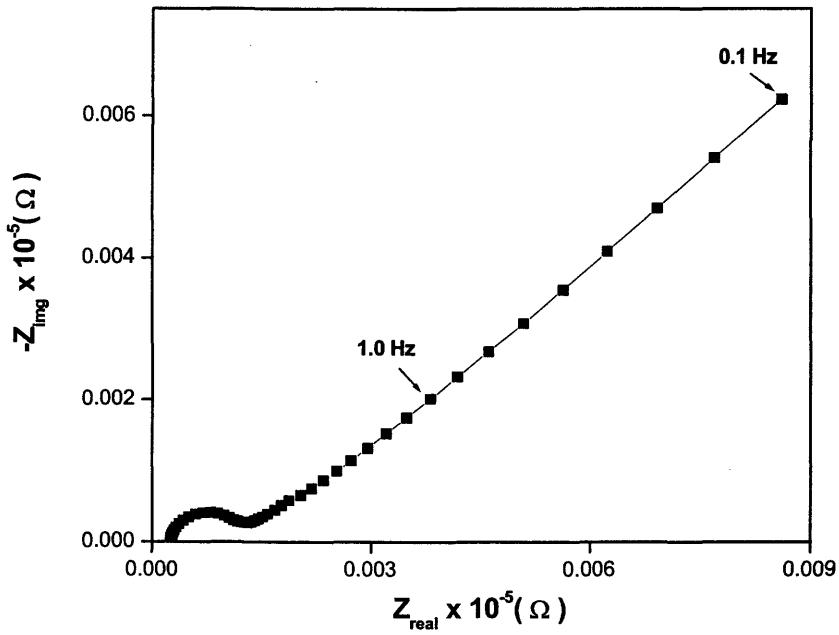

Figure 3.37. Nyquist plots showing AC-EIS response at an applied bias voltage of 250 mV and ac amplitude of 5 mV rms for bare glassy carbon in 3 mM $K_3Fe(CN)_6$ and 3 mM $K_4Fe(CN)_6$ / 0.1 M KCl at room temperature (From 100 kHz to 0.1 Hz)

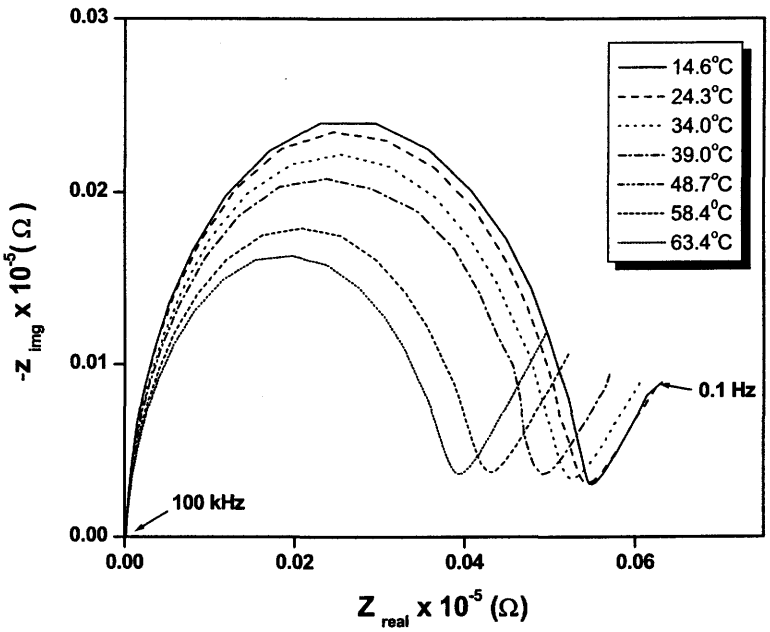

Figure 3.38. Nyquist plots showing AC-EIS response at an applied bias voltage of 250 mV and ac amplitude of 5 mV rms for LB films of ODM on glassy carbon in 3 mM $K_3Fe(CN)_6$ and 3 mM $K_4Fe(CN)_6$ / 0.1 M KCl at different temperatures (From 100 kHz to 0.1 Hz).

3.4. Three-Dimensional Alkanethiol-Capped Gold Colloids

Alkanethiol-capped gold colloids were synthesized using ODM and HDM according to methods described earlier.[23,110,273] These colloids are of interest because of their structural analogies to SAMs on flat surfaces.[30] It has been demonstrated that SAMs generated on 2D metal surfaces (2D SAMs) have very similar properties to SAMs on colloidal surfaces (3D SAMs). However, the limitation of 2D SAMs relative to 3D SAMs is that the latter are easy to isolate, stable in air, and soluble in a wide range of organic solvents. These features

permit facile manipulation and characterization using a variety of traditional 3D techniques, including DSC,[36,86,272] NMR,[37 20,36,116,279,287] and FTIR.[20,23,24,37,40,42,86,116,279,288]

^{1}H and ^{13}C-NMR, and FT-IR were used to characterize the colloids at room temperature. DSC, ^{1}H and ^{13}C-NMR were used to study the alkanethiol-capped gold colloids of HDM and ODM as a function of temperature to compare with the electrochemical studies of the 2D SAMs.

3.4.1. Differential Scanning Calorimetry of Colloids

DSC was used to characterize the thermal properties of the alkanethiol-capped gold colloids of HDM and ODM. Phase transitions of the colloids were characterized by their temperature and enthalpy.[36,86,272] Because the SAMs and LB films studied as a function of temperature revealed distinct discontinuities as the temperature was increased, it was of interest to investigate the thermal properties of these 3D colloids and compare them to the behaviour of the SAMs and LB systems.

It has been reported[119] that these colloids reveal reversible disordering and ordering of the alkyl chains beginning from the terminal groups and gradually proceeding further down the chain as a function of temperature.

The DSC results confirmed that there was no change of the sample mass after heating. This indicates that the samples are thermally stable in the

temperature region under study. For both samples, the DSC measurements indicate irreversible changes in the structure of the alkanethiol layer during first and second heating.

3.4.1.1. Hexadecanethiol-Capped Gold Colloids

The sample Au-HDM colloid exhibited a very small irreversible peak during the first heating at 39.9°C. In the second heating a sharp quasi-reversible peak corresponding to a phase transition was observed at 48.2°C (Figure 3.39). In the third heating the peak became higher and shifted slightly to 48.4°C. The very small peak in the first heating at 39.9°C has a ΔH value on the order of 2.5 Jg^{-1} as indicated in Table 3.5.

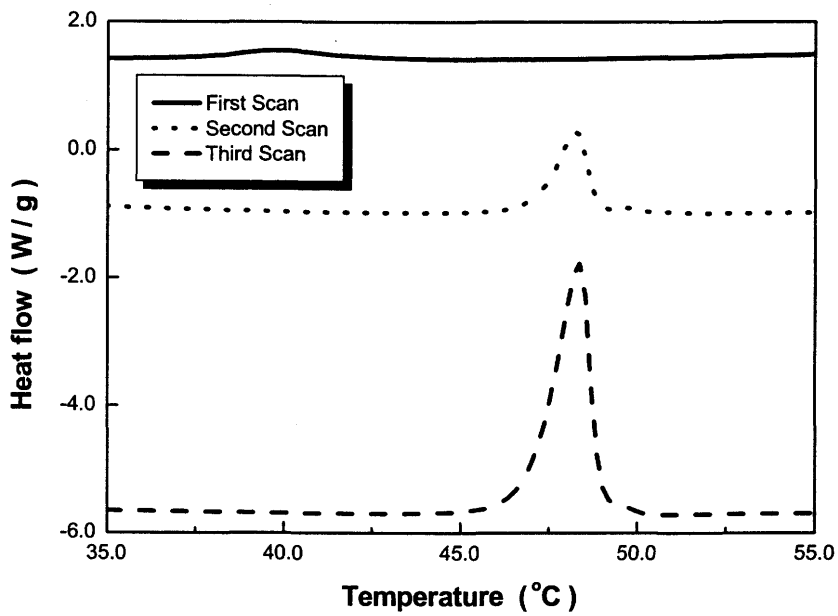

Figure 3.39. DSC thermograms of HDM-Au. Scan rate 5°C min^{-1}. Each heating cycle was from low temperature to high temperature.

Table 3.5 Characteristics of peaks from DSC thermograms.

Colloid Sample	Heating Cycle	Onset Temperature [°C]	Peak Maximum Temperature [°C]	ΔH / J g^{-1}
HDM	1st	37.5	39.9	2.5
	2nd	47.2	48.2	9.1
	3rd	47.0	48.4	30.8
ODM	1st	54.6	55.8	17.6
	2nd	52.0	54.0	14.9
	3rd	51.8	53.9	14.2

3.4.1.2. Octadecanethiol-Capped Gold Colloids

The Au-ODM colloid exhibited a quasi-reversible peak in all heatings (Figure 3.40). In the first and second heatings, the temperatures (55.8°C and 54.0°C) and the shapes of the peak are different (Table 3.5). The peak of the second and third heating at 54.0°C and 53.9°C, respectively, are the same. This is seen from the values of ΔH in Table 3.5 and also from Figure 3.40.

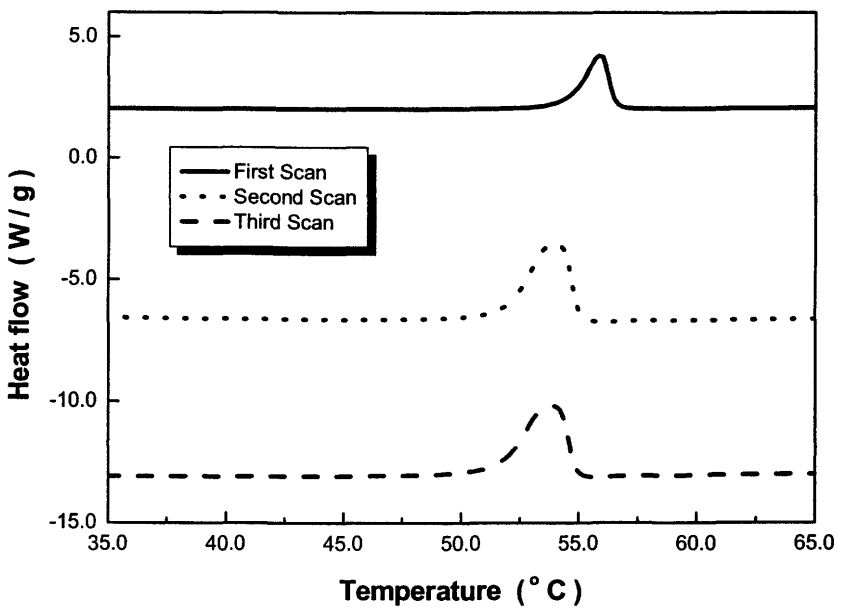

Figure 3.40. DSC Thermograms of ODM-Au. Scan rate 5°C min^{-1}. Each heating cycle was from low temperature to high temperature.

The characteristics of the peaks are summarized in Table 3.5.

3.4.2. Nuclear Magnetic Resonance Spectroscopy Spectra of Colloids

The variable temperature solution state ^{1}H and ^{13}C NMR of the colloids was studied to look for additional evidence of a phase transition in colloid systems, analogous to electrochemical studies in which the SAMs are also in solution.

3.4.2.1. Variable Temperature Nuclear Magnetic Resonance Spectra of Colloids

Variable temperature ^{1}H and ^{13}C solution NMR spectra of ODM colloids are shown in Figures 3.41 and 3.42, respectively. In both cases, there was no significant change except for the slight, steady changes in chemical shifts as the temperature was increased from 25°C to 70°C

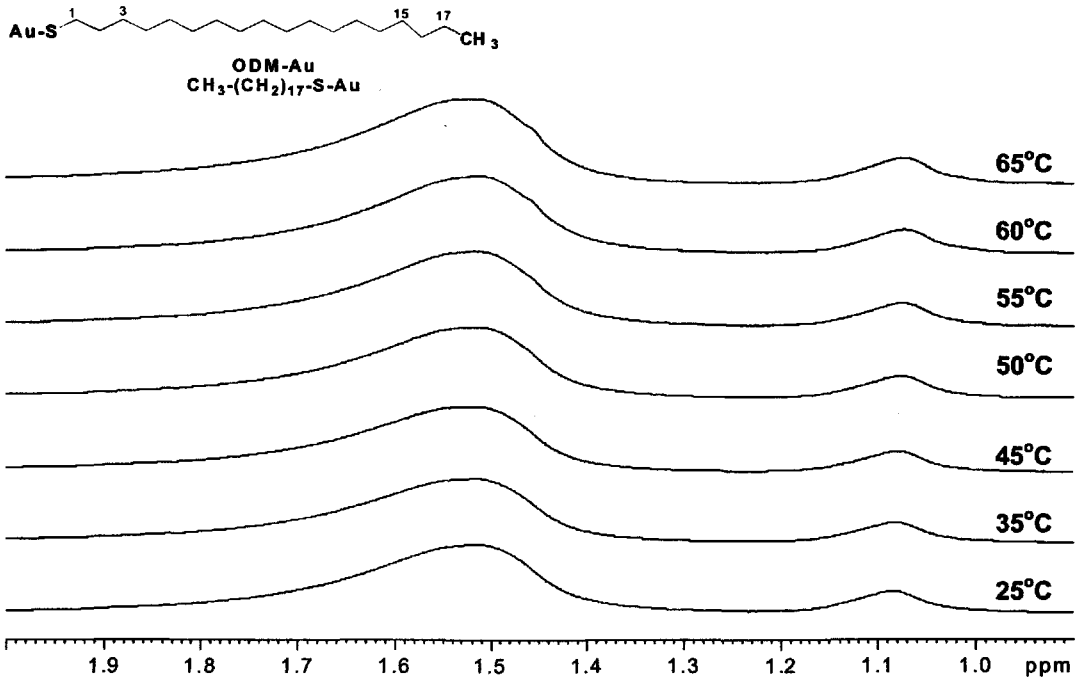

Figure 3.41. ^{1}H-NMR spectra in benzene-d_6 of ODM gold colloid as a function of temperature (order of heating from low to high).

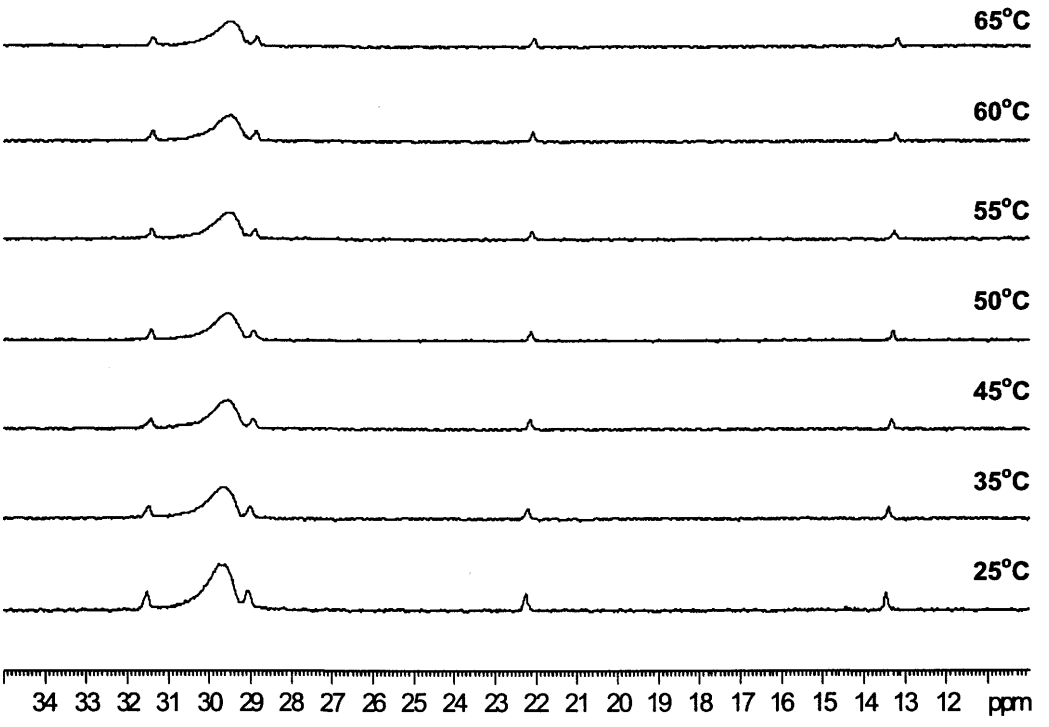

Figure 3.42. ^{13}C-NMR spectra in benzene-d_6 ODM gold colloid as a function of temperature (order of heating from low to high).

The ^{1}H and ^{13}C NMR of the HDM colloid was the same as that of the ODM colloid.

Chapter Four – Discussion

4.1. Bare Gold

The purpose of studies on bare gold was to obtain data for comparison with the response from modified electrodes. Many factors are important in optimizing the bare gold response. In the case of polycrystalline gold electrodes the cleaning and/or polishing is one of the main concerns. Electrochemical cleaning based on the reductive desorption of thiols and the electrochemical oxidation of the gold electrode before chemical reduction in absolute ethanol resulted in an effective, clean, reproducible gold surface. In addition, defects in the subsequent monolayers were minimized.

4.1.1. Cleaning

Cleaning is necessary before the deposition process of alkanethiols on gold electrodes.[176] Methods commonly used for the cleaning and etching of gold include electrochemical cleaning,[197] mechanical and electrochemical polishing,[289] heating the gold in gas/air flame (flame annealing),[290] and etching the bulk gold in dilute aqua regia.[188] These treatments leave a surface oxide

that can become trapped under a self-assembling thiol monolayer, and this can affect the properties of the SAM deleteriously.[189,190] The strategy of cleaning adopted here was based on the electrochemical reductive desorption of thiols, electrochemical oxidation of the bare gold surface in H_2SO_4, and reduction of the resulting gold oxide in ethanol to produce a homogenous reproducible gold surface.

Sometimes, the reductive desorption step had to be repeated several times before oxidation of the bare gold surface to the gold oxide. To do this, repolishing of the electrode surface with different sizes of alumina and rinsing with millipore water in between each of the reduction steps had to be performed.

4.1.2. Surface Roughness of Gold

Surface roughness on the molecular level was evaluated by UPD.[281] During the CA experiment, copper atoms are deposited on the electrode surface as a monolayer at an applied potential (See Figure 3.3). Normally, the rough electrode surface has a higher number of available gold atoms than a smooth gold surface and therefore more copper atoms will be deposited on a rough surface. LSV is performed after deposition to strip the copper monolayer from the surface of the gold electrode. The surface area of the stripping peak in the LSV corresponds directly to the oxidative charge, which can be converted into the amount of copper atoms being stripped from the electrode surface. The

theoretical expected coverage has been previously reported for copper on Au(III) as 2.3 x 10^{-9} molcm^{-2} .[281] The active area of the electrode was calculated by dividing the amount of copper atoms oxidized during the experiments by the expected coverage given above.[281] The area obtained divided by the theoretical geometrical area of the gold electrode (which is 2.27 x 10^{-2} cm^2) gives the surface roughness of an electrode.

Following the cleaning procedure, the value of the surface roughness of bare gold was between 1.16 - 1.27 by UPD. This is comparable to surface roughness values obtained by researchers[84] who studied UPD on gold. The values obtained is representative of an acceptable homogenous clean gold surface for any monolayer studies.

4.2. Formation of Self-Assembled Monolayers and Langmuir-Blodgett Films – A Comparison

Films for these studies were deposited on gold electrodes by two different methods: namely the SA and LB deposition techniques. Fundamentally, these methods may produce similar films if they start with the same "building blocks", as they are both formed based on two processes: chemisorption of alkanethiols on gold and molecular organization of the molecules. However the order in which the two processes occur is different for each method.

SA to produce SAMs involves two consecutive processes, chemisorption and subsequent molecular organization. For one well-known SA system involving long chain n-alkanethiols adsorbed onto gold, the chemisorption occurs when the gold surface is immersed into a homogenous solution of an alkanethiol at room temperature and reacts with the thiol moiety, displacing hydrogen and forming a gold-thiolate bond as shown below.

$$R - S - H + Au^{o}_{n} \longrightarrow R - S^{-} Au^{+} + \tfrac{1}{2}H_2 \quad \text{(Scheme 1)}$$

A monolayer is deposited on the gold in a matter of seconds to minutes by chemisorption. For millimolar or higher concentrations of thiols, a disordered monolayer is deposited. This is followed by molecular organization, which is a much slower transformation, into a highly oriented and densely packed monlayer.[158,179,244] This subsequent molecular organization is driven largely by lipophilic interactions between neighbouring alkyl chains.

LB transfer leading to LB films, by contrast, consists of molecular organization at the air-water interface into Langmuir films, followed by transfer onto the desired solid supports to produce LB films. Presumably, if the additional stability offered by chemisorption could be incorporated into the LB deposition process, the resulting LB films would have greater integrity. Chemisorption of thiols on gold offers one possibility in this regard, but this would involve forming Langmuir films of, and depositing these onto gold

substrates. In this study, LB films of alkanethiols on gold electrodes were produced for direct comparison with SAMs of alkanethiols on gold electrodes.

4.2.1. Langmuir Films

An insoluble monolayer at the air-water interface can be considered as a 2D solution. The main source of thermodynamic data for almost a century[291] was the surface properties, which are generally studied by the measurement of the **π-A** isotherms of the monolayers. By comparing the **π-A** isotherms of individual monolayers, one is able to gain knowledge about interaction between monolayer-forming molecules.[127,292]

4.2.1.1. Langmuir Films of Octadecanol and Stearic Acid

The shape of the isotherms of ODL and stearic acid as shown in Figure 4.1 indicate that the monolayers are condensed monolayers with no phase transition between the liquid-expanded and liquid-condensed states.[96]

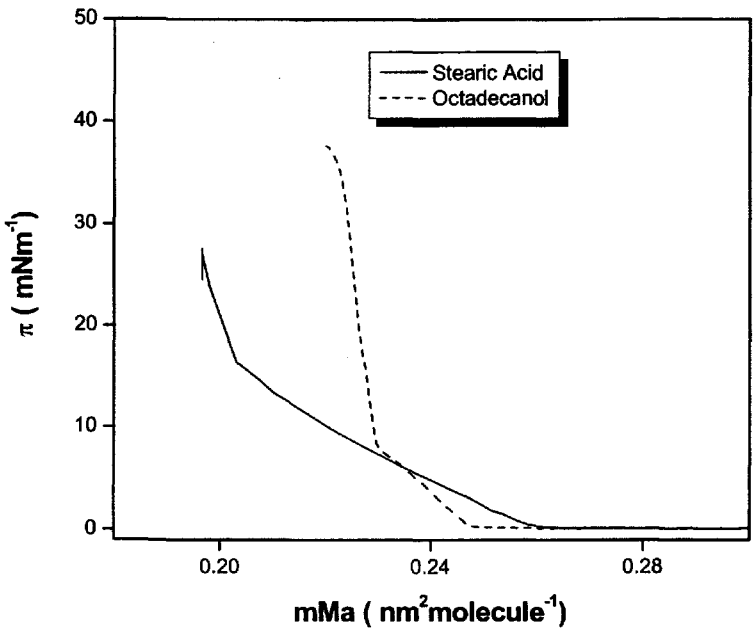

Figure 4.1. **π-A** isotherms of stearic acid and ODL on water subphase.

The shape of ODL has been proven by Brewster-angle microscopy[293] and isotherm measurements[294] to be typical for alcohols, and is attributed to the merger of the transition between the liquid-expanded and liquid-condensed states. The limiting areas lie between 0.212 and 0.219nm^2 molecule^{-1}. This area agrees with the cross-sectional area of a saturated hydrocarbon chain,[127] implying that the chains in monolayers are oriented more or less perpendicular to the air-water interface.[1]

4.2.1.2. Langmuir Films of Hexadecanethiol and Octadecanethiol

The shapes of the isotherms for HDM and ODM resemble that of ODL.[96] Similarly as in ODL and stearic acid, the monolayer is a condensed monolayer with no phase transition between the liquid-expanded and liquid-condensed states.[95] The alcohols and thiols differ in the sulphur and oxygen head groups, which are in the same periodic group so the similarity of an absence of a phase transition between the liquid-expanded and liquid-condensed states in their **π-A** isotherm should be expected. Some properties of the films were shown in Table 3.3.

Similarly, the limiting areas of HDM and ODM also lie between 0.212 and 0.219nm^2 $molecule^{-1}$, and show no significant variation with temperature or chain length. This area agrees with the cross-sectional area of a saturated hydrocarbon chain,[127] suggesting that the chains in monolayers are oriented more or less perpendicular to the air-water interface just as for the ODL and stearic acid.[1] A small tilt angle is possible, and indeed others have investigated such tilt angles in other Langmuir films[95,295,296] but the goal of this work was simply to ascertain that the chains were roughly perpendicular (as opposed to parallel) to the air-water interface, and to effect the deposition accordingly. It is however a fact, that orientational order induces tilt in the monolayers.[291]

On a 0.01 M aqueous NH_4Cl subphase, the isotherms of HDM and ODM show relatively low collapse pressures compared to other commonly deposited

surfactants[1,158,297]. Even at 8°C, the HDM monolayer becomes unstable above 12.0 mNm^{-1}, and the ODM monolayer above 5.5 mNm^{-1}. This poor stability compared to ODL is likely a reflection of the relatively low polarity of the thiol group relative to the hydroxyl group (dipole moments of CH_3OH and CH_3SH are 1.71 and 1.26 D, respectively).[298] Nevertheless, the stability of the alkanethiol monolayer on 0.01 M NH_4Cl is higher than on a pure aqueous subphase. This may be aided by the high pK_a value of the alkanethiols (pK_a of ODM has been estimated to be between 9 and 12) and the relatively acidic pH of the subphase (5.4-5.5).[285] These conditions virtually exclude the possibility of chemical decomposition or oxidation of the thiolate to disulfide at the surface of the subphase or of dissociation.

With the HDM films, there is a decrease in collapse pressure of films as temperature is increased. In ODM films however the collapse pressure is temperature independent. Thermodynamically, we can relate the compression of the films and their temperature dependent behaviour through equation 4.1 and Scheme 5.

$$\Delta G = \Delta H - T\Delta S \qquad (4.1)$$

gas $\rightleftharpoons$ **condensed** $\Delta G < 0$ Scheme 5

Since all the films are compressed from a gaseous state to a condensed state, the forward reaction of Scheme 5 is spontaneous and thus $\Delta \mathbf{G} < 0$.

Three factors account for the behaviour of the Langmuir films: the enthalpy ($\Delta \mathbf{H}$) of compression, the entropy ($\Delta \mathbf{S}$) of the interfacial water layer and the entropy in the chains upon compression of the films. When a solution of HDM or ODM is spread on the surface of the water, the surface tension of the subphase is reduced and this causes an increase in the entropy of the interfacial water layer between the bulk subphase and the Langmuir film formed at the air-water interface. Presumably, the increase in entropy in the interfacial water layer is the same for HDM and ODM. Thus the difference in the two layers lies in the loss of entropy in the chains upon compression from the gaseous state to the condensed state and the enthalpy of compression.

The decrease in the collapse pressure of HDM films as temperature is increased indicates an endothermic compression (positive $\Delta \mathbf{H}$). Thus for spontaneity of compression, the entropy of the system must increase during the course of compression. This can only occur if the obvious decrease in entropy in the HDM monolayer upon compression (from a disordered gaseous state to an ordered condensed state) is offset by the increase in entropy in the interfacial layer of water to give a total gain in the entropy of the system. This increase in entropy of the interfacial water is evidenced by the drop in surface tension, π, or the rise in surface pressure, $\boldsymbol{\pi}$ ($\boldsymbol{\pi} = \pi_0 - \pi$, where π_0 is the surface tension of pure water), which indicates a decrease in the intermolecular order between

interfacial water molecules. This behaviour has also been observed by some researchers that studied **π-A** isotherms of the monolayers of poly(benzyl ether) monodendrons at temperatures varying from 10 to 25°C.[299]

The collapse of ODM is apparently temperature-independent, indicating that this compression requires less of an increase in the overall entropy of the system than the compression of HDM. As stated earlier, the difference in the two layers lies in the loss of entropy in the chains upon compression, and since this loss is larger for the longer ODM chain than for the HDM chains, this is expected.

4.2.2. Deposition of Langmuir-Blodgett Films

LB-deposition of monolayers of HDM and ODM was possible at subphase temperatures of 8, 12 and 16°C, but at 20°C it was only possible to transfer ODM. This supports the notion of higher order in the ODM Langmuir film than in the HDM Langmuir film at all temperatures although HDM has higher collapse pressures at 8°C. It should be noted that the ODM film transferred at 20°C showed poor blocking quality, with little effective passivation and a response more similar to bare gold (Figure 3.29). Also, it had been argued that decreasing temperature enhances hindered rotation, which gives rise to a definite orientation of the backbone plane of the carbon skeleton.[291]

The LB-transfer ratios (defined as A_d/A_c) where A_d is the decrease in the area occupied by the monolayer on the water surface during transfer, and A_c the area of the substrate were difficult to calculate because of the small size of the gold and glassy carbon electrodes relative to the electrode sheath and the overall geometry of the whole electrode unit (Figure 2.1). Excluding all but the area of the gold or glassy carbon surface from the calculation of A_c (that is ignoring possible deposition onto the sheath), transfer ratios obtained were 0.40 - 0.70. This calculation is justified on the grounds that the sheath is a non-stick fluoropolymer specifically chosen to avoid adhesion and only a small fraction of the sheath is perpendicular to the air-water interface, owing to its cylindrical geometry (the perpendicular orientation is required for effective LB transfer). The standard errors of the ratios were large, ± 0.33 - 0.40. Another factor is the small electrode area and hence the small decrease in area occupied by the monolayer, A_d. The instrumentation limits the accuracy of these values to ± 0.11.

An optimal value of the transfer ratio should be 1.0 but even though values obtained were not close to unity, it is not alarming considering the difficulty in assessing the coated surface area of the substrate. The transfer ratio also indicates that the substrates used may not be the best ones. However, the goal of this study was to create a parallel study to that of the SAMs on the same substrates, in order to have a common response of the two types of modified electrodes in the presence of the $[Fe(CN)_6]^{3-/4-}$ redox probe.

4.3. Alternating Current-Electrochemical Impedance Spectroscopy : Data Analyses

One of the techniques used to probe the response of all the modified electrodes was AC-EIS. Data analysis for the results was lengthy. The trends in thermal behaviour of all electrodes observed by AC-EIS were better presented as thermograms of selected circuit elements versus temperature. These circuit elements were obtained from modelling studies using raw AC-EIS data and employing a Non-Linear Least Squares (NNLS) fit with the EQUIVCRT program to match the modelled equivalent circuit to the data. The EQUIVCRT (equivalent circuit version 4.55, 1996), was a program by B. A. Boukamp, University of Twente, Department Chemical Technology, Enschede, The Netherlands.[104,253]

4.3.1. Randles Circuit

The Randles equivalent circuit[103] was used to fit the experimental data for bare gold and all modified electrodes except for MUA below $\mathbf{T_{tr}}$. It is shown in Figure 4.2. It can be described as $\mathbf{R_1}$, representing solution resistance, in series with parallel $\mathbf{Q'}$ (constant phase element associated with the double layer capacitance) and $\mathbf{R_2Q''}$ (activation resistance in series with the variable Warburg impedance) circuits.

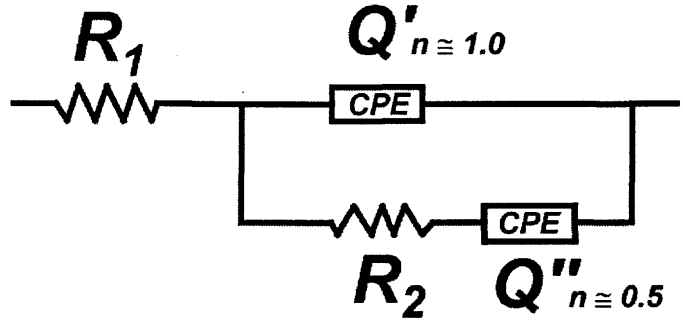

Figure 4.2. The Randles equivalent circuit used to fit AC-EIS data for bare gold and some modified electrodes.

4.3.2. Modified Randles Circuit

The electrode modified with MUA is unique in the sense that, below its T_{tr}, it is modelled with a different equivalent circuit than the Randles circuit. In particular, below T_{tr} it has a unique third resistor, R_3 which is parallel to **Q"**. Figure 4.3, shows the modified Randles circuit that was used to describe MUA at temperatures below T_{tr}.

It was not possible to fit the AC_EIS data of MUA below T_{tr} to the Randles circuit (Figure 4.2). A bad fit was obtained with parameters that did not have much physical meaning or errors obtained were too high. On addition of the resistor R_3 as shown in Figure 4.3, a good fit and of physical meaning was obtained. This resistance may be associated with hydrogen-bonding between the carboxylic head groups.

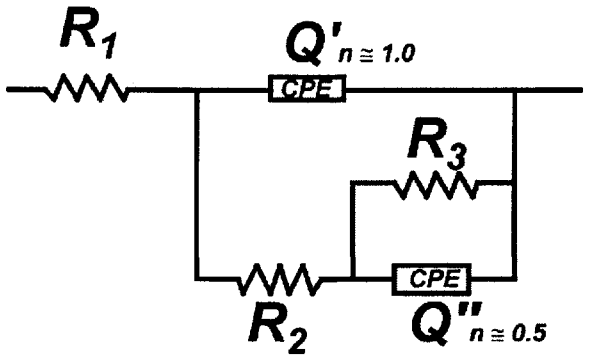

Figure 4.3. The modified Randles circuit – used to fit AC-EIS data for MUA modified electrode below T_{tr}.

The other possible explanation has been used by Fawcett et al.[284] attributing this resistive element arising from defects and pinholes. In this case the resistor R_3 is associated with ionic conductivity from solution through these defects and pinholes to the gold surface.

4.3.3. Circuit Elements

The equivalent circuit elements comprising the Randles circuit include a resistor, R_1, representing solution resistance, and another resistor R_2 representing activation resistance. In the modified Randles circuit, an additional resistor, R_3, is associated with the electrode modified with MUA below T_{tr}. **Q'** and **Q''** are constant phase elements (CPE). **Q'** is used to account for the frequency dispersion of the double layer capacitance with exponent n close to 1.00. For this studies the values obtained were within $0.89 < n < 1.00$). **Q''**

representing Warburg impedance is related to diffusion and associated with mass transport/diffusion. It has n values close to 0.50 but values of $0.46 < n < 0.51$ were obtained from the modeling studies.

4.4. Comparison of Temperature - Dependent behaviour of Self Assembled Monolayers and Langmuir-Blodgett Films on Gold

The temperature dependant behaviour of LB films and SAMs of alkanethiols on gold electrodes is compared below. The passivating behaviour of both types of monolayers of the alkanethiols HDM and ODM on gold electrodes was obtained using CV and AC-EIS with the aid of $[Fe(CN)_6]^{3-/4-}$ as a redox probe. In the case of SAMs, MUA was also studied in addition to HDM and ODM.

It is believed that any differences between LB films and SAMs may be attributed to the fundamentally different processes of film formation. SA is comprised of two processes, namely spontaneous chemisorption when the surfactant comes into contact with the desired substrate followed by molecular organization. The LB deposition process is a reversal of SA, namely molecular organization at the air-water interface (forming Langmuir films) followed by deposition unto the desired substrate by LB transfer[1] and chemisorption when the substrate is gold.

4.4.1. Room Temperature Behaviour of Films

From AC-EIS and CV data, the SAMs of HDM, ODM and MUA and the LB films of HDM and ODM on gold provide good blocking of $[Fe(CN)_6]^{3-/4-}$ from the electrode surface at room temperature.[90] In this case, the barrier properties of the monolayer coatings inhibit the electrode reaction of the redox active species. This can be observed by comparing the modified electrode response to that of a bare gold electrode.

Charge transfer processes at the electrochemical interface are strongly influenced by the nature of the electrode surface and the structure of the electrical double layer.[250,300] Thus they are often studied to gain information about a particular electrode surface, especially ones modified by organic layers, such as SAMs and LB films of alkanethiols.

Some researchers have indicated that CV studies of the $[Fe(CN)_6]^{3-/4-}$ redox marker may be useful in evaluating SAMs as barrier layers based on reduction in charge transfer or depression of the CV peak current relative to that of bare gold.[77,88,301,302] However, the depression of CV peaks cannot easily be used to distinguish between SAMs and LB films. AC-EIS is much more sensitive for this purpose. Therefore, AC-EIS is able to describe the features at the modified electrode-solution interface and distinguish between the fundamental differences in the film forming strategies of the SAMs and LB films.

4.4.2. Thermal Behaviour of Films

The effect of the monolayers on the redox activity of the probe molecule $[Fe(CN)_6]^{3-/4-}$ in solution was studied as a function of temperature. Inhibition of the probe molecule's redox activity was attributed to an impermeability of the monolayer to charge transfer processes, as was the case for room temperature. All films studied on gold show markedly different behaviour below and above a characteristic temperature ($\mathbf{T_{tr}}$) specific to each molecular species. This increase in observable redox activity above $\mathbf{T_{tr}}$ was attributed to an increase in the permeability of the monolayer, brought about by a phase transition. This phase transition was considered to arise from a change in molecular orientation. Variable temperature FT-IR,[303,304], X-ray diffraction[121], electrochemical studies[244,82] as well molecular dynamic simulations[305,306,307], indicate that the dynamic behaviour of the thiol monolayers indeed involves a phase transition, which depends on variables such as the chain length and terminal functional groups. The thermal behaviour of the modified electrodes was analysed by plotting either the reductive current (from CV data) or equivalent circuit elements (from AC-EIS data) versus temperatures at which electrochemical measurements were taken.

4.4.2.1. Determination of Transition Temperature from Electrochemical Data

From CV measurements, plots of thermograms of reductive current versus temperature were used to obtain T_{tr} values. Similarly, from AC-EIS measurements T_{tr} was determined by R_2, and **Q"** from thermograms of circuit elements versus temperature. The values are obtained from plots of the value of the circuit elements as a function of temperature, by drawing a tangent at the inflexion point in the curve. Where this tangent meets the temperature axis (where the circuit element is zero) gives T_{tr}. This is illustrated in Figure 4.4.

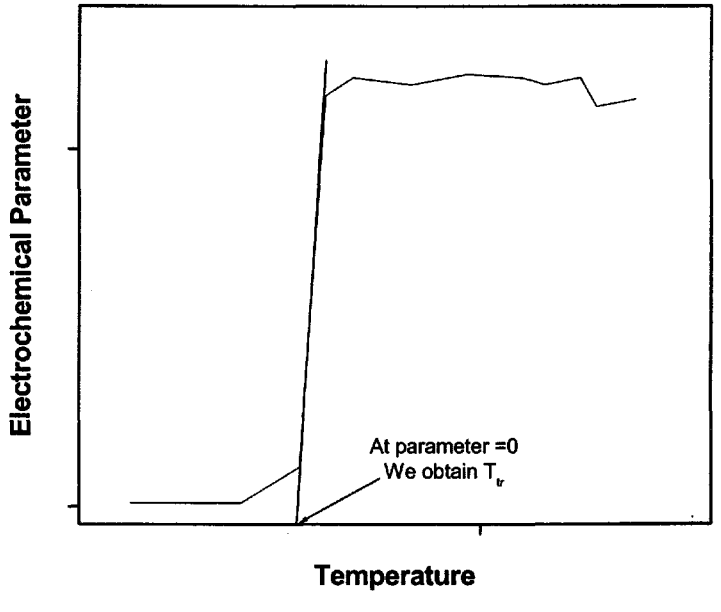

Figure 4.4. Demonstration of how to obtain T_{tr} from a thermogram of any electrochemical parameter versus temperature.

The value of T_{tr} from raw AC-EIS data is simply the temperature at which the whole impedance response changes markedly.

4.4.2.2. Cyclic Voltammetry - Thermograms from Reduction Current

The thermograms for the CV data were plotted as peak reductive current versus temperature. From the thermograms in Fig. 4.5, a transition temperature may be determined (as shown in Figure 4.4) at which the modified electrode properties change appreciably.

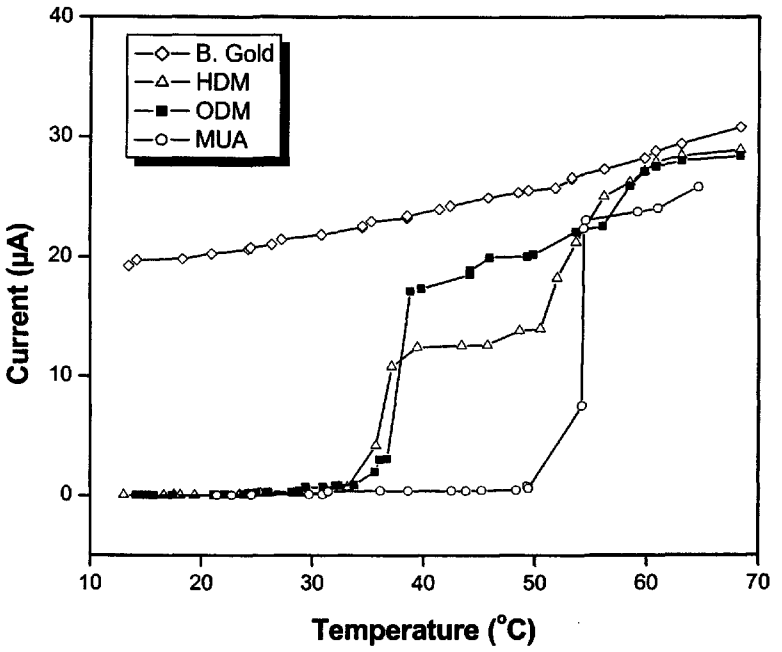

Figure 4.5. Thermogram showing the temperature dependence of the maximum reductive current from CV of SAMs in 3 mM $K_3Fe(CN)_6$ and 3 mM $K_4Fe(CN)_6$ / 0.1M KCl (ν= 50 mV s^{-1}).

The CV response is not very amenable to quantitative analysis, but the large increase in both Faradaic and nonfaradaic current as a monolayer is heated above T_{tr} is consistent with a complex permeability-linked process, which will depend upon the film structure, the diffusion coefficient of the redox couple in the monolayer, the interfacial resistance, and the relationship between these three parameters.[82] The reductive current i_{red} from the redox reaction is plotted as a function of temperature for all modified electrodes and for bare gold, after correcting for overpotential. Specifically, as the temperature is increased, E_{red} decreases in the bare gold response, and so the i_{red} values for the films are not taken at a single E_{red} value, but rather are taken at the E_{red} measured for bare gold at the corresponding temperature. (The peak potential at bare gold must be used because there is no peak in the current from the modified electrodes below T_{tr}.) From the first inflexion point in each thermogram, the T_{tr}, may be deduced as shown in Figure 4.4. Values of T_{tr} extracted from the electrochemical data are listed in Table 4.1 for each film ("From CV Data") for both LB films and SAMs of HDM and ODM.

It should be pointed out that the current of the modified electrodes after T_{tr} is very high and close to currents of the bare gold electrode. However it should be clearly stated that peak current from CV is not good on its own to explain this phase transition.[249,268] In the absence of desorption, which is proved from AC-EIS data, this behaviour can be attributed to non-linear diffusion in the SAMs above T_{tr} where the CV wave resembles that of an array of

ultramicroelectrodes arising from defect sites in the SAMs as temperature is increased.[248,249]

Figure 4.6 shows a thermogram of reductive current versus temperature for the LB-modified electrodes as measured by CV. Each monolayer has a characteristic temperature at which a distinct discontinuity in the current occurs as observed for SAMs of the same compounds.[244]

HDM and ODM have a second inflexion point (Figure 4.5) from which a second T_{tr} has been obtained. Values are also given in Table 4.1. The second inflexion is absent in SAMs of MUA (Figure 4.5) and in LB films of HDM and ODM on gold, as indicated in Figure 4.6.

It can be observed that the first T_{tr} values of the LB modified electrodes are lower than that of the corresponding SAMs. For each compound however, these T_{tr} values tend to be in agreement within experimental error, regardless of film type, strongly supporting the idea that the same transition is being effected in both types of monolayers. This transition was previously attributed to an order to disorder mechanism that increased the permeability of the SAM.[82] With similar results being observed for the SAMs and LB films in this work, it is still believed that an order to disorder mechanism is the most likely mechanism for the transition. Possible explanation from the similar values in currents above T_{tr} coud as stated ealier be due to non-linear diffusion[248,249] in the LB films.

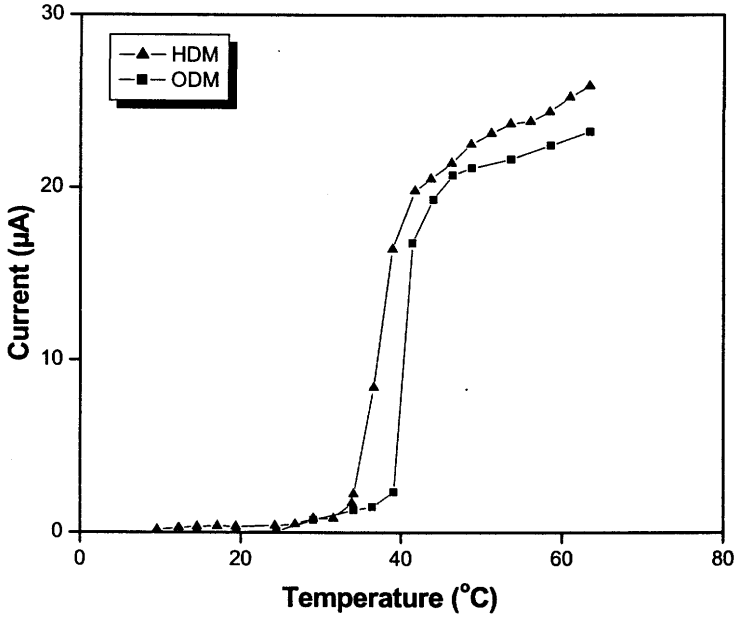

Figure 4.6. Thermogram showing the temperature dependence of the maximum reductive current from CV of LB films in 3 mM $K_3Fe(CN)_6$ and 3 mM $K_4Fe(CN)_6$ / 0.1M KCl (ν= 50 mV s^{-1}).

Table 4.1. Comparison of T_{tr} derived from CV for all modified electrodes from SA and LB technique.

Monolayer Species	Monolayer Type	Phase Transition Temperature T_{tr} (°C) From CV data		Normal Melting Point (°C)
		1st	2nd	
HDM	*SAMs*	*36.8 ± 0.5*	*42.5± 0.5*	18 –20
	LB	33.6 ± 0.7	*	
ODM	*SAMs*	*39.2 ± 0.5*	*48.5± 0.5*	31 – 35
	LB	38.6 ± 0.5	*	
MUA	*SAMs*	*53.6 ± 0.7*	**	46 – 50

*** - Not observed** **** - Not determined**

The lack of a second T_{tr} in the LB films of HDM and ODM can be attributed to the difference between their film forming process with that of the SAMs. From the thermodynamic point of view, the LB deposition process indicates entropy gains in the compressed system, attributed to the decrease in order of the interfacial water molecules. In the SA process, without this driving force, the intermolecular ordering must be exothermic, and must be driven entirely by entropy gains to the surroundings, which are not mechanically coupled to the intermolecular ordering. Thus, the chemisorption step in the SA process appears to be the limiting factor in the effectiveness of organized monolayer formation, undermining the integrity of the subsequent intermolecular organization by laying down an imperfect template. When intermolecular organization at the air-water interface precedes chemisorption through the LB deposition process, the resulting monolayers may maintain their high degree of order during chemisorption because of the nature of the LB technique. The higher degree of order in the LB films over the SAMs, makes it impossible to observe a second transition in the LB films.

Considering the absence of the second T_{tr} values for SAMs of MUA, it is likely due to the higher value of the first T_{tr} value arising from the carboxylic terminal head groups, and is therefore expected that the second T_{tr} may occur at a higher temperature that is outside the temperature range of this work.

The second T_{tr} values from the SAMs of HDM and ODM will be discussed when the DSC data is discussed.

4.4.2.3. Alternating Current-Electrochemical Impedance Spectroscopy - Thermograms from Circuit Elements

From the fitted data, the variation of the circuit elements as a function of temperature was analysed. The circuit elements were $\mathbf{R_1}$, $\mathbf{R_2}$, $\mathbf{R_3}$, **Q'** and **Q"** representing solution resistance, activation resistance, extra resistance in parallel to **Q"** attributed to hydrogen bonding network in MUA, CPE of the double layer capacitance and Warburg impedance, respectively.

4.4.2.3.1. Solution Resistance

The value of the solution resistance $\mathbf{R_1}$, is dependent on the solution concentration and temperature etc., and therefore the distance between the electrodes.[265,308] It was found to decrease steadily with increasing temperature for bare gold and all the modified gold electrodes, independent of the film. The trends in the decrease of the solution resistance is similar to that for the bare gold electrodes shown in Figure 4.7 and could be attributed to thermal motion. However, the modified electrodes have slightly higher values than bare gold, except at a temperature greater than 45°C. Ideally, the modified electrodes may have a significant effect on the solution resistance because the differences found may arise from variations in cell geometry, since distance between the RE and the modified electrodes may be slightly different from that of bare gold.[308] This trend is expected as it has also been observed by previous studies of

SAMs of alkanethiols on gold electrodes.[265] Alternatively, another reason may be decreased ionic mobility near the electrodes which make diffusion coefficients larger and may have resulted in higher solution resistances in the SAM modified electrodes.[100]

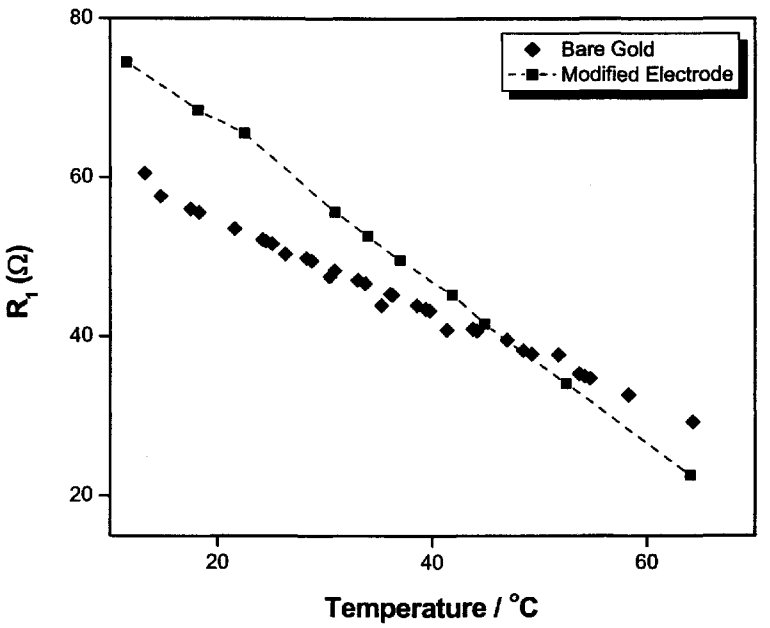

Figure 4.7. Temperature dependence of R_1 for bare gold and modified gold electrode.

4.4.2.3.2. Activation Resistance

R_2, decreased very gradually as temperature increased for bare gold, mainly due to thermal motion. The activation resistance R_2, is expected to vary inversely to the permeability towards ions for electrodes modified with HDM, ODM and MUA films. At lower temperatures R_2 is initially much higher than for

a bare gold electrode, most likely due to the resistance from the highly ordered monolayer. Above a characteristic temperature, T_{tr}, there is a considerable decrease in R_2 for each of these electrodes. This is attributed to a 2D phase transition in which the well-ordered and compact monolayer becomes less resistive, presumably through a loss of order in the monolayer, causing the permeability of the monolayer towards electrolyte and redox probe to increase. The thermograms for resistance R_2 versus temperature are shown in Figures 4.8 and 4.9 for SAMs and LB films, respectively.

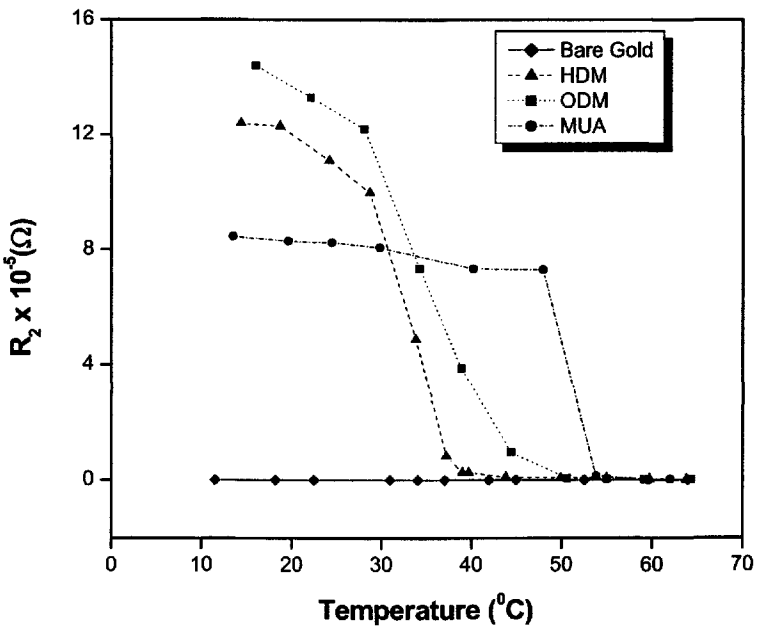

Figure 4.8. Temperature dependence of R_2 for SAM modified gold electrode.

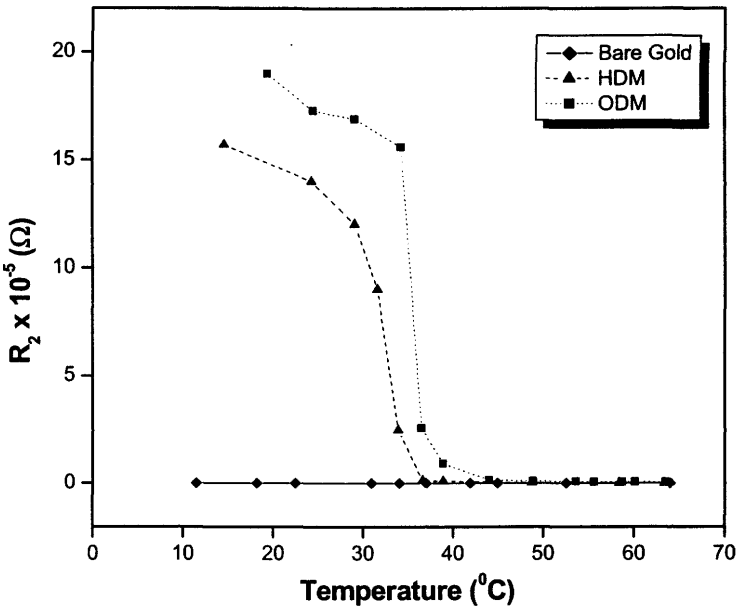

Figure 4.9. Temperature dependence of R_2 for LB modified gold electrode.

The T_{tr} values for the various circuit elements and raw AC-IS data is shown in Table 4.2. The T_{tr} values derived from R_2 follow the trend MUA > ODM > HDM in SAMs and ODM>HDM for the LB films. The trend is similar to that observed by CV. It is also worthy of note that the T_{tr} values of the LB films for R_2 are greater than that of the SAMs, implying that the LB films are likely to be of a higher order than the SAMs.

Generally, the values of T_{tr} were within 3 – 5 °C of each other regardless of method of film formation, which lends support to the argument that similar transition is being effected in both types of monolayers. This type of transition is from a state of order to disorder mechanism.

Table 4.2. Comparison of T_{tr} derived from circuit element R_2 for all modified electrodes from SA and LB technique.

Monolayer Species	Monolayer Type	Phase Transition Temperature T_{tr} (°C) (From Circuit Element R_2)
HDM	*SAMs*	*37.6 ± 1.0*
	LB	35.3 ± 0.5
ODM	*SAMs*	*43.4 ± 1.0*
	LB	36.9 ±0.5
MUA	*SAMs*	*53.5 ± 1.0*

Presumably the LB films are either more highly ordered or have fewer defect sites of bare gold with no bound sulphur (thiol). Likely formation of the Langmuir film before deposition to form an LB film is also known to eliminate grain boundaries and hence lesser defects than SAMs. If the transition occurring at T_{tr} occurs by the same order → disorder mechanism in both types of film (which is likely, given that the transition occurs at virtually the same temperature in both types of film), then above T_{tr}, both types of film should become equally disordered. In this case, any differences in the R_2 values can then be attributed to defect sites and probably thickness of the monolayers.

A comparison of the absolute R_2 values from LB films to those from SAMs is made in Table 4.3. This table lists an R_2 value below T_{tr} and one above T_{tr} for all films. Below T_{tr}, the R_2 values of LB films of HDM and ODM were about 30% higher than those for SAMs, suggesting that LB films of these

compounds have better electrode passivation and blocking properties before heating than the SAMs.

Table 4.3. Comparison of R_2 values from AC-EIS below and above T_{tr} for all HDM and ODM modified electrodes, including both those modified by SA and those modified by the LB technique.

Monolayer Species	Monolayer Type	Below T_{tr}		Below T_{tr}	
		$R_2 \times 10^{-5}$ (± 0.2) (Ω)	Temperature (°C)	$R_2 \times 10^{-5}$ (± 0.005) (Ω)	Temperature (°C)
HDM	*SAMs*	*12.4*	*14.4*	*0.0324*	*59.7*
	LB	**15.7**	**14.6**	**0.0648**	**58.4**
ODM	*SAMs*	*14.4*	*16.0*	*0.0393*	*59.1*
	LB	**19.0**	**19.4**	**0.0700**	**58.7**

Examining the values of R_2 above T_{tr}, it can be seen that the R_2 values for the LB films are now roughly twice as high as those for the SAMs. If these films have the same degree of permeability due to disorder, then the differences in these R_2 values must reflect differences in the number of defect sites, with the SAMs having more.

4.4.2.3.3. Extra Resistance in Modified Randles Circuit

The uniqueness of the MUA modified gold electrode occurs below T_{tr} when the MUA film was described with a third resistor, R_3, in parallel with **Q''** (the modified Randles circuit, Figure 4.3). The value of R_3 is

approximately 497 Ω at 13°C and decreases as the temperature is increased. R_3 approaches infinity at 30°C. This paramter is therefore removed above T_{tr} from the modified equivalent circuit and Randles circuit is used again to fit the datat. Fawcett et al.[284] attributed this to ionic conductivity of the SAM due to the defects and pinholes. However, the fact that the R_3 approaches infinity and does not exist above T_{tr} raises the question about the terminal carboxylic end groups. It is believed that this resistor may contribute to a hydrogen-bonded network of carboxylic acid end groups and water molecules, and is non-Faradaic in origin. If such a hydrogen-bonded network were to dissociate at around 30°C, this would cause a corresponding decrease in the resistance R_3 associated with this network. The cartoon in Figure 4.10 illustrates how the hydrogen-bonding network could be formed.

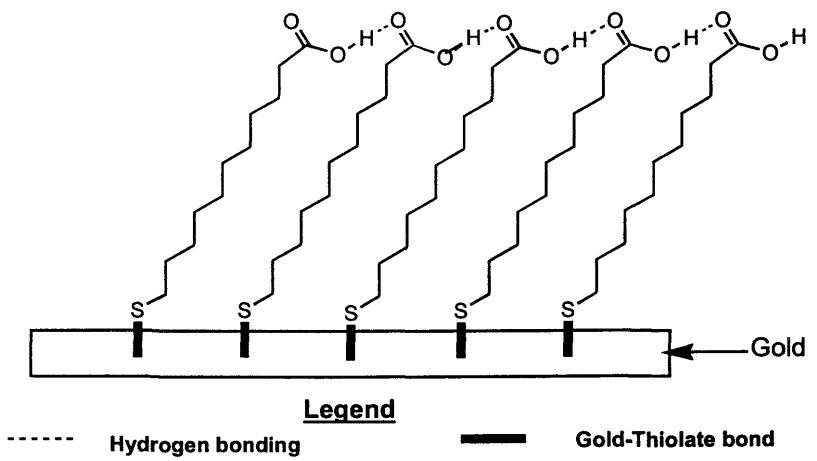

Figure 4.10. Illustration of the possible conformation of a hydrogen-bonding network arising from the terminal carboxylic acid groups in MUA.

The stability from this hydrogen-bonded network[2] could also account for the fact that the transition temperature (54.4 ± °C) is considerably higher than those of HDM and ODM even though these latter films have longer alkyl chains. MUA has a normal melting point of 46-50 °C, which is also considerably higher than the melting points of the two alkanethiols (see Table 4.1).

4.4.2.3.4. Constant Phase Element of the Double Layer Capacitance

The thermograms of **Q'** versus temperature are shown in Figures 4.11 and 4.12. Increasing temperature did not have any effect on the CPE of the double layer capacitance **Q'** of the bare gold electrode.

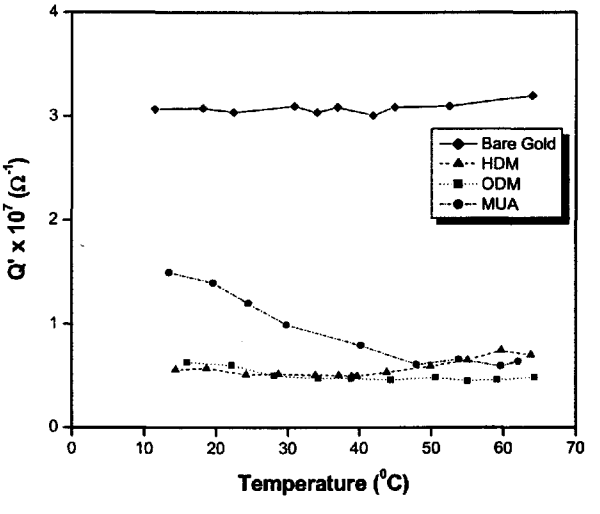

Figure 4.11. Temperature dependence of **Q'** for SAM modified gold electrode.

Also in the SAMs and LB modified electrodes for HDM and ODM, **Q′** values remained fairly constant with increasing temperature, with no significant inflexion at T_{tr} but were of a smaller magnitude than that of bare gold. This is expected because a smaller magnitude of **Q′** means a smaller value of the double layer capacitance. The observed values of the modified electrodes are consistent with a simple dielectric model in which the SAMs and LB films behave ideally as a capacitor.

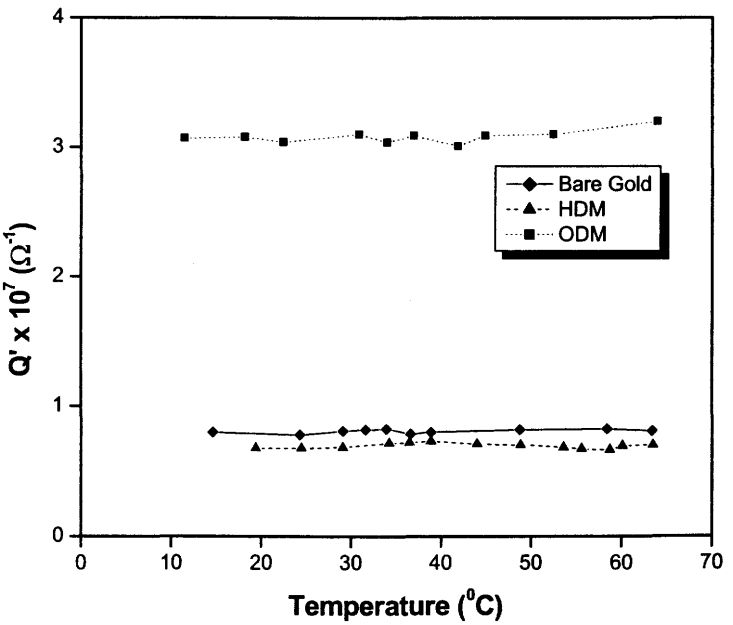

Figure 4.12. Temperature dependence of **Q'** for LB modified gold electrode.

Also, the **Q'** values for the SAMs and LB films of HDM and ODM have similar values. Therefore this suggests that the basic electrical structure of the

electrode-electrolyte interface in these systems is not greatly affected by the temperature-driven increase in film permeability or change in method of film formation. This lends support to the likely reason that long chain alkanethiols are enchored on the gold surface by the gold-sulphur bond, which is not easy to remove from the surface of the gold after chemisorption.

However, the CPE **Q'** of MUA was different. They were generally high and decreased as temperature increased (Figure 4.11). This is in marked contrast to **Q'** values for the alkanethiol systems, which show no particular change at T_{tr}. The latter systems present a hydrophobic, non – polar interface to the electrolyte solution, and so it might not be expected that the transition in the alkyl chains would have an effect on the double layer. On the other hand, the carboxylic acid films present a hydrophilic and polar interface to the electrolyte, possibly with a correspondingly larger influence on the double layer structure. In this case, if the hydrogen bonding network[2] explained earlier becomes disordered and insignificant as R_3 approaches infinity when the temperature is increased then disorder may start at T_{tr}. As can be observed from Figure 4.11, the **Q'** values become constant above 50°C, which is close to the T_{tr} value of MUA for raw AC-IS data (Table 4.7).

Table 4.4. Comparison of **Q'** values from AC-EIS below and above T_{tr} for all HDM and ODM modified electrodes, including both those modified by SA and those modified by the LB technique.

Monolayer Species	Monolayer Type	Below T_{tr}		Above T_{tr}	
		(Q'± .05) x 10^7 (Ω^{-1})	Temperature (°C)	(Q" ±0.05) x 10^7 (Ω^{-1})	Temperature (°C)
HDM	*SAMs*	*0.65*	*14.4*	*0.75*	*59.7*
	LB	**0.80**	**14.6**	**0.83**	**58.4**
ODM	*SAMs*	*0.63*	*16.0*	*0.72*	*59.1*
	LB	**0.68**	**19.4**	**0.67**	**58.7**

(n values for ***Q'*** is between 0.89 – 1.00)

A comparison of the absolute **Q'** values for SAMs and LB films below and above T_{tr} is shown in Table 4.4. Below and above T_{tr}, the magnitudes of the values of **Q'** are fairly constant for LB films for both HDM and ODM but that of the SAMs have values above T_{tr} slightly higher than those below T_{tr}. This difference is within experimental error and by comparison to the slight increase in **Q'** for bare gold, indicates that the difference is not significant.

4.4.2.3.5. Constant Phase Element of the Warburg Impedance

The Warburg constant phase element **(Q")** representing mass transport/diffusion is expected to improve through an increase in permeability of the film. The values for the monolayers HDM and ODM of SAMs and LB films show a pronounced change at the characteristic T_{tr} for each monolayer. The T_{tr}

values are shown in Table 4.5. They indicate that the values from the LB films are lower than that of the SAMs. This suggests that the SAMs may be more diffusive than the LB films since **Q"** may also represent diffusion.

Figures 4.13 and 4.14 show trends in **Q"** versus T for SA and LB films. In Figure 4.13, the values for the monolayers of HDM and ODM of SAMs and LB films show a pronounced change at a characteristic $\mathbf{T_{tr}}$ for each monolayer (Table 4.5). However increasing temperature did not have any significant effect on the **Q"** of bare gold electrode. If **Q"** represents mass transport/diffusion phenomena, then clearly the mass transport properties of the two phases are markedly different for the modified electrodes. This supports the notion of a transition from an ordered, impermeable phase to a disordered and much more permeable one.

Table 4.5. Comparison of T_{tr} derived from circuit element **Q"** for all modified electrodes from SA and LB technique.

Monolayer Species	Monolayer Type	Phase Transition Temperature T_{tr} (°C) (From Circuit Element Q")
HDM	*SAMs*	*34.0 ± 1.0*
	LB	**32.0 ± 1.0**
ODM	*SAMs*	*39.0 ± 1.0*
	LB	**34.0 ± 1.0**
MUA	*SAMs*	*49.5 ± 1.5*

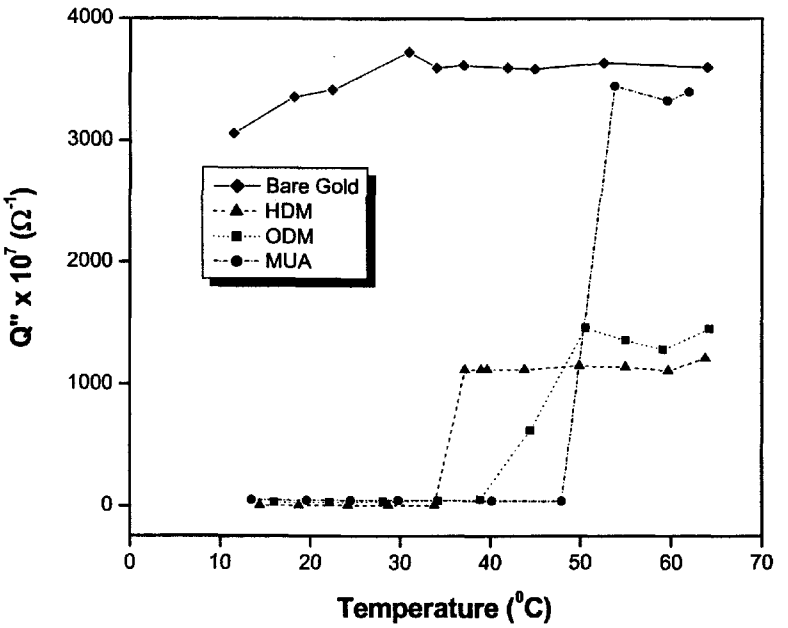

Figure 4.13. Temperature dependence of **Q"** for SAM modified gold electrode.

The trend in the values for **Q"** versus T for the LB films of HDM and ODM are very similar to that of the SAMs of HDM and ODM. This suggests that the films are all undergoing the same kind of transition in the disordering of the alkyl chains. However, the **Q"** values for SAMs modified by MUA increase drastically at T_{tr}, (Figure 4.13) and therefore shows a different behaviour at T_{tr} than for HDM and ODM films.

The presence of defects above T_{tr} from the films will also enhance diffusion and mass transport. In this case, the unusual high **Q"** values from MUA modified electrodes above T_{tr} could be attributed to the fact that it has more defect sites than HDM and ODM. Probably its amount of pinholes

behaving as an array of microelectrodes due to the phenomenon of non-linear[248,249] diffususion is substantial.

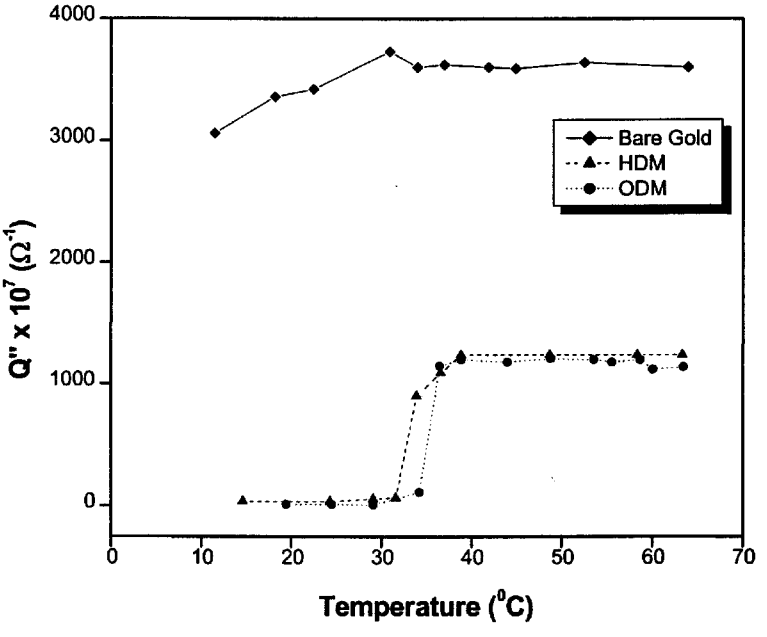

Figure 4.14. Temperature dependence of **Q"** for LB modified gold electrode.

Above T_{tr}, mass transport properties play a significant role in determining the overall impedance, whereas below T_{tr}, the contribution from **Q"** is small as shown by the MUA plots in Figures 3.18 and 3.19. This is largely because, at lower temperatures, the resistance element R_3 representing the highly organized hydrogen bonded network dominates.

Comparison of the absolute values of **Q"** for SAMs and LB films below and above T_{tr} is shown in Table 4.6

Table 4.6. Comparison of **Q"** values from AC-EIS below and above T_{tr} for all HDM and ODM modified electrodes, including both those modified by SA and those modified by the LB technique.

Monolayer Species	Monolayer Type	Below T_{tr}		Above T_{tr}	
		Q" x 10^7 (± 1.0)(Ω^{-1})	Temperature (°C)	Q" x 10^7 (± 50)(Ω^{-1})	Temperature (°C)
HDM	*SAMs*	*32.7*	*14.4*	*1110*	*59.7*
	LB	**34.9**	**14.6**	**1240**	**58.4**
ODM	*SAMs*	*27.6*	*16.0*	*1280*	*59.1*
	LB	**19.00**	**19.4**	**1200**	**58.7**

(n values for ***Q"*** is between 0.46 – 0.51)

Below T_{tr}, **Q"** is small for all species compared to the bare gold electrode. The values for the ODM films indicate a more compact monolayer in both SAMs and LB films than the corresponding HDM monolayers. This is expected as monolayer of longer chain molecules are known to block an electrode better than a shorter chain by observing their activation resistances alone.

The values of **Q"** above T_{tr} are lowest for the SAMs of HDM and highest for those of ODM, however, that of the LB films has the lowest for HDM and highest for ODM. These differences are insignificant within the limits of experimental error, indicating that above T_{tr} both the SAMs and LB films are undergoing similar phase behaviour arising from similar diffusive and mass transport properties.

4.4.2.3.6. Comparison of Absolute Transition Temperature Values

From AC-EIS measurements, the transition temperatures as determined by **R_2, Q"**, and raw AC-EIS data are summarized in Table 4.7. The values are obtained from plots of the value of the circuit element as a function of temperature by drawing a tangent at the inflexion point of drastic change in the curve. The intercept of the tangent with the temperature axis (when the circuit element is zero) gives **T_{tr}**, as was done for thermograms of CV data.

Table 4.7. Comparison of T_{tr} derived from raw and analysed AC-EIS data for all modified electrodes from SA and LB technique.

Monolayer Species	Monolayer Type	Phase Transition Temperature T_{tr} (°C)		
		AC-EIS Data	Equivalent Circuit Elements	
			Q"	R_2
HDM	*SAMs*	*36.8 ± 0.5*	*34.0 ± 1.0*	*37.6 ± 1.0*
	LB	33.6 ± 0.7	32.0 ± 1.0	35.3 ± 0.5
ODM	*SAMs*	*39.2 ± 0.5*	*39.0 ± 1.0*	*43.4 ± 1.0*
	LB	38.6 ± 0.5	34.0 ± 1.0	36.9 ±0.5
MUA	*SAMs*	*53.6 ± 0.7*	*49.5 ± 1.5*	*53.5 ± 1.0*

It can be observed from Table 4.7 that the **T_{tr}** values from **Q"** are slightly lower than those from **R_2**. This indicates that the response of mass transport and diffusion through the electrolyte solution to changes in temperature occurs at a slightly different temperature than the response of the activation resistance

on the surface of the electrode. This suggests that, as the temperature is raised, first the chains open up and allow electrons to penetrate by diffusion to the solution/electrode interface, as indicated by the change in Q". [248]. As the temperature is increased further, the gold surface itself becomes more accessible towards electron transfer, as indicated by the subsequent change in R_2.

All of the T_{tr} values determined from AC-EIS parameters are slightly lower for LB films than for SAMs, although errors for all values are approximately the same. The difference may be due to possible defects in the films obtained by the SA technique, as generally the absolute R_2 values are higher in the LB films than the SAMs both below and above T_{tr} (section 4.4.2.3.2).

The transition temperatures as determined from the plots of equivalent circuit elements versus temperature for HDM and ODM films produced by the SA technique (Figures 4.11 and 4.13) and the LB technique (Figures 4.12, and 4.14) indicate a dependence on alkyl chain length parallel to that exhibited by melting points. In general, a longer alkyl chain will melt at higher temperatures due to increased VDW forces between chains. The higher T_{tr} for the longer chain thiol is believed to arise from an analogous phenomenon in two dimensions. In both species, the melting point, a bulk property, is lower than the transition temperature. This is attributed to the higher degree of order in the monolayers relative to the bulk materials.

4.5. Langmuir-Blodgett Films on Glassy Carbon

LB films of ODM and HDM were successfully deposited on glassy carbon electrodes to determine the role of chemisorption in defining the properties of monolayers. These films are presumed to be physisorbed films because there is no possibility of covalent bonding to the glassy carbon electrode surface. This is in contrast to alkanethiol films on gold that are assumed to chemisorb through the gold-sulphur bond. The reason for forming these films was to compare the behaviour of these films to that of SAMs and LB films of the same molecules on gold electrodes. Thus any difference between films on glassy carbon and films on gold could be attributed to the effect of physisorption versus chemisorption.

The behaviour of the physisorbed films was different from the chemisorbed films as there was no sudden change in circuit parameters or CV responses at a characteristic temperature.

It is interesting to note that the films of HDM and ODM on glassy carbon showed no significant difference in response for either the CV or the AC-EIS data. Figure 4.15 shows CVs of modified glassy carbon electrodes with both HDM and ODM at room temperature. The results are very different from the LB films of HDM and ODM where the addition of just two methylene carbons showed a marked difference in both CV and AC-EIS data. It appears that these presumed physisorbed systems are not ordered enough to show a phase change.

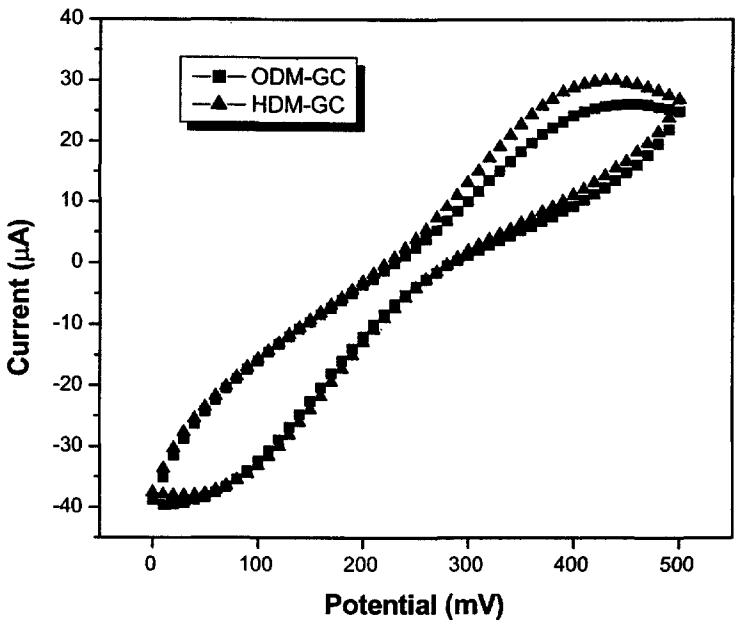

Figure 4.15. Comparison of CV at 50 mV s^{-1}.of LB films of HDM and ODM in 3 mM $K_3Fe(CN)_6$ and 3 mM $K_4Fe(CN)_6$ / 0.1M KCl.

4.5.1 Cyclic Voltammetry of Bare and Modified Glassy Carbon

The CV of the redox couple $[Fe(CN)_6]^{3-/4-}$ measured with bare glassy carbon and ODM-modified glassy carbon electrodes is shown in Figure 4.16. It is seen that both the Faradaic and non-faradaic currents of the modified electrodes are decreased relative to bare glassy carbon even though the film is not completely passivating as in LB films[133] and SAMs of alkanethiols[77,77,78,166,166,244] on gold. This reveals that glassy carbon electrode is a poor substrate for deposition of thiols.

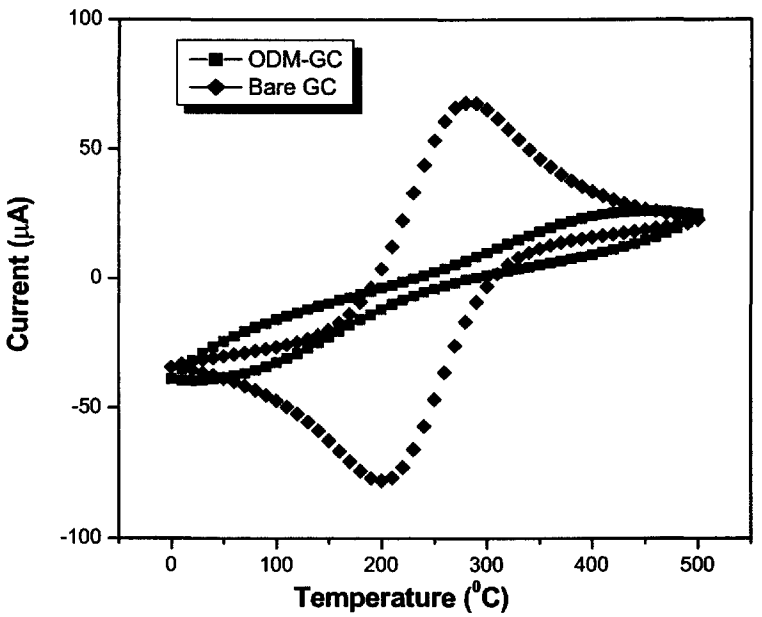

Figure 4.16. Comparison of CV at 50 mV s^{-1} of bare glassy carbon and LB film of ODM in 3 mM $K_3Fe(CN)_6$ and 3 mM $K_4Fe(CN)_6$ / 0.1M KCl.

This also suggests that chemisorption is necessary for the formation of a compact and dense monolayer.[309] This poor barrier action is expected, because the most effective barrier against $[Fe(CN)_6]^{3-/4-}$ for modified glassy carbon electrodes has been achieved by oxidative procedures,[103,13] and also by electrochemical reduction.[309,309,310]

Figure 4.17 shows a thermogram of reductive current versus temperature for the ODM-modified glassy carbon electrode and for a bare glassy carbon

electrode as measured by CV. It can be seen that the current increases steadily with increasing temperature for both bare glassy carbon electrodes and its ODM-modified glassy carbon electrodes.

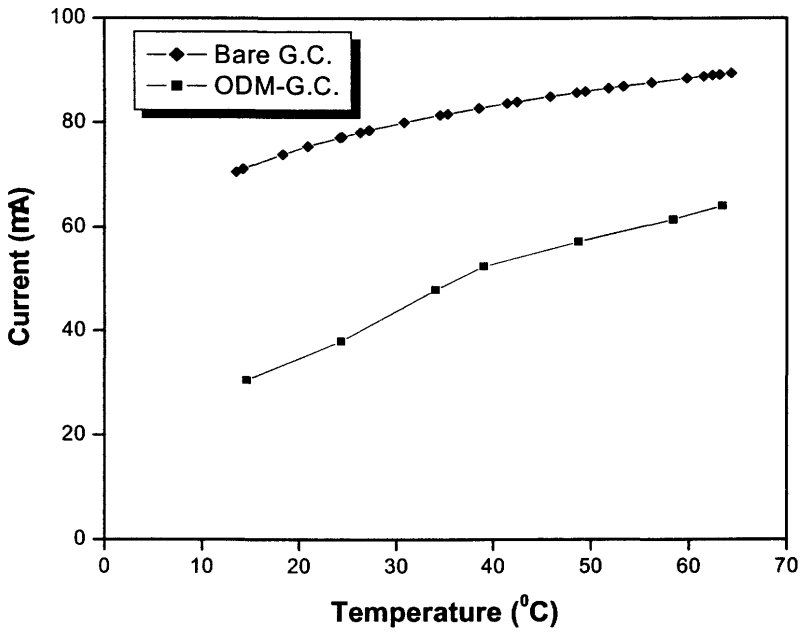

Figure 4.17. Thermogram showing the temperature dependence of the maximum reductive current from CV of bare glassy carbon and LB film of ODM on glassy carbon in 3 mM $K_3Fe(CN)_6$ and 3 mM $K_4Fe(CN)_6$ / 0.1M KCl (ν= 50 mV s^{-1}).

There is clearly no abrupt temperature induced modification of the physisorbed film, suggesting no phase transition leading to permeability. This is different from temperature–dependant permeability behaviour profiles observed for physisorbed phosphatidylcholine lipid vesicles.[311] It is also different from chemisorbed SAMs[244] and LB films.[82,133] It is likely that this method of deposition of an LB film on glassy carbon electrodes forms films that have more

disorder in the film than that of the vesicles and the chemisorbed SAMs and LB films.

HDM did not show any different behaviour from the ODM modified glassy carbon electrodes.

The physisorbed films of HDM and ODM on glassy carbon are different from reported work of physisorbed phosphatidylcholine lipid vesicles.[311] A possible explanations for the difference between the two physisorbed systems of HDM and ODM on glassy carbon in this studies and and reported work may be due to the size and the dimensionality in lipid vesicles system as opposed to an ordinary long chain alkanethiol. Surely organization of vesicles and the aggregates they may form, its geometry and interactions[5] may be different and will not be suitable to compare the behaviour of these alkanethiols to the vesicles even on the same substrates.

4.5.2 Alternating Current-Electrochemical Impedance Spectroscopy of Bare and Modified Glassy Carbon

AC-EIS measurements can be used to evaluate the effect of films on the kinetics of a redox reaction at a glassy carbon electrode[309] just as for gold electrodes. Figures 3.35 and 3.36 present the complex impedance plots for a bare glassy carbon electrode at room temperature and ODM-modified glassy carbon electrodes at various temperatures from 14.6°C to 63.4°C at a potential

of 0.25V in the presence of 3mM $[Fe(CN)_6]^{3-/4-}$. The plot in Figure 3.36 is characterized by a semicircle at high frequency and a low frequency Warburg line. Unsurprisingly this behaviour is similar to a bare gold electrode shown in Figure 3.6. The modified glassy carbon electrode data also show both the semicircle, which is pronounced, and the Warburg line which is not very pronounced (similar to the bare glassy carbon). The impedance data for both bare and modified glassy carbon electrodes were analyzed by modelling the raw AC-EIS data with the Non-Linear Least Squares (NNLS) fit using the Randles Circuit (Figure 4.2) in a manner similar to that for LB films of HDM and ODM on gold.

The results obtained have been plotted as thermograms of the equivalent circuit elements versus temperature. $\mathbf{R_1}$, which is the solution resistance, was found to decrease with increasing temperature for bare glassy carbon and for the electrodes modified with ODM. This is similar in trend but not in magnitude to the responses for bare gold and the alkanethiol-modified electrodes[244] shown in Figure 4.7.

The semicircle from the Nyquist plots (Figures 3.35 and 3.36) corresponds to a parallel combination of the charge transfer resistance, $\mathbf{R_2}$ (activation resistance) and the double layer capacitance **Q'**, whilst the linear response is related to the mass transport **Q"**. As the temperature increases, the semicircle decreases.

Quantitatively, perhaps an increase in the semicircle from the bare glassy carbon to the ODM-modified glassy carbon indicates that the electrode kinetics becomes slower as the glassy carbon is modified with ODM. This trend is shown in Figure 4.18. In this case the charge transfer resistance, R_2, increases dramatically following modification of the glassy carbon electrode. A decrease in R_2 of the modified electrode is observed when temperature is increased but is not sufficiently significant to approach values similar to the bare glassy carbon and, therefore, does not increase the electrode kinetics to magnitudes comparable to that of bare glassy carbon. The decrease may be due to thermal motion as may be expected in an activation process.[88,157,312]

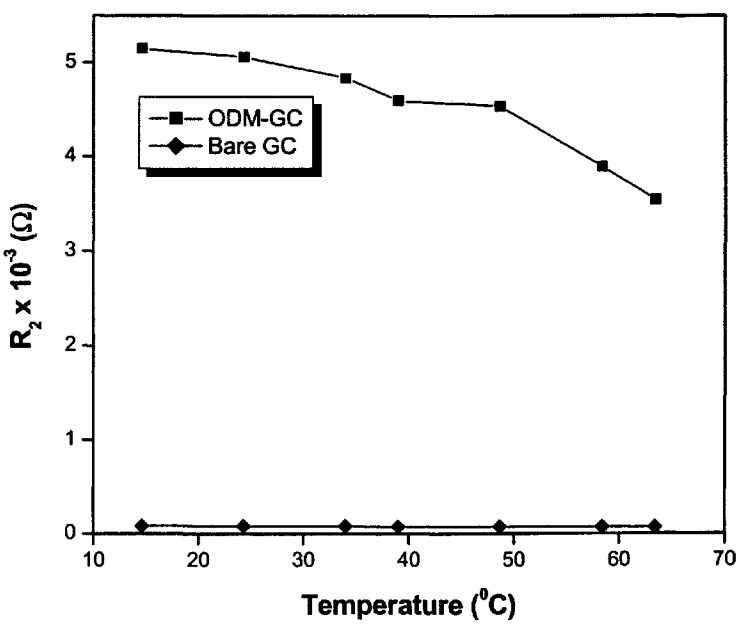

Figure 4.18. Temperature dependence of R_2 for bare glassy carbon and ODM modified glassy carbon electrode.

The CPE of the double layer capacitance **Q'**, is expected to decrease as the glassy carbon is modified with ODM, as the ODM increases the thickness of the double layer and reduces **Q'** drastically. This trend is exhibited in Figure 4.19. Temperature did not have any significant effect on either the bare glassy carbon or the modified electrodes. This is similar to observations for bare gold and the modified gold electrodes of HDM and ODM for both SAMs[244] and LB films.[133] It should be noted that the CPE was used instead of a pure capacitor to account for the effect of microscopic surface roughness and inhomogeneity of the surface on electrode kinetics.

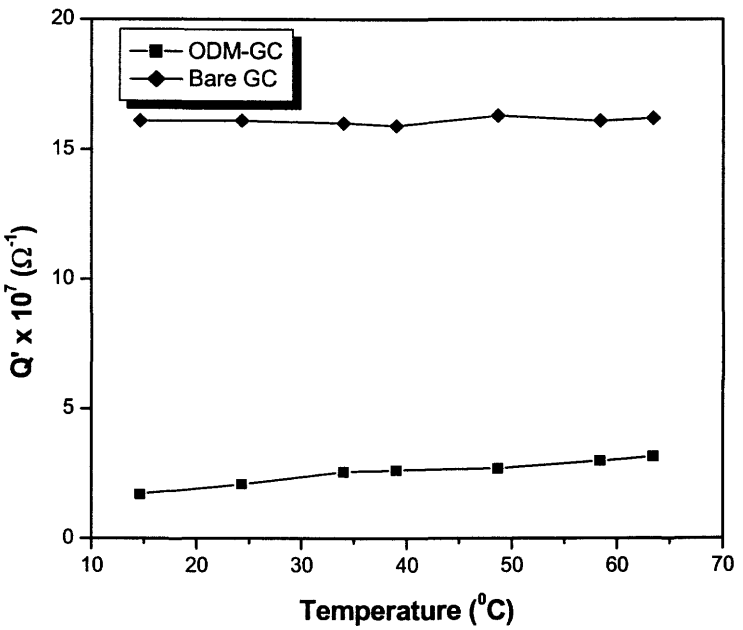

Figure 4.19. Temperature dependence of **Q'** for bare glassy carbon and ODM-modified glassy carbon electrode.

The increase in temperature did not affect the CPE of the Warburg mass transport/diffusion as can be seen from Figure 3.35 for bare glassy carbon. The presence of an adsorbed layer on the glassy carbon reduces the mass transport/diffusion values significantly, as illustrated by Figure 3.36, for ODM-modified glassy carbon. Obviously, when electrode transfer kinetics is slowed down due to high resistance values, mass transport/diffusion of ions in a charge transfer process must also be inhibited. Figure 4.20 shows this trend where the mass transport/diffusion of the bare glassy carbon is about 50% higher than ODM-modified glassy carbon electrode.

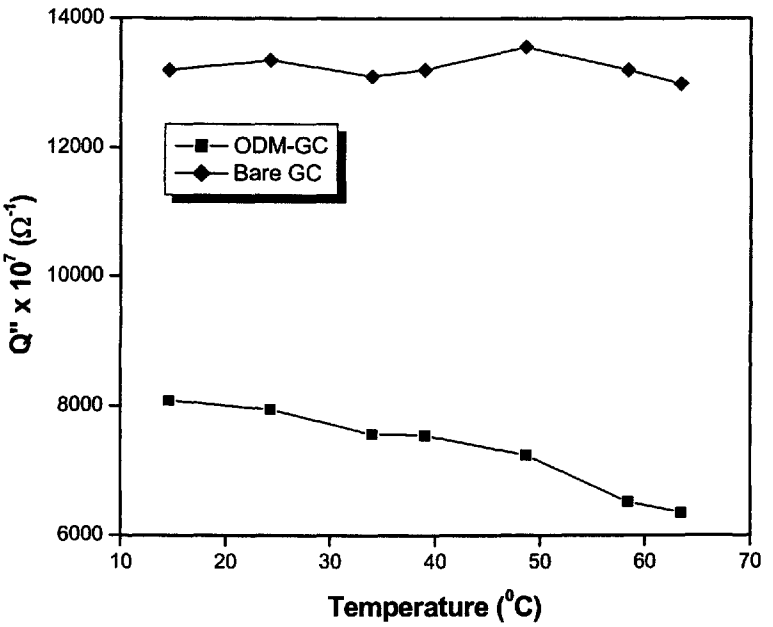

Figure 4.20. Temperature dependence of **Q"** for bare glassy carbon and ODM modified glassy carbon electrode.

Surprisingly, the values of **Q"** for ODM-modified glassy carbon electrode seem to decrease as temperature increases. Ideally it is expected that **Q"** will increase with increase in temperature and thermal motion[61] as is the case in LB films of ODM on gold. This suggests that the absence of chemisorption in the LB films of ODM on glassy carbon [157,312]could be a factor in this unusual behaviour of **Q"** with temperature for the ODM-modified glassy carbon electrodes.

In general, the behaviour of the circuit elements as a function of temperature revealed no temperature dependant phase transition as seen in the LB films of ODM on gold. This trend is consistent and agrees with the CV data obtained earlier on.

HDM-modified glassy carbon was very similar to ODM-modified glassy carbon electrodes.

4.6. Thermal behaviour of Three-Dimensional Alkanethiol-Capped Gold Colloids

Alkanethiol-capped gold colloids are self-assembled alkanethiolate monolayers on spherical metal surfaces achieved by the synthesis of alkanethiol-stabilized gold colloids.[110,273] They are 3D, spherical and provide an analogous system (albeit with a different geometry), to 2D SAMs and LB films,

formed on planar metal surfaces. DSC and ^{13}C and ^{1}H NMR have been used in this work to study the alkanethiol-capped gold colloids of HDM and ODM in the context of the preceding electrochemical studies.

The 2D SAMs and LB films have limitations on the applied techniques that can be circumvented by the 3D analogues.[36,119] Some of the techniques being DSC and NMR. The aim of this work was to use DSC and NMR studies on the 3D SAMs to correlate results of the 2D SAMs and LB films.

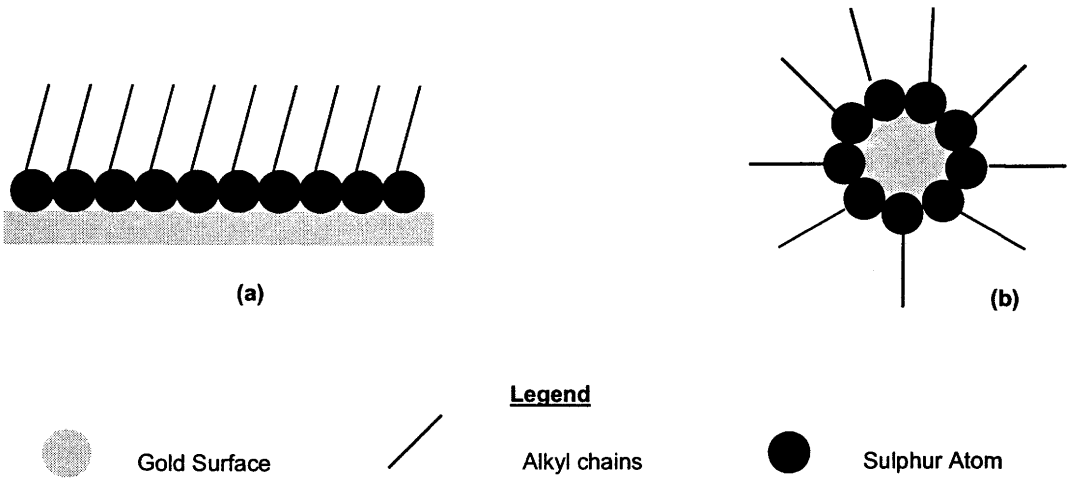

Figure 4.21. (a) Planar geometry of the SAMs and LB films of alkanethiols on gold electrodes and (b) Spherical geometry of the alkanethiol-capped gold colloids.

The cartoon in Figure 4.21, illustrates the contrasting geometry of the spherical colloids, and the planar SAMs and LB films. Both of them are chemisorbed to the surface of gold atoms by gold-thiolate bonds. However, due to the different geometries, the planar systems are expected to have the alkyl chain parallel and equally spaced from each other at the same tilt angle, while

the spherical systems have the distances between the alkyl chains increasing from the core to the end of the chains. In the case of the spherical systems, the end groups of a shorter alkyl chain will be closer to each other than the end groups of a longer alkyl chain.

From FT-IR measurements[279] we can obtain insight into the structures of 3D SAMs on metal colloids.[20,23,24,40,42,86,116,288] FT-IR data is discussed here with respect to the interpretation of how these systems orientate when they are free thiols and when they form 3D systems (alkanethiol-gold capped colloids).

Examination of the C-H and C-C stretching regions in Figures 2.5 and 2.6 provides information regarding the orientation, order and packing of these systems.[39] Analysis of the C-H stretching region may perhaps be the most informative. Consider for example, the C-H stretches of a model hydrocarbon such as polyethylene, with antisymmetric (ν_{as}) and symmetric (ν_s) methylene stretches as relatively broad bands at (ν_{as}) (CH_2) =2928 cm^{-1} and (ν_s) (CH_2) =2856 cm^{-1} when the polymer is dissolved in solution (i.e., randomly oriented and poorly packed). However, in crystalline form, these bands sharpen and shift to (ν_{as}) (CH_2) =2920 cm^{-1} and (ν_s) (CH_2) =2850 cm^{-1}. [313] Thus from the FT-IR spectra of 3-D SAMs, broad bands at high wavenumbers are interpreted to indicate poorly ordered chains having many gauche defects, while sharp bands at lower wavenumbers indicate relatively ordered chains having predominantly trans zigzag conformations.[313]

Some of the useful information from Figure 2.5 and 2.6 has been compiled in Table 4.8.

Comparison of the absorption frequencies for free alkanethiols and alkanethiol-capped gold colloids reveal a detectable ordering in the colloids relative to free alkanethiols, as indicated by the sharper bands (Figures 3.45 and 3.46) and shifting of the absorption bands to lower wavenumbers for the colloids.

Table 4.8. Comparison of FT-IR antisymmetric (ν_{as}) and symmetric (ν_s) methylene stretches for HDM, ODM and their corresponding alkanethiol-capped gold colloids.

Assignment	HDM	HDM-Au	ODM	ODM-Au
	Absorption Bands (cm^{-1})			
$\nu_{as} - CH_2$	2922	2919	2922	2920
ν_s- CH_2	2852	2849	2851	2850

Further support for the order in the 3D SAMs in the solid state was indicated by the appearance of twisting-rocking and wagging progression FT-IR bands between 1097 and 1261cm^{-1}. Furthermore, the sharp scissoring band of the methylene groups appears at 1467 cm^{-1} for both HDM-Au and ODM-Au whereas in free HDM and ODM it is found at 1465 cm^{-1} and 1463 cm^{-1} respectively, indicating lower wavenumbers in the colloids and more ordered chains in them.

4.6.1 Differential Scanning Calorimetry of Colloids

The phase behaviour of thiol derivatized colloids, has previously been characterized by DSC.[36,86,272] The phase behaviour of the thermograms shown in Figures 3.39 and 3.40 both indicate that HDM-Au and ODM-Au in the solid state undergo distinct phase transitions, which can be associated with reversible disordering of the alkyl chains.[119] From Table 3.5, the peak temperature was found to increase with increase in chain length from HDM (16 carbons) to ODM (18 carbons). This trend strongly parallels that seen in other materials undergoing gel-to-liquid crystalline transitions, such as diacylphospholipid vesicles.[311,314] The DSC peak maximum measured for HDM-Au and ODM-Au are close to the main transition temperatures of n-diactylphosphatidylcholines of equivalent chain length.[315] However, it is important to note that whereas the gel-to-liquid crystalline transitions in lipid bilayer membranes occur over a short range of temperature, that of the alkanethiol-gold system is relatively broad (Figures 3.39 and 3.40) for each sample. This may reflect either the existence of a disordered liquid-like chain population or the occurrence of chain motional processes that accompany phase transition. The broadness of the transition may also be caused by poor bulk crystallization of the alkanethiol-gold system.

4.6.1.1. Behaviour of Hexadecanethiol-Capped Gold Colloids

The sample Au-HDM exhibited a very small irreversible peak at 39.9°C during first heating, but in the second heating a sharp quasi-reversible peak corresponding to a phase transition was observed at 48.2°C (Figure 3.39). In the third heating the peak (now at 48.4°C) became higher. This behaviour is quite unusual because, it would have been expected that with the small difference in temperatures which could be more or less an insignificant experimental error, both peaks from the second and third heatings should have been the same. There may be therefore some further rearrangements. The very small irreversible peak in the first heating (39.9°C) has an ΔH value of the order 2.5 Jg^{-1}. This may indicate that, in the freshly prepared sample, there is no tight arrangement of the thiol chains and therefore the small ΔH value could correspond to the rearrangement of the methyl head groups. In addition, there is no indication of a first order phase transition corresponding to the "melting" of the alkyl chains. However, such a phase transition is observed in the second heating. This suggests that a tight arrangement of the alkyl chain is established only during the first cooling/heating cycle. As seen from the values of ΔH (Table 3.5) and also from Figure 3.39, the peak in the third heating is greater than the peak in the second heating. The onset and peak temperatures of the peaks from the second and third heatings are practically the same. Generally we can say that in the sample Au-HDM, the close packed arrangement is induced by

successive heating/cooling cycles, so that the ΔH of the transition from close packed to disorder increases over successive cycles.

4.6.1.2. Behaviour of Octadecanethiol-Capped Gold Colloids

The sample Au-ODM exhibited quasi-reversible peaks in all heatings. This is shown in Figure 3.40. The shape of the peaks and the characteristic temperatures in the first (55.8°C) and second (54.0°C) heating are quite different which suggests a rearrangement of the thiol chains during first heating. In contrast it is seen from the values of ΔH in Table 3.5 and also from Fig.3.40 that the peaks in the second (54.0°C) and third (53.9°C) heating are practically the same implying that the rearrangement is finished after the first heating, and thus further heating/cooling cycles are reversible. It is worthy to note that the first, irreversible peak observed in Au-HDM was not observed in Au-ODM. This could be explained by the difference in the structure of the alkanethiol of HDM and ODM, namely the distance of the methyl terminal group from the spherical gold nucleus of the colloids. With an increased distance of the ODM chains from the core metal compared to the shorter HDM chains it is very likely this irreversible peak seen in Au-HDM was difficult to detect in Au-ODM by DSC.

4.6.1.3. Comparison of Differential Scanning Calorimetry Thermal Behaviour to Electrochemical Behaviour of Self-Assembled Monolayers and Langmuir Blodgett Films

The transition temperatures observed by DSC for Au-HDM and Au-ODM are much higher than those seen by electrochemical methods. However, CV had revealed a set of higher temperature transitions in SAMs of HDM and ODM. These are listed in Table 4.9.

Table 4.9. Comparison of T_{tr} derived from CV for SAMs and from DSC for alkanethiol capped gold colloids.

Method	Species	Transition Temperature T_{tr} (°C)	
		1st	2nd
CV	HDM	36.8 ± 0.5	42.5± 0.5
	ODM	*39.2 ± 0.5*	*48.5± 0.5*
DSC	HDM	39.9 ± 0.2	48.2± 0.2
	ODM	*	***54.5****± 0.5*

*** - Not observed**

In the original thermogram of reductive CV current versus temperature (Figure 4.5), there is a second high temperature inflexion point that was initially not understood.[244] However, the transition temperatures recorded by DSC

corresponded very well with those unexplained high temperature inflexion points observed by CV.

If the two inflexion points in the CV data correspond to two different transitions, what then are the two transitions? The DSC detects two transitions in Au-HDM (one irreversible) but only one in Au-ODM (reversible). This could be because the system examined by the DSC experiments is not the same as the SAMs investigated by CV. Specifically, the alkanethiol-capped gold colloids are 3D[22,23,119] and spherical while the SAMs are known to be 2D and planar.[2] The cartoon of Figure 4.22 illustrates the difference.

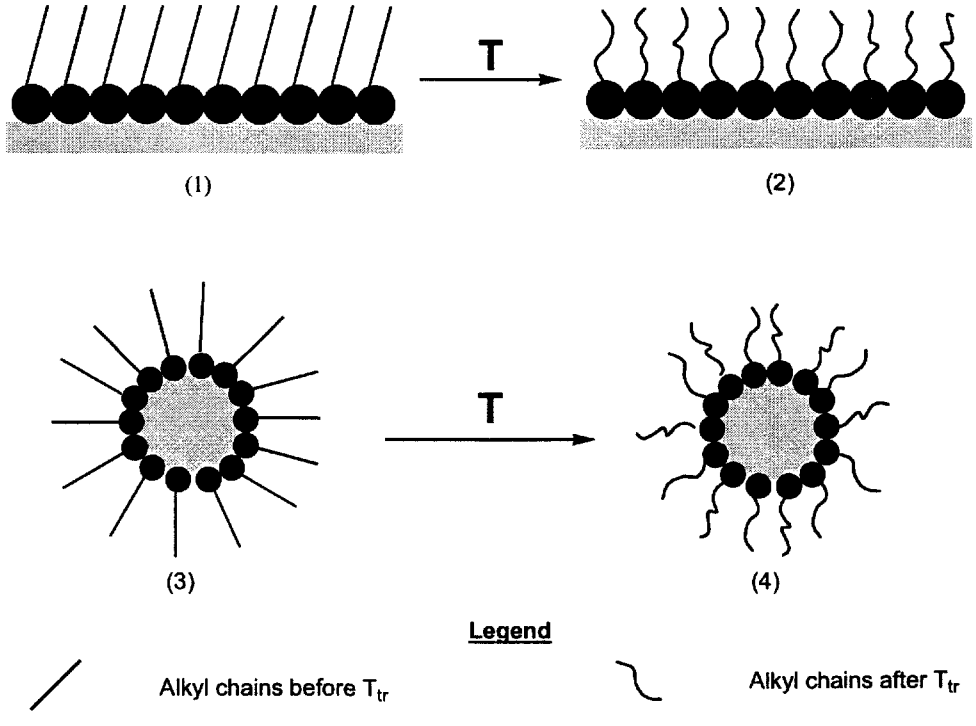

Figure 4.22. Cartoon to show the difference between the planar systems of SAMs and LB films of alkanethiols and spherical systems of alkanethiol-capped gold colloids.

If we assume that the lower temperature transition is one that occurs only in the Au-HDM but not Au-ODM for DSC studies, then it could be attributed to head group interactions in the spherical system. With ODM having a longer alkyl chain length than HDM, the distance of its end gropus would be further apart from the gold substrate surface and also less interaction between adjacent headgroups because, the longer the chain, the further apart the end groups will be from each other as illustrated by Figure 4.22. It is worthy of note that this makes it difficult for DSC experiment to detect the first (irreversible) transition in the ODM system. Furthermore, even though this is detected in Au-HDM, its small energy points more to why in a longer chain like ODM it was non-existent in DSC studies.

The higher temperature transition might then correspond to interchain interactions farther down the chain, which would be present in both planar and in spherical systems. It is reasonable to recognise that the onset of end group mobility occurs at lower transition temperatures and with lower energies, while the onset of chain motion nearer to the gold surface is occurring at higher temperatures and with higher energies.

This second transition temperature is not observed in the LB films of HDM and ODM and has been discussed in section 4.4.2.2. It is very likely the LB films form a better compact monolayer with better alkyl chain packing than the SAMs since it precedes the chemisorption process.

The T_m of the small irreversible peak during the DSC run for Au-HDM (Figure 3.39) agrees well with the lower temperature observed in the HDM modified SAMs. The fact that the small peak observed by DSC was not observed during the next heating/cooling cycle (indicating that it is irreversible), could well explain why we have not been able to observe reversibility in the SAMs and LB films after they go through the first lower temperature transition.[244] However, it should be noted that the second transition temperature observed by CV for the SAMs of HDM and ODM was not reversible, although that of the colloids was reversible in DSC studies.

Although the irreversibility of the temperature-dependent behaviour observed for the SAMs of HDM and ODM by using CV is potentially troubling when attributing the behaviour to an order $\rightarrow$ disorder phase transition, it is believed that these transitions may be kinetically limited, for the following reason. The transition from an ordered to a disordered state will necessarily be accompanied by some diffusion of water and electrolyte into the disordered (and hence permeable) film. Thus, because a return to the original ordered state must involve the expulsion of all foreign species from the array of alkyl chains, which is clearly a slow process, the entire phase transition is kinetically limited. Attempts to accelerate this purification process include incubation of previously heated films in pure water both at temperatures above and below $\mathbf{T_{tr}}$, and cooling of previously heated films to temperatures well below $\mathbf{T_{tr}}$ (by 20-30°C). These have so far been unsuccessful.

Studies in an oven were also done on HDM-modified in air, rather than in solution. A freshly prepared SAM of HDM was heated in an oven above $\mathbf{T_{tr}}$ and the resulting CV taken above $\mathbf{T_{tr}}$. A CV of the modified electrode was again obtained when it was cooled in the electrochemical cell to room temperature. This reversibility was moderately successful but the HDM-modified gold electrode did not recover its original blocking abilities.

In the second case, an HDM-modified SAM was left heated in the oven above $\mathbf{T_{tr}}$ and cooled to room temperature in air. A well-blocked SAM was indicated from the CV data. It is worthy of note that the experiment performed in the oven and air without any contact with redox probe solution yielded results that closely follows a solid-state NMR or DSC measurements in which reversibility of temperature-dependant behaviour was observed.[36,86] However, the results were not reproducible.

4.6.2 Nuclear Magnetic Resonance of Colloids

Variable temperature ^{13}C solid-state NMR[86,119] has revealed phase transitions similar to those detected by DSC that involve reversible disordering of the alkyl chains.[272] In NMR, disordering leads to a drastic change in chemical shift (δ values).[121,280] This present study was designed to compare variable temperature solution NMR to the electrochemical studies in order to explain the

irreversible disordering of the alkyl chains. In this case we studied the variable temperature ^{13}C solution NMR of the colloids of HDM and ODM.

Since it is well known that the disordering starts from the terminal chains, the chemical shift (δ values) from the C16, C15 and C14 for HDM-Au and the C18, C17 and C16 for ODM-Au were compared to those of the free alkanethiols (indicated in Figure 4.23).

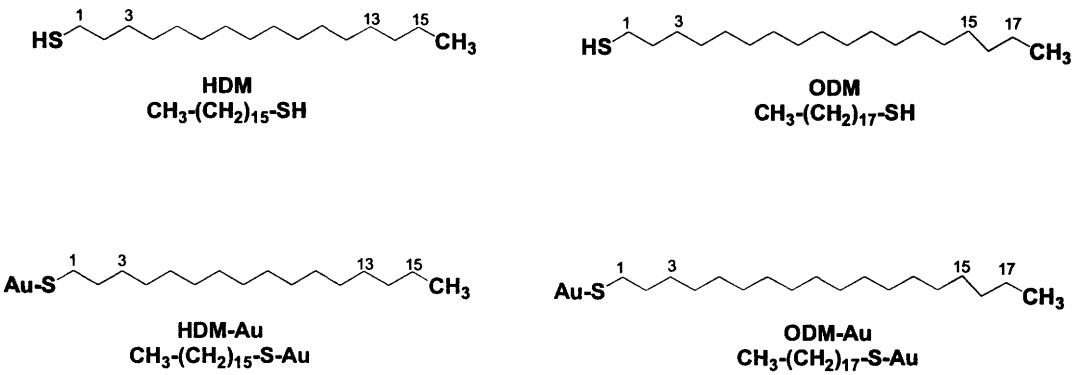

Figure 4.23. Illustration of carbon atoms compared between free alkanethiols of HDM (Carbon A= #16; Carbon B= #15; Carbon C= #14) ODM (Carbon A= #18, Carbon B= #17; Carbon C= #16) and their colloids.

Figures 4.24 to 4.26 show the change in chemical shift of the 3 terminal methyl carbons with temperature. From each of the figures, it can be observed that all systems show only slight decreases in chemical shift as temperature increases. This suggests that the chains of methyl and methylene carbons of the free HDM and ODM and their colloids are dissolved/solvated in the solution

of d_6-benzene[272] and it is also an indicator that there is conformational homogeneity in the systems as temperature was increased.[316,317]

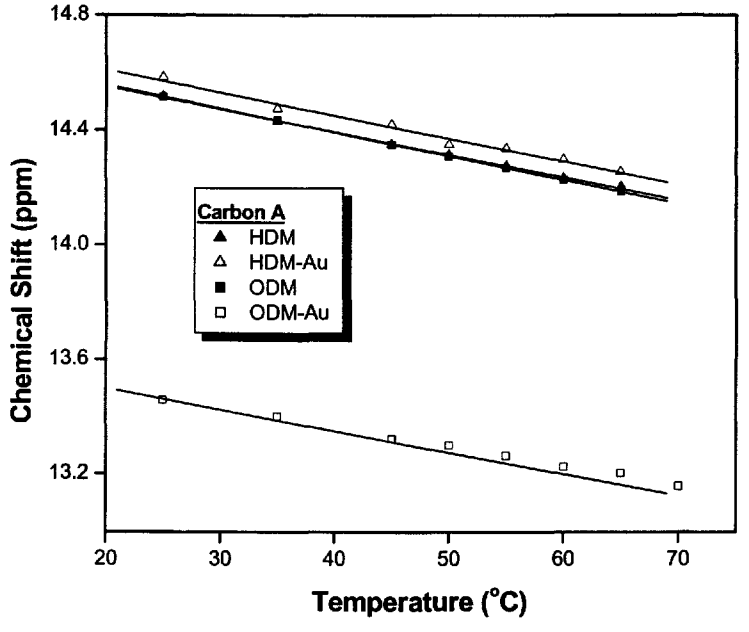

Figure 4.24. Temperature dependence of the chemical shifts for ^{13}C signals of Au-HDM [C 16] and Au-ODM [C 18] for the terminal methyl carbon labelled **A** in d_6-benzene.

Due to this conformational homogeneity, the change in chemical shifts is basically due to thermal motion arising from an increase in temperature. It is worthy of note that the chemical shift of HDM-Au was shifted upfield by about 0.2 ppm from those of HDM, whereas that of ODM-Au was shifted downfield by about 1.0 ppm. This could be attributed to different interactions arising from their different chain lengths, with those of ODM further away from the gold core.

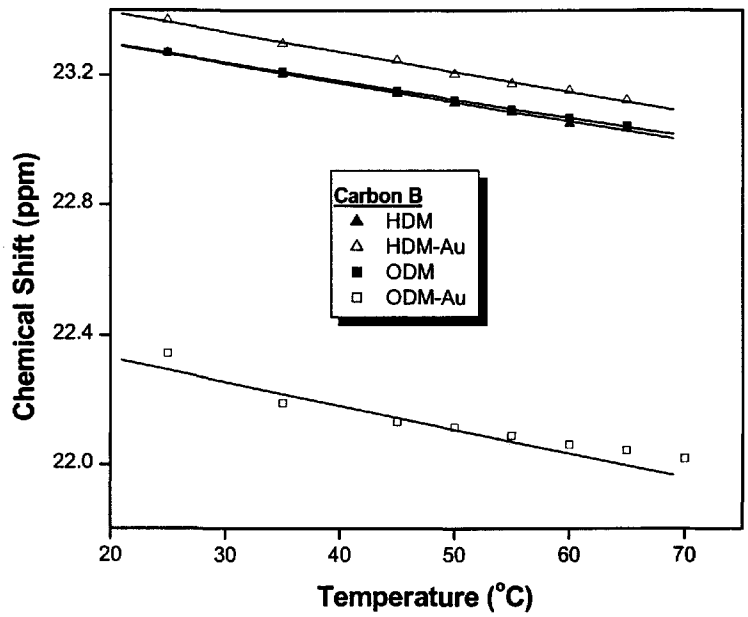

Figure 4.25. Temperature dependence of the chemical shifts for ^{13}C signals of Au-HDM [C 15] and Au-ODM [C 17] for the carbon labelled **B** next to the terminal methyl carbon in d_6-benzene.

The values of the slopes for the various chemical shifts versus temperature plots are given in Table 4.10. It can be observed that there was no significant difference between the slopes for the free alkanethiol or the alkanethiol-capped gold colloids for both HDM and ODM. However, the absolute difference between the free alkanethiol and its corresponding colloid were higher in ODM than in HDM. This is very unusual as it is rather expected that the longer chain of ODM might have less rigidity than HDM and probably less change in chemical shifts. However, the changes are still not significant and indicative of any conformational change.

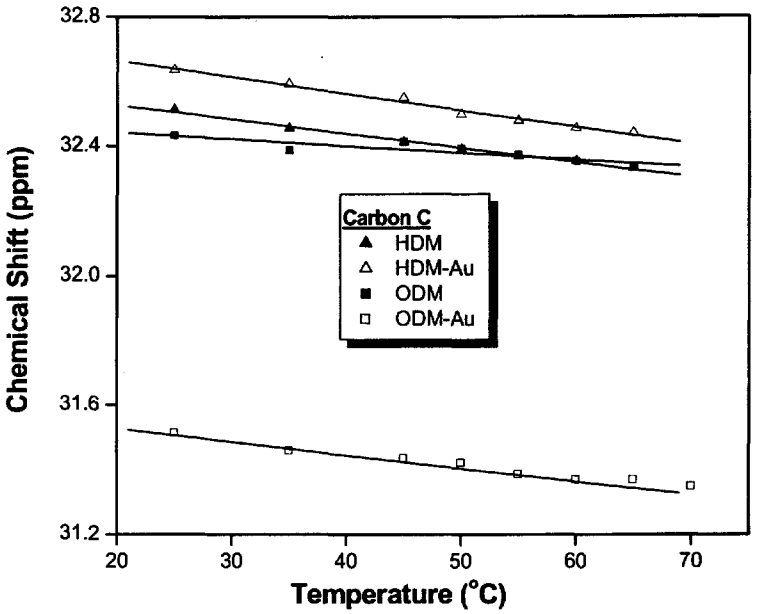

Figure 4.26. Temperature dependence of the chemical shifts for ^{13}C signals of Au-HDM [C 14] and Au-ODM [C 16] for the carbon labelled **C** in d_6-benzene.

These solution studies demonstrate that the reversible temperature dependent disordering observed by solid-state NMR and DSC in alkanethiol-capped gold colloids is absent in the NMR solution studies. This is likely due to the fact that solvent molecules in the solution solvate the alkyl chains of the colloids as well as for the free alkanethiols, removing any ordering between chains.

Table 4.10. Comparison of the slopes of chemical shifts of ^{13}C-δ signals versus temperature for free alkanethiol and alkanethiol-capped gold colloids in d_6-benzene.

Type of Carbon	Compound	Slopes (ppm/°C)
A	HDM	-0.00785
	HDM-Au	-0.00792
	ODM	-0.00822
	ODM-Au	-0.00663
B	HDM	-0.00593
	HDM-Au	-0.00618
	ODM	-0.00571
	ODM-Au	-0.00660
C	HDM	-0.00447
	HDM-Au	-0.00521
	ODM	-0.00214
	ODM-Au	-0.00360

4.6.3 Comparison of Thermal Behaviour of Alkanethiol-Capped Gold Colloids to that of Alkanethiol modified Self-Assembled Monolayers on Gold.

Phase transitions have been reported from variable temperature ^{13}C solid-state NMR spectra[86,119] similar to those detected in this work by DSC. These are known to involve reversible disordering of the alkyl chains.[119] Interestingly, this disordering occurs at temperatures identical to the discontinuities observed in SAMs.[82,244]

In the solution NMR, no such reversible disordering of the alkyl chains was observed. The reason is that in solution NMR, no characteristic T_{tr} was

observed due to the solvation of the alkyl chains on the colloids, removing any ordering between chains.

However, in solution electrochemistry, a T_{tr} was observed even though it was not reversible. The reason may be that electrochemistry is performed on solid films on gold electrodes that are not solvated, but after the transition from an ordered to a disordered state becomes permeable to the $[Fe(CN)_6]^{3-/4-}$ redox probe. The permeability will necessarily be accompanied by some diffusion of water and electrolyte into the disordered film and its array of alkyl chains and cause difficulty in reversing the monolayer to its original ordered state.. This may likely explain why it was difficult to reverse the disordering occurring in the SAMs of HDM and ODM as well as that of MUA.

Chapter Five – Recommendations and Conclusion

5.1 Recommendations

Some of the findings of this study remain difficult to explain. These include the following:

1. The difficulty in reversing the phase transition in the SAMs and LB films, suggesting that probably a more complex mechanism is occurring.
2. The phase transition itself, and in particular its mechanism and origins.

The issues above could be addressed using techniques that will observe the topography of the SAMs and the LB films before and after the phase transitions. Techniques that would enable determination of the molecular orientation and conformations in the SAMs and LB films as a function of temperature may help answer some specific questions about the mechanisms and origins of the phase transitions. In the case of the LB films the Langmuir films could also be observed in situ to assess the film morphology before deposition. The study could be extended to changing the pendant group of the self-assembling compounds. This could address specific questions that have

arisen with respect to the hydroxyl group at the end of the alkyl chain, by observing any changes that arise as a result of carefully chosen functional groups, in particular with respect to hydrogen bonding. Crosslinkable end groups may also be of interest.

It would also be interesting to investigate physisorbed monolayer films of alkanols, in which the hydroxyl group replaces the thiol group, and to consider their behaviour with respect to any phase transitions or temperature dependant behaviour. Specifically, this change in headgroup will allow us to transfer Langmuir films as non-chemisorbed LB films, which will be similar to the chemisorbed alkanethiol LB films. The main difference is the fact that there would be no chemical bond between the gold electrode and the alkanol. Since the process of ordering in the two types of monolayers at the air-water interface is the same, the phase transitions in each of these systems can be compared and contrasted to understand the complete ordering process of the molecules in the different types of monolayers. However it is likely that some of the problems that could arise from this study will be solubility of the films at the air-water interface and the lack of producing passivating films films in the presence of redox probes to block electron transfer.[96]

5.2 Future Work and Strategy

Grazing Incidence Angle (GIA)-FTIR Spectroscopy may be used to study films at room temperature both before and after they have been heated, to address questions regarding orientations and conformations of the SAMs and LB films before and after heating, and how these are related to the possible mechanisms and origins of the phase transition and its reversibility. Atomic Force Microscopy (AFM) and Scanning Tunneling Microscopy (STM) may also be useful and could offer the first topographical information about these films before and after heating.

Similarly, near edge X-ray absorption spectroscopy (NEXAFS) may provide structural (orientational) and chemical information about the SAM surfaces. Probing of the modified electrodes with X-ray photoelectron emission microscopy (X-PEEM) may reveal orientation effects, and help to identify the respective roles of defects and disorder in the phase transitions. This may lead to structural characterisation with topographical resolution, bridging the results from GIA-FTIR and AFM/STM.

With respect to the Langmuir Films, additional in situ characterization such as Brewster Angle Microscopy (BAM) may give insight into the morphology of the films at the air-water interface just before LB deposition.

It should be noted that an appropriate and ideal experiment to monitor any experimental parameter directly as a function of temperature would achieve

far more reaching goals, rather than simply monitoring changes before and after T_{tr}. However, this is often experimentally difficult and/or expensive.

5.2 Conclusion

Two film-forming techniques (SA and LB deposition) have been used to prepare gold electrodes modified with alkanethiols, and the resulting films compared and contrasted. Both techniques are known to involve two steps in the film forming process, with the order of the steps in LB deposition being the reverse of the SA process.

For the SAMs, a highly reproducible experimental protocol for monolayer deposition onto gold electrodes was established. A successful protocol was also developed for the formation of the first stable monomolecular Langmuir films of HDM and ODM at the air-water interface. These films were successfully transferred at low temperatures by the LB technique to form LB monolayers on hydrophilic gold electrodes. The stability of the Langmuir and LB films depends strongly on the subphase composition and temperature.[133]

The electrochemical methods of CV and AC-EIS were used to study the resulting SAMs of HDM, ODM and MUA on gold, and the resulting LB films of HDM and ODM on gold, as a function of temperature. CV and AC-EIS revealed discontinuities in film properties for the SAMs and the LB films at a transition temperature T_{tr} characteristic for each compound, strongly suggesting a phase

transition. T_{tr} for each compound varied with respect to one another in a way analogous to the bulk melting points for HDM, ODM and MUA. The AC-EIS provided a comprehensive picture of the electrode-monolayer-solution interphase and was used to follow changes in this interface as a function of temperature. The T_{tr} values agreed within experimental error for the two monolayer/film forming strategies, this strongly supports the idea that the same transition is being effected in both types of films. This transition was previously observed in SAMs and attributed to an order-disorder mechanism that increased the permeability of the SAMs.[82] From the results of this work, it is still believed that this is the most likely mechanism as similar results have been obtained in this study for the SAMs and LB films.

It is interesting to note that the absolute permeability of the LB films appears to be lower than that of the SAMs of the same compound. This is demonstrated strikingly by comparing the R_2 values from AC-EIS results for the ODM and HDM films from each technique, suggesting that the LB film formation procedure produces a more organized monolayer than the SA strategy. The differences in R_2 above T_{tr} suggest a lower number of defect sites in the LB films compared to the SAMs. One may also consider this from a thermodynamic point of view. The endothermic nature of the compression at the air-water interface in the LB deposition process indicates entropy gains in the compressed system, attributed to the decrease in order of the interfacial water molecules. In the SA process, without this driving force, the intermolecular

ordering must be exothermic, and must be driven entirely by entropy gains to the surroundings, which are not mechanically coupled to the intermolecular ordering.

Thus, the chemisorption step in the SA process appears to be the limiting factor in the effectiveness of organized monolayer formation, undermining the integrity of the subsequent intermolecular organization by laying down an imperfect template. When intermolecular organization at the air-water interface precedes chemisorption through the LB deposition process, the resulting monolayers maintain their high degree of order during chemisorption because of the nature of the LB technique. The exact mechanism by which this order is maintained is not yet clear, and requires further investigation.

The existence of phase transitions in the SAMs and LB films is an observation of critical importance to all future studies of these and similar systems. Therefore, to gain an insight into the mechanism of the phase transitions, synthesis of alkanethiol-capped gold colloids (3D analogues of the 2D SAMs) were performed. From the enthalpy measurements by DSC of the colloids, the mechanism of the phase transition was attributed to molecular disordering which originates from the terminal region of the chains and propagates towards the middle of the chain as temperature increases. However, this disorder does not extend to the sulphur head group, an indication that the thiol-gold at the surface of the gold is intact as temperature is increased.

Based on the thermograms (ΔH versus T) from DSC of the colloids, previously unexplained behaviour - a second transition observed by CV (HDM and ODM in SAMs) was better understood. The second transition temperature was only observed with the HDM gold colloid (not the ODM colloid), because the spherical nature of the gold, made the longer chains (ODM) have lesser interaction between their end gropus and therefore unable to observe head group packing and its corresponding energy.

Solution ^{1}H- and ^{13}C-NMR of the colloids confirmed the reason why it was difficult to reverse the ordering of the films after a phase transition in which their chains are "dissolved" in electrolyte. Specifically, no phase transition was detected in the colloids by solution NMR. (Solid state NMR of the colloids has shown distinct phase transitions as in the 2D SAMs and LB, although these were not reversible).

It is also worthy of note that Langmuir films of HDM and ODM at the air-water interface were transferred as physisorbed LB films onto glassy carbon electrodes and studied by electrochemistry (CV and AC-EIS), but the films were poorly passivating when compared to LB films on gold electrodes, suggesting that the chemisorption was an important feature of the LB films in these systems.

The implications for ultrathin film design are significant for a broad range of systems and applications. The results of this study are extremely interesting, and perhaps surprising, since the SA process has often been viewed as the best

route to perfect monolayers, and long incubation times have certainly produced highly ordered systems.[244] Although LB deposition is usually too complex for mass production, the knowledge gained from this study suggests that any strategy that incorporates some type of pre-organization step prior to chemisorption could improve the integrity of the resulting monolayers. In this regard, vesicle or micelle formation could be investigated as possible candidates for pre-organization methods.

Chapter Six – References

1. Ulman, A. *An Introduction to Ultra-thin Organic Films. From Langmuir-Blodgett to Self-Assembly;* 1991.

2. Cooper, E.; Leggett, G. J. *Langmuir* **1999**, *15*, 1024.

3. Allara, D. L. *Biosen. Bioelectron.* **1995**, *10*, 771.

4. Fendler, J. H. *J. Phys. Chem.* **1980**, *84*, 1485.

5. Nelson, P. H.; Rutledge, G. C.; Hatton, T. A. *J. Chem. Phys.* **1997**, *107* , 10777.

6. Israelachvili, J. N. Thermodynamic and geometric aspects of amphiphile aggregation into micelles, vesicles and bilayers, and the interaction between them, in *Physics of Amphiphiles: Micelles, Vesicles and Microemulsions*, DeGiorgio, V.; Corti, M., editors; Elsevier Sciences Publishers: New York, 1985; pp. 24-58.

7. Ulman, A.; Scaringe, R. P. *Langmuir* **1992**, *8*, 894.

8. Menger, F. M. *Acc. Chem. Res.* **1979**, *12*, 111.

9. Lopez, P.; Rodriguez, A.; Gomez-Herrera, C.; Sanchez, F.; Moya, M. L. *Int. J. Chem. Kinet.* **1995**, *27*, 525.

10. Strom, C.; Hansson, P.; Jonsson, B.; Soderman, O. *Langmuir* **2000**, *16*, 2469.

11. Gebicki, J. M.; Hicks, M. *Nature* **1973**, *243*, 232.

12. Bilewicz, R.; Madja, M. *J. Am. Chem. Soc.* **1991**, *113*, 5464.

13. KSV Corporation *KSV 3000 Instruction Manual*, 96.

14. Markowitz, M. A.; Janout, V.; Castner, D. G.; Regen, S. L. *J. Am. Chem. Soc.* **1989**, *111*, 8192.

15. Conner, M. D.; Janout, V.; Regen, S. L. *J. Am. Chem. Soc.* **1993**, *115*, 1178.

16. Conner, M. D.; Janout, V.; Kudelka, I.; Dedek, K.; Zhu, J.; Regen, S. L. *Langmuir* **1993**, *9*, 2389.

17. Masuda, T.; Isobe, E.; Higashimura, T.; Takada, K. *J. Am. Chem. Soc.* **1983**, *105*, 7473.

18. Jamnik, B.; Vlachy, V. *J. Am. Chem. Soc.* **1993**, *115*, 660.

19. Biebuyck, H. A.; Whitesides, G. M. *Langmuir* **1993**, *9*, 1766.

20. Templeton, A. C.; Hostetler, M. J.; Kraft, C. T.; Murray, R. W. *J. Am. Chem. Soc.* **1998**, *120*, 1906.

21. Templeton, A. C.; Hostetler, M. J.; Warmoth, E. K.; Chen, S.; Hartshorn, C. M.; Krishnamurthy, V. M.; Forbes, D. E.; Murray, R. W. *J. Am. Chem. Soc.* **1998**, *120*, 4845.

22. Templeton, A. C.; Wuelfing, W. P.; Murray, R. W. *Acc. Chem. Res.* **2000**, *33*, 27.

23. Brust, M.; Walker, M.; Bethell, D.; Schiffrin, D. J.; Whyman, R. *J. Chem. Soc. , Chem. Commun.* **1994**, 801.

24. Brust, M.; Fink, J.; Bethell, D.; Schiffrin, D. J.; Kiely, C. J. *J. Chem. Soc. , Chem. Commun.* **1995**, 1655.

25. Lindoy, L. F.; Atkinson, I. M. *Self-Assembly in Supramolecular Systems;* Cambridge University Press: Cambridge, 2000.

26. Jones, W.; Rao, C. N. R. Supramolecular Organization, in *Supramolecular Organization and Materials Design*, Jones, W.; Rao, C. N. R., editors; Cambridge University Press: Cambridge, 2003; pp. 1-445.

27. Fuhrhop, J.-H.; Koning, J. *Membranes and Molecular Assemblies: The Synkinetic Approach;* Cambridge University Press: Cambridge, 1994.

28. Terfort, A.; Bowden, N.; Whitesides, G. M. *Nature* **1997**, *386*, 162.

29. Mirkin, C. A.; Letsinger, R. L.; Mucic, R. C.; Storhoff, J. F. *Nature* **1996**, *382*, 607.

30. Ulman, A. *Chem. Rev.* **1996**, *96*, 1533.

31. Fendler, J. H. *Membrane mimetic chemistry : characterizations and applications of micelles, microemulsions, monolayers, bilayers, vesicles, host-guest systems, and polyions;* John Wiley and Sons: New York, 2003.

32. Israelachvili, J. N. *Intermolecular forces;* 2nd ed.; Academic Press: San Diego, 1992.

33. Ishikawa, Y.; Kuwahara, H.; Kunitake, T. *J. Am. Chem. Soc.* **1994**, *116*, 5579.

34. Erokhin, V.; Vakula, S.; Nicolini, C. *Thin Solid films* **1994**, *238*, 88.

35. Collier, C. P.; Vossmeyer, T.; Heath, J. R. *Annu. Rev. Phys. Chem.* **1998**, *49*, 371.

36. Terrill, R. H.; Postlethwaite, T. A.; Chen, C.; Poon, C.-D.; Terzis, A.; Chen, A.; Hutchison, J. E.; Clark, M. R.; Wignall, G.; Londono, J. D.; Superfine, R.; Falvo, M.; Jonson, C. S. Jr.; Samulski, E. T.; Murray, R. W. *J. Am. Chem. Soc.* **1995**, *117*, 12537.

37. Leff, D. V.; Ohara, P. C.; Heath, J. R.; Gelbart, W. M. *J. Phys. Chem.* **1995**, *99*, 7036.

38. Sarathy, K. V.; Raina, G.; Yadav, R. T.; Kulkarni, G. U.; Rao, C. N. R. *J. Phys. Chem. B* **1997** , *101*, 9876.

39. Porter, L. A. Jr.; Ji, D.; Westcott, S. L.; Graupe, M.; Czernuszewicz, R. S.; Halas, N. J.; Lee, T. R. *Langmuir* **1998**, *14*, 7378.

40. Hostetler, M. J.; Stokes, J. J.; Murray, R. W. *Langmuir* **1996**, *12*, 3604.

41. Whetten, R. L.; Khoury, J. T.; Alvarez, M. M.; Murthy, S.; Vezmar, R.; Wang, Z. L.; Stephens, P. W.; Cleveland, C. L.; Luedtke, W. D.; Landman, U. *Adv. Mater. (Weinheim, Ger.)* **1996**, *8*, 428.

42. Ingram, R. S.; Hostetler, M. J.; Murray, R. W. *J. Am. Chem. Soc.* **1997**, *119*, 9175.

43. Johnson, S. R.; Evans, S. D.; Mahon, S. W.; Ulman, A. *Langmuir* **1997**, *13*, 51.

44. Mayya, K. S.; Patil, V.; Sastry, M. *Langmuir* **1997**, *13*.

45. Sastry, M.; Mayya, K. S.; Bandyopadhyay, K. *Colloids. Surf. A.* **1997**, *127*, 221.

46. Chen, S.; Murray, R. W. *Langmuir* **1999**, *15*, 682.

47. Leff, D. V.; Brandt, L.; Heath, J. R. *Langmuir* **1996**, *12*.

48. Porter, L. A.; Ji, D.; Westcott, S. L.; Graupe, M.; Czernuszewicz, R. S.; Halas, N. J.; Lee, T. R. *Langmuir* **1998**, *14*, 7378.

49. Liu, L.; Xu, R.; Kaifer, A. E. *Langmuir* **1998**, *14*, 7337.

50. Liu, L.; Mendoza, S.; Roman, E.; Lynn, M. J.; Xu, R.; Kaifer, A. E. *J. Am. Chem. Soc.* **1999**, *121*, 4304.

51. Weisbecker, W. S.; Merritt, M. V.; Whitesides, G. M. *Langmuir* **1996**, *12*, 3763.

52. Evans, S. D.; Johnson, S. R.; Ringsdorf, H.; Williams, L. M.; Wolf, H. *Langmuir* **1998**, *14*, 6436.

53. Sastry, M. Nanoparticle Thin Films: An Approach Based on Self-Assembly, in *Handbook of Surfaces and Interfaces of Materials*, Singh, N., editor; Academic press: New york, 2001; Chapter 2, pp. 87-124.

54. Wang, Z. L. *Adv. Mater. (Weinheim, Ger.)* **1998**, *10*, 13.

55. Petit, C.; Taleb, A.; Pileni, M.-P. *Adv. Mater. (Weinheim, Ger.)* **1998**, *10*, 259.

56. Ohara, P. C.; Heath, J. R.; Gelbart, W. M. *Angew. Chem. , Int. Ed. Engl.* **1997**, *36*, 1077.

57. Ohara, P. C.; Gelbart, W. M. *Langmuir* **1998**, *14*, 3418.

58. Dimitrov, A. S.; Nagayama, K. *Langmuir* **1996**, *12*, 1303.

59. Mrksich, M.; Sigal, G. B.; Whitesides, G. M. *Langmuir* **1995**, *11*, 4383.

60. Mrksich, M.; Whitesides, G. M. *Trends Biotechnology* **1995**, *13*, 228.

61. Porter, M. D.; Bright, T. B.; Allara, D. L.; Chidsey, C. E. D. *J. Am. Chem. Soc.* **1987**, *109*, 3559.

62. Strong, L.; Whitesides, G. M. *Langmuir* **1988**, *4*, 546.

63. Bain, C. D.; Evall, J.; Whitesides, G. M. *J. Am. Chem. Soc.* **1989**, *111* , 7155.

64. Bain, C. D.; Whitesides, G. M. *J. Am. Chem. Soc.* **1989**, *111*, 7164.

65. Laibinis, P. E.; Whitesides, G. M. *J. Am. Chem. Soc.* **1992**, *112*, 205.

66. Kind, H.; Bittner, A. M.; Kern, K.; Greber, T. *J. Phys. Chem.* **1998**, *102*, 7582.

67. Cavalleri, O.; Kind, H.; Bittner, A. M.; Kern, K. *Langmuir* **1998**, *14*, 7292.

68. Thomas, R. C.; Sun, L.; Crooks, M. *Langmuir* **1991**, *7*, 620.

69. Chailapakul, O.; Sun, L.; Crooks, M. *J. Am. Chem. Soc.* **1993**, *115*, 12459.

70. Nuzzo, R. G.; Fusco, F. A.; Allara, D. L. *J. Am. Chem. Soc.* **1987**, *109* , 2358.

71. Bain, C. D.; Biebuyck, H. A.; Whitesides, G. M. *Langmuir* **1989**, *5*, 723.

72. Walczak, M. W.; Chung, C.; Stole, S. M.; Widrig, C. A.; Porter, M. D. *J. Am. Chem. Soc.* **1991**, *113*, 2370.

73. Nuzzo, R. G.; Zegarski, B. R.; Dubois, L. H. *J. Am. Chem. Soc.* **1987**, *109*, 733.

74. Li, Y.; Huang, J.; McIver, R. T. Jr.; Hemminger, J. C. *J. Am. Chem. Soc.* **1992**, *114*, 2428.

75. Bryant, M. A.; Pemberton, J. E. *J. Am. Chem. Soc.* **1991**, *113*, 8284.

76. Bryant, M. A.; Pemberton, J. E. *J. Am. Chem. Soc.* **1991**, *113*, 3630.

77. Miller, C.; Cuendt, P.; Gratzel, M. *J. Phys. Chem.* **1991**, *95*, 877.

78. Miller, C.; Gratzel, M. *J. Phys. Chem.* **1991**, *95*, 5225.

79. Fox, M. A.; Collard, D. M.; Creager, S. E. *Langmuir* **1990**, *6*, 1617.

80. Finklea, H. O.; Hanshew, D. D. *J. Electroanal. Chem. Interfacial Electrochem.* **1993**, *347*, 327.

81. Finklea, H. O.; Ravenscroft, M. S.; Snider, D. A. *Langmuir* **1993**, *9*, 223.

82. Badia, A.; Back, R.; Lennox, R. B. *Angew. Chem. , Int. Ed. Engl.* **1994**, *106*, 2332.

83. Parikh, A. N.; Allara, D. L.; Azouz, I. B.; Rondelez, F. *J. Phys. Chem.* **1994**, *98*, 7577.

84. Boubour, E.; Lennox, R. B. *Langmuir* **2000**, *16*, 4222.

85. Badia, A.; Lennox, R. B.; Reven, L. *Acc. Chem. Res.* **2000**, *33*, 475.

86. Badia, A.; Cuccia, L.; Demers, L.; Morin, F.; Lennox, R. B. *J. Am. Chem. Soc.* **1997**, *119*, 2682.

87. Nuzzo, R. G.; Allara, D. L. *J. Am. Chem. Soc.* **1983**, *105*, 4481.

88. Porter, M. D.; Bright, T. B.; Allara, D. L.; Chidsey, C. E. D. *J. Am. Chem. Soc.* **1987**, *109*, 3559.

89. Finklea, H. O.; Avery, S.; Lynch, M.; Furtsch, T. *Langmuir* **1987**, *3*, 409.

90. Sabatani, E.; Rubinstein, I.; Maoz, R.; Sagiv, J. *J. Electroanal. Chem.* **1987**, *219*, 365.

91. Troughton, E. B.; Bain, C. D.; Whitesides, G. M.; Nuzzo, R. G.; Allara, D. L.; Porter, M. D. *Langmuir* **1988**, *4*, 365.

92. Gennes, P. G. *Colloid Polym. Sci.* **1986**, *264*, 463.

93. Sanassy, P.; Evans, S. D. *Langmuir* **1993**, *9*, 1024.

94. Chen, Y. L.; Chen, S.; Frank, C.; Isrealachvili, J. *J. Colloid. Interface Sci.* **1992**, *153*, 244.

95. Bilewicz, R.; Majda, M. *Langmuir* **1991**, *7*, 2794.

96. Bizzotto, D.; Wong, E.; Yang, Y. *J. Electroanal. Chem.* **2000**, *480*, 233.

97. Livingstone, H. K.; Swingley, C. S. *J. Colloid. Interface Sci.* **1972**, *38*, 643.

98. Itaya, A.; Van der Fluweraer, M.; De Schryver, F. C. *Langmuir* **1989**, *5*, 1123.

99. Sondag-Huethorst, J. A. M.; Fokkink, L. G. J. *Langmuir* **1995**, *11*, 2237.

100. Janek, R. P.; Fawcett, W. R.; Ulman, A. *Langmuir* **1998**, *14*, 3011.

101. Boukamp, B. A. *Computer Acquisition of Corrosion Data*; Kenotz, M. W., editor; 1985; pp. 146.

102. Macdonald, D. D.; McKubre, G. H. in *Modern Aspects of Electrochemistry*, 14 ed.; Bockris, J. O.; Conway, B. E.; White, R. E., editors; Plenum: New York, 1982; Chapter 2.

103. Macdonald, J. R. Fundamentals of Impedance Spectroscopy, in *Impedance Spectroscopy, Emphasizing Solid Materials and Systems*, Macdonald, J. R., editor; John Wiley and Sons, Inc.: Toronto, 1987; pp. 1-345.

104. Boukamp, B. A. *Solid State Ionics* **1986**, *18&19*, 136.

105. Gafni, Y.; Weizman, H.; Libman, J.; Shanzer, A.; Rubinstein, I. *Chem. Eur. J.* **1996**, *2*, 759.

106. Dubois, L. H.; Nuzzo, R. G. *Annu. Rev. Phys. Chem.* **1992**, *43*, 437.

107. Ahn, D. J.; Franses, E. I. *J. Phys. Chem.* **1992**, *96*, 9952.

108. Matveeva, E. S.; Calleja, R. D.; Parkhutik, V. P. *Electrochim. Acta* **1996**, *41*, 1351.

109. Aurbach, D.; Moshkovich, M.; Cohen, Y.; Schechter, A. *Langmuir* **1999**, 2947.

110. Sandhyarani, N.; Pradeep, T. *J. Mater. Chem.* **2000**, *10*, 981.

111. Voicu, R.; Badia, A.; Lennox, R. B.; Ellis, T. H. *Chem. Mat.* **2000**, *12*, 2646.

112. Long, Y.-T.; Herrwerth, S.; Eck, W.; Grunze, M. *Phy. Chem. Chem. Phy.* **2002**, *4*, 522.

113. Gao, W.; Dickinson, L.; Grozinger, C.; Morin, F. G.; Reven, L. *Langmuir* **1996**, *12*, 6429.

114. Gao, W.; Dickinson, L.; Grozinger, C.; Morin, F. G.; Reven, L. *Langmuir* **1997**, *13*, 115.

115. Reven, L.; Dickinson, L. *Thin Solid films* **1998**, *24*, 149.

116. Hostetler, M. J.; Wingate, J. E.; Zhong, C.-J.; Harris, J. E.; Vachet, R. W.; Clark, M. R.; Londono, J. D.; Green, S. J.; Stokes, J. J.; Wignall, G.; Glish, G. L.; Porter, M. D.; Evans, N. D.; Murray, R. W. *Langmuir* **1998**, *14*, 17.

117. Pawsey, S.; Yach, K.; Halla, J.; Reven, L. *Langmuir* **2000**, *16*, 3294.

118. Hohne, G. W. H. *Thermochim. Acta* **1999**, *332*, 11.

119. Badia, A.; Gao, W.; Singh, S.; Demers, L.; Cuccia, L.; Reven, L. *Langmuir* **1996**, *12*, 1262.

120. Sabatani, E.; Rubinstein, I. *Langmuir* **1987**, *9*, 2974.

121. Fenter, P.; Eisenberger, P.; Liang, P. *Phys. Rev. Lett.* **1993**, *70*, 2447.

122. Chen, K.; Caldwell, B.; Mirkin, C. A. *J. Am. Chem. Soc.* **1993**, *115*, 1193.

123. Kataby, G.; Prozorov, T.; Koltypin, Y.; Cohen, H.; Sukenik, C. M.; Ulman, A.; Gedanken, A. *Langmuir* **1997**, *13*, 6151.

124. Lee, M.; Chung, C. *Bull. Korean Chem. Soc.* **1999**, *20*, 132.

125. Gorman, C. B.; Biebuyck, H. A.; Whitesides, G. M. *Langmuir* **1995**, *11*, 2242.

126. Dynarowicz-Lakta, P.; Kita, K. *Adv. Colloid Interface Sci.* **1999**, *79*, 1.

127. Gaines, G. L. *Insoluble Monolayers at Liquid-Gas Interfaces;* Interscience Publishers: New York, 1966.

128. Chen, S. *Langmuir* **2001**, *17*, 2878.

129. Huang, Y.; Gan, L.; Huang, C.-H.; Meng, F. *Supramol. Sci.* **1998**, *5*, 437.

130. Wijekoon, W. M. K. P.; Asgharian, B.; Casstevens, M.; Samoc, M.; Talapatra, G. B.; Prasad, P. N. *Langmuir* **1992**, *8*, 135.

131. Bourgoin, J.-P.; Palacin, S. *Langmuir* **1998**, *14*, 3967.

132. Khomutov, G. B.; Tishin, A. M.; Polyakov, S. N.; Bohr, J. *Colloids. Surf. A.* **2000**, *166*, 33.

133. Gyepi-Garbrah, S. H.; Šilerová, R. *Phy. Chem. Chem. Phy.* **2002**, *4*, 3436.

134. Peng, J. B.; Barnes, G. T.; Gentle, I. R. *Adv. Colloid Interface Sci.* **2001**, *91*, 163.

135. Giersig, M.; Mulvaney, P. *Langmuir* **1993**, *9*, 3408.

136. Chailapakul, O.; Sun, L.; Chuanjing, X.; Crooks, R. M. *J. Am. Chem. Soc.* **1993**, *115*, 12459.

137. Valenty, S. J. *J. Am. Chem. Soc.* **1979**, *101*, 1.

138. Day, D.; Lando, J. B. *Macromol.* **1980**, *13*, 1478.

139. O'Brien, K. C.; Rogers, C. E.; Lando, J. B. *Thin Solid films* **1983**, *102*, 131.

140. O'Brien, K. C.; Long, J.; Lando, J. B. *Langmuir* **1985**, *1*, 514.

141. Grieser, F.; Thistlethwaite, P.; Urquhart, R. *J. Phys. Chem.* **1987**, *91*, 5286.

142. Cornell, D. G.; Dluhy, R. A. *Biochem.* **1989**, *28*, 2789.

143. Jehoulet, C.; Bard, A. J. *J. Am. Chem. Soc.* **1991**, *113*, 5456.

144. Obeng, Y. S.; Bard, A. J. *J. Am. Chem. Soc.* **1991**, *113*, 6279.

145. Back, R.; Lennox, R. B. *J. Phys. Chem.* **1992**, *96*, 8149.

146. Jehoulet, C.; Obeng, Y. S.; Kim, Y.-T.; Zhou, F.; Bard, A. J. *J. Am. Chem. Soc.* **1992**, *114*, 4237.

147. Doblhofer, K. R. K. Electrochemistry of Conducting Polymers 50, in *Handbook of Conducting Polymers*, 2nd ed.; Skotheim, T. A.; Elsenbaumer, R. L.; Reynolds, J. R., editors; Marcell Dekker Inc.: New York, 1998; Chapter 20, pp. 531-588.

148. Dubois, L. H.; Zegarski, B. R.; Nuzzo, R. G. *J. Am. Chem. Soc.* **1990**, *112*, 570.

149. Hickman, J. J.; Zou, C.; Ofer, D.; Harvey, P. D.; Wrighton, M. S.; Laibinis, P. E.; Bain, C. D.; Whitesides, G. M. *J. Am. Chem. Soc.* **1989**, *111*, 7271.

150. Steiner, U. B.; Caseri, W. R.; Suter, U. W. *Langmuir* **1992**, *8*, 2771.

151. Tabushi, I.; Kurihara, K.; Naka, K.; Yamamura, K.; Hatakeyama, H. *Tet. Lett.* **1987**, *28*, 4299.

152. Jin, Z. H.; Vezenov, D. V.; Lee, Y. W.; Zull, J. E.; Sukenik, C. N.; Savinell, R. F. *Langmuir* **1994**, *10*, 2662.

153. Finklea, H. O.; Robinson, L. R.; Blackburn, A.; Richter, B.; Allara, D.; Bright, T. *Langmuir* **1986**, *2*, 239.

154. Allara, D. L.; Parikh, A. N.; Rondelez, F. *Langmuir* **1995**, *11*, 2357.

155. Linford, M. R.; Chidsey, C. E. D. *J. Am. Chem. Soc.* **1993**, *115*, 12631.

156. Linford, M. R.; Fenter, P.; Eisenberger, P. M.; Chidsey, C. E. D. *J. Am. Chem. Soc.* **1995**, *117*, 3145.

157. Nuzzo, R. G.; Dubios, L. H.; Allara, D. L. *J. Am. Chem. Soc.* **1990**, *112*, 558.

158. Bain, C. D.; Troughton, E. B.; Tao, Y.-T.; Evall, J.; Whitesides, G. M.; Nuzzo, R. G. *J. Am. Chem. Soc.* **1989**, *111*, 321.

159. Bain, C. D.; Whitesides, G. M. *Angew. Chem. , Int. Ed. Engl.* **1989**, *28*, 506.

160. Bain, C. D.; Whitesides, G. M. *J. Am. Chem. Soc.* **1988**, *110*, 5897.

161. Pale-Grodsdemange, C.; Simon, E. S.; Prime, K. L.; Whitesides, G. M. *J. Am. Chem. Soc.* **1991**, *113*, 12.

162. Laibinis, P. E.; Bain, C. D.; Nuzzo, R. G.; Whitesides, G. M. *J. Am. Chem. Soc.* **1995**, *99*, 7663.

163. Evans, S. D.; Urankar, E.; Ulman, A.; Ferris, N. *J. Am. Chem. Soc.* **1991**, *113*, 4121.

164. Chang, S.-C.; Chao, I.; Tao, Y.-T. *J. Am. Chem. Soc.* **1994**, *116*, 6792.

165. Tao, Y.-T.; Wu, C.-C.; Eu, J.-Y.; Lin, W.-L.; Wu, K.-C.; Chen, C. *Langmuir* **1997**, *13*, 4018.

166. Sabatani, E.; Cohen-Buolakia, J.; Bruening, M.; Rubinstein, I. *Langmuir* **1993**, *9*, 2974.

167. Kim, T.; Crooks, R. M.; Tsen, M.; Sun, L. *J. Am. Chem. Soc.* **1995**, *117*, 3967.

168. Sachs, S. B.; Dudek, S. P.; Hsung, R. P.; Sita, L. A.; Smalley, J. F.; Newton, M. D.; Feldberg, S. W.; Chidsey, C. E. D. *J. Am. Chem. Soc.* **1997**, *119* , 10563.

169. Zehner, R. W.; Sita, L. R. *Langmuir* **1997**, *13*, 2973.

170. Tour, J. M.; Jones, L. J.; Pearson, D. L.; Lamba, J. J. S.; Burgin, T. P.; Whitesides, G. M.; Allara, D. L.; Parikh, A. N.; Atre, S. V. *J. Am. Chem. Soc.* **1995**, *117*, 9529.

171. Liedberg, B.; Yang, Z.; Engquist, I.; Wirde, M.; Gelius, U.; Gotz, G.; Bauerle, P.; Rummel, R.-M.; Ziehler, Ch.; Gopel, W. *J. Phys. Chem. B* **1997**, *101*, 5951.

172. Obeng, Y. S.; Laing, M. E.; Freidli, A. C.; Yang, H. C.; Wang, D. N.; Thulstrup, E. W.; Bard, A. J.; Michl, J. *J. Am. Chem. Soc.* **1992**, *114*, 9943.

173. Evans, S. D.; Goppert-Bearducci, K. E.; Urankar, E.; Gerenser, L. J.; Ulman, A. *Langmuir* **1991**, *7*, 2700.

174. Tam-Chang, S.-W.; Biebuyck, H. A.; Whitesides, G. M. *Langmuir* **1995**, *11*, 4371.

175. Clegg, R. S.; Hutchison, J. E. *Langmuir* **1996**, *12*, 5239.

176. Finklea, H. O. Self-assembled Monolayers on Electrodes, in *Encyclopedia of Analytical Chemistry*, Meyers, R. A., editor; John Wiley & Sons Ltd.: Chichester, 2001; Chapter 1, pp. 1-26.

177. Jeffrey, G. *An Introduction to Hydrogen Bonding;* John Wiley and Sons: New York, 1997.

178. Guo, L.-H.; Facci, J. C.; McLendon, G.; Mosher, R. *Langmuir* **1994**, *10*, 4588.

179. Zhao, X.-M.; Wilbur, J. L.; Whitesides, G. M. *Langmuir* **1996**, *12*, 3257.

180. Walczak, M. M.; Alves, C. A.; Lamp, B. D.; Porter, M. D. *Electroanal. Chem.* **1995**, *396*, 103.

181. Caldwell, W. B.; Chen, K.; Herr, B. R.; Mirkin, C. A.; Hulteen, J. C.; Van Duyne, R. P. *Langmuir* **1994**, *10*, 4109.

182. Gupta, V. K.; Abbott, N. L. *Langmuir* **1996**, *12*, 2587.

183. Stamou, D.; Gourdon, D.; Liley, N.; Burnham, N. A.; Kulik, A.; Vogel, H.; Duschl, C. *Langmuir* **1997**, *13*, 2425.

184. Wagner, P.; Hegner, M.; Guntherodt, H.-J.; Semenza, G. *Langmuir* **1995**, *11*, 3867.

185. DiMilla, P. A.; Folkers, J. P.; Biebuyck, H. A.; Harter, R.; Lopez, G. P.; Whitesides, G. M. *J. Am. Chem. Soc.* **1994**, *116*, 2225.

186. Peterlinz, K. A.; Georgiadis, R. *Langmuir* **1992**, *12*, 4731.

187. Finklea, H. O. *Electroanal. Chem.* **1996**, *19*, 109.

188. Creager, S. E.; Hockett, L. A.; Rowe, G. K. *Langmuir* **1992**, *8*, 854.

189. Ron, H.; Rubinstein, I. *Langmuir* **1994**, *10*, 4566.

190. Ron, H.; Matlis, S.; Rubinstein, I. *Langmuir* **1998**, *14*, 1116.

191. Folkers, J. P.; Laibinis, P. E.; Whitesides, G. M.; Deutch, J. *J. Phys. Chem.* **1994**, *98*, 563.

192. Laibinis, P. E.; Bain, C. D.; Whitesides, G. M. *J. Phys. Chem.* **1991**, *95*, 7017.

193. Laibinis, P. E.; Whitesides, G. M.; Allara, D. L.; Tao, Y.-T.; Parikh, A. N.; Nuzzo, R. G. *J. Am. Chem. Soc.* **1991**, *113*, 7152.

194. Laibinis, P. E.; Whitesides, G. M. *J. Am. Chem. Soc.* **1992**, *114*, 1990.

195. Scherer, J.; Vogt, M. R.; Magnussen, O. M.; Behm, R. J. *Langmuir* **1997**, *13*, 7045.

196. Schoenfisch, M. H.; Pemberton, J. E. *J. Am. Chem. Soc.* **1998**, *120*, 4502.

197. Schoenfisch, M. H.; Ross, A. M.; Pemberton, J. E. *Langmuir* **2000**, *16*, 2907.

198. Jennings, G. K.; Laibinis, P. E. *Langmuir* **1996**, *12*, 6173.

199. Jennings, G. K.; Laibinis, P. E. *J. Am. Chem. Soc.* **1997**, *119*, 5208.

200. Burgess, J. D.; Hawkridge, F. M. *Langmuir* **1997**, *13*, 3781.

201. Zamborini, F. P.; Campbell, J. K.; Crooks, R. M. *Langmuir* **1998**, *14*, 640.

202. Demoz, A.; Harrison, D. J. *Langmuir* **1993**, *9*, 1046.

203. Muskal, N.; Turyan, I.; Mandler, D. *J. Electroanal. Chem.* **1996**, *409*, 131.

204. Magnussen, O. F.; Ocko, B. M.; Deutsch, M.; Regan, M. J. *Nature* **1996**, *384*, 250.

205. Slowinski, K.; Chamberlain, R. V.; Miller, C. J.; Majda, M. *J. Am. Chem. Soc.* **1997**, *119*, 11910.

206. Mekhalif, Z.; Pireaux, J.-J.; Delhalle, J. *Langmuir* **1997**, *13*, 2285.

207. Vogt, A. D.; Han, T.; Beebe, T. P. *Langmuir* **1997**, *13*, 3397.

208. Kondo, T.; Takechi, M.; Sato, Y.; Uosaki, K. *J. Electroanal. Chem.* **1995**, *381*, 203.

209. Gu, Y.; Lin, Z.; Butera, R. A.; Smentkowski, V. S.; Waldeck, D. H. *Langmuir* **1995**, *11*, 1849.

210. Chen, K.; Xu, F.; Mirkin, C. A.; Lo, R.-K.; Nanjundaswamy, K. S.; Zhou, J.-P.; McDevitt, J. T. *Langmuir* **1996**, *12*, 2622.

211. Finklea, H. O.; Liu, L.; Ravenscroft, M. S.; Punturi, S. *J. Phys. Chem.* **2003**, *100*, 18852.

212. Whitesides, G. M.; Folkers, J. P.; Laibinis, P. E. *Langmuir* **1992**, *8*, 1330.

213. Fenter, P.; Eberhardt, A.; Liang, K. S.; Eisenberger, P. *J. Chem. Phys.* **1997**, *106*, 1600.

214. Camillone, N.; Leung, T. Y. B.; Scoles, G. *Surf. Sci.* **1997**, *373*, 333.

215. Whitesides, G. M.; Liabinis, P. E. *Langmuir* **1990**, *6*, 87.

216. Yan, J. C.; Dong, S. J. *Langmuir* **1997**, *13*, 3251.

217. Delamarche, E.; Michel , B.; Gerber, Ch.; Anselmetti, D.; Guntherodt, H.-J.; Wolf, H.; Rongsodrdf, H. *Langmuir* **1994**, *10*, 2869.

218. Camillone, N.; Chidsey, C. E. D.; Eisenberger, P.; Fenter, P.; Li, J.; Laing, K. S.; Liu, G. Y.; Scoles, G. *J. Chem. Phys.* **1993**, *99*, 744.

219. Dynarowicz-Lakta, P.; Dhanabalan, A.; Olivera Jr, O. N. *Adv. Colloid Interface Sci.* **2001**, *91*, 221.

220. Collins, S. J.; Dhathathreyan, A.; Ramasami, T.; Mohwald, H. *Thin Solid films* **2000**, *358*, 229.

221. Banerjee, S.; Bhattacharyaa, S. R.; Chakraborty, P.; Datta, A.; Ghose, D.; Kundu, S.; Sanyal, M. K. *Curr. Sci.* **2000**, *78*, 1507.

222. Yagi, K.; Fujihira, M. *Appl. Surf. Sci.* **2000**, *157*, 405.

223. Lu, W. X.; Zhou, H. L.; He, P. S.; Guo, W. H. *Thin Solid films* **2000**, *365*, 67.

224. Yoo, S.-Y.; Shin, H.-K.; Jeong, H.; Park, J.-C.; Kwon, Y.-S. *Mol. Cryst. Liq. Cyrst.* **1999**, *337*, 357.

225. Losch, R.; Stratmann, M.; Viefhaus, H. *Electrochim. Acta* **1994**, *39*, 1215.

226. Adamson, A. W.; Gast, A. P. *Physical Chemistry of Surfaces;* Sixth ed.; John Wiley and Sons, Inc.: Toronto, 1997.

227. Biddle, M. B.; Rickert, S. E.; Lando, J. B. *Thin Solid films* **1985**, *134*, 121.

228. Moore, B.; Knobler, C. M.; Broseta, D.; Rondelez, F. *J. Chem. Soc. , Faraday Trans.* **1986**, *282*, 1753.

229. Mojtabni, F. *Thin Solid films* **1989**, *178*, 115.

230. Kago, K.; Furst, M.; Matsuoka, H.; Yamaoka, H.; Seki, T. *Langmuir* **1999**, *15*, 2237.

231. Viitala, T. J. S.; Peltonen, J.; Linden, M.; Rosenholm, J. B. *J. Chem. Soc. , Faraday Trans.* **1997**, *93*, 3185.

232. Dluhy, R. A.; Ping, Z.; Faucher, K.; Prockman, J. M. *Thin Solid films* **1998**, *327/329*, 308.

233. Loschek, R.; Mobius, D. *Che. Phys. Lett.* **1988**, *151*, 176.

234. Moigne, J. L.; Gallani, J. L.; Wautelet, P. *Langmuir* **1998**, *14*, 7484.

235. Qian, D.-J.; Yang, K.-Z.; Nakahara, H.; Fukuda, K. *Langmuir* **1997**, *13*, 5925.

236. Patino, J. M. R.; Sanchez, C. C.; Nino, M. R. R. *Langmuir* **1999**, *15*, 2484.

237. Zhao, J.; Abe, K.; Akiyama, H.; Liu, Z.; Nakanishi, F. *Langmuir* **1999**, *15*, 2543.

238. Nakamura, T.; Yumoto, T.; Akutagawa, T. *Thin Solid films* **1998**, *327/329*, 450.

239. Chamberlain, J. R.; Pemberton, J. E. *Langmuir* **1997**, *13*, 3074.

240. Gallant, J.; Lavoie, H.; Tessier, A.; Munger, G.; Leblanc, R. M. *Langmuir* **1998**, *14*, 3954.

241. Weidemann, G.; Brezesinski, G.; Vollhardt, D.; Mohwald, H. *Langmuir* **1998**, *14*, 6485.

242. South Hampton Electrochemistry Group *Instrumental Methods in Electrochemistry* *40;* John Wiley & Sons Ltd.: Toronto, 1985.

243. Shen, H.; Mark, J. F.; Seliskar, C. J.; Mark, H. B. Jr.; Heineman, W. R. *J. Solid State Electrochem.* **1997**, *1*, 148.

244. Gyepi-Garbrah, S. H.; Šilerová, R. *Phy. Chem. Chem. Phy.* **2001**, *3*, 2117.

245. Finklea, H. O.; Snider, D. A.; Fedyk, J. *Langmuir* **1990**, *6*, 371.

246. Cui, X.; Jiang, D.; Diao, P.; Li, J.; Tong, R.; Wang, X. *J. Electroanal. Chem.* **1999**, *470*, 9.

247. Seung-Yeop, Y.; Hoon-Kyu, S.; Hyein, J.; Jae-Chul, P.; Young-Soo, K. *Mol. Cryst. Liq. Cyrst.* **1999**, *337*, 357.

248. Bard, A. J.; Faulkner, L. R. *Electrochemical methods;* John Wiley and Sons, Inc.: 1980.

249. Amatore, C.; Saveant, J. M.; Tessier, D. *J. Electroanal. Chem.* **1983**, *147*, 39.

250. Fawcett, W. R.; Opallo, M. *Angew. Chem. , Int. Ed. Engl.* **1994**, *23*, 21.

251. Boukamp, B. A. *Electrochem. Soc.* **1985**, *85*, 146.

252. Gileadi, E. *Electrode Kinetics for Chemists, Chemical Engineers, and Materials Scientists;* VCH Publishers, Inc.: New York, 1993.

253. Boukamp, B. A. *Solid State Ionics* **1986**, *20*, 31.

254. Jiang, S. P.; Love, J. G.; Badwal, S. P. S. *Key Eng. Mater.* **1997**, *125-126*, 81.

255. Macdonald, J. R.; Hooper, A.; Lehnen, A. P. *Solid State Ionics* **1982**, *6*, 65.

256. Macdonald, J. R.; Schoonman, J.; Lehnen, A. P. *J. Electroanal. Chem.* **1982**, *131*, 77.

257. Macdonald, J. R. *Solid State Ionics* **1984**, *13*, 147.

258. Raistrick, J. D.; Ho, C.; Huggins, R. A. *J. Electrochem. Soc.* **1976**, *123*, 1469.

259. Botelberghs, P. H.; Broers, G. H. J. *J. Electroanal. Chem.* **1976**, *67*, 155.

260. Baranski, A.; Krogulec, T.; Nelcon, L. J.; Norouzi, P. *Anal. Chem.* **1998**, *70*, 2895.

261. Rodes, A.; Achi, K. E.; Zamakhchari, M. A.; Clavilier, J. *J. Electroanal. Chem.* **1990**, *284*, 245.

262. Conway, B. E.; Barnett, B.; Angerstein-Kozlowska, H. *J. Chem. Phys.* **1990**, *93*, 8361.

263. Baranski, A. S.; Szulborska, A. *Electrochim. Acta* **1996**, *41*, 985.

264. Heyd, D. V.; Harrington, D. A. *J. Electroanal. Chem.* **1992**, *335*, 19.

265. Janek, R. P.; Fawcett, W. R.; Ulman, A. *J. Phys. Chem. B* **1997**, *101*, 8550.

266. Boubour, E.; Lennox, R. B. *J. Phys. Chem. B* **2000**, *104*, 9004.

267. Boubour, E.; Lennox, R. B. *Langmuir* **2000**, *16*, 7464.

268. Tokuda, K.; Gueshi, T.; Matsuda, H. *J. Electroanal. Chem.* **1979**, *102*, 39.

269. Finklea, H. O.; Snider, D. A.; Fedyk, J. *Langmuir* **1993**, *9*, 3660.

270. White, M. A. Thermal Analysis and calorimetry, in *Instrumental techniques for Supramolecular Chemistry*, Academic Press: New York, 2001; Chapter 4, pp. 179-223.

271. White, M. A.; Wasylishen, R. E.; Eaton, P. E.; Xiong, Y.; Pramod, K.; Nodari, N. *J. Phys. Chem.* **1992**, *96*, 421.

272. Badia, A.; Singh, S.; Demers, L.; Cuccia, L.; Brown, G. R.; Lennox, R. B. *Chem. Eur. J.* **1996** , *2*, 359.

273. Voicu, R.; Badia, A.; Morin, F.; Lennox, R. B.; Ellis, T. H. *Chem. Mat.* **2001**, *13*, 2266.

274. Strella, S.; Erhardt, P. F. *Journal of Applied Polymer Science* **1969**, *13*, 1373.

275. Cinelli, S.; Onori, G.; Santucci, A. *Colloids. Surf. B.* **2001**, *20*, 297.

276. Giacomelli, C. E.; Norde, W. *J. Colloid. Interface Sci.* **2001**, *233*, 234.

277. Akitt, J. W. *NMR and Chemistry;* 2nd ed.; Chapman and Hall: London, 1983.

278. Skoog, D. A.; Holler, J. F.; Nieman, T. A. *Principles of Instrumental Analysis;* 5th ed.; Harcourt Brace College Publishers: Philadelphia, 1997.

279. Hostetler, M. J.; Green, S. J.; Stokes, J. J.; Murray, R. W. *J. Am. Chem. Soc.* **1996**, *118*, 4212.

280. Gao, W.; Reven, L. *Langmuir* **1995**, *11*, 1860.

281. Deakin, M. R.; Melroy, O. *J. Electroanal. Chem.* **1988**, *239*, 321.

282. Mahjani, M. G.; Gobal, F.; Jafarian, M. *Indian J. Chem.* **1997**, *36A*, 177.

283. Abellà, J.; Barceló, J.; Vicotri, L. *Affinity* **1997**, *467*, 1.

284. Protsailo, L. V.; Fawcett, W. R. *Langmuir* **2002**, *18*, 8933.

285. Widrig, C. A.; Chung, C.; Porter, M. D. *J. Electroanal. Chem.* **1991**, *310*, 335.

286. Muscik, M. D.; Pena, D. J.; Botsko, S. L.; McEvoy, T. M.; Richardson, J. N.; Natan, M. J. *Langmuir* **1999**, *15*, 844.

287. Badia, A.; Demers, L.; Dickinson, L.; Morin, F.; Lennox, R. B.; Reven, L. *J. Am. Chem. Soc.* **1997**, *119*, 11104.

288. Kang, S. Y.; Kim, K. *Langmuir* **1998**, *14*, 226.

289. Kolb, D. M.; Schneider, J. *Electrochim. Acta* **1986**, *31*, 929.

290. Hamm, U. W.; Kolb, D. M. *J. Electroanal. Chem.* **1992**, *332*, 339.

291. Kaganer, V. M.; Mohwald, H.; Dutta, P. *Rev. Mod. Phys.* **1999**, *71*, 779.

292. Chen, K.-B.; Chang, C.-H.; Yang, Y.-M.; Maa, J.-R. *Colloids. Surf. A.* **2000**, *170*, 199.

293. Overbeck, G. A.; Honig, D.; Mobius, D. *Langmuir* **1993**, *9*, 7999.

294. Lawrie, G. A.; Barnes, G. T. *J. Colloid. Interface Sci.* **1994**, *162*, 36.

295. Reitzel, N.; Greve, D. R.; Kjaer, K.; Howes, P. B.; Jayaraman, M.; Savoy, S.; McCullough, R. D.; McDevitt, J. T.; Bjornholm, T. *J. Am. Chem. Soc.* **2000**, *122*, 5788.

296. Kegami, K.; Lan, M.; Nakamura, T. *J. Chem. Phys.* **2000**, *112*, 881.

297. Aizenberg, J. *J. Chem. Soc. , Chem. Commun.* **2000**, *21*, 3963.

298. *Handbook of Chemistry and Physics;* Chemical Rubber Company: New York, 1998.

299. Kampf, J. P.; Frank, C. W. *Langmuir* **1999**, *15*, 227.

300. Fawcett, W. R.; Opallo, M. *Angew. Chem. , Int. Ed. Engl.* **1994**, *33*, 2131.

301. French, M.; Creager, S. E. *Langmuir* **1998**, *14*, 2129.

302. Cheng, Q.; Brajter-Toth, A. *Anal. Chem.* **1992**, *64*, 1998.

303. Nuzzo, R. G.; Korenic, E. M.; Dubios, L. H. *J. Chem. Phys.* **1990**, *93*, 767.

304. Dubois, L. H.; Zegarski, B. R.; Nuzzo, R. G. *J. Electron. Spectrosc. Relat. Phenom.* **1990**, *54/55*, 1143.

305. Hauptman, J.; Klein, M. L. *J. Chem. Phys.* **1990**, *93*, 7483.

306. Hauptman, J.; Bareman, J. P.; Mar, W.; Klein, M. L. *J. Chem. Soc. , Faraday Trans.* **1991**, *87*, 2031.

307. Siepman, J. I.; McDonald, I. R. *Langmuir* **1993**, *9*, 2351.

308. Dijksma, M.; Boukamp, B. A.; Kamp, B.; van Bennekom, W. P. *Langmuir* **2002**, *18*, 3105.

309. Downard, A. J.; Prince, M. J. *Langmuir* **2001**, *17*, 5581.

310. Downard, A. J. *Langmuir* **2000**, *16*, 9680.

311. Corvera, E.; Mouritsen, O. G.; Singer, M. A.; Zuckerman, M. J. *Biochim. Biophys. Acta* **1992**, *1107*, 261.

312. Laibinis, P. E.; Whitesides, G. M.; Allara, D. L.; Tao, Y.-T.; Parikh, A. N.; Nuzzo, R. G. *J. Am. Chem. Soc.* **1991**, *112*, 7167.

313. Snyder, R. G.; Strauss, H. L.; Ellinger, C. A. *J. Phys. Chem.* **1982**, *86*, 5145.

314. Papahadjopoulous, D.; Jacobson, K.; Nir, S.; Isac, T. *Biochim. Biophys. Acta* **1973**, *311*, 33.

315. Marsh, D. *Handbook of Lipid Bilayer Membranes;* CRC Press: Boca Raton, 1991.

316. Steven, E. S.; Sugawara, N.; Bonora, G. M.; Toniolo, C. C. *J. Am. Chem. Soc.* **1980**, *102*, 7044.

317. Kessler, H. *Angew. Chem. , Int. Ed. Engl.* **1982**, *21*, 512.